Alma Mater Studiorum - Università di Bologna

DOTTORATO DI RICERCA IN

INGEGNERIA CIVILE, CHIMICA, AMBIENTALE E DEI MATERIALI

Ciclo 35

Settore Concorsuale: 08/A2 - INGEGNERIA SANITARIA - AMBIENTALE, INGEGNERIA DEGLI IDROCARBURI E FLUIDI NEL SOTTOSUOLO, DELLA SICUREZZA E PROTEZIONE IN AMBITO CIVILE

Settore Scientifico Disciplinare: ING-IND/28 - INGEGNERIA E SICUREZZA DEGLI SCAVI

NUMERICAL MODELLING OF ROCK MASSES INTERACTING WITH DAMS: THE CASE OF RIDRACOLI

Presentata da: Edoardo Lusini

Coordinatore Dottorato

Alessandro Tugnoli

Supervisore

Daniela Boldini

Co-supervisore

Guido Gottardi

Esame finale anno 2023

Abstract

A three-dimensional Direct Finite Element procedure is here presented which takes into account most of the factors affecting the interaction problem of the dam-water-foundation system, whilst keeping the computational cost at a reasonable level by introducing some simplified hypotheses. A truncated domain is defined, and the dynamic behaviour of the system is treated as a wave-scattering problem where the presence of the dam perturbs an original free-field system. The rock foundation truncated boundaries are enclosed by a set of free-field one-dimensional and two-dimensional systems which transmit the effective forces to the main model and apply adsorbing viscous boundaries to ensure radiation damping. The water domain is treated as an added mass moving with the dam. A strategy is proposed to keep the viscous dampers at the boundaries unloaded during the initial phases of analysis, when the static loads are initialised, and thus avoid spurious displacements. A focus is given to the nonlinear behaviour of the rock foundation, with concentrated plasticity along the natural discontinuities of the rock mass, immersed in an otherwise linear elastic medium with Rayleigh damping. The entire procedure is implemented in the commercial software Abaqus®, whose base code is enriched with specific user subroutines when needed. All the extra coding is attached to the Thesis and tested against analytical results and simple examples. Possible rock wedge instabilities induced by intense ground motion, which are not easily investigated within a comprehensive model of the dam-water-foundation system, are treated separately with a simplified decoupled dynamic approach derived from the classical Newmark method, integrated with FE calculation of dam thrust on the wedges during the earthquake. Both the described approaches are applied to the case study of the Ridracoli arch-gravity dam (Italy) in order to investigate its seismic response to the Maximum Credible Earthquake (MCE) in a full reservoir condition.

Key words: Ridracoli Dam, dynamic analysis, dam-water-foundation interaction, free-field boundaries, Abaqus, user subroutines, rock wedge stability, Newmark method

Acknowledgement

The present PhD research has been funded by Romagna Acque – Società delle Fonti S.p.A. I wish to acknowledge the single individuals that collaborated with me during these three years, namely Dr. Eng. Giuseppe Montanari (Chief Technical Manager of Romagna Acque) and Dr. Eng. Giulia Buffi (Engineer of Romagna Acque and my primary internal reference person). I also express my gratitude to Dr. Tonino Bernabè (President of Romagna Acque), Dr. Eng. Nicola Scarcella (General Manager of Romagna Acque) and Dr. Piero Lungherini (Manager of Romagna Acque) for their support and esteem. I wish to pay a special tribute the memory of Dr. Eng. Andrea Gambi (former General Manager of Ramagna Acque) who made this experience possible and always supported my work from the first time we met. A special thank for their willingness to Dr. Fabrizio Cortezzi (Technical Manager of Ridracoli Dam) and Mr. Massimo Baccini (Ridracoli Dam technician) which provided me with precious data about the monitoring system of Ridracoli.

I would like to thank my supervisor Prof. Dr. Eng. Daniela Boldini for her constant presence, guidance and spur. I also acknowledge my co-supervisor Prof. Dr. Eng. Guido Gottardi who included me in the activities of the department, and all the colleagues, technicians and professors of DICAM department at Bologna University.

I would like to thank all the people outside my university which whom I had the honour to collaborate with or simply provided me with precious advices, namely Dr. Eng. Luca Verrucci, Prof. Dr. Eng. Alessandro Graziani, Dr. Eng. Arnkjell Løkke and Prof. Dr. Eng. Luigi Callisto.

Table of contents

1. Introduction

1.1 Problem statement and motivations

For the Italian code specific for dams and barrages, "Norme tecniche per la progettazione e la costruzione degli sbarramenti di ritenuta (dighe e traverse)" (NTD, 2014), a "large dam" is defined as a barrier which is either higher than 15 m or impounds a water volume larger than 1.000.000 m^3 (NTD, 2014). At present, there are 531 dams classified as large in the Italian territory, with an average age of about 64 years (CNIT, 2019), higher than the so called "alert" age of 50 years. Moreover, a significative portion of these structure are built in seismic areas. In the NTD code a distinction is made between existing dams and new structures. A whole section is dedicated to the dams whose construction works were terminated before 2014, year of publication of the code. In these cases, an evaluation of the overall safety of all existing dams is prescribed under the control of a surveillance authority. The importance of an adequate geological and geotechnical characterization, also in the context of the evaluation of the seismic response of the dam, is expressly stated.

Romagna Acque – Società delle Acque S.p.A., as the founder of the present PhD work and managing body of Ridracoli large concrete arch-gravity dam, expressed interest in deepening the comprehension of the rock mass behaviour underlying the dam under severe seismic conditions. In particular, it was required to include in an existing Finite Element model of the dam, realised with the commercial code Abaqus® as part of a previous PhD work (Buffi, 2018), the possible non-linear behaviour in correspondence of known rock-mass discontinuities which outcrop at the level of dam base and are characterised by a considerable extension (i.e., a fault and some specific bedding planes). The use of the code Abaqus® was strongly recommended because of the compatibility with the model in Buffi (2018). The main focus in Buffi (2018) work was given to the structural aspects, with the underlying rock mass considered as monolithic, linear elastic and fixed at the base and at the side boundaries. On the contrary the dam was realistically represented with single blocks and joints geometrically reconstructed from a UAV dense point cloud. The water mass was modelled with the help of solid acoustic elements and the radiation damping at water boundary was included by means of non-reflecting surfaces. The static and dynamic behaviour of the dam was investigated, giving a particular attention to the modal analysis of the system and the verification of natural frequencies against experimental values.

As far as it can be ascertained, none of existing large concrete dams with full reservoir has experienced an extremely intense ground shaking, comparable to the Maximum Credible Earthquake (MCE). At least two gravity dams, however, were subjected to quite intense ground shaking when the reservoir level was close to the maximum, namely Koyna Dam (India) and Hsinfengkiang Dam (China) during 1967 and 1962 earthquakes, respectively. Both dams exhibited a significative cracking pattern in the upper part at the end of the shaking which, however, did not cause an outflow of the impounded water. Other few dams

have withstood very intense ground shaking with little or no damage such as in the case of the 42-m-high Lower Crystal Springs Dam (USA), because of their extremely prudential design strategies (Chopra, 2020).

In the chapter dedicated to arch dams of the American Federal Energy Regulatory Commition guidelines (FERC, 2018) a list of intense seismic events occurred in the vicinity of concrete arch dams is presented. In general, this typology of construction exhibits an excellent level of performance with respect to earthquake motion and no failure has ever been recorded. The statistic validity of this assumption however is strongly affected by the low number of major earthquakes occurred at arch dam locations. Among 43 arch dams which have experienced significant earthquake excitation, only 4 were subjected to a seismic event comparable to the MCE and close to the dam site (but with a water level considerably lower than the maximum regulation level). They were Pacoima, Lower Crystal Springs, and Gibraltar dams in the United States, and Ambiesta Dam in Italy. Among these only Pacoima Dam (113-m-high) suffered damage during two seismic events (1971 and 1993). The dam survived both earthquakes, despite showing some cracking near the left abutment and some unrecoverable slips and opening along the contraction joints, mostly at the crest level. Two rock wedges were observed forming on the left abutment and were suspected to drive the irreversible deformations of the dam body. One of wedge slipped of about 9 cm after 1993 earthquake (FERC, 2018).

It is clear from the preceding case history that, although being less susceptible than gravity structure, also arch dams can experience a significative level of damage due to intense ground shaking. From the Pacoima Dam experience it is also clear that one of the most concerning damage mode is related to the stability of rock wedges possibly present at the level of the abutment rock mass, which my act as a trigger for joint opening and cracking in the structure. The ability to accurately simulate the effects of the MCE by means of numerical models which can adequately take into account the complexity of the problem is essential in order to assess the safety of existing concrete structures like Ridracoli Dam. However, the prediction of performance during earthquakes is challenging and affected by numerous uncertainties. The main factors that should be included in a numerical analysis are (Chopra, 2020):

- complicated shapes dictated by the topography of the site;
- interaction of the motions of the dam with the impounded water and the foundation rock (important aspects to consider are the mass, the stiffness, the material damping and the radiation damping of the foundation, as well as the earthquake-induced hydrodynamic pressures);
- opening or slip in contraction joints (inside the structure), lift joints (at dam-foundation interface) and along natural discontinuities of the rock mass; all these phenomena are highly non-linear;
- topographic site effects on the seismic signal.

After introducing the Ridracoli Dam case study in the remaining part of **Chapter 1**. A performance-based displacement approach for the analysis of rock wedges on arch-dam

abutments in seismic conditions is presented in **Chapter 2**, applying a three-dimensional version of Newmark method (Newmark, 1965) to two wedges on the right abutment of Ridracoli Dam. In **Chapter 3** a Direct Finite-Element procedure to evaluate the seismic response of a dam–water–foundation systems subjected to ground shaking is described, considering all the factors in the bullet list. **Chapter 4** is dedicated to the application of the Direct FE procedure to the Ridracoli Dam case study: the building of the model from available date sources is described together with the numerical strategies to deal with the structure, the impounded water and the rock mass. A conclusive final chapter is then provided which summarises the main results obtained in **Chapter 2** and **Chapter 4**.

1.2 Ridracoli Dam

Ridracoli Dam is a concrete arch-gravity dam across the upper valley of the Bidente River, in the municipality of Bagno di Romagna (FC), Italy (**Figures 1.1** and **1.2**). Since the early sixties the valley had been investigated for its potential to support a dam that would had supply drinking water, control floods, and, only secondarily, produce hydroelectric power (RA, 2001). The location of the valley, not far from the Appenine ridge, in an unpopulated wooded area, made it particularly propitious for storing and intaking water, owing to the high quality of the water and the low erosion rate. A positive decision was made in 1974; the winning bid to build the dam was submitted by a consortium named Coridra General Contractor, which began construction work in spring 1975 (RA, 2001). The dam was completed in seven years by spring 1982 and entered the commissioning phase, with the first reservoir filling in 1986 (Buffi, 2018). It was dedicated as the main feature of Romagna Aqueduct in 1988, in the presence of Giovanni Spadolini (then-president of Italian Senate). It has been completely operational since 1995 (RA, 2022). In the Italian context, Ridracoli Dam is one of the youngest large dams.

The storage reservoir is managed by Romagna Acque – Società delle Fonti S.p.A. and serves to supply drinking water to around 50 communities in Forlì-Cesena, Rimini and Ravenna Provinces, including the microstate of San Marino. Enel Green Power S.p.A. has been granted a 50-years concession of a hydroelectric power plant which exploits a 250-m head from the dam to the bottom of the valley downstream (near the village of Santa Sofia, in province of Forlì-Cesena) (RA, 2022).

Ridracoli dam general data are (Oberti et al., 1986):

- maximum height 103.50 m
- maximum water level 557.30 m a. s. l.
- reservoir storage capacity 30 Mm^3
- power generation (2021) (RA, 2022) 31.8 GWh

Figure 1.1. Aerial view of Ridracoli Dam during construction work (courtesy of Romagna Acque – Società delle Fonti S.p.A.)

Figure 1.2. View of Ridracoli Dam in 1982, at the end of construction works (courtesy of Romagna Acque – Società delle Fonti S.p.A.)

1.2.1 Structure

The dam body consists in a double-curvature arch structure, nearly symmetrical with respect to the main section, resting on a foundation pulvinus that runs along the excavation profile with varying thickness, and extends to the crowning with a minimum width of 10 meters (RA, 2001).

The structure is radially divided into 27 blocks separated by 26 joints consisting of nearly vertical surfaces (RA, 2001), which in their lower section are curved so that the angle of incidence with the upper surface of the pulvinus is approximately right. This surface, which constitutes the peripheral joint, is sole-shaped in correspondence of the main section, but it gradually changes into a cradle-shaped outline while proceeding toward the abutments to better support the thrust of the arches.

Both within the pulvinus and within the body of the dam, inspection tunnels are arranged to allow all waterproofing and consolidation works and to ensure the complete drainage of seepage water, which can then be measured and discharged downstream of the dam. Some of these tunnels further extend into the rock mass of both abutments at different elevations. A grout curtain extends from these tunnels down to a minimum depth of 75 m below the pulvinus base level, upstream dipping with an inclination of 30 - 35°. It covers the entire longitudinal development of the dam and further extends in the rock mass at both sides where it reaches a depth of 200 m (Oberti et al., 1986).

The entire structure was built using specially designed mixture of sand and crushed stone with a maximum grain size of 120 mm, bonded with pozzolanic cement type 325 with low heat development. Although it is an unreinforced concrete work, improved adhesion steel bars were used extensively to minimize the shrinkage phenomenon (RA, 2001).

The spillway crest is of the ogee type. It is 119 m long and divided into 8 openings of 14 m each. At toe of the dam there is a stilling basin trapezoidal-shaped in plan, with a maximum width of about 120 m and a minimum one of 60 m corresponding to an end-sill with a 14 m wide spillway (RA, 2001).

Ridracoli dam structural data are (Oberti et al., 1986):

- crest elevation 561.00 m a. s. l.
- minimum pulvinus base elevation 457.50 m a. s. l.
- longitudinal development of the crest 432.00 m
- chord of the crest arc 341.45 m
- volume of the dam 590 000 m^3
- thickness of the main section at different elevations:
  - crest level (561.00 m a. s. l.) 6.62 m
  - structure base level (475 m a. s. l.) 25.18 m
  - pulvinus base level (460 m a. s. l.) 36.46 m

1.2.2 Geology

The area under study consists of Miocene rocks of the Marly-Arenaceous Formation (FMA). In particular, the Premilcuore Member (FMA3) and the Galeata Member (FMA4) outcrops at the bottom of the lake, while the structure is founded on the Premilcuore Member only (RER, 2022). A geological map of the area is extracted from regional online database (RER, 2022) and shown in **Figure 1.3**.

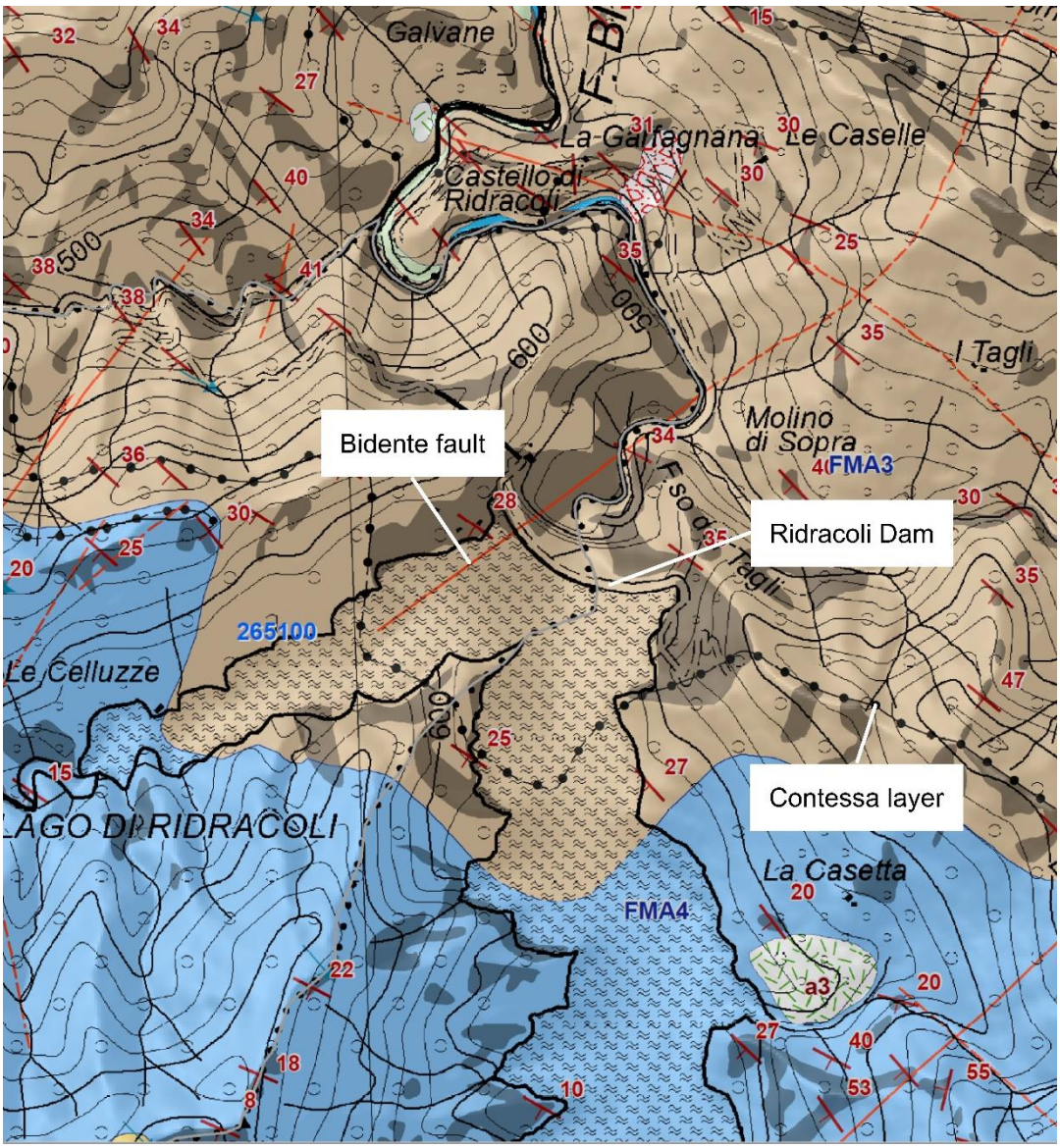

Figure 1.3. Geologic map Ridracoli area, scale 1:10 000 (RER, 2022): (in light-blue) Marly Arenaceous Formation – Galeata Member; (in light-brown) Marly Arenaceous Formation – Premilcuore Member. Contessa.

The Marly-Arenaceous Formation is an example of a turbiditic deposit formed in a foreland basin; turbiditic sequences are alternated with hemipelagic sediments. It therefore consists in alternating strata of sandstones, siltstones and marls. Each sequence has a thickness varying from a few centimetres to over 7 m. The sandstones are graded, generally medium to very fine, with sedimentary structures (flute and groove-casts at the base, plane-parallel lamination in the lower part, ripples and convolute lamination in the upper part); layers range from very thick to medium, sometimes thin, with generally tabular geometry. The drag marks at the base indicate predominant turbiditic contributions from WNW/NW and subordinately from ESE/SE. At the roof of arenitic levels the pelites are grey and laminated; in less arenaceous successions, above the laminated pelites, in direct contact with the overlying arenites, silty, light grey, compact marls are frequently observed (RER, 2022).

In the Premilcuore Member the pelite-sandstone ratio is 2>A/P>1/2. Sandstones are mainly thick and very thick beds with uniform-tabular geometry, the upper limit is sometimes placed at the Contessa key bed (RER, 2022).

The Contessa key bed is a graded megastratum where the arenite, with generally medium-fine to very fine grain size, is rich in limestone fragments. The lithic arenite part varies in thickness from 2.8 to more than 5 meters while the pelite part varies from 5 to 8 meters; the A/P ratio is fairly constant and always less than 1 (RER, 2022).

In the Galeata Member the pelite-sandstone ratio is 1/2>A/P>1/3. The arenite is generally in thin to thick beds with tabular geometry. Several key beds with predominantly calcareous composition and SE provenance have been mapped in this Member (i.e. Contessa) (RER, 2022).

Overall, in the reservoir area the percentage of the marly fraction is equal to that of the arenaceous fraction, and the formation can be considered as homogeneous. The average thickness of the sandstone beds is about 1.00 m, with infrequent maxima of 3.00 m. Marl layers are on average thinner, and the maxima do not usually exceed 2.00 m. The percentage of marl varies within the succession affecting the dam basement from a minimum of 48.5% to a maximum of 64%, with average value of 56.3% (Alpina, 1974). Limiting the analysis to the portion of the stratigraphic sequence directly affected by the dam, the mean spacing between bedding planes is about 0.48 cm (Alpina, 1976).

On a tectonic point of view, the whole regional setting is the expression of a general compression from SW to NE. In the mountainous area under study this trend resulted in vast zones elongated in the NE-SW direction, from 3 to 6 km wide and separated by subparallel, SW-dipping reverse faults (Alpina, 1974). Ridracoli zone exhibits monoclinal strata dipping on average 25-35° to the SW. These structures are affected by disjunctive high-angle faults arranged with an “Antiapennine” direction. One of these faults, the Bidente Fault (F), affects the imposing area of the dam on the left abutment and causes a mismatch of the stratigraphic sequence: the fault is oriented 140°/70°-90° with a normal slip, which going from north to south, varies from 18 m downstream of the dam to 41 m at

the dam base. It is formed by a shear band, approximately 1.5 m thick, with a core zone of 0.5 m where the rock mass is reduced to a breccia (Alpina, 1974).

The local jointing pattern shows three main discontinuity sets (**Figure 1.4**), namely, the bedding planes (ST, average orientation 218°/27°), dipping upstreamward relative to the dam, and two set of subvertical joints, approximately directed parallel (KKD) and perpendicular (KKI) to the bedding direction. These subvertical joints have openings of 1 to 3 mm, filled with calcite and at times with clay only in the most decompressed and surface areas (Oberti et al., 1986). The orientation of the main discontinuity sets with respect to the dam structure is schematically depicted in **Figure 1.5**.

In few cases, four in total, at sandstone-marl bed contacts a centimetre-thick laminated marl interbedding can be detected. Their traces on the right abutment of the dam are shown in **Figure 1.6**. It is formed mostly by overlapping sheets of fibrous calcite which sandwich thin layers of clay. Clear displacement marks are present. On the basis of this evidence, Lembo Fazio et al. (1990) hypothesised that these laminated marl layers are shear veins of tectonic origin formed by a crack-seal mechanism with a relatively large shear displacement.

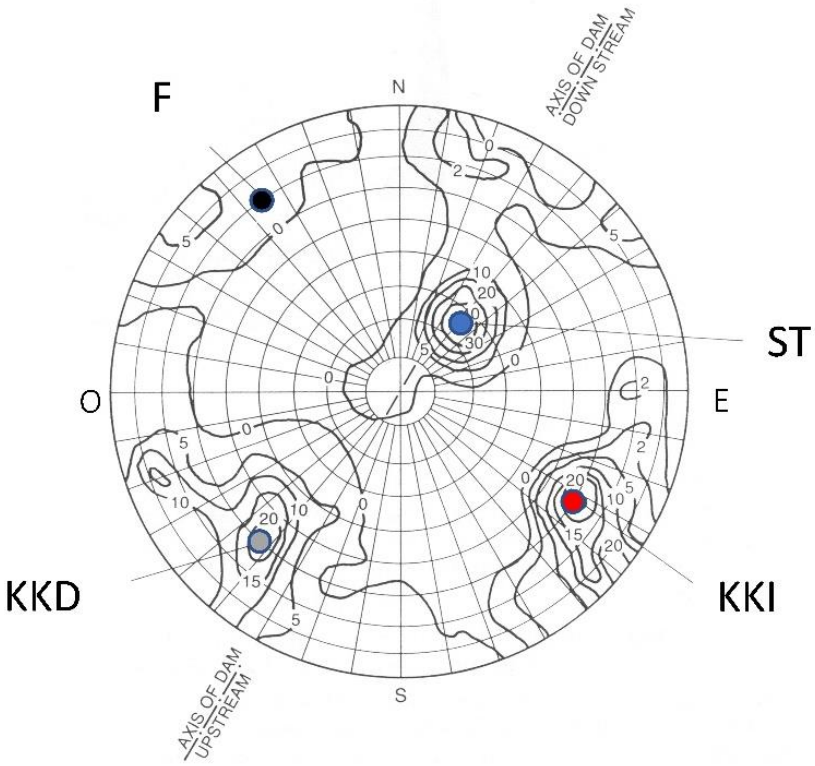

Figure 1.4. Stereographic projection of the mean planes of the main discontinuity sets (SST, KKI, KKD) and single structures (F) affecting Ridracoli site (modified from Oberti et al., 1986)

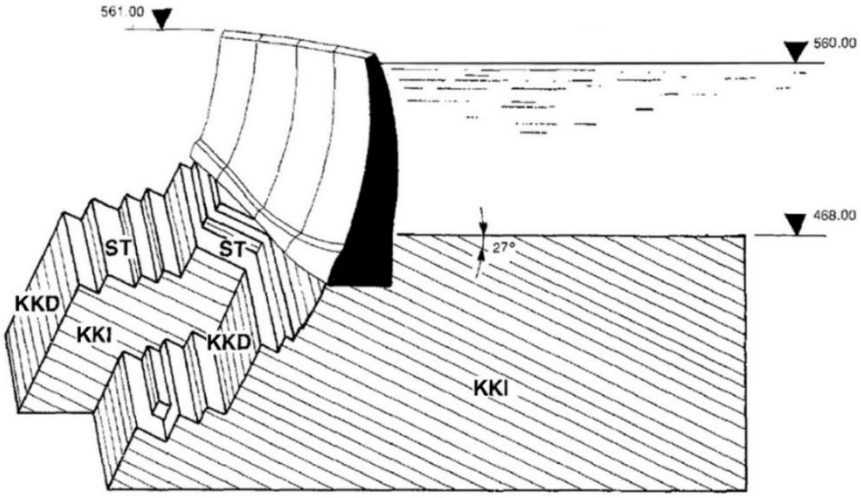

Figure 1.5. Structural scheme of the rock foundation (modified from Oberti et al., 1986)

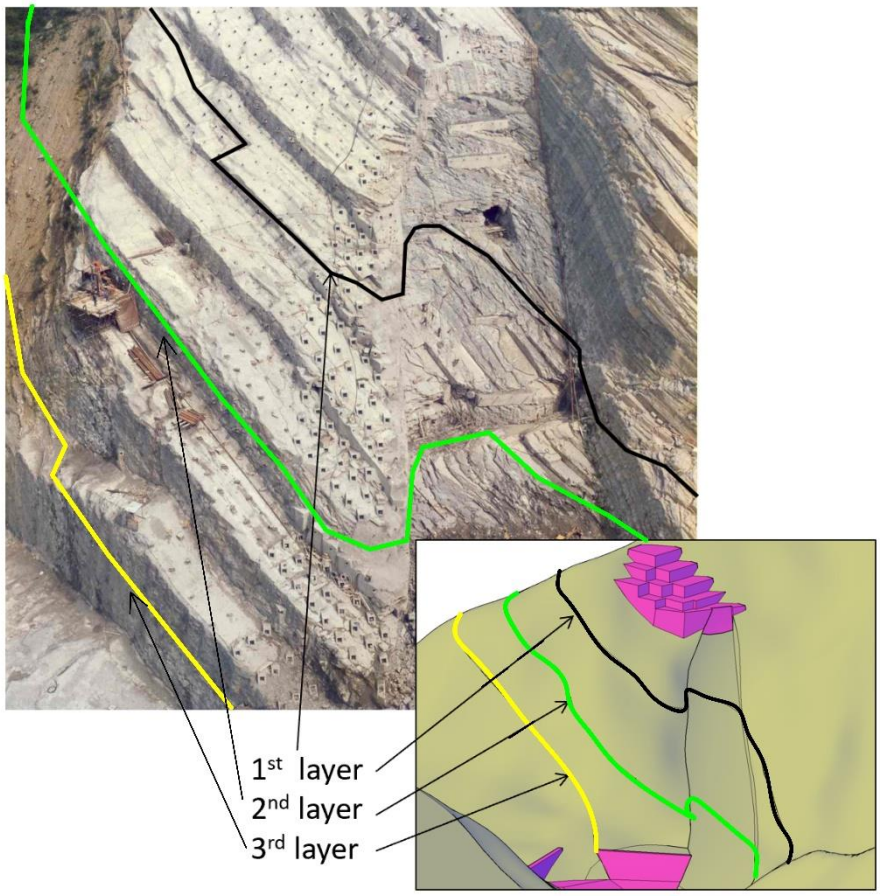

Figure 1.6. Laminated marl layers on the right abutment.

In a final note included in the design project of the dam (Alpina, 1981) the authors observed that at least two other laminated layers interest the rock foundation of the left abutment below the so-called "third laminated layer", and some minor diaclase associated with Bidente fault are present on both abutments. Their modest extension, however, was considered as a valid reason to not include their representation in the dam-foundation-water system here developed.

As stated in the Geomechanical Report included in the final project of the dam (Alpina, 1976), the persistence of ST set (i.e., the bedding planes) is considered as infinite with respect to the characteristic length of the problem (i.e., about 80 m). In general, the disturbance which the rock mass withstood in his relatively young geological history is low; it can be assumed that the marl layers deformed in a ductile fashion whereas sandstone fractured.

KKI/D are orthogonal joint sets exclusively affecting the sandstone layers that are the most brittle *facies* of the rock formation. Since they were originated by tension stresses, their joint walls are rough or little wavy. The mean opening for both sets is in the interval 1-3 mm, with frequent calcite veins. A mean spacing of about 1.80 m and 1.60 m characterise respectively the KKI and KKD joints. A clear dependency of the spacing on the thickness of the sandstone layer is observed: the thicker the layer the larger the spacing. In the marly component minor, less distinguishable and more dispersed joint sets can be found, which tend to generate conchoidal fractures at failure. Therefore, persistence of KKI/D joints cannot be extended beyond the boundaries of single sandstones layers, while the alternated marly layers can be considered as rock bridges with degraded shear and tensile strength, as schematically depicted in **Figure 1.7**.

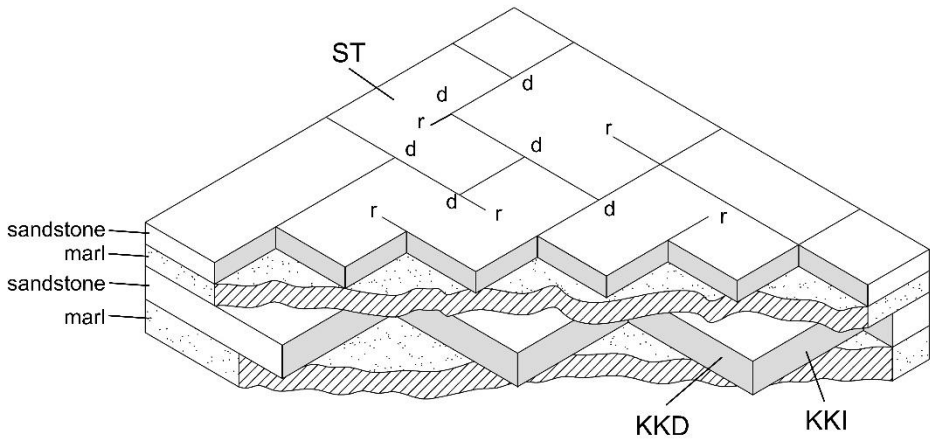

Figure 1.7. Detailed structural scheme of the rock formation with orthogonal joint sets KKI and KKD and their typical pattern; joints are limited to the sandstone *facies*; the relative spacing proportions are maintained.

Within every single sandstone layer, adopting a persistence parameter, K, expressed as the percent ratio between the "discontinuous area" and the total area of the plane (Einstein et al., 1983), KKI joints present a persistence of K = 14%, while KKD joints of K = 25%. At Ridracoli site KKI and KKD joint terminations are frequently of d-r, r-d or d-d type (**Figure 1.7**), where r denotes a termination against intact rock and d a termination against another discontinuity. Since they are orthogonal and the spacing is small if compared to the scale of the problem, it can be supposed that a failure surface could develop simultaneously involving both sets. A K = 100% would be appropriate in this case for a single sandstone layer, while a K = 45% should be assumed when the whole sequence is considered, corresponding to the sandstone percentage. The possible developing of a failure surface is depicted in the scheme of **Figure 1.7**, with a stepped failure surface involving both KKI and KKD joints in the sandstone layers and a new-developed fracture cutting across the marl layers.

A sliding event of modest extension along a weak bedding plane occurred in the past during the construction work, as reported in Bavestrello (1983) and in **Figure 1.8**. The sliding mass consisted of a single sandstone layer laterally delimited by a plane oriented as KKI joints. The event was facilitated by the presence of a sub-horizontal diaclasis, which interrupted the continuity of the strata.

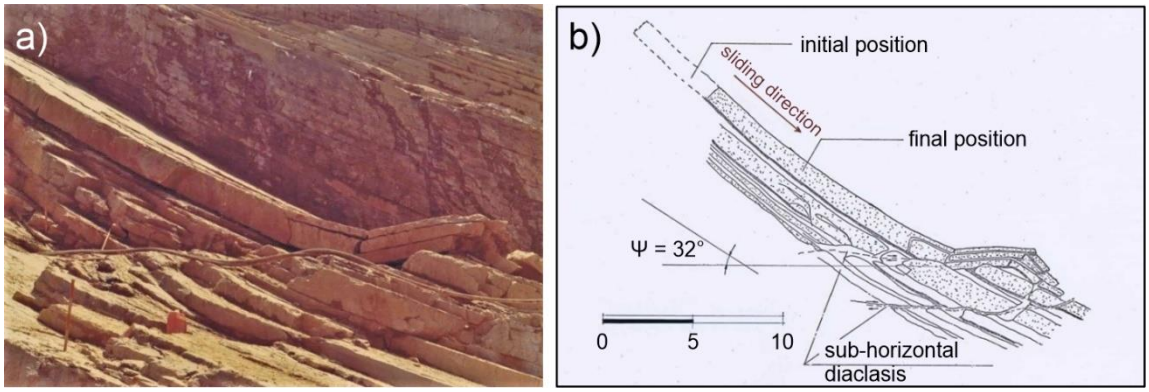

Figure 1.8. Slid sandstone block at Ridracoli during construction works (November 1977): a) photographic documentation (courtesy of F. Bavestrello Engr.); b) pictorial scheme of the sliding event (modified from Bavestrello (1983)).

1.2.3 Geotechnical characterization

A wide investigation was carried out to determine the mechanical characteristics of the different lithotypes, particularly of the marl and siltstone materials. Over 200 undisturbed samples were cored from the foundation area.

Uniaxial and triaxial compressive tests were performed mainly on marl and siltstone specimens to study the deformability and strength characteristics of these lithotypes (generally weaker than sandstones) as a function of the relative angle between the specimen axis and the bedding planes. For this purpose, samples were cored with three different inclinations 0° - 30° - 45°. The results of tests carried out with the confining pressures of 0 - 2.5 - 5.0 - 10 - 15 MPa showed a marked fall in the strength with increasing angles. Such a decrease is more evident for low values of the confining pressure. Regardless of specimen orientations, a mean value of uniaxial shear strength of 46.5 MPa was found, limited to siltstones and marls. Additional uniaxial compression tests were carried out in order to determine the strength characteristics of marl after 20 loading cycles (between 0 and 6 MPa) and after 10 wetting-drying cycles. It was observed that these severe testing conditions determine only a slight decrease of uniaxial strength (less than 20%) (Oberti et al., 1986). Concerning the sandstone lithotype, a mean uniaxial shear strength of 55 MPa (with maximum values above 100 MPa) was obtained from specimens sampled during the excavation of the diversion tunnel (Grandori et al., 1990).

During the construction phase, several in situ tests, including hydraulic chamber tests and plate loading tests, were performed in order to assess the stiffness characteristics of the rock mass under operational conditions, i.e., for the normal stress interval predicted at the rock-concrete interface (2–4 MPa) (Oberti et al., 1986). Special attention was given to the anisotropy of the rock mass owing to its stratified structure. The elastic and deformability moduli measured in directions respectively parallel and perpendicularly to the bedding planes are summarized in **Table 1.1**. The results, rather dispersed, suggest a mild anisotropy, with slightly larger stiffness in the direction parallel to the bedding. Some flat jack tests were performed to determine the rheological properties, particularly of the marly lithotype, by means of long-term loading tests under a sustained pressure of 10 MPa (about 3 times the maximum normal stress induced by the dam). Under these very conservative testing conditions the creep deformation measured after 50 days was about the 60 – 70% of the instantaneous one (Oberti et al., 1986).

Several Lugeon permeability tests allowed to define a mean permeability coefficient in the interval $1 \cdot 10^{-7} – 4 \cdot 10^{-7}$, decreasing with depth (Oberti et al., 1986). The foundation rock mass may be considered, as a whole, to be slightly permeable, with seepage limited to joints affecting the sandstone lithotype.

Table 1.1. Reversible (elastic) mean modulus, E_e, obtained from in situ tests (Oberti et al., 1986).

	E_e // (MPa)	$E_e \perp$ (MPa)
Hydraulic chamber test	18.0	16.0
Plate loading test	24.0	18.0

Within the exploration tunnels bored during the construction work, 6 direct shear tests were performed on specially prepared blocks, including 3 on joints consisting of laminated marl with local levels of recrystallization calcite, 2 on sandstone/marl contacts and 1 on intact marl block. At the ground surface 7 additional shear tests were carried out on one of the four detected laminated marl joints (Lembo Fazio et a., 1990; Alpina, 1976). All direct shear tests data points in terms of peak and residual τ - σ_n couples are plotted in **Figure 1.9**.

A marked difference in the friction angle can be observed between common sandstone/marl contacts and laminated marl joints, from over 30° to about 13° (Lembo Fazio et al., 1990). The cohesion is very variable also depending on different test equipment: a relatively high value (c' = 200 kPa) can be obtained for laminated marl layers interpolating only surface-test data points (Oberti et al., 1986), while a near-zero value was obtained for the same layer in an exploratory tunnel (with a less precise equipment) (Lembo Fazio et al., 1990).

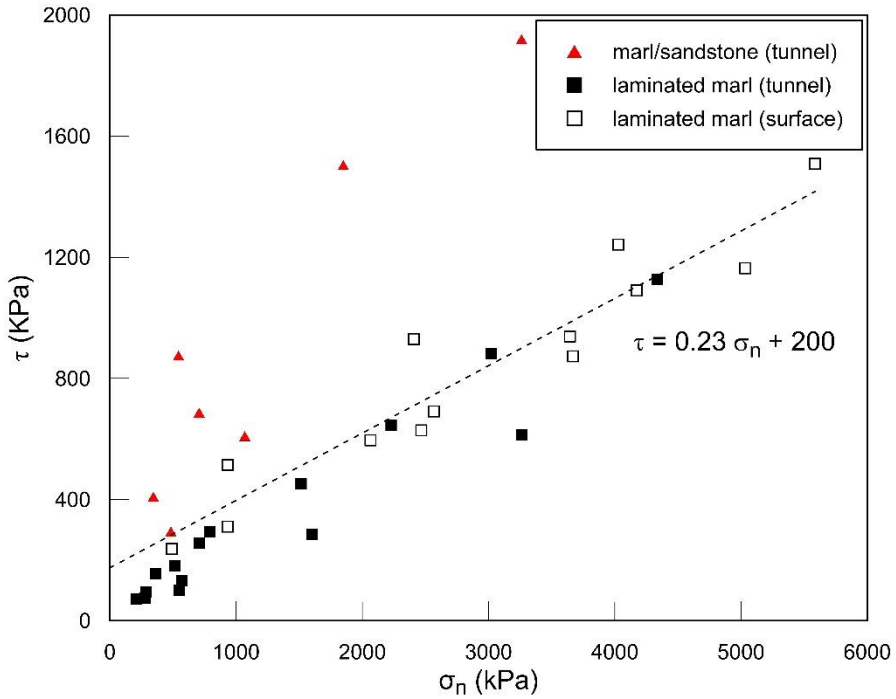

Figure 1.9. Direct shear tests results in terms of τ - σ_n pairs

The relatively high value of cohesion for very low stress levels can be explained by the presence of recrystallization calcite platelets between the thin clay layers forming the sheared bedding joints.

Stress-displacement curves in the normal and tangential directions denote an elastoplastic behaviour with negligible brittleness and dilatancy. Shear and normal stiffness moduli of about 2 MPa/mm and 2.5 MPa/mm respectively can be considered as representative of the laminated joints in the test stress interval (0-6 MPa) (Lembo Fazio et al., 1990).

Cross-hole tests performed at the design stage in 20 vertical boreholes, along the curved axis of the dam, gave P-waves velocities generally higher than 4000 m/s (Alpina, 1976). The highest velocities, up to 5000 m/s, were measured in the bottom part of the valley. The right abutment resulted slightly stiffer than the left, possibly for the presence of the fault. The effect of construction work was investigated repeating the measurement in the same boreholes, before and after the casting of the dam and the grouting of the curtain. An overall increase in stiffness was detected (Oberti et al., 1986).

On May 9, 2020 a down-hole test was performed (SolGeo, 2020) in a new borehole 40-m deep and vertically oriented, located on the right abutment. Results of this test are plotted in **Figure 1.10** and confirm previous findings. Apart from the first loosened 10 meters, wave velocities are almost constant with depth, oscillating around 2000 m/s and 4000 m/s, for shear and compressive waves respectively.

1.2.4 Seismicity

The seismic hazard model MPS04 (Stucchi et al., 2011), referred to by the Italian technical regulations (NTC, 2018), is based on the seismogenetic zonation (ZS9) of the entire national territory first published in 2004 (Meletti et al., 2006).

Ridracoli area was the subject of a specific seismotectonic study performed by the Italian National Institute of Oceanography and Applied Geophysics (OGS, 2014). The study is based on a different zonation, especially regarding the definition of homogeneous seismogenetic zones in northern Apennine territory, between Emilia-Romagna and Tuscany.

In particular, Ridracoli site is affected by the so-called "zone 531 – Appennino Romangnolo" which is characterized by frequent earthquakes, even of high intensity, with evidence of predominantly (OGS, 2014):

- compressional and transcurrent motion: along 10°-30° south-dipping planes, with hypocentral depths between 10 and 20 km;
- extensional motion: along approximately NW/SE-dipping planes, with shallow hypocentral depths (< 10 km).

The maximum expected magnitude is about 6 (OGS, 2014).

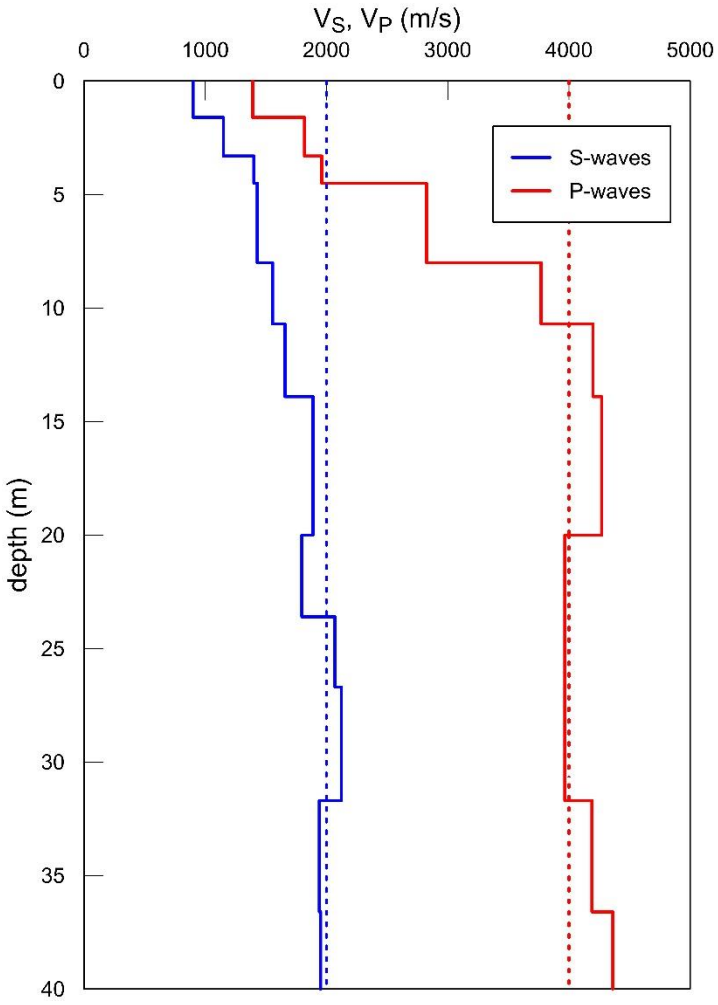

Figure 1.10. V_S and V_P profile with depth from 2020 Down-hole test (SolGeo, 2020)

Estimated PGA values are given in **Table 1.2**. They are calculated for reference periods (T_R) of 101, 475 and 1950 years. The same table also shows the values obtained adopting the MPS04 model for a reference period of 1950 years.

Table 1.2. PGA values for Ridracoli site, type A (rock) soil and different T_R.

	OGS (2014)			MPS04
T_R (years)	101	475	1950	1950
PGA (g)	0.156	0.281	0.449	0.316

The uniform hazard response spectra in horizontal and vertical directions derived in the OGS study (2014) for a reference period of 1950 years are plotted in **Figure 1.11**. A comparison is made with the design spectra obtained with Spectra-NTCver1.0.3, which is based on MPS04 model.

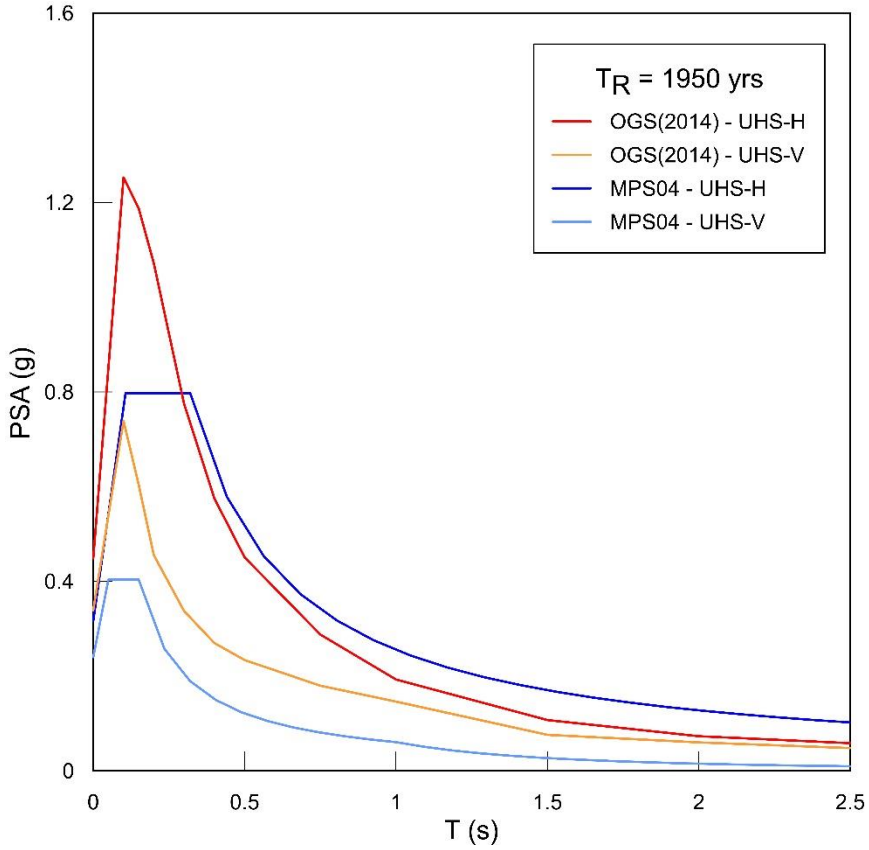

Figure 1.11. Horizontal and vertical UHS for Ridracoli site and type-A soil

1.2.5 Monitoring system

Ridracoli Dam is provided with a comprehensive monitoring network which controls every aspect of its operational life.

The dam structure and the rock foundation underneath are equipped with a great number of instruments, mainly grouped in five vertical sections: the main section, two far lateral and two intermediate lateral sections. The main ones are depicted in **Figure 1.12**.

In the main section, the horizontal displacements are controlled with one direct pendulum fixed just below spillway level (PD/1-2) and two inverted pendulums fixed at depth of 50 m and 25 m below the foundations level (PR/1-2/1 and PR/1-2/2 respectively). In the same section three multi-point borehole extensometers are also installed, inclined to the vertical

of +45°, -5° and -27°, respectively, where a positive angle indicates a borehole axis pointing upstream (ITCOLD, 1988).

The two far lateral sections are equipped with a direct pendulum (PD/20-22 and PD/19-21 for the right- and the left-side section, respectively) and a single inverted pendulum (PR/20-22 and PR/19-21 for the right- and the left-side section, respectively), completely embedded in the rock foundation, and two borehole extensometers. The extensometers are of the same length of those of the main section, but the inclinations are different, +45° and -45°, and are read at the same depth of the inverted pendulum (ITCOLD, 1988).

The intermediate sections have the same disposition of three extensometers as the main section, but without pendulums (ITCOLD, 1988).

Within the structure, a seismic surveillance system is installed. It is composed of 4 triaxial accelerometers (A, B, C and D), 6 electrical extensometers and 2 pressure switch (ITCOLD, 1988).

Accelerometer A is embedded in a borehole, 40 m below the base level of the pulvinus, in vertical correspondence to the main section of the dam. Along the same vertical, accelerometers D and C are placed in the pulvinus and below the spillway level, respectively. Finally, sensor B records ground motion of left abutment, just below the crest level.

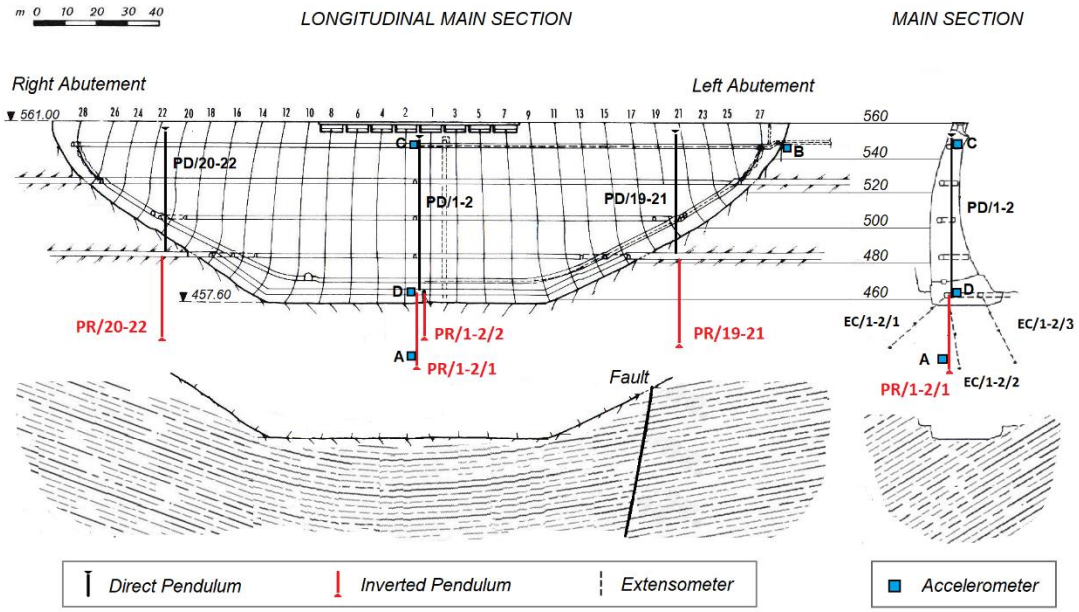

Figure 1.12. Main instruments for the control of displacements and accelerations of Ridracoli Dam monitoring system, and their relative position and orientation with respect to the main geological features (bedding planes and fault).

The strongest seismic event ever recorded by the 4 accelerometers took place on January 26, 2003. The epicentral distance of the earthquake was about 10 km, with a local magnitude estimated in 4.3 (Buffi, 2018). The structure did not suffer any damage. The recordings of this event are attached in **Appendix A**.

Other installed instruments include (ITCOLD, 1988):

- 3 pendulums in rock to control abutment movements,
- 6 levelling networks at different elevations outside and inside (tunnels) the structure,
- a trigonometric levelling network,
- long base extensometers in the abutments,
- piezometers in the foundation and in the abutments,
- axial extensometers and dilatometers at joint locations in the dam body to monitor their opening,
- extensometers and dilatometers across the fault,
- load cells and electric extensometer to monitor tensions and deformations in the dam body,
- thermometers at different elevations in the dam body and immersed in the reservoir water,
- measuring spillways,
- a complete weather station,
- a network of 5 seismometers for the microseismic surveillance of the reservoir.

Chapter bibliography

Alpina (Alpina S.p.A), 1974 (unpublished results). Progetto Esecutivo – Relazione Geologica.

Alpina (Alpina S.p.A), 1976 (unpublished results). Progetto Esecutivo Definitivo – Relazione Geomeccanica.

Alpina (Alpina S.p.A), 1981 (unpublished results). Verifiche geomeccaniche di stabilità delle spalle.

Bavestrello, F., 1983. Stabilizzazione temporanea degli scavi di imposta della Diga di Ridracoli. INARCOS. 444, 564-578.

Buffi, G., 2018. Assessment of seismic behaviour of large concrete dams by means of geomatics techniques and finite element modelling. PhD Thesis.

Chopra, A. K., 2020. Earthquake engineering for concrete dams: analysis, design, and evaluation, Wiley-Blackwell, Hoboken (NJ), USA.

CNIT, 2019. Conto Nazionale delle Infrastrutture e dei Trasporti - Anni 2018-2019 (CNIT 2018-2019). Ministero delle Infrastrutture e dei Trasporti. Ufficio di Statistica.

Einstein, H., Veneziano, D., Baecher, G., O'Reilly, K. J., 1983. The effect of discontinuity Persistence on Rock Slope Stability. International Journal of Rock Mechanics and Mining Sciences & Geomechanics Abstracts. 20(5), 227-236. https://doi.org/10.1016/0148-9062(83)90003-7

FERC (Federal Energy Regulatory Commission), 2018. Engineering guidelines for the evaluation of hydropower projects – chapter 11: arch dams. Washington DC, USA.

Grandori, R., Lembo Fazio, A., Ribacchi, R., 1990. Excavation of the Ridracoli hydraulic tunnels using a double-shield TBM. Rock Mechanics and Rock Engineering, 23, 141-165.
https://doi.org/10.1007/BF01022951

ITCOLD (Comitato Nazionale Italiano Per Le Grandi Dighe), 1988. Tecniche e realizzazioni italiane per il monitoraggio delle dighe e delle loro fondazioni. *Group Report* (coord. Marazio, A.).
https://www.itcold.it/wpsysfiles/wp-content/uploads/2016/07/RAPP-FIN-1988-MARAZIO.pdf [online]

Lembo Fazio, A., Tommasi, P., Ribacchi, R., 1990. Sheared bedding joints in rock engineering: two case histories in Italy. in Barton, N., Stephansson, O. (Eds), Rock Joints, Balkema, Rotterdam/Brookfield, Netherlands/USA.

Meletti, C., Montaldo, V., Stucchi, M., Martinelli, F., 2006. Database della pericolosità sismica MPS04. Istituto Nazionale di Geofisica e Vulcanologia (INGV). https://doi.org/10.13127/SH/MPS04/DB

Newmark, N. M., 1965. Effects of earthquakes on dams and embankments. Géotechnique. 15(2), 139-160.
https://doi.org/10.1680/geot.1965.15.2.139

NTC, 2018. Aggiornamento delle norme tecniche per le costruzioni. Ministero delle Infrastrutture e dei Trasporti. Gazzetta Ufficiale della Repubblica Italiana. Serie Generale n. 42. Rome, Italy.

NTD, 2014. Norme tecniche per la progettazione e la costruzione degli sbarramenti di ritenuta (dighe e traverse). Ministero delle Infrastrutture e dei Trasporti. Gazzetta Ufficiale della Repubblica Italiana. Serie Generale n. 156. Rome, Italy.

Oberti, G., Bavestrello, F., Rossi, P. P., Flamigni, F., 1986. Rock mechanics investigations, design and construction of the Ridracoli dam. Rock Mechanics and Rock Engineering. 19(3), 113-142.
https://doi.org/10.1007/BF01024952

OGS (Istituto Nazionale di Oceanografia e di Geofisica Sperimentale), 2014 (unpublished results). Accelerazioni attese e analisi di accelerogrammi per il sito della diga di Ridracoli (FC).

RA (Romagna Acque S.p.A.), 2001. L'acquedotto della Romagna. Romagna Acque S.p.A., Ravenna, Italy.

RA (Romagna Acque – Società delle Fonti S.p.A.), 2022. Website https://www.romagnacque.it/ [online]

RER (Regione Emilia-Romagna), 2022. Geoportale https://geo.regione.emilia-romagna.it/cartografia_sgss/ [online]

Solgeo (Solgeo s.r.l.), 2020 (unpublished results). Diga di Ridracoli (FC) - Prospezioni geofisiche in foro: Down-Hole

Stucchi, M., Meletti, C., Montaldo, V., Crowley, H., Calvi, G.M., Boschi, E., 2011. Seismic Hazard Assessment (2003-2009) for the Italian Building Code. Bull. Seismol. Soc. Am. 101(4), 1885-1911.
https://doi.org/10.1785/0120100130.

2. Seismic analysis of rock wedges at the abutments

2.1 Introduction

One of the most important issues in a seismic response analysis of an arch dam from a geotechnical point of view relies on the assessment of the stability of rock wedges present at the level of the foundation rock mass, and, in particular, at the level of the abutments. It is possible, although not straightforward, to include these known rock wedges (i.e., the single discontinuities that isolate them from the rest of the rock mass) in a complete numerical model of the dam-water-foundation system (see **Chapter 3**). A completely numerical approach via explicit FEM was presented by the U.S. Regulatory Commission (Mills-Bria et al., 2008). A similar inclusive strategy, despite being desirable, is not always easy to implement. In fact, a need to simplify local features arises when dealing with large complex models. As an example, a small change in the geometry of the abutments in order to smoothen the flanks of the valley may largely affect shapes and volumes of possible wedges which are present at those locations. Similar considerations can be made for the definition of seepage conditions, local consolidation works, or interaction properties between adjacent rock volumes. Despite being essential for analysing the dynamic behaviour of a single wedge, these aspects may be cumbersome to implement in a dam-water-foundation model at a reservoir scale. Moreover, the level of detail needed for including rock wedges may greatly increase the computational effort.

A simpler approach to investigate the seismic behaviour of single rock wedges under seismic excitation consists in directly integrating their relative displacement in the time domain under proper boundary conditions. Verrucci et al. (2018) developed a method that consider all the three acceleration components independently applied to the rock mass. Possible changes in the kinematics of the motion can also be followed during the seismic event: the sliding on either one or two planar discontinuities, the complete detachment and subsequent recovering of contacts. It is an evolution of the original 2D rigid-block method named after Newmark (1965), adapted to consider the 3D nature of the wedge stability problem, and allows for a performed-based assessment of dam abutment behaviour during seismic events. A similar approach has been recently implemented by Mostafai and Behnamfar (2021).

This chapter focuses on the extension of the Newmark displacement method to the analysis of 3D sliding rock wedges at arch-dam abutments. Part of the material included in this **Chapter 2** has already been included in Lusini et al. (2023), currently under review. The major difficulty for applying the method to dam abutment stability, which in contrast is well established for the back analysis of seismic-induced rockslides, relies on the need to include the effects of the dam-wedge interaction, owing to the large variability of the forces transmitted during the earthquake. The method is then applied to Ridracoli case study.

2.2 3D Newmark method

The 3D Newmark method developed by Verrucci et al. (2018) considers rock wedges as rigid and initially in contact with the underlying rock mass through three planar discontinuities forming a niche. Non-inertial actions include self-weight, normal and tangential reactions along the contact surfaces, uplift forces due to water pressure and possible reinforcement measures such as prestressed bar or anchors systems. The dynamic equilibrium is invariably applied to the rock wedge and, in particular, the inertial force with all its three spatial components is considered as a further body force acting on the wedge. A relative motion of the wedge with respect to the rock mass arises when the shear strength on the contact planes is exceeded; no tensile strength is considered. Only a translational motion is admissible, while rotations are neglected. This assumption makes the method more suitable for not very slender blocks, whose motion is less influenced by the resultant moment of the applied forces. When the relative motion ceases, the wedge returns to be tight to the rock mass at its updated position as long as the shear strength is not exceeded again. In this method endless contact planes are considered and therefore an *ex post* verification should be carried out in order to check whether the final calculated displacement is consistent to the actual niche extension and other possible mechanisms are avoided.

The input data include the three components of the accelerograms, the mass of the wedge, the orientation of the planes forming the niche, the sides of the half-spaces occupied by the block (i.e. the inward normal of the wedge faces), the shear strength of each plane according to a Mohr-Coulomb criterion and, if any, the external forces applied to the wedge. If a cohesive contribution is considered, the surface areas of the contact planes are also needed. The effective removability of the wedge, as defined in Goodman and Shi (1985), should be preliminary assessed.

After an initial calculation of the required vector entities that describe the geometrical condition, the method is implemented through a finite difference explicit integration in the time domain. For each time step the following phases are required: (a) identification of the current constraint configuration (active contacts on the discontinuity planes); (b) calculation of the resultant force (i.e. the resultant of static and dynamic external forces in addition to gravitational and inertial forces); (c) identification of the current mechanism among sliding on either one or two planes, complete detachment and impossibility of relative motion; (d) calculation of the block acceleration relative to the rock mass and (e) integration of the relative velocity and displacement.

The recovery of a plane contact that was previously lost is treated through a simplified assumption with respect to the impact phenomenon: the normal and tangential velocity components are respectively nulled and preserved. In a restitution coefficient logic this corresponds to consider a normal coefficient K_N equal to 0 and a tangential coefficient K_T equal to 1. Additional details on the integration method are given in Lusini et. al. (2023).

2.3 Wedges and loads

Concerning arch dam abutments, a classical assumption after Londe (1973) is to consider three planar discontinuities separating the wedge from the rest of the rock mass. The U.S. Federal Energy Regulatory Commission (FERC, 2018) guidelines suggest that two of these planes consist of planes of weakness (joints) of the rock mass while the third one is a release vertical plane in correspondence of the dam upstream face (**Figure 2.1**). The release plane is not an actual joint and should only behave as a detachment surface, due to the negligible tensile strength of the rock mass; therefore, a check should be introduced in order to ensure the proper mechanism with respect to the release plane and to avoid possible sliding on it before the occurrence of the first detachment.

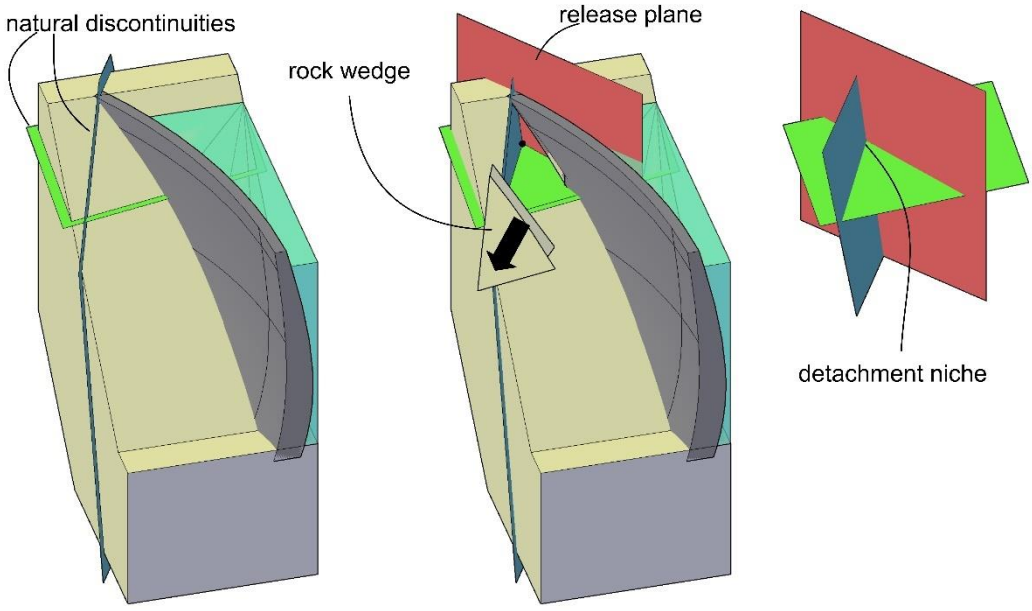

Figure 2.1. Definition of wedges on a generic arch-dam abutment.

2.3.1 Shear strength along discontinuity planes

Analyses are usually carried out using simple constitutive laws to model the shear strength of the discontinuities which separate the wedge from the rest of the rock mass, such as the classical Mohr-Coulomb strength criterion or the non-linear Barton criterion. In lack of a sufficient number of in situ shear tests, as is often the case, a Barton law based on easily ascertainable parameters (JRC, JCS, φ'_b) can be estimated and then linearised in the pressure range of interest in order to obtain the two parameters of a Mohr-Coulomb strength criterion: the equivalent cohesion (c') and friction angle (φ'). Although less refined, the

Mohr-Coulomb strength criterion is independent from the actual stress distribution along the discontinuity plane, making it more suitable for an approach that considers the equilibrium of the resultant forces rather than the real stress distribution. A distinction should be made between peak and residual strength parameters of the discontinuity. In a step-by-step dynamic analysis, the progressive transition from peak to residual parameters could be considered, especially in terms of cohesion, which is typically the parameter most affected by the strength reduction.

2.3.2 Seismic input selection

The seismic input should be selected on the basis of a spectrum compatibility analysis. Starting from a target elastic spectrum derived from a seismotectonic analysis of the site, an interval of periods for the spectrum-compatibility can be determined as suggested by Chopra (2020) for arch dams as $0.25\ T1 < T < 2.5\ T1$, where T1 is the fundamental period of the dam that can be obtained from vibrodyne tests, actual recorded seismic responses or modal numerical analyses. In a range of periods determined in this way, the forces transmitted by the dam are expected to experience large variations compared to those computed considering a pseudo-static approach, because the vibration modes of the structure are excited. For the wedge stability analyses, however, it could be useful to also consider the periods for which the condition $T < 0.25\ T1$ holds, considering the main period of the rock slope itself, that is more rigid than the structure. Accordingly, it is reasonable to extend the spectrum compatibility from a near-zero multiplier up to 2.5 times the fundamental period of the structure.

For geotechnical applications it is usually recommended to avoid the use of artificial accelerograms (NTC, 2018). International strong motion databases are typically searched to find earthquake recordings compatible with the site-specific target spectrum and sharing similar characteristics (such as focal mechanisms, MW, PGA, epicentral distance, $V_{S,30}$ etc...). In addition, it should be avoided an excessive scaling of the effective signals to enforce a compatibility. A possible strategy consists in selecting a certain number of real strong motion recordings which singularly matches the compatibility with the target elastic spectrum at least in a portion of the interval of periods considered. The envelope of the maximum spectral ordinates of selected accelerograms must well approximate the target spectrum by falling within a band of tolerance.

In the Italian building code (NTC, 2018) a minimum number of seven recording is suggested. The spectrum compatibility, however, is only checked for the mean spectral value of the seven selected ground motions. In the Italian guidelines for the seismic analysis of large dams (Lanzi and Paoliani, 2018) a number of 3 accelerogram is allowed for concrete dams, but the spectrum compatibility is assessed for each recording separately

2.3.3 Dam thrust

An important task of the abutment stability analysis is the proper definition of the forces transmitted by the dam. The analytical approaches, as the Trial Load method (Howell and Jaquith, 1929) and the Tölke method (Tölke, 1938), were found overestimating the effective forces transmitted to the abutments in Ridracoli case. Nowadays, static finite-element models of dams are in the daily engineering practice. Therefore, the structural loads on the faces of the analysed wedge can be determined from either the nodal point reaction forces or the contact stresses extracted from these numerical models. In the latter case, the output stresses (in terms of cartesian components or principal stresses) should be projected into one normal and two shear stress components in the local reference system of the contact surface to apply the proposed method. Because rock masses are often incapable of sustaining tension, it is prudent to null any tensile normal stress (Goodman and Powell, 2003).

The calculation of dynamic forces exerted by an arch dam on a generic wedge in dynamic conditions is not an easy task, currently impossible with analytical tools, because they depend on the inertial characteristics of the dam, the foundation and the impounded water and on their mutual interactions. A fixed-base dynamic FE analysis of the dam may be sufficient for the level of detail required in this kind of analysis, especially when considering the uncertainties behind the definition of other forces.

Further details on analytical and numerical methods for arch-dam static and dynamic analysis are given in **Chapter 3**.

2.3.4 Uplift forces

Following the scheme proposed by Goodman and Powell (2003) and the suggestions of FERC guidelines, a hydrostatic distribution of the pore pressure, referring to the maximum regulation level of the reservoir, can be applied to the discontinuity edges that outcrop upstream of the dam, below the water level, or located in the rock mass just beneath the dam. A linear reduction is assumed on the discontinuities planes until a null pressure is reached at the edges that outcrop on the rock mass surface downstream of the dam (**Figure 2.2**). This corresponds to underestimate the decrease in pore pressures due to the presence of a grout curtain and a drain system, on the safe side. As long as displacements and openings of joints during the seismic action are sufficiently small it is reasonable to neglect the dynamic variation of pore pressure during the earthquake.

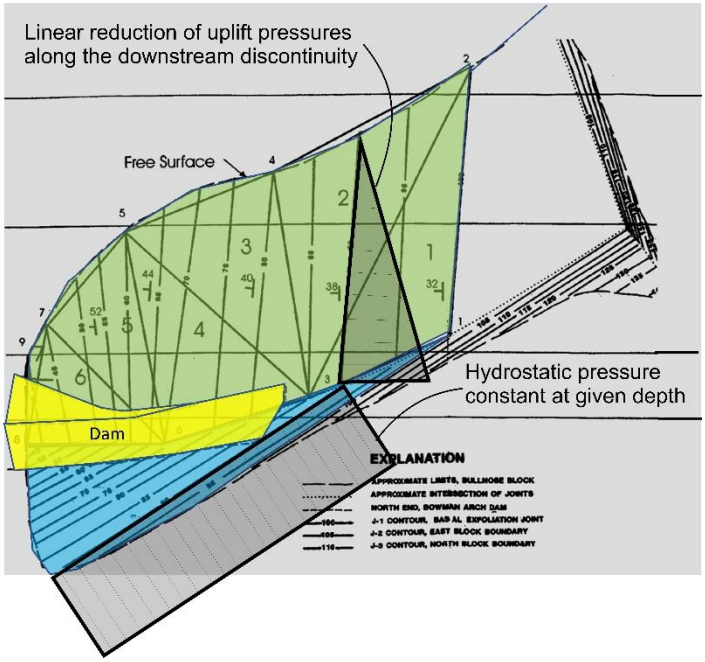

Figure 2.2. Uplift forces on wedge lower faces (modified from Goodman & Powell, 2003).

2.4 Ridracoli Dam: wedges and loads

For its orientation and geomorphology, the right abutment of Ridracoli dam presents the most critical stability conditions (Bavestrello, 1983). As outlined in **Chapter 1** the foundation rock mass is characterized by a typical cubic joint system, generated by the sets ST (corresponding to the bedding planes), KKI (lined with the strata dip direction) and KKD (lined with the strike of the strata). Among bedding planes, the most concerning strength parameters can be found along 4 sheared marl strata (variable c' 0-200 kPa and φ' = 13°), while all the other stratigraphic contacts show quite higher friction angles and variable cohesions.

Therefore, it is assumed that any possible collapse mechanism should necessarily involve one of the laminated marl layers. Only two of them emerge on the flank of the right abutment and are used for defining two possible unstable wedges. The other boundaries of the wedges are the vertical plane of potential detachment beneath the upstream face (where a subvertical grout curtain interrupts the rock mass continuity) and a supposed wide-extended joint of the KKI set, located as to maximize the thrust of the dam. The stereographic projection of the defining planes are plotted in **Figure 2.3**. The dimensions of the wedges are listed in **Table 2.1**. Since the two laminated interbedding planes are quite close one another, the upper wedge (W1) is a smaller portion of the other one (W2) (**Figure 2.4**).

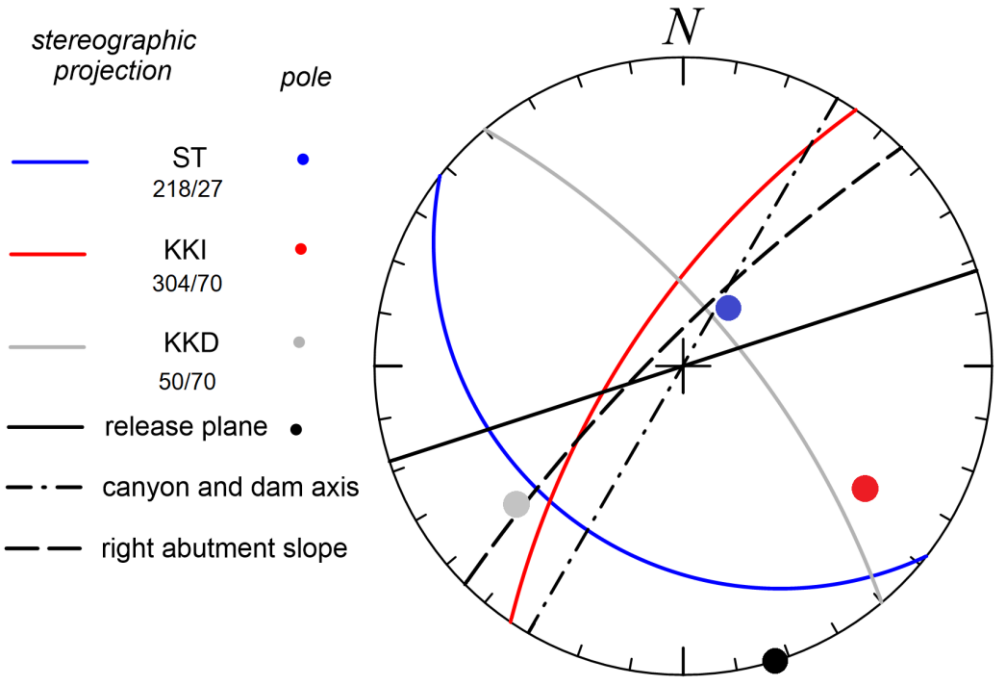

Figure 2.3. Stereographic projection of the planes defining the wedges and the right abutment slope.

A first attempt to assess the stability of the two wedges, with the aim of revaluating the stability condition of the right abutment in seismic conditions, was presented in Lusini et al. (2022) using a limit equilibrium approach. The results were not completely satisfactory, since a safety factor less than 1 was obtained for the most critical directions of the pseudo-static force and for a no-cohesion hypothesis along the discontinuities (i.e., the same approach followed in the design project of the dam, on the safe side), in agreement with the assumptions made at the detailed project stage, both for wedge W1 and W2. A comparison with the results of the analyses described in this paper will be presented in the Section Result and discussion.

Table 2.1. Size of the wedges defined for the seismic analysis of the right abutment.

wedge	volume (m^3)	ST face area (m^2)	KKI face area (m^2)
W1	49532	4602	1654
W2	83504	6340	2346

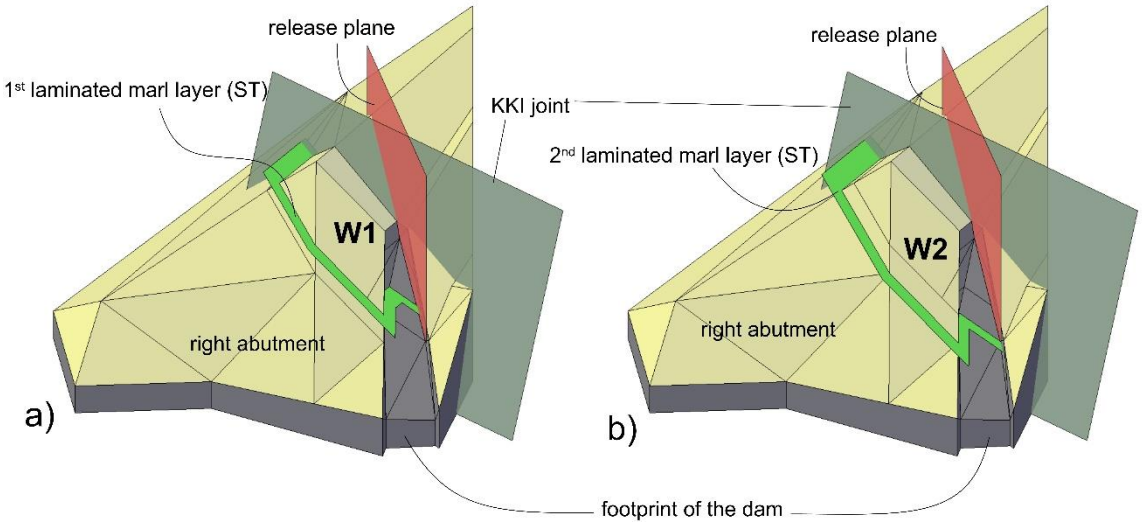

Figure 2.4. Definition of wedges: a) W1 and b) W2 on Ridracoli dam right abutment.

2.4.1 Ridracoli Dam: shear strength along discontinuity planes

For the laminated marl layers the experimental value of the friction angle is adopted (13°), as measured through the in-situ shear tests, while a mean cohesion of 50 kPa, equal to 1/4 of the measured value at ground surface (200 kPa) but larger than the value obtained for the same laminated layer in exploratory tunnels (near-zero), can be considered as representative, also after scale-effect considerations. For the other two joint surfaces, in lack of experimental data, a typical value of friction angle for the joint walls of that rock formation is assigned, equal to 36°. A cohesion of 50 kPa is finally adopted also for these surfaces, owing to the certain presence of rock bridges. All the planes have no tensile strength. However, several authors conducted their analyses with a no-cohesion hypothesis on each discontinuity owing to the difficult to determine its effective value at true scale (Londe, 1969; Goodman and Powell, 2003). Other analyses are then performed in order to investigate the influence of the cohesive component considering: a no-cohesion hypothesis (borrowed from the design project), a ductile behaviour (the nominal cohesion of 50 kPa is maintained for the whole analysis), a 'brittle' rupture (cohesion suddenly drops to zero as soon as the block starts to move), and two different linear decay laws for which the cohesion is annulled after a threshold of the displacement magnitude of 0.001 m and 0.01 m is reached, respectively.

2.4.2 Ridracoli Dam: seismic input selection

From a site-specific seismotectonic study (OGS, 2014) the uniform hazard response spectra (UHRS) are available in the horizontal and vertical directions for various return periods (T_R) and for a critical damping ratio of 5%. A T_R = 1950 years is considered, which corresponds to the return period of an earthquake associated to the ultimate limit state as defined in the Italian Building Technical Code (NTC, 2018) and Italian Dam Code (NTD, 2014). Recorded seismic events are chosen from PEER (Pacific Eartquake Engineering Research Center) NGA-West2 database (Ancheta et al., 2013) and Rexel software (Iervolino et al., 2010) ESM (European Strong Motion) databases. The selected signals share the same soil type and show Moment Magnitude (MW) and Peak Ground Acceleration (PGA) not far from the expected seismic action in the Ridracoli area (**Table 2.2**): the horizontal scale factors (SF) to reach the horizontal expected PGA are kept in the range 1 < SF < 2. The events exhibit a certain variability in terms of Arias intensity (IA), significant duration (TD) and mean period (TM) to cover a large range of possible events. For each event two accelerograms are tested for the spectrum compatibility with the UHRS, namely the horizontal one (i.e. the square root sum of squares of the recorded North and East components), and the vertical one. In order to account for the composition of the two horizontal spectra, the target UHRS is multiplied times 1.414. The range of compatibility, according to the interval discussed in the previous section, extends from 0.04 s to 0.72 s, the main period of the dam being about 0.36 s (Buffi, 2017).

Table 2.2. Seismic characteristics of the selected records in the three direction N = North, E = East and U = Up.

Earthquake		Coalinga (1983)	Umbria-Marche (1997)	L'Aquila (2009)
Seismic Database		PEER - NGA-West2	REXEL - ESM	PEER - NGA-West2
Arias intensity (m/s)	N	0.5592	0.2836	0.6487
	E	0.8445	0.4502	0.8067
	U	0.2390	0.2026	0.3332
significative duration (s)	N	8.5110	2.9690	3.4830
	E	6.2035	1.8620	2.3715
	U	11.5775	3.5820	6.5830
mean period (s)	N	0.2964	0.1295	0.1923
	E	0.2656	0.1794	0.2355
	U	0.2949	0.1571	0.2342

Spectrum compatibility is first assessed in the horizontal direction (**Figure 2.5**) checking whether the three scaled SRSS spectra fall below the target spectrum plus a 30% increase in the entire interval, and at least one of them for every period of the interval also fall above the target spectrum minus a 10% decrease. Less stringent conditions are fixed for the vertical component Up-Down (U-D), which is scaled independently (**Figure 2.6**). For every period of interest at least one of the three vertical spectra must fall below the target spectrum plus a 30% increase, and one of them above the target spectrum minus a 10%. However, these limits are not strictly satisfied in the interval 0.6 s < T < 0.72 s. Vertical scale factors reach a maximum value of 3.5.

The baseline correction is applied to all acceleration time histories before using them for the numerical analyses. When utilised as input for the 3D displacement method to calculate the block inertial forces they are also corrected for the topographic amplification factor S_T = 1.4. This correction is not adopted when the accelerograms are used for the seismic excitation of the FE model to obtain the dam thrust on the abutment, as described in the next section. The horizontal seismic components, N-S and E-W, extracted from seismic databases are applied in the downstream-upstream and the right-left cross directions of the valley, respectively, in the local reference system of the dam, which results as rotated of 28° clockwise with respect to the cartographic one.

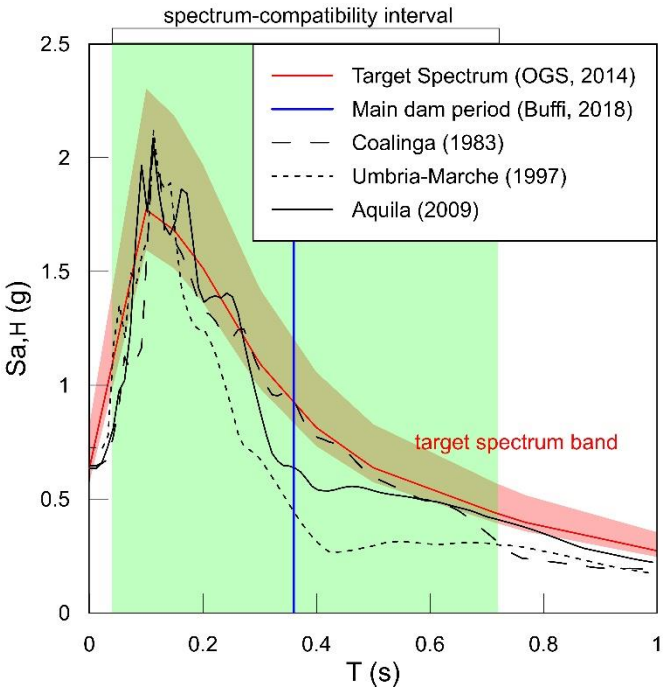

Figure 2.5. UHRS in horizontal direction (composition N-E) and SRSS of compatible earthquake records selected for the analyses. The greeb band indicates the interval of periods considered and the red one the tolerance range around the Target Spectrum.

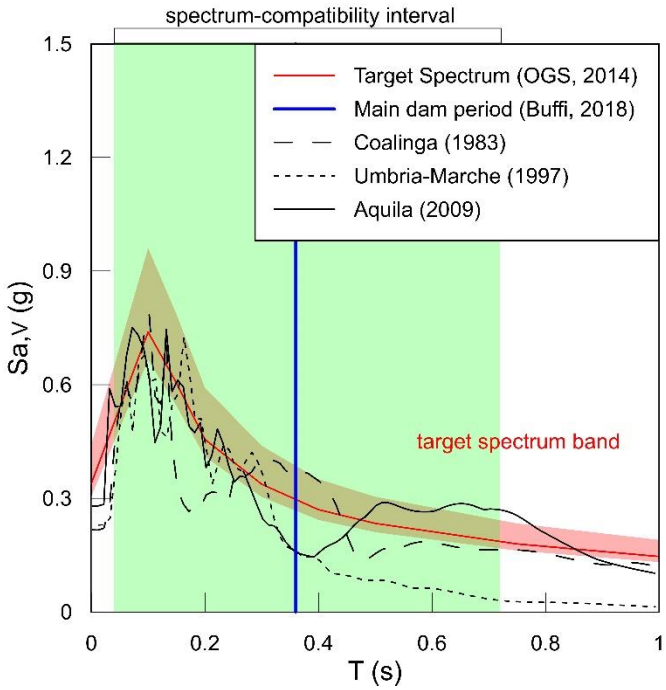

Figure 2.6. UHRS in vertical direction and vertical spectra of compatible earthquake records selected for the analyses. The green band indicates the interval of periods considered and the red one the tolerance around the Target Spectrum.

2.4.3 Ridracoli Dam: dam thrust

The analyses presented in this paper are performed using three different schemes for the interaction forces between the dam and the rock block on the abutment: (a) only static forces calculated through the analytic method that was adopted for the original design project of the dam; (b) static forces calculated from the analytic method and a dynamic force surplus from a FE model, (c) both static and dynamic forces calculated through a FE model.

For the design of Ridracoli Dam an evolution of the Tölke method, proposed by Swaminathan (1960) to take into account the foundation deformability, was adopted, consisting in applying the Vogt (1925) solutions for rigid foundations on an elastic half-space as boundary conditions both for cantilever and arch elements (see **Chapter 3**).

The FE static analysis is conducted in the implicit FE Abaqus® environment, simulating the elastic behaviour of both the dam and the underlying rock mass with a model slightly modified from that presented in Buffi (2017). The dynamic FE model corresponds to the core (the dam body) of the static model, fixed at the base and equipped with Westergaard added masses (Westergaard, 1933) to simulate the inertial effects of the impounded water. The dynamic analyses are conducted under the assumption of a monolithic elastic

behaviour of the concrete structure and a critical damping ratio of 5%. Both static and dynamic FE models are reported in **Figure 2.7**.

First the static thrust transmitted by the dam to each wedge is calculated (**Table 2.3**): when the analytical method is considered the thrust values are extracted from tabular results of the design project (Alpina, 1976), while when the FE model is used the thrust values are extracted from Abaqus® output database as nodal quantities, the resulting force (F) is calculated vectorially summing the nodal contact forces and nodal reaction forces for the static and dynamic model, respectively. It has three components in the three directions of the local coordinate system of the dam. The dynamic surplus time history of the thrust is then summed *ex-post* to the static thrust of the dam-foundation model (case c) (**Figure 2.8**) or to the analytic static thrust (case b), holding the superimposition of effects for elastic media.

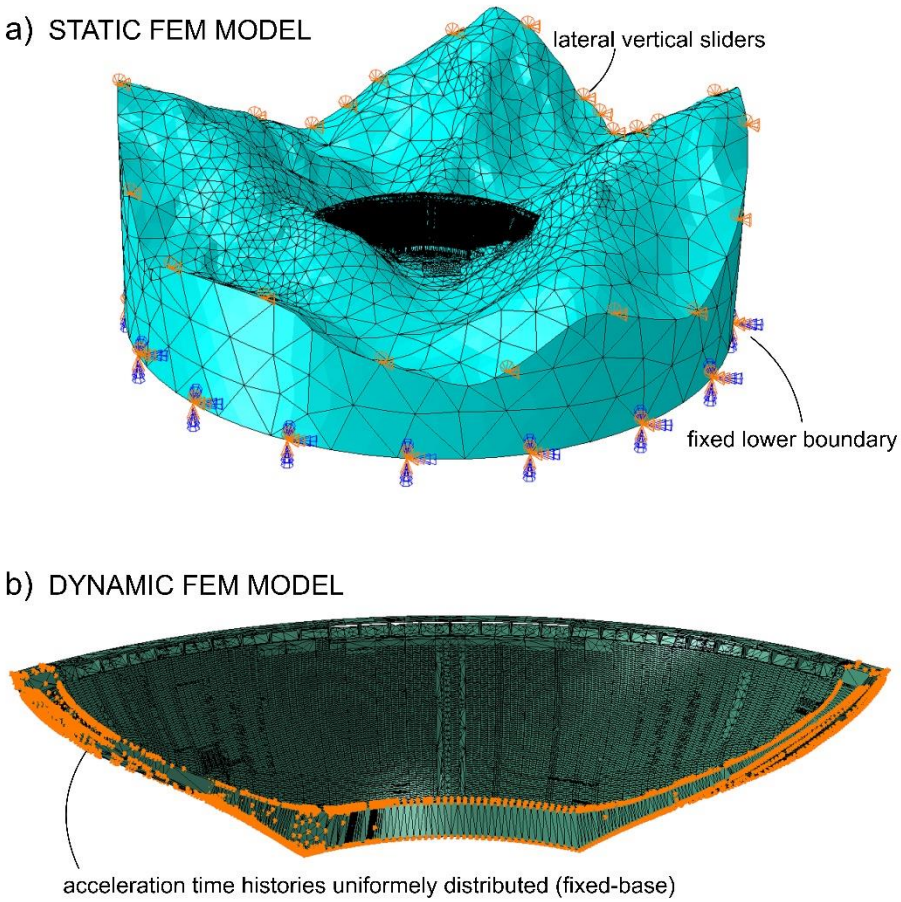

Figure 2.7. FE model of the dam and underlying rock mass for static elastic analysis (a), and mesh of the fixed-base dynamic model (b).

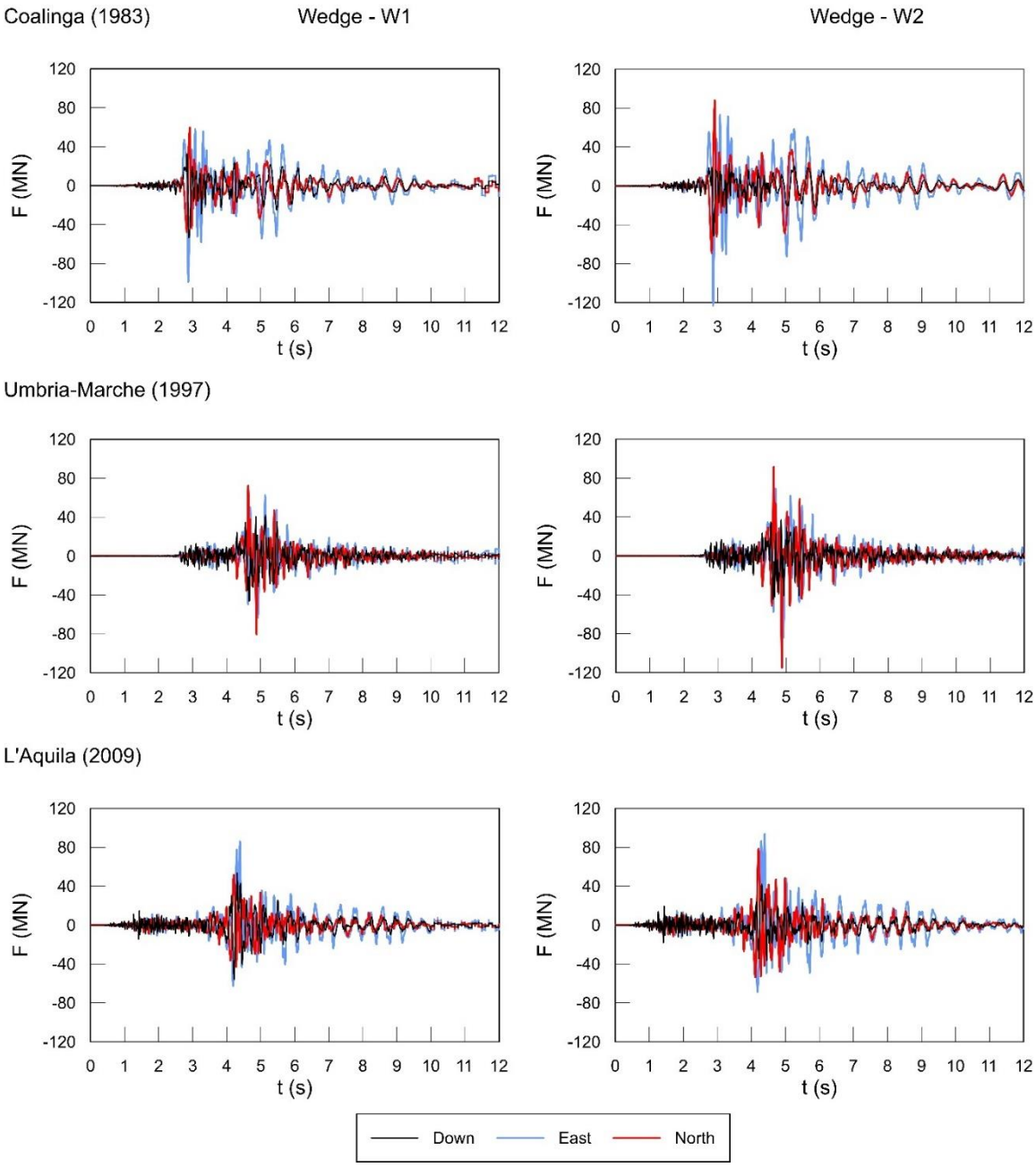

Figure 2.8. The dynamic oscillations of the dam thrust in the three orthogonal components (Down, East, North) and for the three selected earthquake under the (c) approach for the definition of the thrust.

Table 2.3. Static dam thrust on the wedges.

	Thrust components from the analytical method (MN)			Thrust components from the complete FEM (MN)		
wedge	North	East	Up	North	East	Up
W1	641.87	1167.61	-365.07	174.77	632.76	-51.33
W2	758.46	1357.47	-484.32	214.43	705.73	-149.19

2.4.4 Ridracoli Dam: uplift forces

Water pressures on the discontinuity planes are calculated with a reference water level equal to the maximum regulation level of the dam (560 m a.s.l.). The maximum pressure (for wedge W2) is the hydrostatic pressure at the lowest point of the face corresponding to the release plane (u_{max} = 602.1 kPa). The scheme of uplift forces and pressures, following the framework of Goodman and Powell (2003), is shown in **Figure 2.9** for the wedge W2. The resultant uplift water forces are reported in **Table 2.4**.

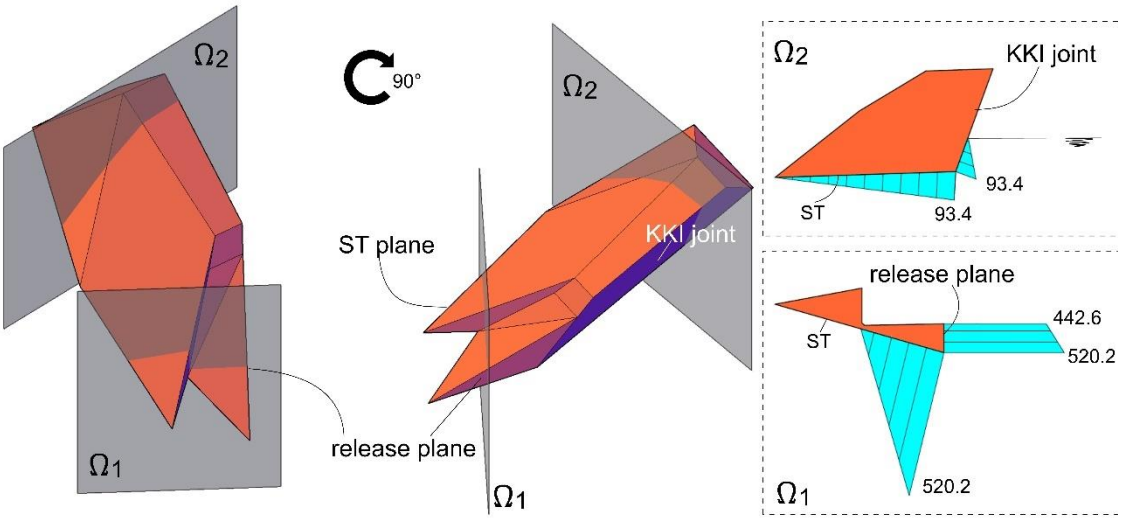

Figure 2.9. Hydraulic conditions for W2: vertical sections Ω1 and Ω2 help visualizing water pressures in 2D (in light-blue).

2.4.5 Ridracoli Dam: other forces

An overall force on the right abutment of about 965 MN is exerted by 543 rock anchors, with working tensions of 1475 kN or 1770 kN and an average length of 37 m, so that the anchoring zone is all below the second laminated layer (Bavestrello, 1983). A recent measure of the residual tension of the anchors showed a loss of about 50% with respect to the initial value applied during the construction. Such a reduction of the anchor forces is not considered in the analyses on the safe side. This apparent contradiction is further explained in Lusini et al. (2022): the anchor forces, in fact, are inclined with respect to the intersection of ST and KKI planes (I_{SK}) in such a way that the tangential component is directed downstream, tending to lift the wedge and pushing it away from the dam. This arrangement was the most efficient for the consolidation of the abutment during the excavation work preliminary to the dam construction (Bavestrello, 1983). The resultant anchor forces, together with other structural weights, are reported in **Table 2.4**.

Table 2.4. Uplift water forces and other static forces applied on the wedges.

Wedge	Load type	Force (MN)		
		North	East	Up
W1	Uplift water forces	-36.56	-197.50	376.21
	Anchor forces	79.17	295.46	-142.63
	Structural weights	0	0	-140.00
W2	Uplift water forces	293.66	-190.91	54.13
	Anchor forces	107.74	402.08	-194.11
	Structural weights	0	0	-140.00

2.5 Ridracoli Dam: results and discussion

All the results in terms of cumulated displacements for wedges W1 and W2 are summarised in **Table 2.5** and **Table 2.6**, respectively. For both wedges the kinematics activated during the application of the acceleration time histories of the three earthquakes are always limited to two cases, i.e. sliding along the intersection line I_{SK} between planes ST and KKI, I_{SK}, and sliding on the ST plane only. To estimate the entity of the total sliding developed along the niche surfaces, in addition to the magnitude of the residual relative displacement ($|d_r|_{res}$)

also the maximum magnitude of the displacement reached during the seismic excitation ($|d_r|_{max}$) and the total path length (ℓ) covered along the curvilinear trajectory are reported in the tables, being $|d_r| \leq |d_r|_{max} \leq \ell$.

Table 2.5. Displacements calculated for wedge W1 under all the considered combination of assumptions. Seismic input: C = Coalinga (1983); UM = Umbria-Marche (1997); A = L'Aquila (2009). Empty values of $|d_r|_{max}$ mean that $|d_r|_{res} = |d_r|_{max}$.

		(a)			(b)			(c)		
static interaction:		analytic method			analytic method			FE method		
dynamic interaction:		none			FE method			FE method		
cohesion hypotheses	seismic input	$\|d_r\|_{res}$ (mm)	$\|d_r\|_{max}$ (mm)	ℓ (mm)	$\|d_r\|_{res}$ (mm)	$\|d_r\|_{max}$ (mm)	ℓ (mm)	$\|d_r\|_{res}$ (mm)	$\|d_r\|_{max}$ (mm)	ℓ (mm)
c' = 0	C	12.6	-	13.6	16.7	-	18.7	0.1	5.9	15.1
	UM	55.5	-	56.0	**55.6**	-	56.1	9.4	-	10.8
	A	8.2	-	8.6	10.4	-	11.2	0.1	0.4	1.1
c' = 50 kPa, (brittle behaviour)	C	11.5	-	12.2	15.6	-	17.2	0.1	4.6	10.2
	UM	52.6	-	53.0	52.7	-	53.1	8.5	-	9.8
	A	5.2	-	5.2	8.2	-	8.3	0.0	-	0.0
linear decreasing cohesion (0-0.001m)	C	7.2	-	7.5	11.1	-	11.9	0.2	1.4	3.5
	UM	42.9	-	43.3	43.0	-	43.4	4.9	-	5.8
	A	0.2	-	0.2	2.0	-	2.0	0.0	-	0.0
linear decreasing cohesion (0-0.01m)	C	2.3	-	2.5	3.8	-	4.4	0.2	0.5	1.5
	UM	29.2	-	29.6	29.3	-	29.6	1.7	-	2.4
	A	0.1	-	0.1	0.3	-	0.3	0.0	-	0.0
c' = 50 kPa (ductile behaviour)	C	2.0	-	2.3	3.1	-	3.8	0.1	0.5	1.5
	UM	12.0	-	12.3	12.1	-	12.4	1.5	-	2.1
	A	0.1	-	0.1	0.3	-	0.3	0.0	-	0.0

Table 2.6. Displacements calculated for wedge W2 under all the considered combination of assumptions. Seismic input: C = Coalinga (1983); UM = Umbria-Marche (1997); A = l'Aquila (2009). Empty values of $|d_r|_{max}$ mean that $|d_r|_{res} = |d_r|_{max}$.

		(a)			(b)			(c)		
static interaction:		analytic method			analytic method			FE method		
dynamic interaction:		none			FE method			FE method		
cohesion hypotheses	seismic input	$\|d_r\|_{res}$ (mm)	$\|d_r\|_{max}$ (mm)	ℓ (mm)	$\|d_r\|_{res}$ (mm)	$\|d_r\|_{max}$ (mm)	ℓ (mm)	$\|d_r\|_{res}$ (mm)	$\|d_r\|_{max}$ (mm)	ℓ (mm)
c' = 0	C	6.2	7.5	14.4	9.2	-	19.5	22.3	-	43.8
	UM	33.0	-	34.9	**33.0**	-	34.9	2.9	6.7	27.0
	A	2.8	-	5.3	4.0	-	7.5	2.1	7.1	21.6
c' = 50 kPa, (brittle behaviour)	C	5.5	6.8	12.9	8.3	8.7	17.9	20.9	-	42.4
	UM	31.3	-	33.0	31.1	-	33.1	0.1	6.2	24.5
	A	2.3	-	2.3	3.2	-	5.6	0.5	5.5	18.3
linear decreasing cohesion (0-0.001m)	C	3.5	4.3	8.0	5.1	6.2	11.9	15.5	-	36.2
	UM	24.7	-	26.4	24.7	-	26.4	0.1	4.6	19.7
	A	0.1	-	0.1	0.2	-	0.3	0.4	3.1	10.2
linear decreasing cohesion (0-0.01m)	C	1.4	2.4	4.3	2.4	3.8	7.3	12.9	-	28.7
	UM	18.2	-	19.8	18.2	-	19.8	0.1	2.4	11.7
	A	0.0	-	0.0	0.1	-	0.1	1.4	-	2.3
c' = 50 kPa (ductile behaviour)	C	1.3	2.2	3.9	1.9	3.5	6.2	6.0	8.2	16.3
	UM	9.1	-	10.2	9.1	-	10.3	0.9	2.3	7.0
	A	0.0	-	0.0	0.1	-	0.1	1.3	-	2.0

The maximum values of $|d_r|_{res}$ (in bold in **Tables 2.5** and **2.6**) are obtained for the Umbria-Marche (1997) seismic input and the zero-cohesion hypothesis, using the so called 'hybrid' approach for the definition of dam thrust (c method). They are equal to 56 mm and 33 mm for W1 and W2 respectively. In general, when excited with L'Aquila input, the wedges tend to remain locked in the niche for most of the cases considered. Sometimes the maximum reached level of displacement $|d_r|_{max}$ and the path length ℓ significantly differ from the final $|d_r|_{res}$, thus meaning that the wedges complete a nearly closed loop or a path with a significant retrogressive phase. This happens in many cases for W2, while only using the (c) method for W1. In some cases, the difference rises up to more than an order of magnitude.

Further details of the influence of different hypotheses on dam thrust and cohesion contribution are given in the following.

2.5.1 Ridracoli Dam: influence of the interaction forces

For comparing the influence of the different approaches used to define the dam-wedge interaction forces a condition with a null cohesion along the discontinuities is considered (**Figure 2.10**). In case of W1, the accumulated displacements are always less than 60 mm, with a moderate variability between the three earthquakes. The largest values are obtained with the Umbria-Marche (1997) signal ($|d_r|$ = 56 mm), which has the highest spectral ordinates for the lowest periods, despite having the lowest energy content. Coalinga (1983) earthquake follows, with maximum displacements in the order of 16 mm. Finally, the L'Aquila (2009) earthquake induces about 10 mm of displacements. When the fully numerical thrust estimation ((c) method) is applied, the magnitude of the static dam thrust is much smaller for all the considered earthquakes and, consequently, the related displacements are from one to two orders of magnitude smaller than those computed with (a) and (b) methods, which include the analytical static solution. Also, the activated kinematics is different, depending on the orientation of the resultant force: there is a prevalent sliding on the ST plane for (c), while a sliding on the intersection line I_{SK} is produced in cases (a) and (b).

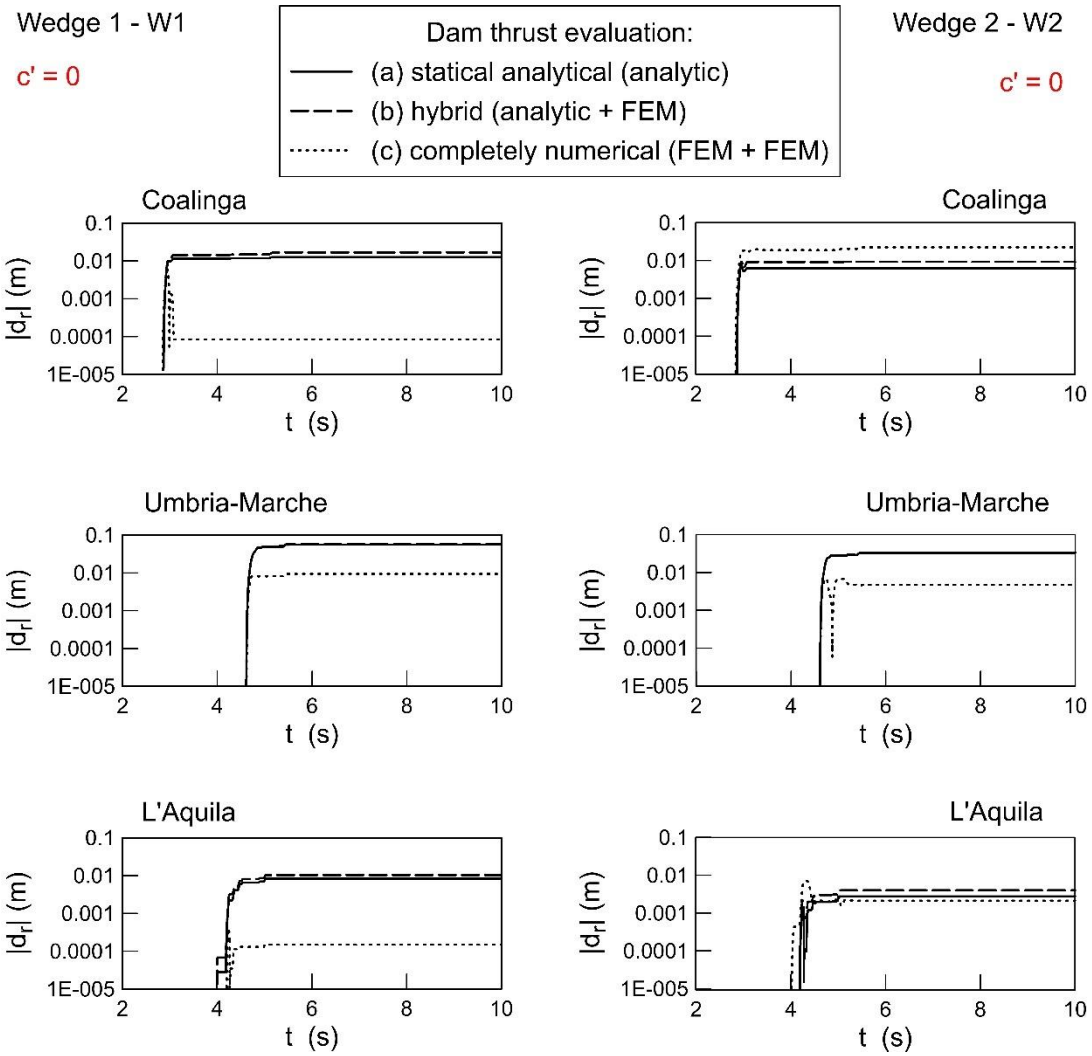

Figure 2.10. Displacement cumulation in the time domain when a c' = 0 ('no cohesion') condition is applied on wedge contact faces.

For wedge W2 the general trend is similar to W1, with slightly smaller displacements (the maximum is less than 33 mm). Nevertheless, the fully numerical thrust estimation ((c) method) causes for all the input signals maximum displacements quite similar to those calculated with (a) and (b) methods. This change of susceptibility of the wedge in the case of the UM input may be due to the prevalent direction of the total forces applied to the wedges, related to the wedge-dam relative position: those acting on W2 induce a sliding on the ST plane, with a significant downward component, while W1 is induced to move upward on the same plane. Therefore, the seismic performance can significantly differ.

In both cases the wedges tend to stop when one of the contacts lost during the excitation is regained, i.e., the KKI plane or the release plane. This same difference in the behaviour between W1 and W2 is not observed when the analytical static thrust is considered, as the wedges move upward without reversal and always stop along or close to the intersection

line I_{SK}. To better focus on this aspect, the most typical trajectories of the wedges observed under the hypotheses (b) and (c) are reported in **Figures 2.11** and **2.12**, for wedges W1 and W2 respectively. Hypothesis (a) shows the same tendency to hypothesis (b), with slightly smaller displacements, and therefore is disregarded. These results confirm that, although the irreversible displacements develop in seismic condition, the static part of the dam thrust, in term of both magnitude and orientation, is always one of the most critical factors influencing the final amount of the displacements. Due to the complexity of the three-dimensional conditions, this effect cannot be summarised by an explicit critical acceleration such as the one that can be estimated in the 1D/2D Newmark analyses.

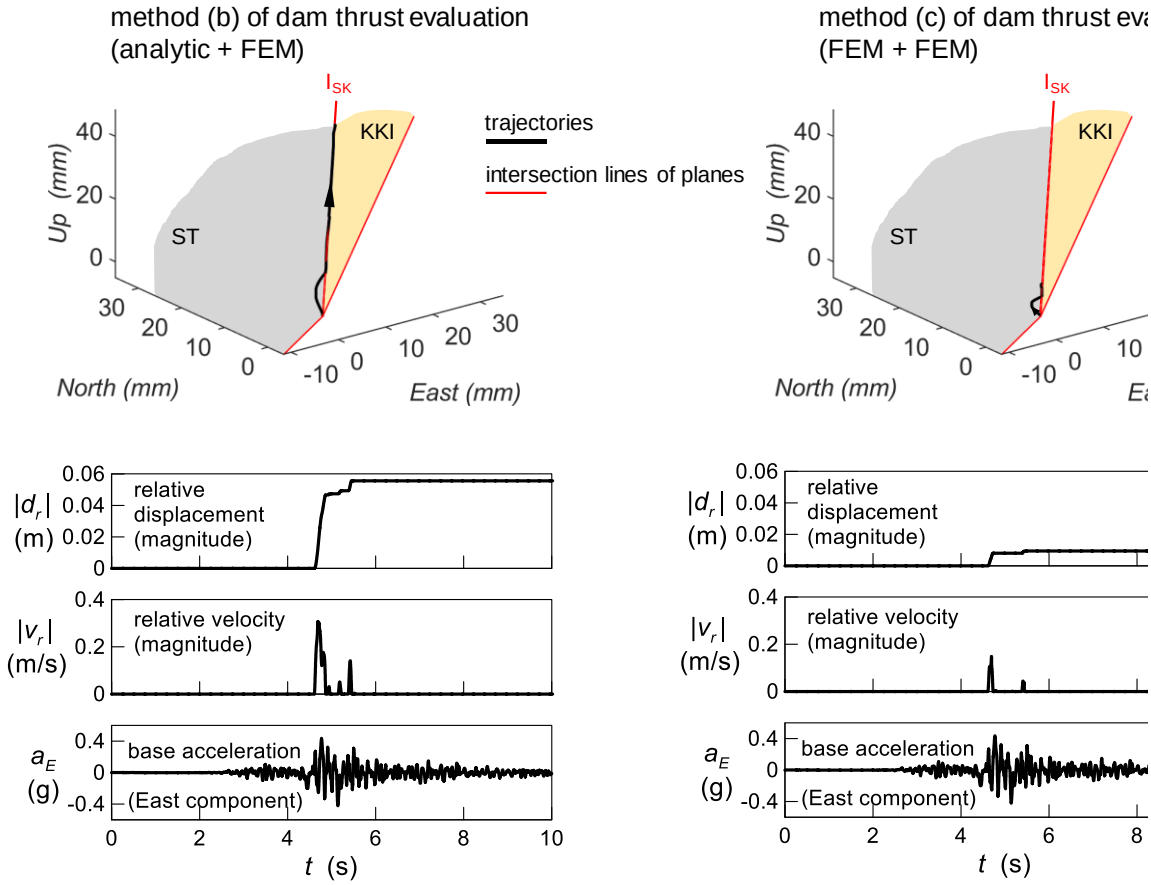

Figure 2.11. Trajectories and time histories of displacement and velocity magnitude of wedge W1 under the UM earthquake and considering a c' = 0 condition for the cohesion of wedge contact faces.

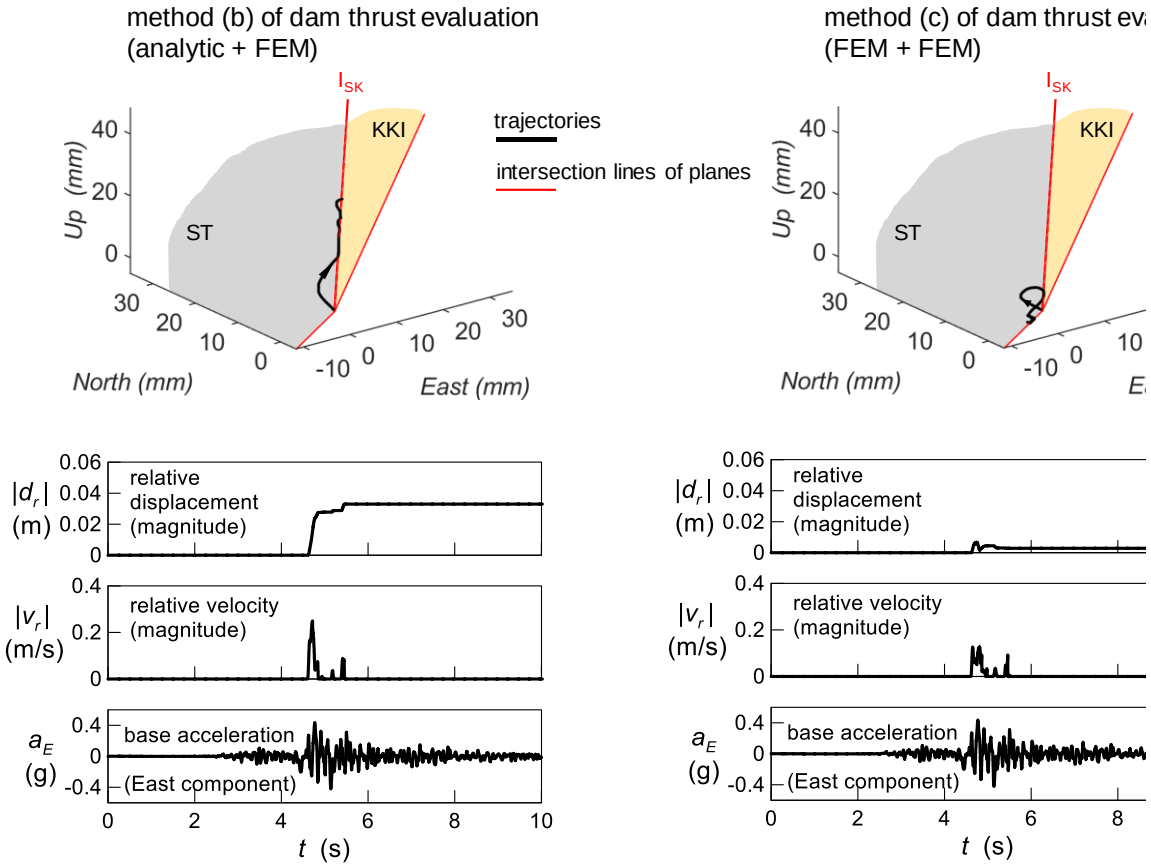

Figure 2.12. Trajectories and time histories of displacement and velocity magnitude of wedge W2 under the UM earthquake and considering a c' = 0 condition for the cohesion of wedge contact faces.

2.5.2 Ridracoli Dam: influence of cohesion

Different hypotheses on the initial cohesion and on the transition to residual conditions clearly affect the final calculated displacement $|d_r|_{res}$. First, for the sake of comparison, the same conditions graphically depicted in **Figure 2.10** are plotted again under the assumption of 'ductile' behaviour (c' = 50 kPa) in **Figure 2.13**. The 'ductile' case curves follow comparable trends with respect to the 'null cohesion' case (**Figure 2.10**). In general, smaller displacements are cumulated, as expected.

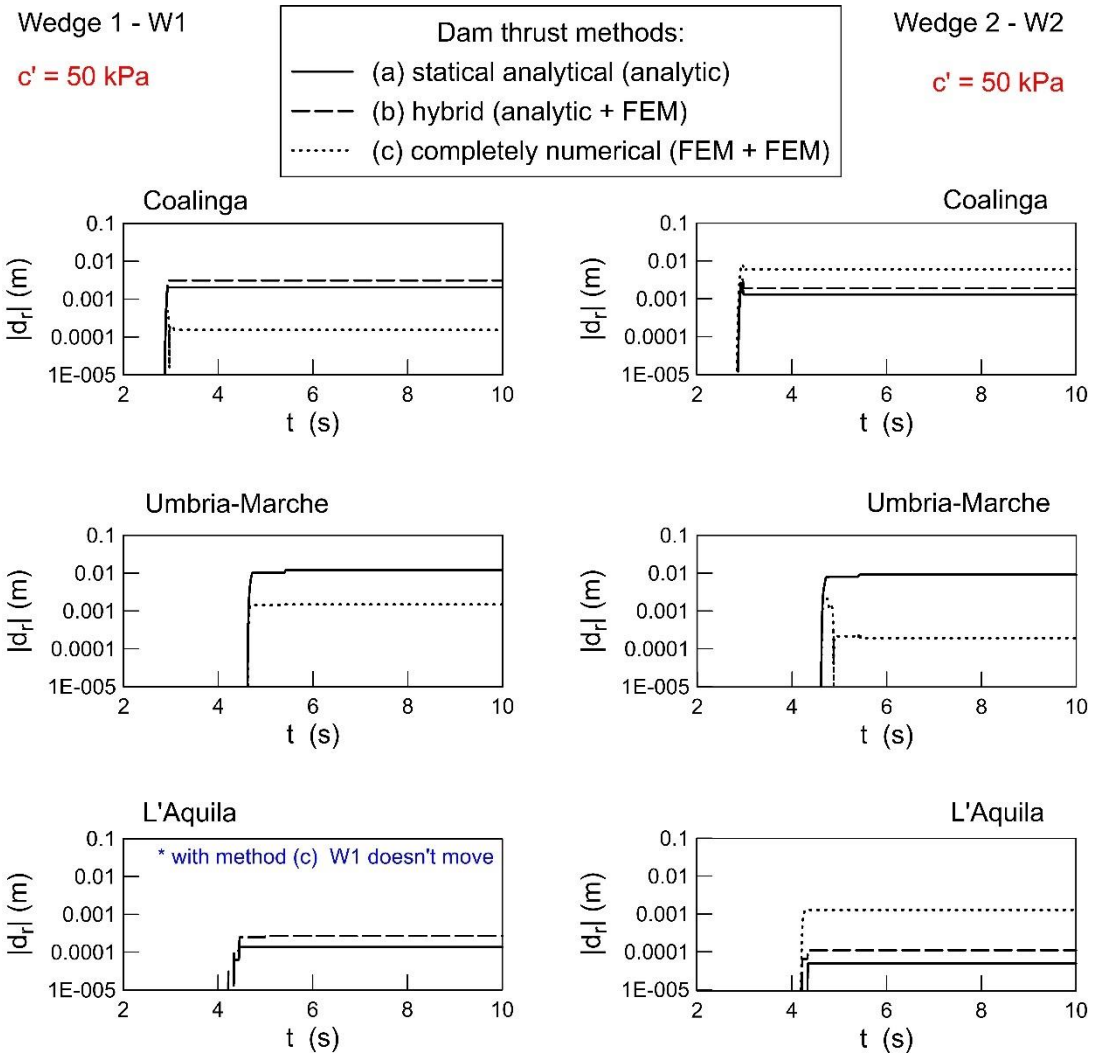

Figure 2.13. Displacement cumulation in the time domain when a c' = 50 kPa condition is applied on wedge contact faces.

If the only combination of analytic and numerical dam thrust estimation (b) and the Umbria-Marche (1997) input is considered, which always generates the largest displacements, the effect of different cohesion hypotheses along the wedge faces can be visualised in **Figure 2.14**. Between the two limit conditions (c' = 0 kPa and c' = 50 kPa), a range of intermediate level of residual displacement ($|d_r|_{res}$) is obtained. The 'brittle' hypothesis case is practically coincident to the no-cohesion one. The two linear decay hypotheses, assuming zero cohesion at displacement thresholds of 0.001 m and 0.01 m, respectively, roughly correspond to 1/2 and 2/3 of the no-cohesion case displacements and to 2 and 3 times the 'ductile' case displacements.

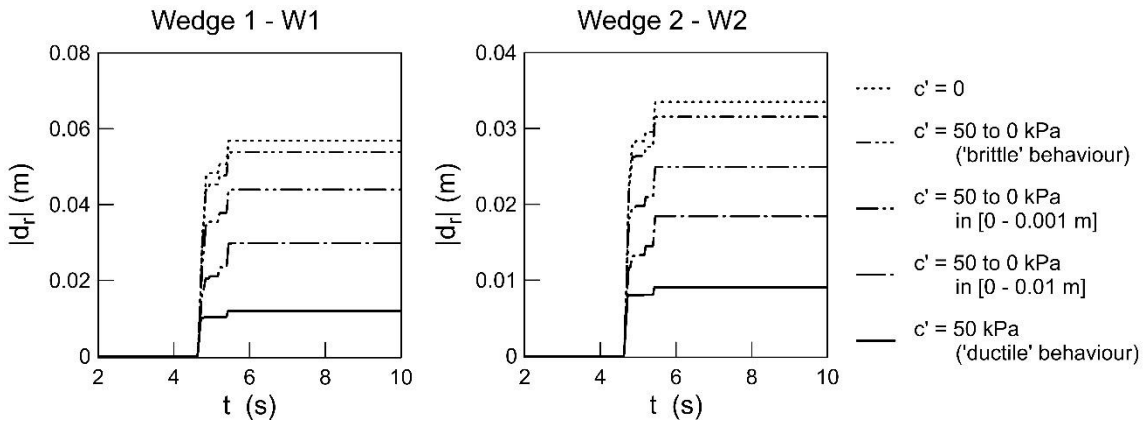

Figure 2.14. Influence of cohesion hypotheses on the wedge contact faces on the cumulated displacement calculated via Newmark integration; only Umbria-Marche (1997) earthquake and (c) approach for calculating dam thrusts is considered (FEM + FEM).

2.5.3 Comparison with limit equilibrium analyses

Lusini et al. (2022) analysed the seismic stability of the two wedges by adopting the limit equilibrium approach. A complete rotation was applied to the horizontal component of the pseudo-static seismic action calculated following the Italian Building Code (NTC, 2018). In particular, the horizontal seismic coefficient, k_H, was considered as equal to 0.24 and the vertical seismic coefficient, k_V, was taken as half of it. This derives from applying a reduction coefficient of 0.38 (from tabular values in NTC, 2018) to the maximum expected acceleration. Rampello et al. (2010) emphasise that this value pertains a displacement performance larger than 5 cm, for a lower threshold a higher coefficient can be more suitable. The thrust of the dam in static conditions was derived using the analytical method ((a) method), while the dynamic effect of the interaction was neglected. For Wedge 1 the factor of safety SF was lower than 1 for a horizontal seismic action with an azimuth in the -60° – 60° range and under the no-cohesion hypothesis (the range reduced to the azimuth range -30° – 40° for Wedge 2). SF was higher than 1 for every possible direction of the pseudo-static force when a c' = 50 kPa was considered on wedge faces. The results are compared in **Figure 2.15** with the residual displacements calculated through the 3D Newmark method. For the sake of comparability, the Newmark approach is here slightly modified: in addition to the vertical component only one of the two horizontal components of the earthquake is applied, i.e. the one with the highest energy content. The most severe performance and the minimum SF are obtained for approximately the same orientation of the horizontal seismic action (approximately North). For both type of analyses W1 is less stable (i.e. prone to higher irreversible seismic displacements) than W2.

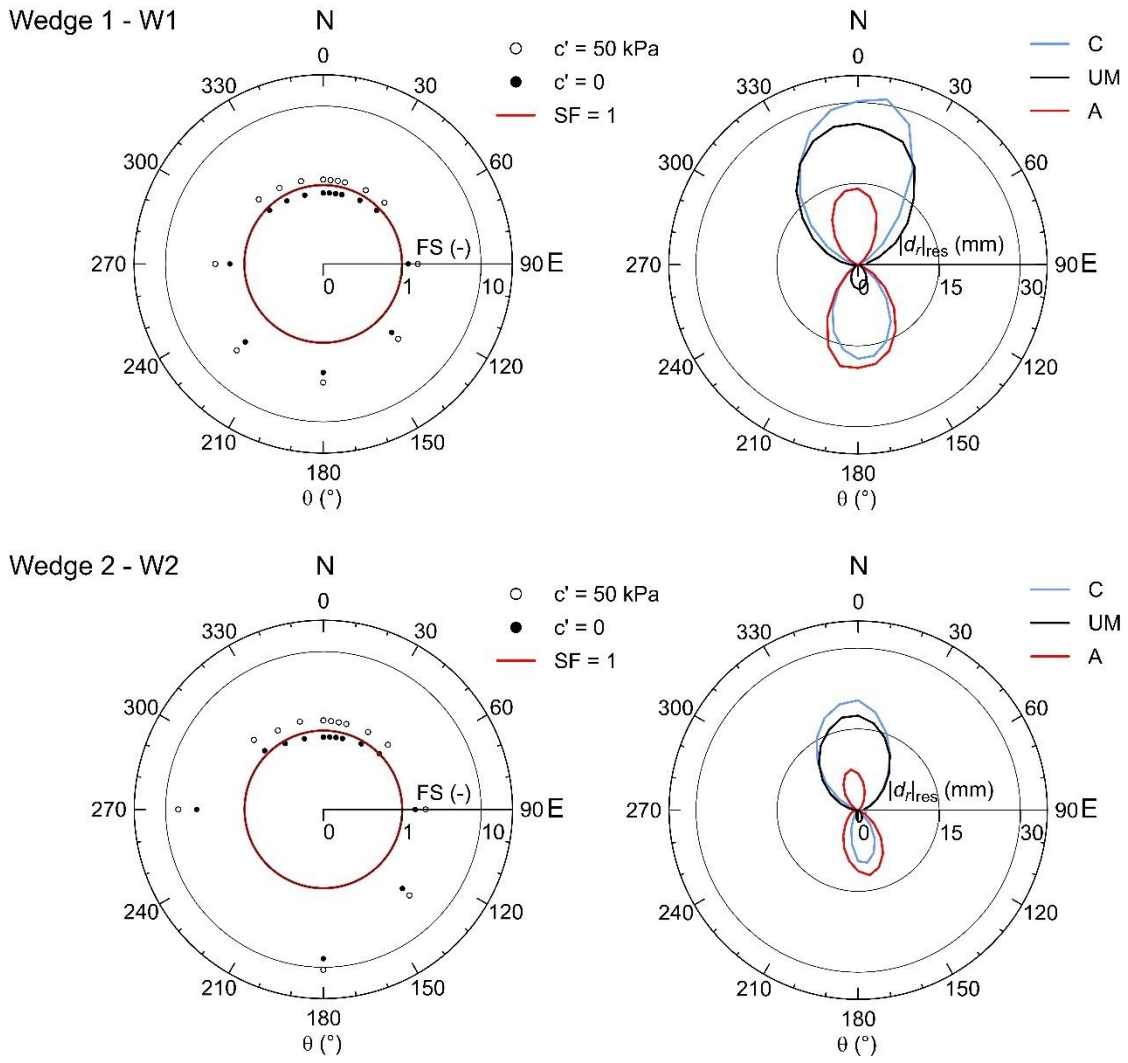

Figure 2.15. Influence of the azimuth of the seismic horizontal input: factor of safety (on the radial axis) calculated by the LEM pseudo-static analyses (left) and left). Right: cumulated displacements calculated via Newmark integration (right).

Chapter bibliography

Alpina (Alpina S.p.A), 1976 (unpublished results). Progetto Esecutivo Definitivo – Relazione Geomeccanica.

Ancheta, T. D., Darragh, R. B., Stewart, J. P., Seyhan, E., Silva, W.J., Chiou, B. S. J., Wooddell, K. E., Graves, R. W., Kottke, A. R., Boore, D. M., Kishida, T., Donahue, J. L., 2013. NGA-West2 Database. Earthquake Spectra. 30(3), 989-1005. https://doi.org/10.1193/070913EQS197M

Bavestrello, F., 1983. Stabilizzazione temporanea degli scavi d'imposta della Diga di Ridracoli, in Proc. XV Convegno Nazionale di Geotecnica (XVCNG), Spoleto, Italy.

Buffi, G., Manciola, P., De Lorenzis, L., Cavalagli, N., Comodini, F., Gambi, A., Gusella, V., Mezzi, M., Niemeier, W., Tamagnini, C., 2017. Calibration of finite element models of concrete arch-gravity dams using dynamical measures: the case of Ridracoli. Procedia Engineering. 199, 110-115. https://doi.org/10.1016/j.proeng.2017.09.169

Chopra, A. K., 2020. Earthquake engineering for concrete dams: analysis, design, and evaluation, Wiley-Blackwell, Hoboken (NJ), USA.

FERC (Federal Energy Regulatory Commission), 2018. Engineering guidelines for the evaluation of hydropower projects – chapter 11: arch dams. Washington DC, USA.

Goodman, R. E., Powell, C., 2003. Investigations of blocks in foundations and abutments of concrete dams. Journal of Geotechnical and Geoenvironmental Engineering. 129(2), 105-116. https://doi.org/doi:10.1061/(ASCE)1090-0241(2003)129:2(105)

Goodman, R. E., Shi, G., 1985. Block theory and its application to rock engineering. Prentice-Hall, Englewood Cliff (NJ), USA.

Howell, C. H., Jaquith, A. C., 1929. Analysis of arch dams by the trial load method. Transactions of the American Society of Civil Engineers. 93(1), 1191-1225. https://doi.org/doi:10.1061/TACEAT.0004040

Iervolino, I., Galasso, C., Cosenza, E., 2010. REXEL: computer aided record selection for code-based seismic structural analysis. Bull Earthquake Eng. 8, 339–362. https://doi.org/10.1007/s10518-009-9146-1

Lanzi, A., Paoliani, P., 2018. Verifiche sismiche delle grandi dighe, degli scarichi e delle opere complementari e accessorie - Istruzioni per l'applicazione della normativa tecnica di cui al D.M. 26.06.2014 (NTD14) e al D.M. 17.01.2018 (NTC18). Ministero delle Infrastrutture e dei Trasporti.

Londe, P., 1973. Analysis of the stability of rock slopes. Quarterly Journal of Engineering Geology. 6(1), 93-124. https://doi.org/doi:10.1144/GSL.QJEG.1973.006.01.04

Londe, P., Vigier, G., Vormeringer, R., 1969. Stability of Rock Slopes, A Three-Dimensional Study. Journal of the Soil Mechanics and Foundations Division. 95,235-262. https://doi.org/doi:10.1061/JSFEAQ.0001220

Lusini, E., Boldini, D., Montanari, G., Gambi, A., Fabbri, C., 2022. Analisi delle condizioni di stabilità della spalla destra della diga di Ridracoli alla luce degli sviluppi tecnici e normativi, in Proc. XXVII Convegno Nazionale di Geotecnica (XVII CNG), July 13-15 (2022), Reggio Calabria, Italy. (in Italian)

Lusini, E., Verrucci, L., Boldini, D., 2023 (under review). Computation of irreversible seismic displacements of rock wedges: an application to dam abutment safety assessment. *Computer and Geotechnics*.

Mills-Bria, B., Nuss, L. K., Chopra, A. K., 2008. Current methodology at the bureau of reclamation for the nonlinear analyses of arch dams using explicit finite element techniques, in Proc. 14th World Conference on Earthquake Engineering, October 12-17 (2008), Beijing, China.

Mostafaei, H., Behnamfar, F., 2021. Wedge movement effects on the nonlinear behavior of an arch dam subjected to seismic loading. International Journal of Geomechanics. 22(3), 1-16.
https://doi.org/10.1061/(ASCE)GM.1943-5622.0002277

Newmark, N. M., 1965. Effects of earthquakes on dams and embankments. Géotechnique. 15(2), 139-160.
https://doi.org/10.1680/geot.1965.15.2.139

NTC, 2018. Aggiornamento delle norme tecniche per le costruzioni. Ministero delle Infrastrutture e dei Trasporti. Gazzetta Ufficiale della Repubblica Italiana. Serie Generale n. 42. Rome, Italy.

NTD, 2014. Norme tecniche per la progettazione e la costruzione degli sbarramenti di ritenuta (dighe e traverse). Ministero delle Infrastrutture e dei Trasporti . Gazzetta Ufficiale della Repubblica Italiana. Serie Generale n. 156. Rome, Italy.

Oberti, G., Bavestrello, F., Rossi, P. P., Flamigni, F., 1986. Rock mechanics investigations, design and construction of the Ridracoli dam. Rock Mechanics and Rock Engineering. 19(3), 113-142.
https://doi.org/10.1007/BF01024952

OGS (Istituto Nazionale di Oceanografia e di Geofisica Sperimentale), 2014(Unpublished results). Accelerazioni attese e analisi di accelerogrammi per il sito della diga di Ridracoli (FC).

Rampello, S., Callisto, L., Fargnoli, P., 2010. Evaluation of Slope Performance under Earthquake Loading Conditions. Rivista Italiana di Geotecnica (RIG).

Swaminathan, K. V., 1960. Su di una estensione del calcolo Tölke a dighe arco-gravità con fondazioni cedevoli. L'energia elettrica. (7), 614-624.

Tölke, F., 1938. Talsperren, Staudämme und Staumauern, in Ludin, A. (Ed.), Wasserkraft Anlagen. Verlag von Julius Springer, Berlin, Germany.

Verrucci, L., Lanzo, G., Rotonda, T., Tommasi, P., Di Giulio, A., 2018. Valutazione del comportamento sismico 3D di blocchi di roccia mediante il metodo degli spostamenti, in Proc. Incontro Annuale dei Ricercatori di Geotecnica (IARG 2018), July 26-27 (2018), Genova, Italy.

Vogt, F., 1925. Über die Berechnung der Fundament Deformation, in Det Norske Videnskaps-Akademi (Ed.), Avhandlinger utgitt av det Norske Videnskaps-Akademi i Oslo: Matematisk-naturvidenskapelig klasse. Jacob Dybwad, Oslo, Norway.

Westergaard, H. M., 1933. Water pressures on dams during earthquakes. Transactions of the American Society of Civil Engineers. 98(2), 418-433. https://doi.org/doi:10.1061/TACEAT.0004496

3. Analysis of dam-water-foundation interaction

3.1 Introduction

In both static and dynamic conditions, the interaction of a dam with its rock-foundation plays a key role in order to obtain reliable results from a stress-strain analysis. The first analytical methods developed to conduct elastic static analyses of arch (or arch-gravity) dams, however, did not include the deformability of the rock foundation, considering the dam as fixed at the base (Ritter, 1931). Further developments of these methods, such as the advanced versions of the Trial Load Method (1938), tried to model these aspects by imposing elastic springs at the base of structural elements in which the dam body is ideally subdivided. These approaches may be effective to model the base deformability on the structural side but gives no information about the actual distribution of stresses in the foundation.

With the advent of numerical methods in the second half the twentieth century, such as the Finite Element Method (FEM), and efficient computers that can implement them, the dam-foundation interaction in static conditions ceased to represent a problem. The dam body and the portion of the foundation influenced by its presence may be modelled together and discretized in an arbitrary number of smaller elements; higher order differential equations needed for solving analytical methods can be substituted by simple (even if very large) systems of linear equations.

Numerical models offer also the possibility to conduct dynamic analyses of the dam-foundation system, that have long been impossible via analytical approaches. A practical way to do this in a Finite Element (FE) environment consists in solving the governing equations of the entire model in the time domain, with the so-called Direct Method, as opposed to the Substructure Method that operates in the frequency domain. Such analyses, however, are often conducted in commercial softwares with some major simplifications which substantially alter the real problem in order to reduce to a minimum the computational cost, as stated in Løkke and Chopra (2019).

For many years, the dam engineering profession has used FE models that include a limited extent of foundation rock, assumed as massless, and approximate hydrodynamic effects by an added mass of water moving with the dam. The design ground motion is applied at the bottom fixed boundary of the foundation domain without any modification.

In contrast, realistic modelling of dam–water–foundation systems require a FE model that includes a truncated fluid and foundation domains with wave-absorbing boundaries (Wolf 1988) to simulate the semi-infinite size of these domains. The seismic input should be specified by effective earthquake forces applied directly to these boundaries (Wolf 1988; Zienkiewicz et al. 1989), or alternatively, in a single layer of elements interior of the boundaries (Bielak et al. 2003; Bielak and Christiano 1984). Utilizing the latter approach, Basu (2004) developed an advanced analysis procedure using Perfectly Matched Layer (PML) boundaries (Basu and Chopra 2004) and the Effective Seismic Input method (ESI) (Bielak and Christiano 1984) to specify effective earthquake forces. However, ESI and PML methodologies require modification of the FE source code, and the procedure is currently only available in LS-DYNA (Chopra, 2020). Simple viscous damper

absorbing boundaries (Lysmer and Kuhlemeyer, 1969) may substitute these complex solutions at cost of a larger extension of the rock foundation domain.

Discontinuities in the rock mass are the primary source of non-linearities within the rock foundation domain. Their dynamic behaviour has been studied thoroughly in a discrete element (DE) environment (Lemos, 1999, 2008, 2021), while it has been less investigated by authors working with FE. Some attempts were made by Pan et al. (2015), and Mahmoudi et al. (2016). The first modelled the single features, such as faults, as a weaker and more densely meshed part of an elastoplastic continuum (a Drucker Prager criterion was assumed); the second used contact elements with an elastoplastic Mohr-Coulomb criterion only active in the compressive stress states.

The objective here is to derive a methodology in the context of a Direct FEM approach that can be implemented in the commercial code Abaqus/Standard® with limited modification of the source code. Abaqus was chosen among FE software upon request of Romagna Acque – Società delle Fonti S.p.A., owner of the dam and founder of the PhD project, owing to the presence of a previous model of the dam there implemented (Buffi, 2018). After presenting the analytical method used for designing Ridracoli Dam in the seventies, the static and dynamic formulation of the Finite Element method are recalled and applied at the dam-water-foundation system. The resulting method is a simplified version of the Direct FE method presented by Løkke and Chopra (2018), which includes:

- viscous-damper adsorbing boundaries at the truncated rock foundation domain,
- effective forces calculated in a free-field state and applied at the truncated rock foundation boundary,
- an added mass approach to model the hydrodynamic forces acting on the upstream face of the dam (thus neglecting the water-rock foundation interaction),
- a strategy to initialize static stresses only in the inner portion of the model where non-linearities are concentrated,
- non-linearities concentrated along discontinuities of the rock mass (nonlinearities in the dam body and at dam-foundation rock interface are neglected).

3.2 Analytical methods

The first analytical results were obtained in the 1920-1930 decade, thanks to the studies carried out by Guidi (1928) and Ritter (1931), which employed the complete theory of the circular fixed arch. This approach is generally referred to as the "independent arches" method and can be effective for a first estimation of tension-deformative response of arch dams in case of a very thin vertical section (arch effect clearly prevailing on the cantilever one). The virtual arches in which the dam is subdivided cannot transfer any internal stress one another. An important step toward the solution of the problem of an arch dam with a generic shape was made with the development of the Trial Load method, initially issued in U.S.A. by members of the Bourou of Reclamation (Howell and Jaquith, 1929), and then further developed after being applied in the dimensioning of the Hoover dam (USBR, 1938). At the same time in Europe an easier but less precise method was developed by Tölke (1938), based on the assumption of arch-dams as simple or double curvature plates. In both methods arch dams are assumed as composed of two systems of structural members: horizontal arch units and vertical cantilever units (**Figure 3.1**).

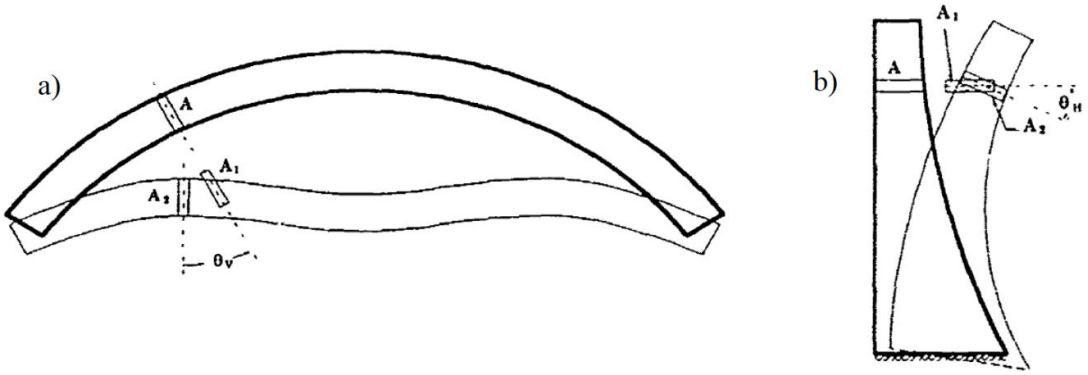

Figure 3.1. a) arch, and b) cantilever elements of an arch-gravity dam (mod. from Ghaanat, 1993).

Each system occupies the entire body of the dam, and the loading is assumed to be divided between the two systems in such a way that the resulting arch and cantilever deflections for any point in the dam were equal. The most complete version of these methods has been used for a long time in dimensioning arch dams all around the world. By including a simplified spring bed approach (Vogt, 1925), they are also able to simulate the dam-foundation interaction in static conditions and the dam-water-foundation interaction in pseudostatic conditions but cannot be extended to the solution of dynamic problems.

3.2.1 Tölke method

In its simplest form the Tölke method (1938) enforces compatibility of radial deflections between a discrete number of horizontal arches and a single cantilever, the crown cantilever (i.e., the main section cantilever). An assumption is made on the static behaviour of arch elements under a distributed load uniformly applied at the extrados of the arch. This requirement is generally fulfilled since the main static loads that affect a dam (i.e., hydrostatic pressures and thermal forces due to restraint) can be approximated as constant on arch extrados if the thickness of the arch is sufficiently small.

Under the hypothesis of a linear elastic material for a monolithic arch gravity dam, the arch element is confused with a thin cylinder of the same dimension (i.e., same thickness, intrados, and extrados radii). The portion of external pressure applied on the extrados (e.g., due to hydrostatic pressure) that is carried by the arch, p_a, is given by the following:

$$p_a = \frac{8}{15} \frac{E w s}{r_e r} \tag{3.1}$$

where E is elastic modulus of concrete, w is the radial deflection at crown, s is the thickness of the arch (in horizontal direction), r_e is the extrados radius, r is the mean radius and 8/15 is a correction coefficient suggested by the author (Swaminathan, 1960) that is optimal for arches subtended by a 120° angle. The normal force can then be calculated as:

$$N = p_a\, r = \frac{8}{15}\,\frac{E\, w\, s}{r_e} \tag{3.2a}$$

$$N = F'\, E\, w \tag{3.2b}$$

The equilibrium equation for an element of the crown cantilever (**Figure 3.2**) can then be written as a function of the radial deflections w and its spatial derivate in a local reference system with the axis, l, directed downward and the origin at the crest level:

$$r_e\, p = N + \frac{dT}{dZ} r \tag{3.3}$$

In a linear elastic thin shell, the bending moment, M, and the shear, T, are linked to the deflections as follows:

$$M = EJ\frac{d^2w}{dl^2} = \frac{E\, s^3}{12(1-\upsilon^2)}\frac{d^2w}{dl^2} \tag{3.4a}$$

$$T = \frac{dM}{dl} \tag{3.4b}$$

where ν is the Poisson coefficient. Substituting for M in **Equation 3.4a** and then for T in **Equation 3.3**, and dividing both sides by r, the following fourth order differential equation is derived:

$$\frac{r_e\, p}{r} = \frac{N}{r} + \frac{E}{12(1-\upsilon^2)}\,\frac{d^2}{dl^2}\left((\Delta L)^3\,\frac{d^2w}{dl^2}\right) \tag{3.5}$$

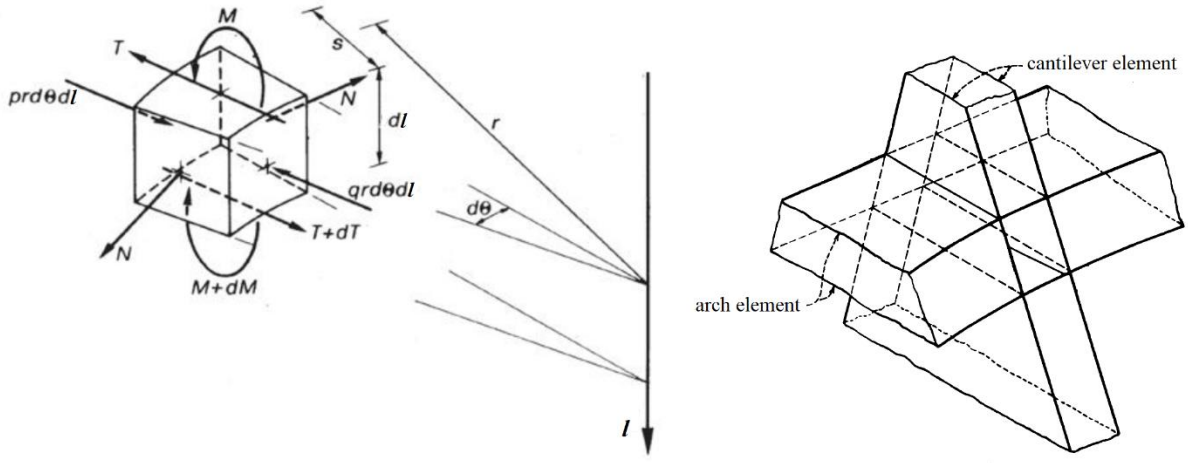

Figure 3.2. Cantilever element force diagram and pictorial view in the Tölke method (modified from Buffi, 2018; and USBR, 1977).

The second derivate of the product at the right-hand side of **Equation 3.5** can be developed to obtain:

$$w'''' + \frac{6}{s}\, w''' \, s' + 3w'' \left(\frac{1}{s} s'' + \frac{2}{s^2}(s')^2\right) + \frac{12(1-\upsilon^2)}{r\, s^3} F'\, w - \frac{12(1-\upsilon^2)\, r_e\, p}{E\, r\, s^3} = 0 \qquad (3.6)$$

where w',…, w"" and s', s" are the spatial derivates along l-coordinate in compact notation.

Equation 3.6 may be conveniently solved by applying a finite differences scheme, dividing the cantilever in a discrete number of equally spaced nodes (and thus considering only a discrete number of arches passing through those nodes). Boundary conditions at the two ends of the cantilever can be written as:

$$w'''(l = 0) = 0 \qquad (3.7a)$$
$$w''(l = 0) = 0 \qquad (3.7b)$$

for the free top end (M = 0 and T = 0); and for the fixed base under the original Tölke hypothesis of rigid foundation:

$$w\,(l = L) = 0 \qquad (3.8a)$$
$$w'(l = L) = 0 \qquad (3.8b)$$

where L is the total height of the crown cantilever, with the origin at crest level, Swaminathan (1960) proposed to include the elastic deformation of the rock foundation at the base of both arches and cantilever. The bottom-end boundary conditions for the crown cantilever become:

$$w\,(l = L) = \mu_2\, M + \lambda\, T \qquad (3.9a)$$
$$w'(l = L) = (\mu\, M + \mu_2\, T)\, L \qquad (3.9b)$$

where λ, μ and μ_2 are elastic coefficients of the Vogt theory (Vogt, 1925), which models the elastic deformation of the rock foundation as independent distributed springs. The hyperstatic arch elements are solved as in the Trial Load method (1938), based on the Vogt theory. The normal force can still be expressed as in **Equation 3.2b**. In case of an elastic foundation the solution is obtained after some iterations, starting with trial values of M and T at the base. They can be initially assumed as equal to those obtain for a rigid foundation.

3.2.2 The Trial Load method

The Trial Load method (Howell and Jaquith, 1929; USBR, 1938) takes its name from the self-balancing trail loads which are imposed to arch and cantilever elements in order to obtain equal displacements and rotations at cross points. These loads produce a redistribution of external loads dividing them between arch and cantilever elements, without altering the total load applied to the dam. The procedure is iterative and trial loads are updated at each iteration until convergence is achieved. The convergence rate is usually high. The analyses may be performed with varying degrees of accuracy depending on the number of degrees of freedom which are requested to be compatible between arch and cantilever elements. Progressing from the simplest to the most comprehensive, they include (Ghanaat, 1993): crown-cantilever analysis, radial deflection analysis and complete adjustment analyses.

In general, the agreement between the arch and cantilever should be enforced for all degrees of freedom (i.e. 3 translational DOFs and 3 rotational DOFs), and this is required in a complete adjustment analysis. On the contrary, the first two types of analysis only consider the compatibility of radial deflections (in a cylindrical coordinate system), while all other DOFs are not checked. In a radial defection analysis radial deflections crown and quarter-points of the arches are brought into agreement with corresponding cantilever elements, in a crown-cantilever analysis, only the crown cantilever is considered.

The mechanism of load transfer is briefly explained in the case of radial displacements (which are the only needed adjustment in crown-cantilever and radial deflection analyses). Similar considerations can be extended to tangential displacements and twist in a complete adjustment analysis. The external load is initially applied to the arch element. In order to transfer a portion of the load to the cantilever element a set of trail loads as those represented in **Figure 3.3** is applied, with forces T_A and T_C in equilibrium in radial direction and moments M_A and M_C added to ensure equilibrium against ration. T_C and M_C are applied for transmitting a portion of external load to the cantilever element, while T_A and M_A are applied to the arch element in order to reduce the effect of external load. Arches and cantilevers are solved separately, and the procedure is repeated until the same radial deflection is achieved at each intersection.

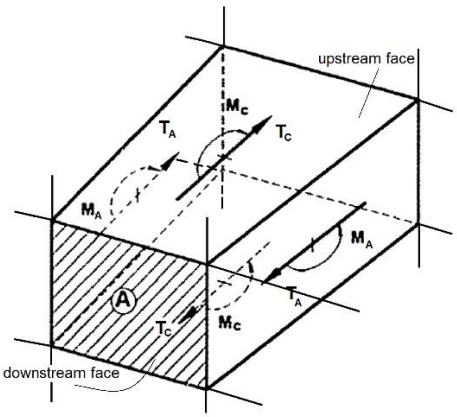

Figure 3.3. Self-balancing trial loads for radial adjustment (modified from Ghanaat, 1993).

3.3 Finite Element method

The stresses in a dam-water-foundation system are computed more accurately using the Finite Element Method (FEM) (Zienkiewicz, 1971; Bathe and Wilson, 1976; Ghanaat, 1993). On the opposite of analytical methods, the continuum domain which idealise the dam structure is discretized into arbitrary small elements interconnected at a finite number of points called nodes.

The subdivision of a whole domain into simpler parts has several advantages (Reddy, 2006), i.e.:

- accurate representation of complex geometry,
- inclusion of dissimilar material properties,
- easy representation of the total solution,
- capture of local effects.

The Finite Element Method is a variational method of the Galerkin family, usually applied for the solution of partial differential equations, under known boundary conditions. It approximates the unknown fields as continuous piecewise-defined functions of a discrete number of nodal quantities.

As a system of partial differential equations, the governing equations of continuum mechanics can be solved with the FEM. In the displacements-based approach nodal displacements are the system primary unknowns. They are obtained from the solution of equilibrium equations for the entire system, assembled by combining the stiffness matrices and the load vectors of the individual elements. The stresses are then obtained from the computed displacements using the stress-displacement relationship for each finite element. For this reason, the resulting stresses are relatively less precise than resulting displacements which are directly obtained by solving the system of equations. The solution, in general, overestimate the actual stiffness of the system and thus underestimate the effective displacements. A better convergence to the exact solution can be achieved by reducing the size of finite elements or increasing the order of the elements, at the cost of higher computational costs.

Finite Element formulation of the continuum equations in static and dynamic conditions are given in the following. The specific reference for the notation of generic FE static and dynamic formulations is Brinkgreve et al. (2022), while for the dam-water-foundation system in dynamic conditions is Løkke and Chopra (2019).

3.3.1 Static Formulation

In static conditions the system of equilibrium equations of an infinitesimal cubic element isolated from a continuum solid body can be written in compact and expanded matrix notation as:

$$\mathbf{D}^{\mathrm{T}}\underline{\mathrm{s}} + \underline{\mathrm{f}} = \begin{bmatrix} \partial_{\mathrm{x}} & 0 & 0 & 0 & \partial_{\mathrm{z}} & \partial_{\mathrm{y}} \\ 0 & \partial_{\mathrm{y}} & 0 & \partial_{\mathrm{z}} & 0 & \partial_{\mathrm{x}} \\ 0 & 0 & \partial_{\mathrm{z}} & \partial_{\mathrm{y}} & \partial_{\mathrm{x}} & 0 \end{bmatrix} \cdot \begin{bmatrix} \sigma_1 \\ \sigma_2 \\ \sigma_3 \\ \tau_{23} \\ \tau_{13} \\ \tau_{12} \end{bmatrix} + \begin{bmatrix} \mathrm{f}_1 \\ \mathrm{f}_2 \\ \mathrm{f}_3 \end{bmatrix} = 0 \tag{3.10}$$

where $\underline{f}$ is the vector of body forces, $\underline{s}$ is the vector form of Cauchy stress tensor and **D** denotes a differential operator.

Defined $\underline{e}$ and $\underline{u}$ as the strain vector and the displacement vector, respectively (Timoshenko and Goodier, 1970):

$$\underline{e} = \begin{bmatrix} \varepsilon_1 \\ \varepsilon_1 \\ \varepsilon_1 \\ \gamma_{23} \\ \gamma_{13} \\ \gamma_{12} \end{bmatrix} \qquad \underline{u} = \begin{bmatrix} u_1 \\ u_2 \\ u_3 \end{bmatrix} \tag{3.11}$$

the compatibility relation which links strains and displacements can be expressed as:

$$\underline{e} = \mathbf{D}\underline{u} \tag{3.12}$$

Finally, the constitutive law that links increments of deformation and increments of stress reads:

$$\Delta\underline{s}^{i} = \mathbf{E^i}\Delta\underline{e}^{i} \tag{3.13}$$

where **E** is the matrix form of a generic constitutive law and $\Delta\underline{s}^{i}$ and $\Delta\underline{e}^{i}$ are the variation of stress and strain respectively at the i-th increment of an incremental procedure. The stress at the end of the increment can then be written as the summation of the stress at the previous increment $\underline{s}^{i-1}$ and the stress increment $\Delta\underline{s}^{i}$ itself:

$$\underline{s}^{i} = \underline{s}^{i-1} + \Delta\underline{s}^{i} \tag{3.14}$$

or, omitting the superscripts and substituting the stresses at the previous increment with the notation $\underline{\check{s}}$, as:

$$\underline{s} = \underline{\check{s}} + \Delta\underline{s} \tag{3.15}$$

The system in **Equation 3.10** is the strong form of equilibrium. In order to apply a finite element approximation, it is conveniently rewritten in a weak form multiplying the left-hand side by a generic test function, $\delta\underline{\tilde{u}}$, and integrating over the domain. In a three-dimensional problem the domain corresponds to the volume of the solid body. It reads:

$$\int \delta\underline{\tilde{u}}^{T}\left(\mathbf{D}^{T}\underline{s}+\underline{f}\right)=0 \tag{3.16}$$

This weak form can be interpreted as the well-known principle of virtual work and $\delta\underline{\tilde{u}}$ can be seen as virtual increments of displacement kinematically admissible and derivable as needed. Splitting the integral in **Equation 3.16** in two contribution and moving the body force part to the right-hand side leads to:

$$\int \delta\underline{\tilde{u}}^{T}\mathbf{D}^{T}\underline{s}=-\int \delta\underline{\tilde{u}}^{T}\underline{f} \tag{3.17}$$

The left-hand side of **Equation 3.17** can be furtherly manipulated by applying the rule of integration by parts, the Gauss-Green theorem and the properties of transpose operators, yielding to:

$$\int\left(\mathbf{D}\,\delta\underline{\tilde{u}}\right)^{T}\underline{s}=\oint \delta\underline{\tilde{u}}^{T}\mathbf{N}^{T}\underline{s}-\int\left(\mathbf{D}\delta\underline{\tilde{u}}\right)^{T}\underline{s} \tag{3.18}$$

where the first integral at the right-hand side is defined over the closed boundary of the solid body (i.e. the bidimensional outer surface) and **N** is a matrix which contains the components of the local normal unit vector to the surface, and can be expressed in expanded notation as:

$$\mathbf{N}=\begin{bmatrix} n_1 & 0 & 0 \\ 0 & n_2 & 0 \\ 0 & 0 & n_3 \\ 0 & n_3 & n_2 \\ n_3 & 0 & n_1 \\ n_2 & n_1 & 0 \end{bmatrix} \qquad \underline{n}=\begin{bmatrix} n_1 \\ n_2 \\ n_3 \end{bmatrix} \tag{3.19}$$

Applying **Equations 3.19** to the left-hand-sided product into brackets and recognizing that the matrix product of the transpose of **N** and $\underline{s}$ corresponds to the tractions acting on the local tangent plane to the surface, **Equation 3.18**. can be reformulated as:

$$\int \delta\underline{\tilde{e}}\,\underline{s}=\oint \delta\underline{\tilde{u}}^{T}\underline{t} \tag{3.20}$$

where $\delta\underline{\tilde{e}}$ is the vector of virtual strains and $\underline{t}$ the vector of tractions on the boundary.

In conclusion, the principle of virtual works reads:

$$\int \delta\underline{\tilde{e}}\,\underline{s}=\int \delta\underline{\tilde{u}}^{T}\underline{f}+\oint \delta\underline{\tilde{u}}^{T}\underline{t} \tag{3.21}$$

Equation 3.21, considering the incremental formulation in **Equation 3.15**, can be conveniently rearranged in:

$$\int \delta\tilde{\underline{e}}\,\Delta\underline{s} = -\int \delta\tilde{\underline{e}}\,\underline{\check{s}} + \int \delta\tilde{\underline{u}}^{T}\underline{f} + \oint \delta\tilde{\underline{u}}^{T}\underline{t} \tag{3.22}$$

In the displacement-based finite element method, displacements are interpolated by polynomial over the single elements, via the so-called shape functions, which carry the dependency on the position vector, $\underline{x}$. They have unit value in correspondence of a certain degree of freedom of the element (DOF), while they are null for every other DOF. In a three-dimensional problem each node has three DOFs corresponding to the three components of nodal displacements. In matrix notation this can be written as:

$$\underline{u}(\underline{x}) = \underline{S}_1^{(e)}(\underline{x})\, q_1^{(e)} + \cdots + \underline{S}_i^{(e)}(\underline{x})\, q_i^{(e)} + \cdots + \underline{S}_n^{(e)}(\underline{x})\, q_n^{(e)} = \mathbf{S}^{(e)}(\underline{x})\ \underline{q}^{(e)} \tag{3.23}$$

where $q_i^{(e)}$ is the i-th DOF of the element, $\underline{S}_i^{(e)}$ is the i-th coloumn of the element shape function matrix $\mathbf{S}^{(e)}$ and n is the number of DOFs in the element.

Passing from the single element to the whole domain, element shape functions must be assembled in global shape functions which are piecewise polynomial and can be derived enforcing compatibility of displacement components at shared nodes. The final system of equation that represents the displacement field in the whole domain as function of nodal displacements can be analogously written as:

$$\underline{u}(\underline{X}) = \underline{S}_1(\underline{X})\, q_1 + \cdots + \underline{S}_i(\underline{X})\, q_i + \cdots + \underline{S}_n(\underline{X})\, q_N = \mathbf{S}\,(\underline{X})\,\underline{q} \tag{3.24}$$

where $\mathbf{S}$ and $\underline{q}$ are global shape function matrix and nodal displacement vector, respectively, and N is the number of DOFs of the whole domain.

Let displacements and strains be written as a function of nodal displacements. The dependency on the position is omitted hereafter for sake of conciseness.

$$\underline{u} = \mathbf{S}\,\underline{q} \tag{3.25a}$$

$$\underline{e} = \mathbf{D}\,\underline{u} = \mathbf{D}\,\mathbf{S}\,\underline{q} = \mathbf{B}\,\underline{q} \tag{3.25b}$$

where $\mathbf{B}$ is the matrix product of the differential operator $\mathbf{D}$ and the shape function matrix $\mathbf{S}$.

The principle of virtual works can be finally specialized to the case of FEM combining **Equations 3.22** and **3.13** substituting displacements and strains (actual and virtual) with their FE approximation (**Equations 3.25**).

$$\int \left(\mathbf{B}\,\delta\tilde{\underline{q}}\right)^{T} \mathbf{E}\,\mathbf{D}\,\mathbf{S}\,\Delta\underline{q} = -\int \left(\mathbf{B}\,\delta\tilde{\underline{q}}\right)^{T} \bar{\underline{s}} \; + \int \left(\mathbf{S}\,\delta\tilde{\underline{q}}\right)^{T} \underline{f} + \oint \left(\mathbf{S}\,\delta\tilde{\underline{q}}\right)^{T} \underline{t} \tag{3.26}$$

The vector of virtual nodal displacements ($\delta\tilde{q}$) multiplies every integrand function and is independent from the position. Therefore, in may be taken out of integral,

$$\delta\tilde{\underline{q}} \int \mathbf{B}^{T}\,\mathbf{E}\,\mathbf{D}\,\mathbf{S}\,\Delta\underline{q} = -\delta\tilde{\underline{q}} \int \mathbf{B}^{T}\,\bar{\underline{s}} + \delta\tilde{\underline{q}} \int \mathbf{S}^{T}\,\underline{f} + \delta\tilde{\underline{q}} \oint \mathbf{S}^{T}\,\underline{t} \tag{3.27}$$

and cancelled, in order to obtain the final form of the system of equations:

$$\int \mathbf{B}^{T}\,\mathbf{E}\,\mathbf{B}\,\Delta\underline{q} = -\int \mathbf{B}^{T}\,\bar{\underline{s}} + \int \mathbf{S}^{T}\,\underline{f} + \oint \mathbf{S}^{T}\,\underline{t} \tag{3.28}$$

The integral of the matrix product at the left-hand side is generally referred to as the stiffness matrix, **K,** and multiplies the variation of nodal displacements ($\Delta\underline{q}$) at the i-th increment, which is independent on the position and goes out of the integral. The adding terms at the right-hand side form the global residual vector, $\underline{R}$, of the system of equations and is composed of the summation of internal (from previous iteration) and external forces applied to the body.

$$\mathbf{K} = \int \mathbf{B}^{T}\,\mathbf{E}\,\mathbf{B} \tag{3.29a}$$

$$\underline{R} = \left(\int \mathbf{S}^{T}\underline{f} + \oint \mathbf{S}^{T}\underline{t}\right) - \int \mathbf{B}^{T}\,\bar{\underline{s}} \tag{3.29b}$$

Substituting for **K** and $\underline{R}$ in **Equation 3.28** a compact notation of the solving system of equations is obtained, that will be numerically integrated in a Finite Element code at every increment, i.

$$\mathbf{K^{i}}\;\Delta\underline{q}^{i} = \underline{R}^{\,i} \tag{3.30}$$

In the special case of a linear elastic constitutive the Hooke law holds (Ghaanat, 1993):

$$\underline{s} = \mathbf{E}\,\underline{e} \tag{3.31}$$

with matrix **E** independent on increment i. With an analogous procedure, and substituting **Equation 3.13** with **Equation 3.31** the governing system of equations is expressed as:

$$\mathbf{K}\,\underline{q} = \underline{R} \tag{3.32}$$

and can be solved without iterating.

3.3.2 Isoparametric elements

Discretization of dam-foundation models is generally carried out by means of isoparametric finite elements, which are not restricted to regular element shapes, but may tolerate a certain degree of distortion to adapt to actual geometries. Their most promising feature consists in the use of the same interpolation functions to describe both the unknown field variable (i.e., the displacements) and the geometry of the elements. As a consequence, the shape functions S_{ij} (comprised in **S** matrix) are written in a ξ-η-ζ-coordinate system of a parent domain where a regular finite element is defined and are used for mapping it into the effective distorted finite element defined in the global domain with the usual X-Y-Z-coordinate system.

The aspects that characterize a finite element are (Smith, 2009):

- the family,
- the DOFs,
- the number of nodes,
- the formulation,
- the integration.

A reference is made to the family of three-dimensional continuum finite elements, which are generally used to describe complex geometries which cannot be idealized as bidimensional or one-dimensional elements. The elements of a family can have different shapes (e.g., hexahedron, wedge, tetrahedron, etc…) and a different number of nodes. The DOFs are the unknowns of the system of solving equations. In a pure mechanical simulation of solid volumes, degrees of freedom correspond to nodal translations. Given a shape of the finite element, the interpolation order depends on the number of nodes of the element. Elements with nodes only at their corners employ first-order interpolation of displacements and are called linear elements (e.g., 8-node hexahedron, 6-node wedge, 4-node tetrahedron, etc…), elements with mid-edge nodes, in addition to those at the corners, allow for a second-order interpolation and are called quadratic elements (e.g., 20-node hexahedron, 15-node wedge, 10-node tetrahedron, etc…). Typical three-dimensional isoparametric elements in their parent domain are depicted in **Figure 3.4.**

The formulation of an element depends on whether a Lagrangian or Eulerian description is supported. In solid continuum mechanics, a Lagrangian description is generally adopted, with finite elements following the deformation of the solid body.

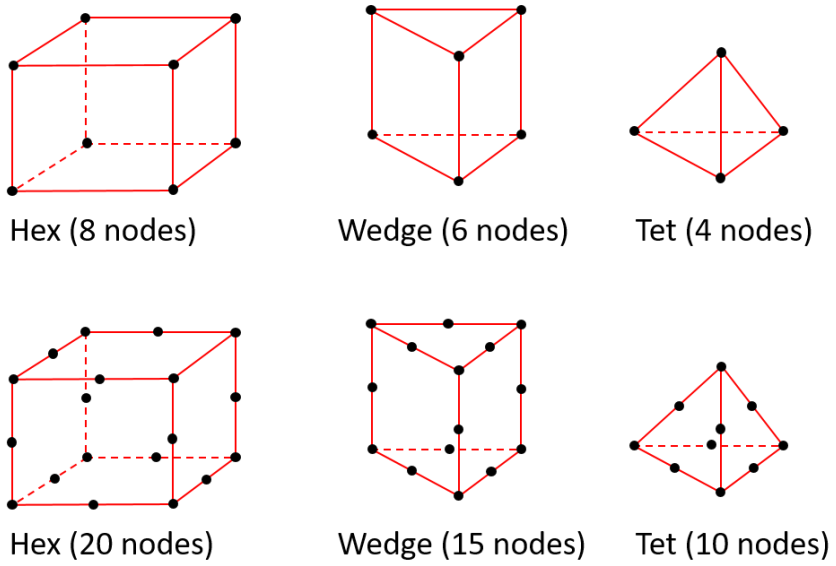

Figure 3.4. Typical three-dimensional isoparametric elements (from Vedvik, 2021).

Finally, the integration accounts for to the numerical technique used for integrating over the volume of each element (e.g., for calculating the elements of the stiffness matrix **K**). The most commonly used is the Gaussian quadrature, which approximates the exact integral as a weighted summation of the integrand function evaluated at a discrete number of inner points called Gauss points.

3.3.3 Dynamic Formulation

In dynamic conditions, holding the principle of D'Alembert, the system of equilibrium equations changes as follow:

$$\mathbf{D}^{T}\underline{s}(t) = \rho(\underline{X})\,\mathbf{I}\,\underline{\ddot{u}}(t) - \underline{f}(t) \tag{3.33}$$

where ρ is the mass density dependent on the position $\underline{X}$, **I** is the identity matrix, and their product by nodal accelerations, $\underline{\ddot{u}}$, represents the inertial forces. All vectors depend on time, t.

Moreover, if a viscus damping is associated with the system, the balance of forces reads:

$$\mathbf{D}^{T}\underline{s}(t) = \rho(\underline{X})\,\mathbf{I}\,\underline{\ddot{u}}(t) + \mathbf{c}\,\underline{\dot{u}}(t) - \underline{f}(t) \tag{3.34}$$

where **c** is the matrix of damping coefficients which multiplies the velocities.

Applying the standard procedure for derivation of the virtual work principle as described in the **Section 3.3.1** and considering geometric relationships between displacements and strains, constitutive equations, and initial conditions, the variational formulation of the FEM results in a

system of the second order. For sake of simplicity, it is written for an elastic material, but it supports an incremental formulation as seen for the static problem:

$$\mathbf{M}\,\underline{\ddot{q}}(t) + \mathbf{C}\,\underline{\dot{q}}(t) + \mathbf{K}\,\underline{q}(t) = \underline{R}(t) \tag{3.35}$$

where **M** and **C** are the mass and material damping matrices, respectively. A mass matrix defined this way is called consistent.

$$\mathbf{M} = \rho(\underline{X}) \int \mathbf{S}^T \mathbf{I}\,\mathbf{S} \qquad \mathbf{C} = \int \mathbf{S}^T \mathbf{c}\,\mathbf{S} \tag{3.36}$$

Viscous damping is, in effect, a fictitious device, since material damping is caused by friction (which develops heat) or by irreversible deformations at constant stress level (i.e., plasticity or viscosity). However, damping can still be easily taken into account using the matrix **C**. To determine the damping matrix, extra parameters are required, which are difficult to calibrate. In finite element formulations, **C** is often formulated as a function of the mass and stiffness matrices (Rayleigh damping) (Zienkiewicz and Taylor, 1991; Hughes, 1987) as:

$$\mathbf{C} = \alpha_R\,\mathbf{M} + \beta_R\,\mathbf{K} \tag{3.37}$$

with Rayleigh coefficients, α_R and β_R.

This strategy is very attractive because it allows to express **Equation 3.35** in terms of only **M** and **K**. Unfortunately, a dependency on the frequency arises, which prevents from defining a single damping coefficient, ζ, for all periods. Coefficients α_R and β_R should be chosen carefully to ensure an adequate damping coefficient in the interval of periods of interest (**Figure 3.5**).

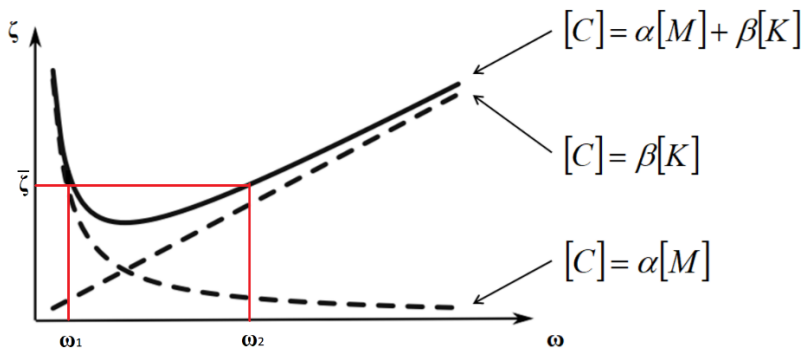

Figure 3.5. Dependency of the damping coefficient ζ on the frequency of the signal when assuming a Rayleigh damping: ζ is correctly represented only for two frequencies while it is overestimated or underestimated elsewhere (modified from Buffi, 2018).

3.3.4 Dam-water-foundation interaction as a scattering problem

During a seismic excitation a dam interact with its foundation rock and with the water stored in its reservoir. The problem is theoretically semi-unbounded since the rock-foundation extends till and beyond the hypocentre of the earthquake. To reduce the computational effort to a reasonable amount a model can be defined with a truncated domain and adsorbing boundaries that avoid the reflection of seismic waves and thus allow for radiation damping of the system. Løkke and Chopra (2019) developed a Direct FEM method that includes a finite element discretization of the fluid domain with acoustic elements and solve the dynamic problem in the time domain. Herein a simplified approach specific for dams is followed: the water domain corresponding to the reservoir is treated as a hydrodynamic load acting on the upstream face of the dam, by appending an added mass of water to it, which contributes to the total inertia of the system. The interaction of the water body with the rock foundation is neglected.

The governing equations of the dynamic problem can be specialized for this special case as follow:

$$\mathbf{M}\,\underline{\ddot{q}}^{t}(t) + \mathbf{C}\,\underline{\dot{q}}^{t}(t) + \mathbf{K}\,\underline{q}^{t}(t) = \underline{R}^{t}_{h}(t) + \underline{R}^{t}_{f}(t) + \underline{R}^{st}(t) \tag{3.38}$$

where $\underline{R}^{st}$ are the static reaction forces on the foundation-rock bottom and lateral boundaries, $\underline{R}^{t}_{f}$ are the dynamic forces transmitted by the adsorbing boundaries to the model and $\underline{R}^{t}_{h}$ are the hydrodynamic forces. The dependency on time will be omitted hereafter.

This interaction problem may be interpreted as a scattering problem, in which the presence of the dam perturbs a free-field state of the system. The free-field state corresponds to the seismic response of an auxiliary foundation rock system which is fictitious at present and can be interpreted as the real domain before the dam construction has started. It consists of two subdomains (**Figure 3.6a**):

- Ω^0 denotes the foundation region with an irregular valley interior to the future absorbing boundary (Γ_f),
- Ω_f^+ is the semi-unbounded, regular foundation region exterior to Γ_f. The displacement field in this auxiliary foundation rock system is defined as $\underline{r}^0$.

The dam–foundation system representing the current state is also separated into two subdomains (**Figure 3.6b**):

- Ω denotes the dam and foundation region interior of the absorbing boundary (Γ_f),
- Ω_f^+ is the semi-unbounded external region, identical to that defined for the free-field system.

Following the approach first proposed by Herrera and Bielak (1977), the displacement field in the dam–foundation rock system is defined by the variables:

- $\underline{r}^t$, total displacement field in the interior region Ω^0,
- $\underline{r}^t - \underline{r}^0$, scattered motion field in the exterior region Ω^f_+.

This substitution of variables allows to reformulate adsorbing boundary forces, $\underline{R}^t_f$, as function of free-field displacements $\underline{r}^0$.

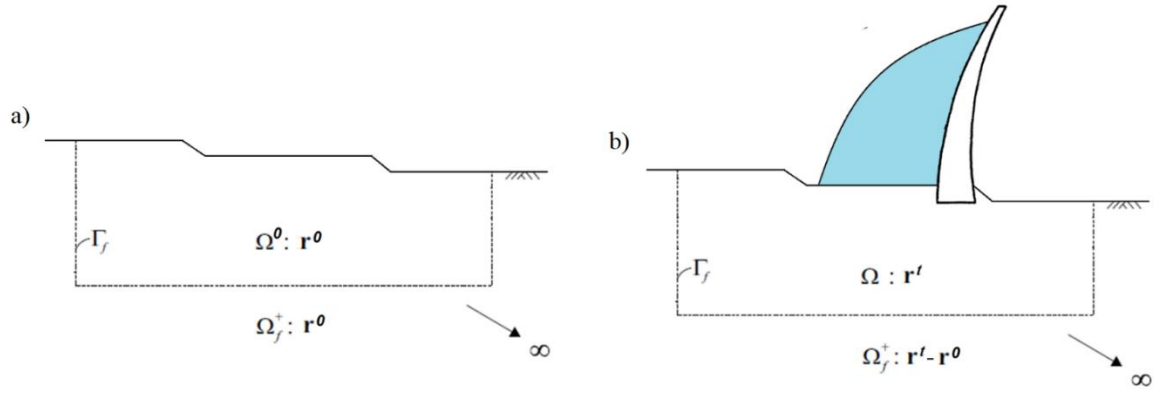

Figure 3.6. a) subdomains in the free-field state; b) subdomains in the main model.

3.3.5 Boundary conditions

One simple and efficient way to allow the radiation damping at the boundaries consists in placing a set of continuously distributed viscous dampers. The radiation damping is correctly modelled only in case of waves impinging normally to the boundary, but the error can be acceptable when the truncated domain is sufficiently large.

The radiation condition is granted if the following conditions (Lysmer and Kuhlemeyer, 1969) hold:

$$\sigma + \rho_f V_p \dot{u} = 0 \tag{3.39a}$$

$$\tau_i + \rho_f V_s \dot{w}_i = 0 \tag{3.39b}$$

where ρ_f is the foundation rock mass density; V_P and V_S are primary and secondary waves velocities of the foundation rock; σ and τ_i are the normal and tangential stress component in the tangential plane to Γ_f ; u and w_i are the normal and tangential displacement components to Γ_f and are here present with their first time derivate (i.e., the velocity); in 3D problems i = 1, 2.

The viscous boundary simulates the external domain that has been truncated. The motion there is defined by the scattered motion, $\underline{r}^t - \underline{r}^0$.

$$u = u_t - u_0 \tag{3.40a}$$

$$w_i = w_{t_i} - w_{0_i} \tag{3.40b}$$

where subscripts t and 0 stand for total and free field, respectively.

Because the foundation rock is assumed to be linear the following holds:

$$\sigma = \sigma_t - \sigma_0 \tag{3.41a}$$

$$\tau_i = \tau_{t_i} - \tau_{0_i} \tag{3.41b}$$

Substituting for total displacements in **Equations 3.40** and **3.41** in **Equations 3.39**, and reformulating in a Finite Element notation (i.e., as function of nodal velocities) yields to:

$$\underline{R}_f^t = \underline{R}_f^0 - \mathbf{C}_f \left(\underline{\dot{q}}_f - \underline{\dot{q}}_f^0 \right) \tag{3.42}$$

where $\mathbf{C}_f$ is a damping coefficient matrix with non-null entries only in correspondence of nodes belonging to Γ_f. In a discretized domain dampers are not uniformly distributed but applied at boundary nodes, damping coefficients are therefore function of the node density at the boundary, or, in other words, of their influence area (A). The non-null entries of matrix $\mathbf{C}_f$ are given in the form:

$$c_p = A\, \rho_f\, V_p \tag{3.43a}$$

$$c_s = A\, \rho_f\, V_s \tag{3.43b}$$

Substituting for $\underline{R}^t_f$ in **Equation 3.38** the governing equations become:

$$\mathbf{M}\, \underline{\ddot{q}}^t + (\mathbf{C} + \mathbf{C}_f)\underline{\dot{q}}^t + \mathbf{K}\, \underline{q}^t = \underline{R}_h^t + \underline{R}^{st} + \underline{P}_f^0 \tag{3.44}$$

where:

$$\underline{P}_f^0 = \underline{R}_f^0 + \mathbf{C}_f\, \underline{\dot{q}}_f^0 \tag{3.45}$$

This formulation applies directly to the side boundaries. Since the input motion is applied uniformely to the bottom boundary as upward propagating P and S waves, **Equation 3.45** can be further specialized for this boundary.

Because the free-field foundation–rock system is assumed to be linear and homogenous, the following expression can be derived as first obtained by Joyner and Chen (1975)

$$\sigma^0 + \rho_f\, V_p (2\dot{u}_{UP}^0 - \dot{u}^0) = 0 \tag{3.46a}$$

$$\tau_i^0 + \rho_f\, V_s \left(2\dot{w}_{UP_i}^0 - \dot{w}_i^0\right) = 0 \tag{3.46b}$$

where u_{UP} and $w_{UP,i}$ are displacements due to upward propagating P and S waves.

Equations 3.46 can be expressed in finite element notation, with corresponding $\underline{P}^0_f$ defined as in **Equation 3.45**.

$$\underline{R}^0_f = \mathbf{C}_f \left(2\underline{\dot{q}}^0_{UP} - \underline{\dot{q}}^0_f \right) \tag{3.47a}$$

$$\underline{P}^0_f = 2\, \mathbf{C}_f\, \underline{\dot{q}}^0_{UP} \tag{3.47b}$$

and so, the system of governing equations become:

$$\mathbf{M}\, \underline{\ddot{q}}^t + (\mathbf{C} + \mathbf{C}_f)\underline{\dot{q}}^t + \mathbf{K}\, \underline{q}^t = \underline{R}^t_h + \underline{R}^{st} + 2\, \mathbf{C}_f\, \underline{\dot{q}}^0_{UP} \tag{3.48}$$

3.3.6 Free-field effective forces

The free-field motion to be applied at side and bottom viscous boundaries of the truncated domain is the local seismic response of the original valley without the dam. In a three-dimensional problem the semi-unbounded domain is truncated by vertical parallel planes in two orthogonal plane directions so that two sides are parallel to the valley in which the dam is located, and the remaining two planes cross the valley perpendicularly, downstream and upstream of the structure. The bottom boundary is a horizontal plane at a certain depth. A horizontal section of the model has a rectangular shape. The geometry of the three-dimensional problem is schematically depicted in **Figure 3.7a**.

Since only the motion at the boundaries of this free-field auxiliary model is of interest for the dynamic analysis of the main model, the effective forces can be approximately calculated as the free-field response of eight auxiliary system (**Figure 3.7b**):

- 4 one-dimensional columns,
- 4 two-dimensional sections.

It corresponds to consider the motion in each of the four 2D systems as independent on that of other 2D systems. This approximation is particularly valid if the valley has a very regular canyon-like shape and are identical to the exact solution in case of a square box. The meshes of auxiliary systems should match exactly the boundary mesh of the main model.

The procedure starts with the definition of an input motion at the base. The simplest assumption, often used for site response analyses and soil–structure interaction analyses, is vertically propagating SH-waves and P-waves (Schnabel et al., 1972; Wolf, 1985). This is clearly a major simplification of the actual seismic wave field but is often justified on the basis that most sites are located relatively far away from the earthquake source, and that the gradual softening of rock and soil towards the Earth's surface leads to diffraction of seismic waves towards vertical incidence (Kramer, 1996). The input motion can be selected from actual recordings on the basis of a good matching with the Uniform Hazard Spectrum (UHS) determined by probabilistic seismic hazard analysis (McGuire, 2004) (see **Sections 2.3.2** and **2.4.2**).

Each component of the input motion is then applied from **Equation 3.47b** at the base of the four angular columns separately, in that direction a viscous damper is placed, while the other two directions are fixed. Once calculated and stored the effective seismic force at the nodes along the height of the column, the input motion is applied at the base of 2D systems with **Equation 3.47b**. Each system is fixed at the two sides, simulating an infinite extension, while viscous dampers are applied at the base and at the boundaries shared with 1D-columns. Effective forces calculated for 1D columns are applied at shared boundaries by means of **Equation 3.45**. Nodal values of effective seismic forces, $\underline{R}^t_f$, and nodal velocities from 2D systems are calculated and stored, to be applied on the corresponding nodes of the main model with **Equation 3.45**.

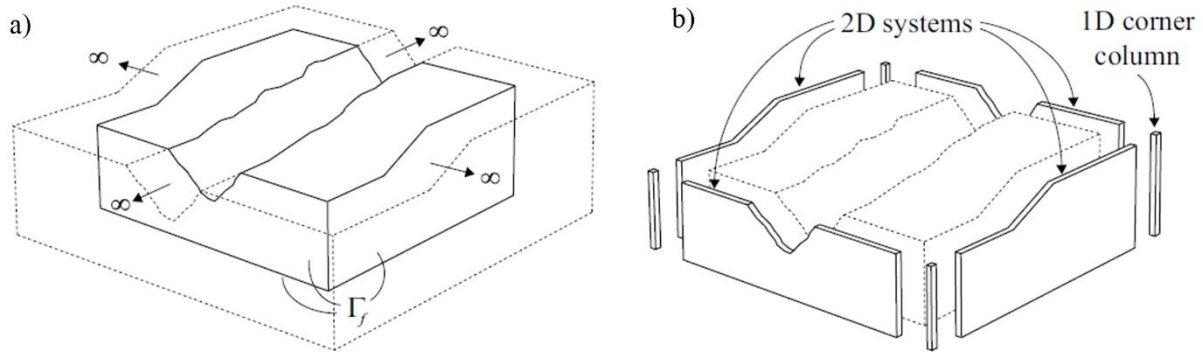

Figure 3.7. a) truncation of the semi-unbounded three-dimensional problem; b) one-dimensional and two-dimensional free-field systems at foundation rock lateral boundaries (modified from Løkke and Chopra, 2019).

The auxiliary analyses can be performed separately, with a high amount of data to be stored and transferred, or it can be run in parallel within the Finite Element code.

In the commercial code Abaqus/Standard this last can be done by implementing a special purpose user-defined finite element. Nielsen (2014) developed a free-field family of finite elements for two-dimensional and three-dimensional analyses.

The system matrices (i.e., K, C and M) can be written for the free-field elements in the form:

$$\mathbf{A} = \begin{bmatrix} \mathbf{A}_{\mathrm{ff}} & \mathbf{A}_{\mathrm{fm}} \\ \mathbf{A}_{\mathrm{mf}} & \mathbf{A}_{\mathrm{mm}} \end{bmatrix} \tag{3.49}$$

where $\mathbf{A}$ is the generic system matrix, $\mathbf{A}_{\mathrm{ff}}$ rapresents the properties of the free-field, $\mathbf{A}_{\mathrm{mm}}$ the free-field element contribution to the main model and $\mathbf{A}_{\mathrm{mf}}$ and $\mathbf{A}_{\mathrm{fm}}$ the coupling between the two systems. The free-field system is not influenced by the main model, as a consequence $\mathbf{A}_{\mathrm{fm}} = 0$, whereas $\mathbf{A}_{\mathrm{mf}}$ is in general non-null. This leads to unsymmetric system matrices.

The free-field element does not contribute to any mass of the main model, so $\mathbf{M}_{\mathrm{mf}} = \mathbf{M}_{\mathrm{mm}} = 0$. $\mathbf{M}_{\mathrm{ff}}$ can be either lumped or consistent.

The stiffness matrix of the free-field, $\mathbf{K}_{ff}$, is given by **Equation 3.29b**; the free-field element does not contribute to the stiffness of the main model, so $\mathbf{K}_{mm} = 0$.

At the contact face, the free-field element exerts a surface traction on the main model corresponding to the enforcing of plain strain conditions in the form:

$$\underline{t}_{PS} = \int_{\Delta\Gamma_f} \mathbf{S^T E' B}\, \underline{q}_{ff} \tag{3.50}$$

where $\underline{t}_a$ is the vector of nodal tractions, **S** is the shape function matrix, **E'** is an elastic material matrix, **B** is obtained as the product of the differential operator **D** and the shape function matrix **S,** and $\underline{q}_{ff}$ is the vector of nodal free-field displacements. $\Delta\Gamma_f$ is the element portion of the truncated foundation boundary Γ_f. The coupling element of the stiffness matrix, $\mathbf{K}_{mf}$, can be calculated as:

$$\mathbf{K}_{mf} = -\int_{\Delta\Gamma_f} \mathbf{S^T E' B} \tag{3.51}$$

Th free-field portion of the damping matrix, $\mathbf{C}_{ff}$, may be calculated under the assumptions of a Raileigh damping with **Equation 3.37**. The other two non-null submatrices, $\mathbf{C}_{mf}$ and $\mathbf{C}_{mm}$, are used to apply a viscous boundary condition to the vertical faces of the model.

At the contact face, the free-field element exerts a surface traction on the main model corresponding to the radiation damping conditions in the form:

$$\underline{t}_{VB} = \rho \int_{\Delta\Gamma_f} \mathbf{S^T H S} \left(\dot{\underline{q}}_{ff} - \dot{\underline{q}}_{mm}\right) \tag{3.52}$$

where **H** is diagonal matrix containing the waves velocities (V_P and V_S), while $\underline{q}_{ff}$ and $\underline{q}_{mm}$ are nodal velocities. The remaining submatrices of the damping matrix can be calculated as:

$$\mathbf{C}_{mm} = -\mathbf{C}_{mf} = \rho \int_{\Delta\Gamma_f} \mathbf{S^T H S} \tag{3.53}$$

3.3.7. Hydrodynamic forces

Hydrodynamic pressures in a dam-water system can be included in a finite element analysis using the added mass concept. It allows to investigate the dynamical response of the structure without explicitly modelling the fluid motion and consequently reducing the modelling efforts. The added mass approach was first derived analytically by Westergaard (1933) for the simple case of a rigid dam with a vertical upstream face subjected to a horizontal harmonic ground motion, and then extended by Kuo (1982) to inclined faces. The fluid is considered as an incompressible acoustic medium. Under these assumptions the hydrodynamic forces applied on the dam face correspond to

the normal pressure exerted by a mass of water adjacent to the dam, and are function of the global vertical coordinate (Z), and the time (t):

$$p\,(Z,t) = \rho_w\ b(Z)\ \ddot{u}_n(Z,t) \tag{3.54}$$

where ρ_w is water density, $\underline{\ddot{u}}$ is the vector of normal accelerations to the upstream face and b is defined as:

$$b(Z) = \frac{7}{8}\sqrt{(H-h)(H-Z)} \tag{3.55}$$

where H and h are the elevation of the water level in the reservoir and of the base level of the upstream face, respectively. A bidimensional scheme of the Westergaard method is given in **Figure 3.8.**

Zangar (1952) extended Westergaard work by considering the sloping upstream face of a dam. He derived experimentally an equation for the pressure distribution over the height of the dam for different inclinations of the dam. Based on the assumptions of water incompressibility and rigid structure, the expression for the hydrodynamic pressure distribution is given as:

$$b(Z) = (H-h)\ \frac{c_m}{2}\left[\frac{H-Z}{H-h}\left(2-\frac{H-Z}{H-h}\right)+\sqrt{\frac{H-Z}{H-h}\left(2-\frac{H-Z}{H-h}\right)}\right] \tag{3.56}$$

where c_m is a coefficient that accounts for dam face sloping, calculated as function of the sloping angle θ on the horizontal measured in degrees, with the following empirical relation:

$$c_m = -0.0073\theta + 0.7412 \tag{3.57}$$

In the finite element notation, the added mass is generally described as a matrix which models the interaction between water pressure and the structure (Brinkgreve et al., 2022). Recognizing that the upstream face is part of the external boundary of the system, the following holds for the vector of hydrodynamic forces, $\underline{R}^t_h$:

$$\underline{R}^t_h = \int_{\Gamma_h} \mathbf{S}^T \underline{t}\ = \int_{\Gamma_h} \rho_w\, b(Z)\, \mathbf{S}^T \underline{\ddot{u}}_n \tag{3.58}$$

where **S** is matrix of the shape functions already defined, hydrodynamic pressures are traction, $\underline{t}$, on the boundary.

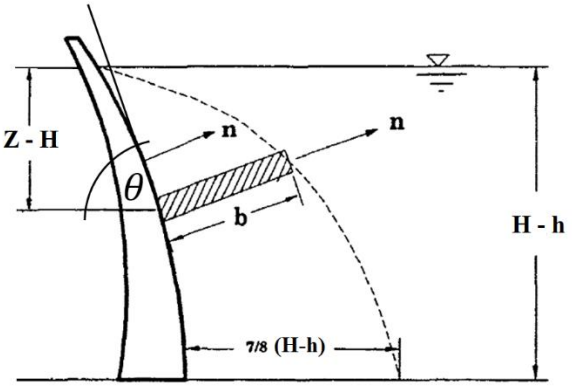

Figure 3.8. Westergaard added mass concept (modified from Buffi, 2018).

In a FEM notation the vector of normal accelerations to the upstream face should be expressed as a function of nodal quantities. The following relation can be derived:

$$\underline{\ddot{u}}_n = \mathbf{T}^T \mathbf{T}\, \mathbf{S}\, \underline{\ddot{q}}^t \tag{3.59}$$

where $\underline{q}$ is the vector of nodal displacements and here appears with its second derivate (i.e., nodal accelerations), and matrix $\mathbf{T}$ is derived form a complete three-dimensional rotation matrix by cancelling the second and the third columns as follows:

$$\mathbf{T} = \begin{bmatrix} \cos\alpha \cos\beta & 0 & 0 \\ \sin\alpha \cos\beta & 0 & 0 \\ -\sin\beta & 0 & 0 \end{bmatrix} \tag{3.60}$$

where α and β are angles of rotation about the global X and Y axes (counter clockwise positive).

The resulting equation for $\underline{R}^t_h$ can be written as:

$$\underline{R}^t_h = \int_{\Gamma_h} \rho_w\, b(Z)\, \mathbf{S}^T \mathbf{T}^T \mathbf{T}\, \mathbf{S}\, \underline{\ddot{q}}^t = -\mathbf{M}_a\, \underline{\ddot{q}}^t \tag{3.61}$$

where $\mathbf{M}_a$ is a consistent added-mass matrix with non-null elements only in correspondence of upstream face nodes.

Substituting for $\underline{R}^t_h$ in **Equation 3.44** the following final form of the governing equations is obtained:

$$(\mathbf{M} + \mathbf{M}_a)\underline{\ddot{q}}^t + (\mathbf{C} + \mathbf{C}_f)\Delta\underline{\dot{q}}^t + \mathbf{K}\,\underline{q}^t = \underline{R}^{st} + \underline{P}^0_f \tag{3.62}$$

3.3.8 Integration in time

For solving the governing equation of dynamic problems in the time domain an explicit or an implicit integration scheme may be adopted. Explicit methods calculate the state of a system at a current time increment (Δt) from the state of the system an earlier time; while implicit methods combine both the previous and current states to find a solution for the current increment. While the explicit algorithm is simpler to formulate, it is strongly dependent on the chosen time step and can diverge from the solution if it becomes too large. The implicit algorithm is more stable and robust, at the cost of an additional computational cost (Sluys, 1992). An implicit time stepping method was developed by Newmark (1959). It is based on the following equations that link displacements, velocities and accelerations at current time (t+Δt) to those at the previous time increment (t):

$$\underline{u}^{t+\Delta t} = \underline{u}^{t} + \underline{\dot{u}}^{t}\,\Delta t + \left[\left(\frac{1}{2} - \alpha_N\right)\underline{\ddot{u}}^{t} + \alpha_N\,\underline{\ddot{u}}^{t+\Delta t}\right]\Delta t^2 \tag{3.63a}$$

$$\underline{\dot{u}}^{t+\Delta t} = \underline{\dot{u}}^{t} + \left[(1-\beta_N)\underline{\ddot{u}}^{t} + \beta_N\,\underline{\ddot{u}}^{t+\Delta t}\right]\Delta t \tag{3.63b}$$

where α_N and β_N are Newmark coefficients. Depending on the choice of these parameters the Newmark method takes different names. With the following combination of coefficients:

$$\alpha_N = \frac{1}{2} \qquad \beta_N = \frac{1}{4} \tag{3.64}$$

the algorithm is called trapezoidal rule and is unconditionally stable (i.e., for every time step).

Rearranging **Equations 3.61** in a more compact form by incorporating Newmark coefficients and time increments (Δt) in constant (for the current step) coefficients (c_0, …, c_5) the following can be written for accelerations, velocities, and displacements as:

$$\underline{\ddot{u}}^{t+\Delta t} = c_0\left(\underline{u}^{t+\Delta t} - \underline{u}^{t}\right) - c_2\,\underline{\dot{u}}^{t} - c_3\;\underline{\ddot{u}}^{t} \tag{3.65a}$$

$$\underline{\dot{u}}^{t+\Delta t} = c_1\left(\underline{u}^{t+\Delta t} - \underline{u}^{t}\right) - c_4\,\underline{\dot{u}}^{t} - c_5\;\underline{\ddot{u}}^{t} \tag{3.65b}$$

$$\underline{u}^{t+\Delta t} = \underline{u}^{t} + \left(\underline{u}^{t+\Delta t} - \underline{u}^{t}\right) \tag{3.65c}$$

Substituting for these quantities in in **Equation 3.35** everything is function of usual matrices **M**, **C** and **K** and constant coefficients c_i and can be solved with the same strategies adopted for the static case:

$$(c_0\,\mathbf{M} + c_1\,\mathbf{C} + \mathbf{K})\left(\underline{q}^{t+\Delta t} - \underline{q}^{t}\right) = \underline{R}(t) + \mathbf{M}\left(c_2\,\underline{\dot{q}}^{t} + c_3\;\underline{\ddot{q}}^{t}\right) + \mathbf{M}\left(c_4\,\underline{\dot{q}}^{t} + c_5\;\underline{\ddot{q}}^{t}\right) \tag{3.66}$$

3.3.9 Discontinuities

In commercial software automated mesh algorithms not always succeed in discretising the domain directly. Therefore, it can be convenient to subdivide complex geometries into smaller parts connected at shared surfaces. These discontinuities may be fictitious or correspond to actual discontinuities in a continuum (i.e., rock mass joints), to thins layers that cannot be adequately represented by solid finite elements (i.e., aperture fillings), or to material discontinuities between different bodies in contact (i.e., dam-foundation interface). Regardless of their typology, they allow for separately meshing different parts without an exact matching of nodes at the contact surfaces. They can be particularly useful to abruptly change mesh density. In the following a reference is made to the Finite Element code Abaqus/Standard (Smith, 2009).

For each discontinuity, a "master" and a "slave" role to the two surfaces that are (or will likely be) in contact during the analysis should be assigned. For a surface that is initially in contact, if no relative motion is allowed along the discontinuity, regardless of the stress level, a tie constraint may be enforced, which supresses the DOFs of the slave surface by imposing equal displacements at the two sides.

If the behaviour of the discontinuity, as it happens in realty, depends on the stresses developed on the contact surfaces, an interaction may be enforced. This feature is particularly appropriate for modelling a plastic behaviour that is limited to specific interfaces of an otherwise elastic domain. For modelling this behaviour, other than surface roles, a contact discretization (i.e., node-to-surface or surface-to-surface discretization) and a tracking approach (i.e., finite sliding or small sliding formulation) should be chosen as well.

Abaqus/Standard offers two contact discretization options: a "node-to-surface" discretization and a "surface-to-surface" discretization. In a "node-to-surface" discretization each "slave" node on one side of a contact interface effectively interacts with its projection on the "master" surface on the opposite side of the contact interface. Thus, each contact condition involves a single slave node and a group of nearby master nodes from which values are interpolated to the projection point. The surface-to-surface formulation enforces contact conditions in an average sense over regions nearby slave nodes rather than only at individual slave nodes, thus resulting in smoothened contact pressures. The averaging regions are approximately centred on slave nodes, so each contact constraint will predominantly consider one slave node but will also consider adjacent slave nodes.

In Abaqus/Standard there are two tracking approaches to account for the relative motion of interacting surfaces in mechanical contact simulations, i.e. a "finite-sliding" formulation and a "small-sliding" formulation. The first case is more adequate for simulations that involve arbitrary large relative motion between parts in contact, contact conditions are updated during the analysis depending on the current relative position. In the second case a relatively little sliding of one surface along the other is assumed and therefore nodes involved in a single contact condition don't change throughout the analysis.

An interaction property enforces contact between approaching surfaces depending on a normal behaviour. As an example, in the linear "penalty" contact method the contact force, applied with opposite sign on both contacting surfaces, is proportional to the penetration distance (i.e., a small elastic penetration takes place).

$$K_N = \frac{\sigma_n}{\gamma_n} \tag{3.67}$$

where K_N is the normal stiffness modulus σ_n is the developed stress level and γ_n is the penetration in normal direction.

A tangential behaviour can be defined when the surfaces are in contact, varying from free sliding to perfectly sticking. Among a variety of tangential behaviours, the classical elastoplastic Mohr-Coulomb criterion can be applied. In this case the surfaces in contact can sustain tangential stresses up to a plastic threshold. Elastic recoverable slip developed within this limit is linearly proportional to the applied stress:

$$\Delta\tau_i = K_S \, \Delta\gamma_i \tag{3.68}$$

where $\Delta\tau_i$ is the increment of shear stress, K_S is the shear stiffness modulus and $\Delta\gamma_i$ is the increment of slip along the two in-plane local directions (i = 1, 2).

When the threshold is reached no more stresses can build up and surfaces will freely slip on each other. For three-dimensional problems the Mohr-Coulomb criterion can be written as:

$$\tau_{cr} = \tau_{eq} = \sqrt{\tau_1^2 + \tau_2^2} = (\tan\varphi') \, \sigma_n + c' \tag{3.69}$$

where τ_{cr} is the plastic limit of the shear stress, τ_{eq} is the composition of shear stresses, φ' and c' are the friction angle and the cohesion available along the discontinuity, and σ_n is the current normal stress level.

If a discontinuity is submerged and water can flow inside the aperture the Mohr-Coulomb criterion should be written in terms of effective stresses (σ_n'):

$$\tau_{eq} = \tan\varphi' \; \sigma_n' + c = \tan\varphi' \, (\sigma_n - u) + c' \tag{3.70}$$

where u denotes the water pore pressure acting on the two sides of the discontinuity.

In a penalty approach K_S is not constant but depends on a slip threshold (γ_{cr}) and on the current critical shear stress (τ_{cr}), as follows:

$$K_S = \frac{\tau_{cr}}{\gamma_{cr}} \tag{3.71}$$

If an elastic cohesive behaviour is defined along contact surfaces and chosen stiffness coefficients are considerably higher than those of neighbouring materials, the two side of the discontinuity will be permanently sticked together during the analysis, limiting to an elastic minimum the relative motion. A cohesive law can be written as:

$$\begin{bmatrix} \Delta\sigma_n \\ \Delta\tau_1 \\ \Delta\tau_2 \end{bmatrix} = \begin{bmatrix} K_N & 0 & 0 \\ 0 & K_S & 0 \\ 0 & 0 & K_S \end{bmatrix} \begin{bmatrix} \Delta\gamma_n \\ \Delta\gamma_1 \\ \Delta\gamma_2 \end{bmatrix} \tag{3.72}$$

Since in Abaqus/Standard interactions are a Step dependent features, a cohesive interaction can be activated at an arbitrary moment of the analysis (e.g., at the end of the static step/steps), linking from then on surfaces that were independent. This capability can be used to reduce the domain where initial static stresses apply to the zone of the model where plasticity is considered. The phases of this process can be summarized as follows:

a) to conduct the static analysis in a truncated domain applying static boundaries conditions (e.g., fixing all base displacements and horizontal displacements at side boundaries);
b) to extract reaction forces along "static" boundary from results and apply them at boundary nodes;
c) to deactivate static boundary conditions: no deformation should occur;
d) to activate cohesive interaction properties that "glue" together the inner model to the outer unloaded model;
e) to perform a dynamic step of analysis of the entire domain with absorbing boundaries.

The same phases are depicted in **Figure 3.9** for a better understanding.

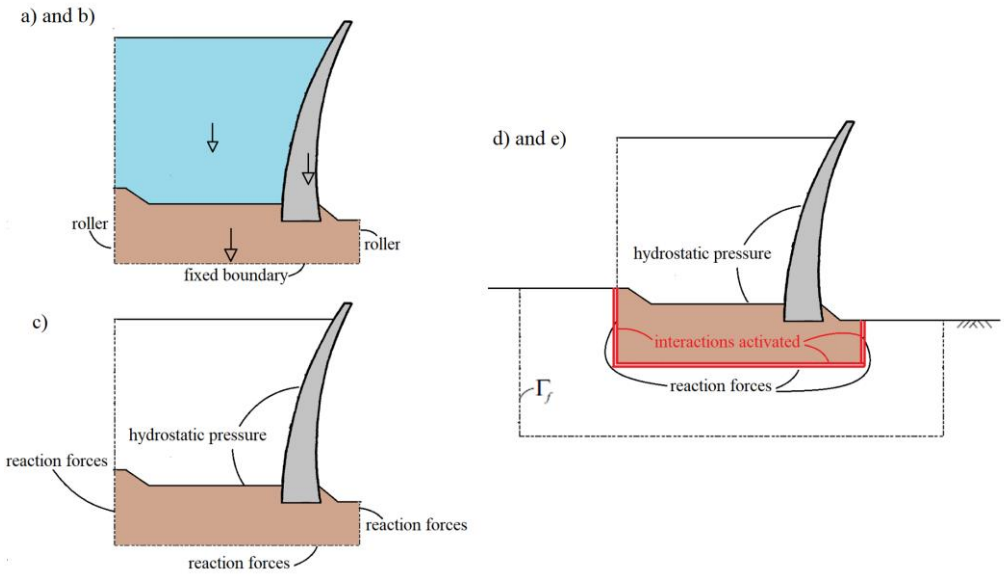

Figure 3.9. Phases a) … e) of a complete (static+dynamic) analysis of a dam-water-foundation system, with delayed activation of a cohesive interaction at the beginning of the dynamic phase.

Chapter bibliography

Basu, U., 2004. Perfectly Matched Layers for Acoustic and Elastic Waves: Theory, Finite-Element Implementation and Application to Earthquake Analysis of Dam–Water–Foundation Rock Systems. PhD thesis. Department of Civil and Environmental Engineering, University of California, Berkeley, California (USA).

Basu, U., Chopra, A.K., 2004. Perfectly matched layers for transient elastodynamics of unbounded domains. *Int. J. Numer. Methods Eng*. 59 (8), 1039-1074. https://doi.org/10.1002/nme.896

Bathe, J. K., Wilson, E. L., 1976. Numerical methods in finite element analysis. Prentice-Hall, Englewood Cliffs, New Jersey (USA).

Bielak, J., Christiano, P., 1984. On the effective seismic input for non-linear soil-structure interaction systems. *Earthquake Eng. Struct. Dyn*. 12 (3), 107-119.

Bielak, J., Loukakis, K., Hisada, Y., Yoshimura, C., 2003. Domain reduction method for three-dimensional earthquake modeling in localized regions, Part I: Theory. *Bull. Seismol. Soc. Am*. 93 (2), 817-824.

Brinkgreve, R.B.J., Kumarswamy, S., Swolfs, W.M., Fonseca, F., Ragi Manoj, N., Zampich, L. M., Zalamea, N., 2022. PLAXIS 3D CONNECT Edition V22 Update 1 Manual.

Buffi, G., 2018. Assessment of seismic behaviour of large concrete dams by means of geomatics techniques and finite element modelling. PhD thesis. Firenze-Braunschweig, Italy-Germany.

Chopra, A. K., 2020. Earthquake engineering for concrete dams: analysis, design, and evaluation, Wiley-Blackwell, Hoboken, New Jersey (USA).

Ghanaat, Y., 1993. Theoretical manual for analysis of arch dams - Technical Report ITL-93-1. US Army Corps of Engineer. Washington D.C., District of Columbia (USA).

Guidi, C., 1928. Statica delle dighe per laghi artificali Bona. Turin, Italy.

Herrera, I., Bielak, J., 1977. Soil-structure interaction as a diffraction problem, in Proceedings, 6th World Conference on Earthquake Engineering, Vol. 2, New Delhi, India.

Howell, C. H., Jaquith, A. C., 1929. Analysis of arch dams by the trial load method. Transactions of the American Society of Civil Engineers. 93(1), 1191-1225.

Hughes, T. J. R., 1987. The Finite Element Method: Linear Static and Dynamic Finite Element Analysis. Prentice-Hall, Englewood Cliffs, New Jersey (USA).

Joyner W.B., Chen A.T.F., 1975. Calculation of nonlinear ground response in earthquakes, Bulletin of the Seismological Society of America. 65 (5), 1315-1336. https://doi.org/10.1785/BSSA0650051315

Kramer, S.L., 1996. Geotechnical earthquake engineering. Prentice-Hall, Englewood Cliffs, New Jersey (USA).

Kuo, J. S., 1982. Fluid-Structure Interactions: added mass computations for incompressible fluid - UCB/EERC-82/09. Earthquake Engineering Research Center, University of California, Berkeley, California (USA).

Lemos, J. V., 1999. Discrete element analysis of dam foundations. in Sharma, V. M., Saxena, K. R., Wood, R.D. (Eds.) Distinct Element Modelling in Geomechanics. 89-115. Balkema, Rotterdam, The Netherlands.

Lemos, J. V., 2008. Block modelling of rock masses: Concepts and applications to dam foundations. *Eur. J. Environ. Civ. Eng.*, 12 (7-8), 915-949.
https://doi.org/10.1080/19648189.2008.9693054

Lemos, J.V., 2021. Arch dam static and dynamic modelling with discrete elements. *IOP Conf. Ser.: Earth Environ. Sci.*, 861.
https://doi.org/10.1088/1755-1315/861/7/072085

Lysmer, J., Kuhlemeyer, R. L., 1969. Finite dynamic model for infinite media. *ASCE J. Eng. Mech. Div.*, 95 (4), 859-878.

Løkke, A., Chopra, A., 2018. Direct finite element method for nonlinear earthquake analysis of 3-dimensional semi-unbounded dam-water-foundation rock systems. *Earthquake Engng Struct Dyn.*, 47, 1309-1328.
https://doi.org/10.1002/eqe.3019

Løkke, A., Chopra, A., 2019. Direct-Finite-Element Method for Nonlinear Earthquake Analysis of Concrete Dams Including Dam–Water–Foundation Rock Interaction - PEER 2019/02. Pacific Earthquake Engineering Research Center, Headquarters at University of California, Berkeley, California (USA).

Mahmoudi, P. P., Mirzabozorg, H., Varmazyari, M., Aghajanzadeh, S. M., 2016. Effect of foundation nonlinearity on seismic response of an existing arch dam. *Civil Eng. J.*, 2(5), 197-207.

McGuire R.K., 2004. Seismic Hazard and Risk Analysis. Earthquake Engineering Research Institute, Oakland, California (USA).

Newmark, N. M., 1959. A method of computation for structural dynamics. *Journal of the Engineering Mechanics Division*, 85 (3), 67-94.
https://doi:10.1061/JMCEA3.0000098

Nielsen, A. H., 2014. Towards a complete framework for seismic analysis in Abaqus. *Proceedings of the Institution of Civil Engineers - Engineering and Computational Mechanics*, 167(1), 3-12.
https://doi.org/10.1680/eacm.12.00004

Pan, J., Xu, Y., Jin, F., Wang, J., 2015. Seismic stability assessment of an arch dam-foundation system. *Earthq. Eng. Eng. Vib.*, 14, 517-526.
https://doi.org/10.1007/s11803-015-0041-2

Reddy, J. N., 2006. An Introduction to the Finite Element Method (3rd Ed.). McGraw-Hill.

Ritter, H., 1931. Die Berechnung von bogenförmingen Staumauern. Karlsruhe, Germany.

Schnabel, P. B, Lysmer, J., Seed, H. B., 1972. SHAKE: A computer program for earthquake response analysis of horizontally layered sites - UCB/EERC-72/12. Earthquake Engineering Research Center, University of California, Berkeley, California (USA).

Sluys, L. J., 1992. Wave propagation, Localisation and Dispersion in softening solids. PhD thesis. Delft University of Technology, Delft, The Netherlands.

Smith, M., 2009. ABAQUS/Standard User's Manual, Version 6.9. Dassault Systèmes Simulia Corp, Providence, Rhode Island (USA).

Swaminathan, K. V., 1960. Su di una estensione del calcolo Tölke a dighe arco-gravità con fondazioni cedevoli. L'energia elettrica. (7), 614-624.

Timoshenko, S. P., Goodier, J. N., 1970. Theory of Elasticity (3rd Ed.). McGraw-Hill, New York, New York (USA).

Tölke, F., 1938. Talsperren, Staudämme und Staumauern, in Ludin, A. (Ed.), Wasserkraft Anlagen. Verlag von Julius Springer, Berlin, Germany.

USBR (U.S. Bureau of Reclamation), 1938. Trial Load Method of analysing arch dams. in Boulder Canyon Final Project: Part 5, Bulletin 1. United States Department of the Interior, Bureau of Reclamation, Denver, Colorado (USA).

USBR (U.S. Bureau of Reclamation), 1977. Design of Arch Dams – design manual for concrete arch dams. United States Department of the Interior, Bureau of Reclamation, Denver, Colorado (USA).

Vedvik, N. P., 2021. TMM4175 Polymer Composites – online NTNU course. https://folk.ntnu.no/nilspv/TMM4175/elements.html [online]

Vogt, F., 1925. Über die Berechnung der Fundament Deformation, in Det Norske Videnskaps-Akademi (Ed.), Avhandlinger utgitt av det Norske Videnskaps-Akademi i Oslo: Matematisk-naturvidenskapelig klasse. Jacob Dybwad, Oslo, Norway.

Westergaard, H. M., 1933. Water pressures on dams during earthquakes. Transactions of the American Society of Civil Engineers. 98(2), 418-433. https://doi.org/doi:10.1061/TACEAT.0004496

Wolf, J. P., 1985. Dynamic Soil-Structure Interaction. Prentice-Hall, Englewood Cliffs, New Jersey (USA).

Wolf, J. P., 1988. Soil-Structure Interaction in Time Domain. Prentice-Hall, Englewood Cliffs, New Jersey (USA).

Zangar, C. N., 1952. Hydrodynamic Pressures on Dams due to Horizontal Earthquake Effects. Engineering Monographs No. 11. Denver, Colorado (USA).

Zienkiewicz, O. C., Bicanic, N., Shen, F. Q., 1989. Earthquake input definition and the transmitting boundary conditions, in Doltsinis, I. S. (Ed.), Advances in Computational Nonlinear Mechanics. Springer, Vienna, Austria. https://doi.org/10.1007/978-3-7091-2828-2_3

Zienkiewicz, O. C., 1971. The finite element method in engineering science (2nd Ed.). McGraw-Hill, New York, New York (USA).

Zienkiewicz, O. C., Taylor, R. L., 1991. The Finite Element Method. McGraw-Hill, London, United Kingdom.

4. Case study: Ridracoli Dam FE model and numerical analyses

4.1 Introduction

The Direct FE procedure described in **Chapter 3** is here applied to the case study of Ridracoli Dam. This structure was the object of a previous PhD project (Buffi, 2018), as mentioned in **Chapter 1.**

This chapter can be ideally subdivided in two parts, namely the description of the finite element model and the numerical analyses. The model is first introduced, starting from the geometrical data. The whole domain is subdivided in smaller parts with homogenous characteristics in a CAD environment. The mesh, the materials, the applied loads, the boundary conditions chosen for Ridracoli case are then described in detail. An important space is given to the strategies adopted for representing the dynamic interaction of the reservoir and the foundation rock mass with the dam structure. Coding work, in particular, is thoroughly described. The second part of the chapter covers two main topics, the testing of the user-subroutines written to integrate Abaqus® native capabilities, and the results of the dynamic analyses of Ridracoli Dam.

4.2 Geometrical model

The geometrical model of the dam is the result of the composition of different data. The aim is to obtain a model which is at the same time representative of the effective shape of the dam and the valley, and simple enough to be easily edited in a CAD environment and correctly read by Abaqus/CAE® importer. The different origins of the data and the editing process to obtain the final model are summarised in the following.

4.2.1 Origin of the data

The general overview of the area is provided by the Digital Elevation Model (DEM) TINITALY/01 (Tarquini et al., 2012). The spatial reference system is WGS84/UTM32 and the spatial resolution is 10 m (**Figure 4.1**). The DEM is quite imprecise in the vicinity of the dam, owing to the presence of the structure which shades the ground surface, and does not contain information about the actual shape of the submerged part of the valley, owing to the presence of the water.

In order to integrate these pieces of information, other sources of geometric data are needed. The submerged bottom surface of the reservoir is derived from the contour lines of a bathymetry provided by the owner of the dam and referenced to the Gauss-Boaga

cartographic system (**Figure 4.2**). Similarly, contour lines in Gauss-Boaga cartographic coordinate system are extracted from a dense point cloud of the dam area realized on the basis of a UAV (Unmanned Aerial Vehicle) survey (Buffi, 2017).

The solid bodies corresponding to the pulvinus, the stilling basin and the weight blocks (placed at the level of the abutments in order to compensate the weight loss due to excavations during the construction work) are derived and simplified from the corresponding solids in Buffi (2018), available in the local reference system of the dam. These latter were originally obtained from the aforementioned point cloud, integrated with technical drawings on the blind sides (i.e., the submerged portions of the dam and the interfaces with the rock foundation). The simplification is made here in a CAD environment with the software Autocad® and mainly consists in a reduction of the number of facets (**Figure 4.3**).

The dam body geometry is derived from the input data of arches elements for the analytical analysis of the dam. They mainly consist in central angles and extrados and intrados radii of a selection of horizontal arches at different elevations. A control is preliminarily made on the reliability of these data by overlapping the dam solid obtained in this way with the one used by Buffi (2018). The bottom boundary is obtained by subtracting the pulvinus from the dam body solid with Autocad®. A good agreement is found, although the simplified model is monolithic (not subdivided in blocks) and lacks local features such as spillways (**Figure 4.4**).

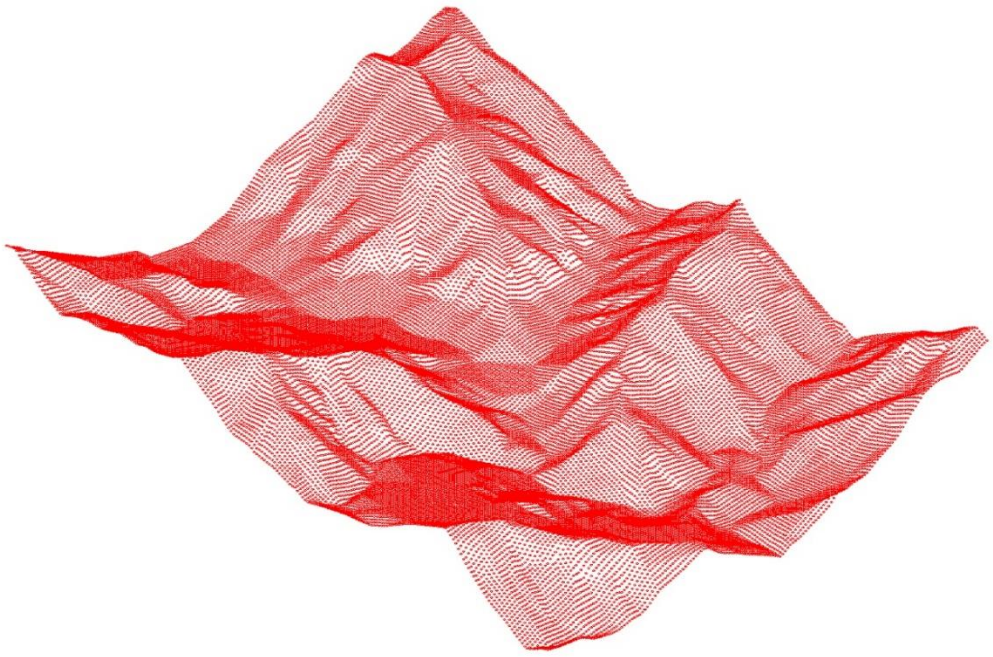

Figure 4.1. TINITALY/01 DEM of Ridracoli area (Tarquini et al., 2012).

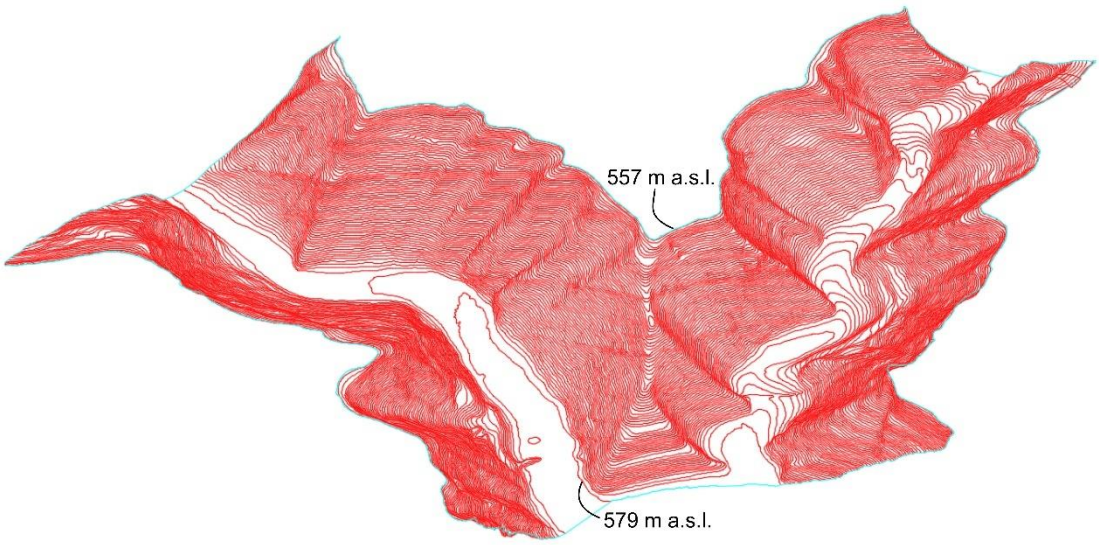

Figure 4.2. Bathymetry of Ridracoli lake in the vicinity of the dam.

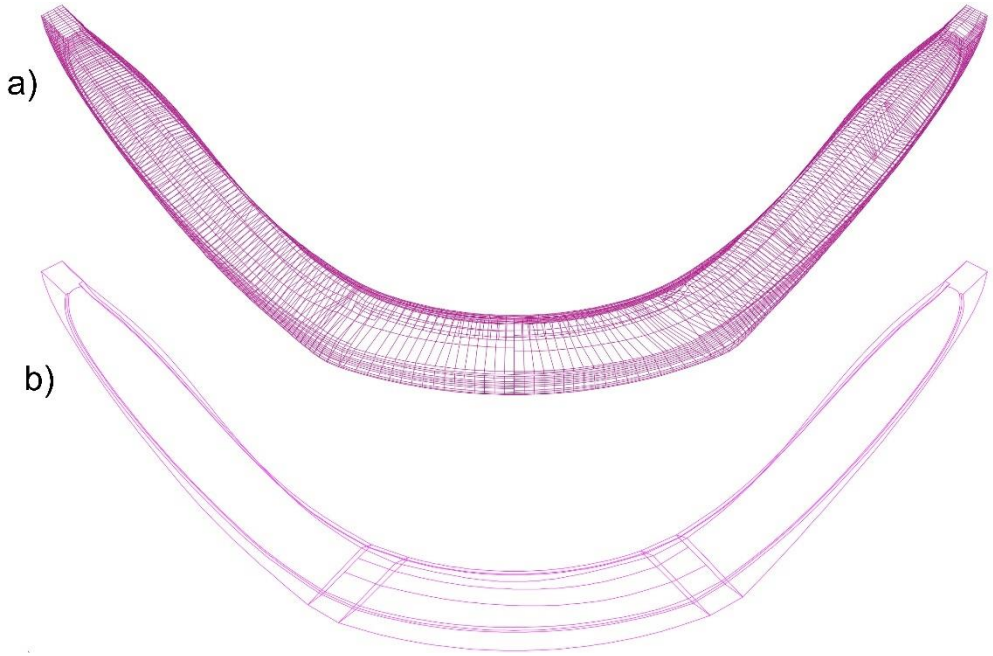

Figure 4.3. a) original geometrical model of the pulvinus from Buffi (2018); b) simplified geometry.

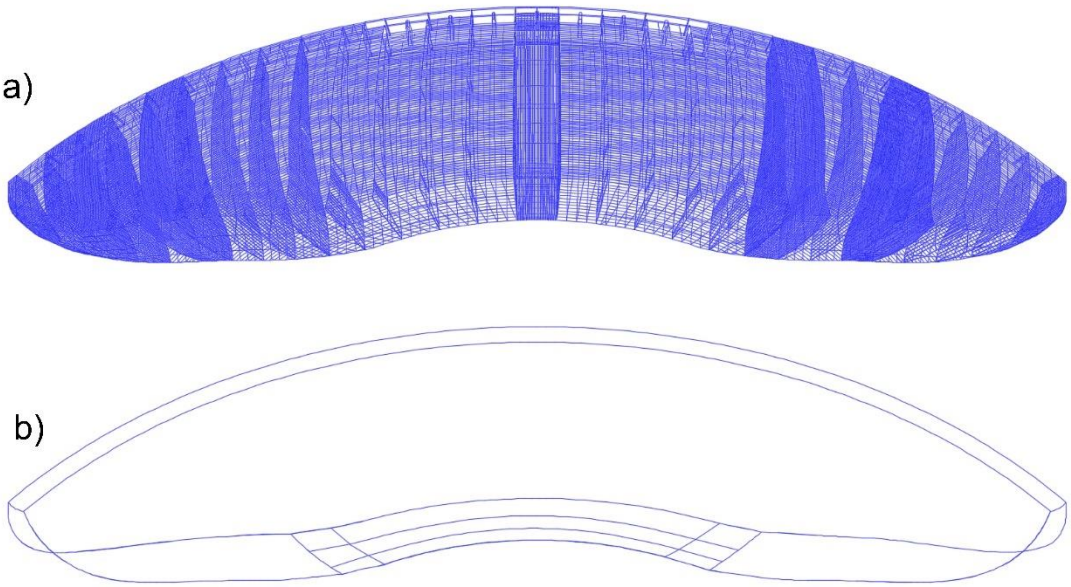

Figure 4.4. a) original geometrical model of the dam body from Buffi (2018); b) simplified geometry.

4.2.2 Merging of the data

As a first step, the free-field model is assembled, without any structural solid bodies. All the data sets are homogenized to punctual format and aligned to the common WGS84/UTM32 reference system by means of a geographic information system. Every cluster of georeferenced points, however, has a different density, and some discrepancies could be observed in the overlap areas.

A choice is made to reduce the point density to the 10x10 grid of the DEM. Falcone et al. (2022) noted, in fact, that for high wave velocities (> 1000 m/s) the Local Seismic Response is, in practise, insensible to the level of detail of the topographic surface. The reduction is made by means of a specially designed Matlab® code written by the author and given in **Appendix B**. The simple implemented algorithm is specific for a point cloud extracted from contour lines. A regular grid (in this case the 10x10 DEM grid) is preliminary overlapped to the contour lines, and all the points of the grid which are external to the contour line area are deleted. The two set of points, contour points and grid points respectively, are imported in Matlab® separately. An infinite vertical cylinder is centred on each grid point with a trial radius sufficiently small (i.e., comparable to the minimum planimetric distance between two contour lines), the radius being progressively increased with a fixed increment until contour points with two different elevations are found inside

the cylinder. The elevation of the grid point is updated with a weighted mean of the elevations of the inner points (the weights are the planimetric distances from the grid point). The updated grid is checked to verify that points from different sources integrate smoothly, and manually adjusted when needed. It is then imported in Rhinoceros® and an interpolating surface is created with the patch command.

Once the free-field surface is defined, also structural solid bodies are imported in Autocad® and aligned to the WGS84/UTM32 reference system exploiting specific common points (i.e., corner points of weight blocks, known in both reference systems). If the intersection of the free-field surface with solid bodies is not precise, the point grid is resumed and locally adjusted by manually updating the vertical coordinates of the grid points near and across the structural elements. The final version of the free-field surface interpolated in Rhinoceros® is reimported in Autocad® and used to cut a cuboid oriented along the geographic coordinates with the dimensions 1000x1000x1000 m, approximately centred at the dam and with an absolute base elevation of 200 m a.s.l.. The lower parted is kept while the upper is discarded. The structural solids are finally subtracted from the rock foundation solid with Boolean operations. A particular attention is given to the correct definition of the lower interfaces of weight blocks which, differently from the pulvinus and the stilling basin, are not embedded in the underlying rock mass.

The resulting monolithic model of the foundation rock has a rectangular base and vertical side boundaries in order to be used for a dynamic analysis with free-field boundaries. Each side face is oriented toward a cardinal point. The side length is equal to 10 times the dam height.

4.2.3 Cut of the model

The final model is obtained within Autocad® introducing discontinuities in the rock foundation by means of cutting tools.

The following procedure is followed:

- the rock foundation solid is subdivided in an external and an internal part: the internal part (plane dimensions: 500x500 m) is surrounded by the external one;
- the external part is furtherly divided in two concentric subparts, the innermost has a thickness of only 10 m, and envelopes the inner part in order to regularise the contact with the outermost part;
- the internal part is furtherly subdivided in three subparts by two parallel faces which define the Bidente Fault: the exact position of the fault with respect to the structure is derived from geological maps of the design project (Alpina, 1974), while the orientation of the planes and the thickness of the layer are extracted from geological studies (see **Section 1.2.2**);
- the fault layer is furtherly split in two halves by a mean plane (**Figure 4.5**);

– the two remaining subparts in which the fault divides the internal part are furtherly cut by means of three bedding planes corresponding to the laminated layers: since the fault causes a normal slip of about 40 metres at dam location, the cutting planes are different on the two sides (see **Section 1.2.2**).

All different parts are saved as ACIS files (.sat) in Rhinoceros® in order to be imported in the Abaqus/CAE® environment. The resulting geometrical model is shown in **Figure 4.6**.

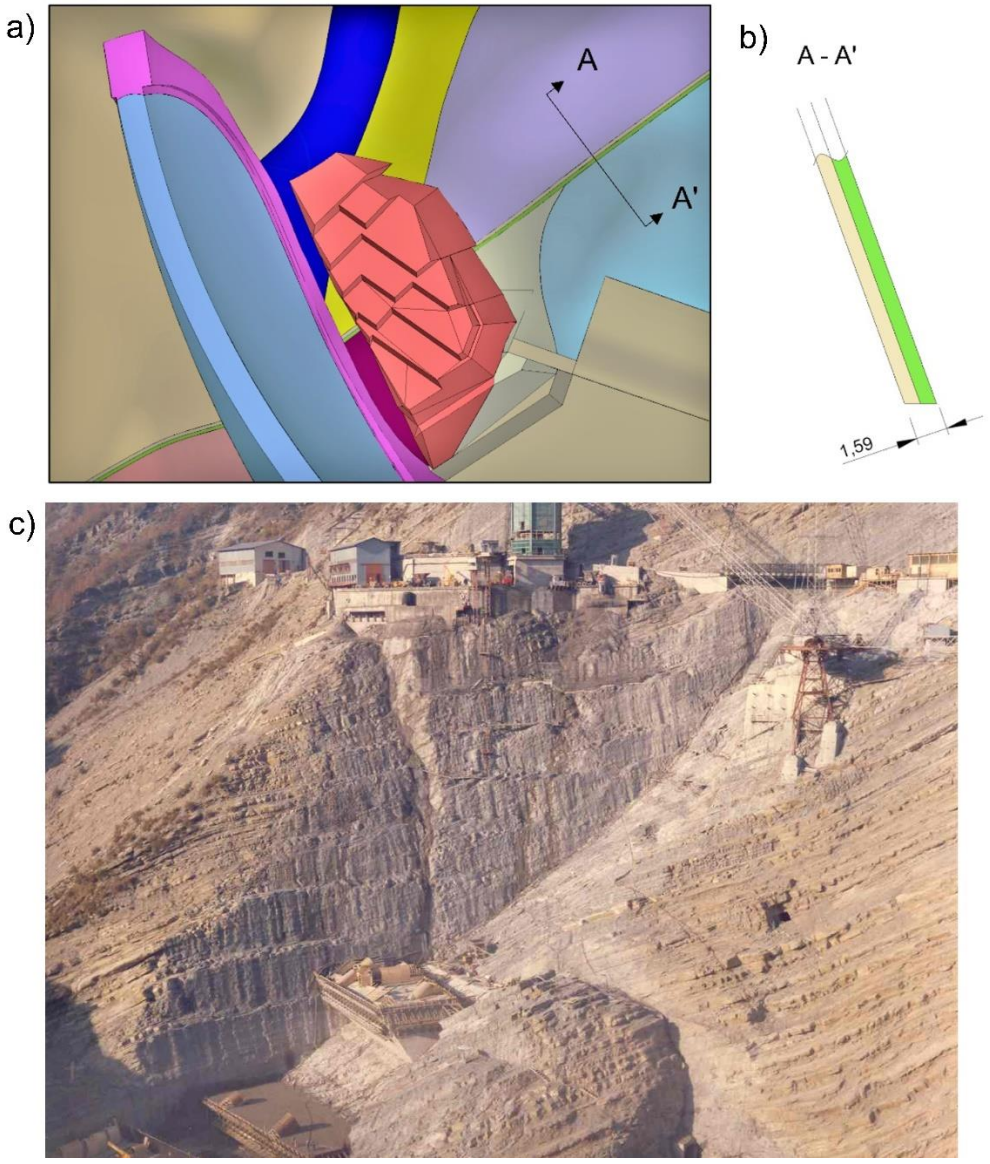

Figure 4.5. a) plane view of the fault in the geometrical mode with indicated section A-A'; b) section A-A', normal to the fault, with the two parts in which it is subdivided; c) photographic view of the actual fault (Romagna Acque – Società delle Fonti S.p.A.).

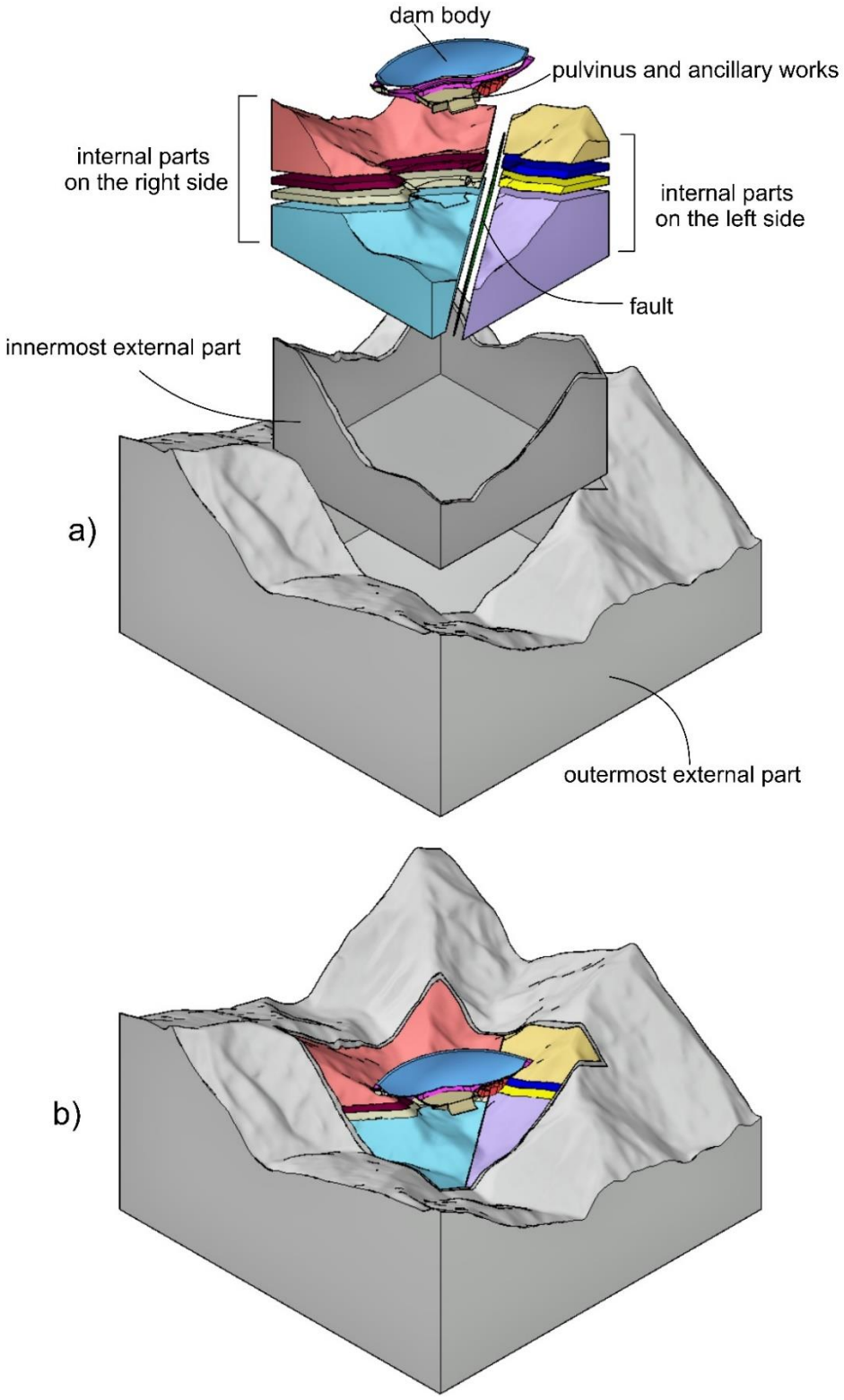

Figure 4.6. a) exploded view of the geometrical model with all the parts deriving from the cutting; b) complete model.

4.3 Abaqus FE model

An Abaqus/Standard® model is created in the Abaqus/CAE® environment. All the parts are imported from ACIS files (.sat). The validity of the geometry is automatically checked by the software and, if the imported solid results as invalid, a number of repairing tools is suggested.

For the parts of Ridracoli Dam model the following tools are used (Smith, 2009):

- Geometry Edit,
- Virtual Topology,
- Partition Tools.

A significative pre-processing work is done with Autocad® to reduce to a minimum the need for repairing. All the editing to the geometry, in fact, cannot be easily exported outside Abaqus®. Each part is separately meshed. In general, the element size ranges from a maximum side length of 20 m to a minimum of 1.5 m. A regular loose mesh is adopted for the outermost external part of the rock foundation. The innermost external part is more densely meshed in order to match the size of internal part elements (side length of about 15 m). At the contact with the pulvinus and the ancillary concrete structures the size furtherly reduce to about 5-m-sided elements. Linearly distributed Edge Seeds are used for a smooth reduction of mesh size while approximating the centre of the model, where the dam is placed. Structural parts have a quite dense mesh with element sides ranging from 5 to 2 meters. Other parts densely meshed are the two fault sides with less than 1-m-sided elements in the tinier details.

4.3.1 Concrete structures

Eigth-noded hexaedral elements (C3D8 in Abaqus® terminology) are used to discretize the dam body (i.e., the part of the dam resting on the pulvinus). Four-noded tetrahedral elements (C3D4) are used to discretize the remaining concrete structures: the pulvinus and the ancillary works such as weight blocks and stilling basin. All the concrete structures are assigned a linear elastic material behaviour with Rayleigh damping. A set of Rayleigh coefficients is chosen corresponding to a reference damping coefficient (ζ) of 2%. The first two natural frequencies of the dam observed by Buffi (2018) are chosen as anchor points (i.e., frequencies for which Rayleigh damping coincides with the mean damping coefficient) for the estimation of α_R and β_R. The dynamic elastic modulus and the Poisson coefficient are the same used in Buffi (2018): they are based on experimental tests on the dam concrete, increased for taking into account the surplus of stiffness under dynamic loading. A mass density of 2470 kg/m^3 is considered as representative of the concrete structures. Mesh and material data are listed in **Table 4.1** and **4.2**, respectively. The structural meshes are visible in **Figure 4.7a**.

4.3.2 Rock mass

The external parts of the rock mass have a relatively simple geometry with plane lateral and bottom sides, and squared edges. The upper surface is a single analytic surface and is easily treated by the advanced meshing algorithms of Abaqus/CAE®. Each part is furtherly partitioned in order to obtain smaller regions where Abaqus® can apply a structured hexahedral mesh. On the contrary, the internal parts of the rock mass exhibit in general a very complex geometry due to the presence of the footprints of structural parts and the variably oriented cutting planes representing discontinuities. Therefore, they are not good candidates for structured meshing with hexahedral finite elements. Free meshing algorithm with tetrahedral elements is applied, instead. All rock foundation parts are modelled with low order finite elements (i.e., C3D4 or C3D8 elements with only corner nodes). For the outermost external part this choice is forced because of the compatibility requirement with the free-field elements that will be described in **Section 4.4.1**.

The rock mass is considered as linear elastic and Rayleigh coefficients corresponding to a reference damping coefficient (ζ) of 3% are adopted. Since no rigid bedrock is considered and the elastic material is imagined infinitely extending in vertical direction without any increase in stiffness, the signal inputted at the base is not amplificated for any frequency and, therefore, the choice of anchor points for α_R and β_R is quite arbitrary, the same as in Buffi (2018) is made where, on the contrary, a perfectly rigid bedrock at the base was defined. The dynamic elastic modulus and the Poisson coefficient are directly derived from sonic testing of the rock mass (see **Section 1.2.3**). A mass density of 2650 kg/m^3 is considered as representative of the rock formation. All parts are assigned the same material properties, which are listed in **Table 4.2**, while mesh characteristics are summarized in **Table 4.1**. The rock foundation meshes are visible in **Figure 4.7b** and **4.7c.**

4.3.3 Fault

The modelled fault corresponds to the whole sheared zone at the contact between the two sides. It is composed of two solid layers with a thickness of 0.75 m each, and an interaction at the shared faces of the mid-plane. The two parts are discretized in tetrahedral elements with a free mesh algorithm, and a relatively high mesh density to avoid the possible distortion of finite elements due to the small thickness of the layer. Owing to the expected high deformability of the layer, quadratic finite elements (C3D10) are chosen, with mid-edge nodes in addition to corner nodes. The solid volumes accounts for the deformability of the fault and are therefore assigned, in lack of real data, with a reduced elastic modulus with respect to the rock mass (1/10) and a higher reference damping coefficient (5%). The fault behaviour in the normal direction is linear elastic. In the tangential direction the total behaviour is the composition of the elastic deformation of the solid layers and the elasto-plastic behaviour at the interface.

A user interaction property is defined to model the latter, further details are given in **Section 4.4.3**. Mesh and material data are listed in **Table 4.1** and **4.2**, respectively.

Table 4.1. Mesh data of the solid parts of Ridracoli Dam model.

Part	Description	Mesh elements	
		type	number
EXT-1	outermost external part	C3D8	38799
EXT-2	innermost external part	C3D8	9776
INT-R-1	lowest internal part on the right side	C3D4	61691
INT-R-2	second internal part from the bottom on the right side	C3D4	17470
INT-R-3	third internal part from the bottom on the right side	C3D4	21257
INT-R-4	uppermost internal part on the right side	C3D4	39182
INT-L-1	lowest internal part on the left side	C3D4	25195
INT-L-2	second internal part from the bottom on the left side	C3D4	3028
INT-L-3	third internal part from the bottom on the left side	C3D4	3002
INT-L-4	uppermost internal part on the left side	C3D4	7678
F-R	right side of the fault	C3D10	28773
F-L	left side of the fault	C3D10	27068
WB-R	weight blocks on right side	C3D4	8367
WB-L	weight block on the left side	C3D4	6624
SB	stilling basin	C3D4	10295
PULV	pulvinus	C3D4	21308
DB	dam body	C3D8	35856

Table 4.2. Material properties assigned to Ridracoli Dam solid parts.

Parts	Mass density	Linear elastic properties		Damping coefficients		
	ρ (kg/m3)	E (GPa)	ν (-)	ζ (%)	α_R (-)	β_R (-)
EXT- INT	2650	27.8	0.37	3	0.107	0.0084
F	2600	2.78	0.30	5	0.178	0.014
WB-SB-PULV-DB	2470	39.8	0.19	2	0.082	0.0046

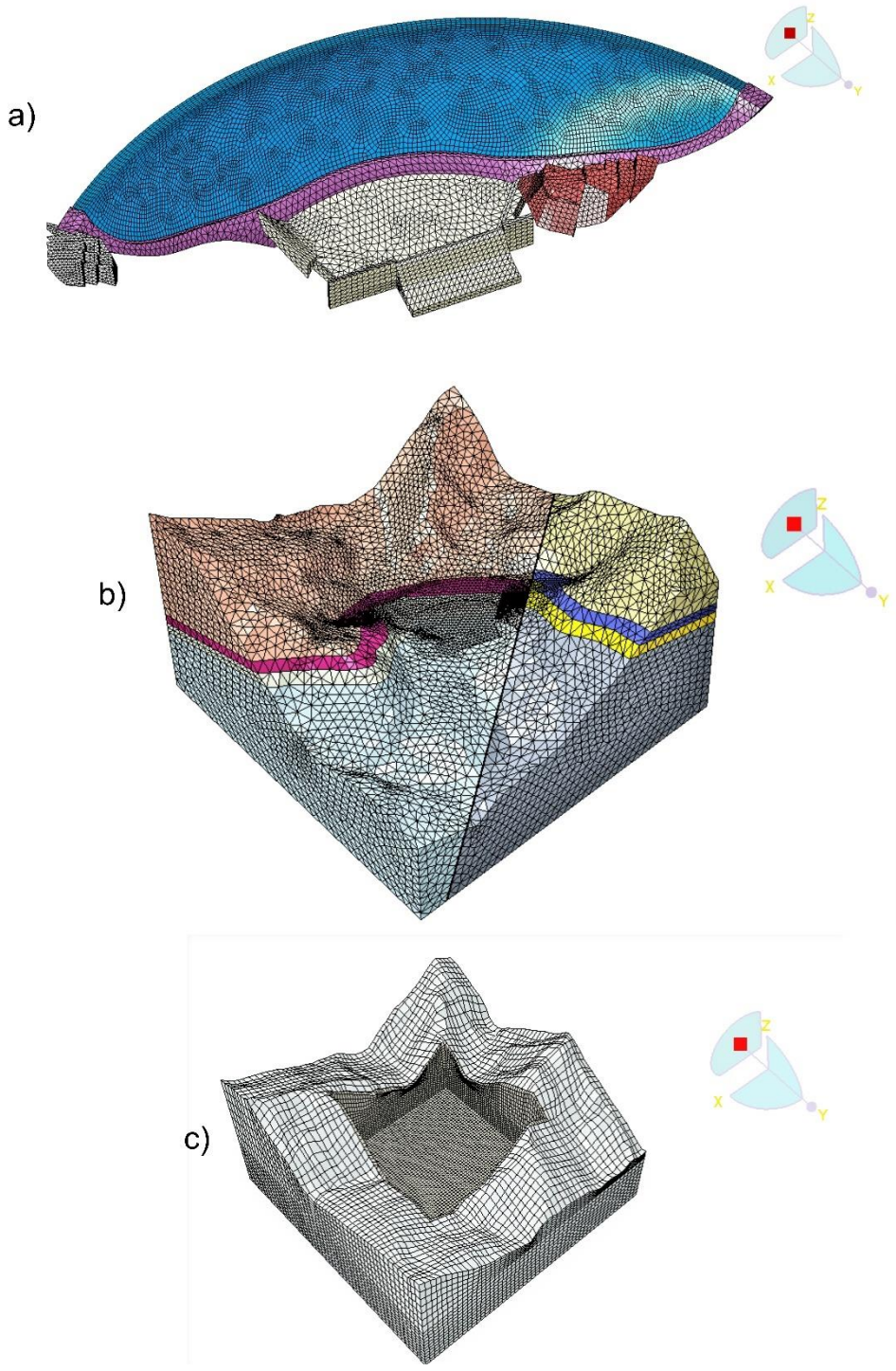

Figure 4.7. Mesh of the model: a) dam and ancillary works (DB-WB-SB-PULV); b) internal parts (INT-F)); c) external parts (EXT)

4.3.4 Discontinuities

The shared surfaces between parts in contact are treated with either Tie Constraints or Interactions (Smith, 2009). Details on the formulations of these features are described in **Section 3.3.9**.

Tie Constraints are used for the interfaces between two structural parts, or a structural part and its rock foundation, since no relative motion is expected at these contacts due to the embedding. They are also used to stick together the external and the internal parts of the rock foundation domain.

Interactions are defined in correspondence of real discontinuities of the rock mass (i.e., the 3 laminated layers and the fault), and at the interface between the two external parts. In the first case the interface behaviour is described with an "hard" contact penalty method in the normal direction (**Equation 3.67**) and with a user-defined subroutine in the tangential direction, which implements a Mohr-Coulomb friction criterion (**Equations 3.70** and **3.71**, details about the subroutine are given in the **Section 4.4.3**, together with the elastic and plastic properties of all interactions used for Ridracoli Dam). In the second case, a cohesive behaviour is assigned to the interface, with high moduli in normal and tangential directions (**Equation 3.72**) in order to simulate a perfect sticking between surfaces once in contact. Since tie constraints cannot be activated in a particular step but are active during the entire simulation, they are not an adequate solution to connect the two external parts, which are originally disconnected, only at some point during the analyses.

4.3.5 Boundary conditions

Different boundary conditions (BCs) are defined for static and dynamic phases. The static BCs (base fixed and side boundaries horizontally constrained) are applied to EXT-2 instead of EXT-1 (see **Table 4.1** for symbols), in order to reduce the portion of the model affected by static loads to the only parts for which a non-elastic behaviour is admitted in the vicinity of the dam (due to the presence of natural discontinuities). In this phase EXT-1 is disconnected from EXT-2 since the corresponding interaction is inactive. As a consequence, EXT-1 results as unloaded throughout the static phases and does not transmit anything to its free-field boundaries. The "static" fixities are released at the end of the static phase and substituted with corresponding nodal forces (extracted from the output database) before sticking together the disconnected portions (EXT-1 and EXT-2) with the cohesive interaction described above (see **Section 4.3.4**).

The outermost external part has free-field elements attached to its side boundaries which simultaneously apply viscous boundaries and free-field equivalent seismic forces. At the bottom boundary the same role is played by a bed of discrete dashpots. The seismic input, in the form of an upward propagating combination of P-waves and SH-waves, is applied at

this boundary as effective seismic forces. Although being active throughout the analyses, these viscous boundaries are in practice inactive during the static phases due to the disconnection of the outermost external part from the rest of the model. The main characteristics of the BCs used in the Ridracoli Dam model are listed in **Table 4.3.**

Table 4.3. Boundary conditions of Ridracoli Dam model.

Part	BC description	Activity flag	
		Static steps	Dynamic steps
EXT-1	Viscous adsorbing boundary at the bottom boundary (dashpots)	✓	✓
EXT-1	Viscous adsorbing side boundaries (free-field elements)	✓	✓
EXT-2	all components of displacement fixed at the bottom boundary	✓	✕
EXT-2	horizontal components of displacements fixed at the side boundaries	✓	✕

4.3.6 Dashpot elements

In Abaqus/Standard® a special purpose fine element is available for modelling a viscous damper between a mesh node and a fixed support (Smith, 2009). It is called DASHPOT1 to distinguish it from a viscous damper between two mesh nodes (DASHPOT2). Each dashpot element enforces a viscous damping condition for a single DOF; therefore, three of them are needed for each node of the bottom boundary, one vertical and two horizontals. The damping coefficient is calculated with **Equations 3.43**: the mass density (ρ) and the wave velocity (V_p or V_s depending on the DOF, vertical or horizontal respectively) are taken from the elastic properties in **Table 4.2** (EXT-INT), the influence area (A) is derived from graphical consideration as explained in **Figure 4.8**. The finite elements at the bottom boundary have a regular mesh with square faces of 20x20 m. The influence area is equal to 400 m^2 for all the nodes, with the exception of edge nodes (A = 200m^2) and corner nodes (A = 100m^2).

Dashpot elements are applied also at the base of free-field elements; details on the calculation of influence areas in that case are given in **Section 4.4.1**.

4.3.7 Loads

Static loads applied to the dam and the rock foundation include gravity loads and hydrostatic pressures due to impounded water. They are activated during the static phases in the whole model with the exception of the disconnected outermost external parts, and remain active throughout the analyses. The reference zero-pressure elevation for the hydrostatic load is set equal the maximum water level (557.3 m a.s.l.). Hydrostatic pressure at a given node below that elevation is linear function of the hight of the column of water above it. When the static BCs are realised at the end of static phases, the corresponding reaction forces extracted from the output database are applied to the previously fixed nodes of EXT-2 in order to ensure the equilibrium. They can be thus considered as additional static loads.

Dynamic loads include the effective seismic forces at the absorbing boundaries and hydrodynamic forces at the upstream face of the dam body. Only the effective seismic forces at the bottom boundary are applied in form of loads, calculated as in **Equation 3.47b** considering the mass density and the elastic properties in **Table 4.2** (EXT-INT), and the influence areas in **Figure 4.8**. The other dynamic forces are defined within user subroutines, as explained in the following **Section 4.4**. In Abaqus® terminology both gravity (GRAV) and hydrostatic pressures (HP) are sub-options of the keyword *DLOAD (distributed loads), while the static reaction forces and the effective seismic forces are defined as concentrated loads (*CLOAD) (Smith, 2009).

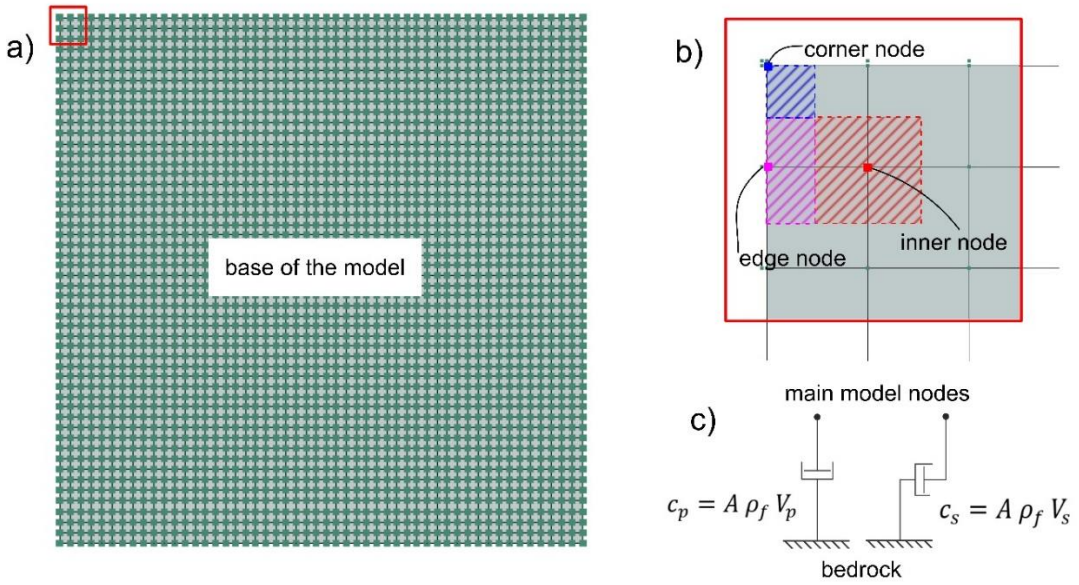

Figure 4.8. a) nodal dashpots at the bottom boundary of the outermost external part (EXT-1); (b) definition of influence areas for inner (in blue), edge (in purple), and corner (in blue) nodes of the base; c) scheme of vertical and horizontal dashpots.

4.4 Abaqus® user subroutines

At the end of the procedure described so far, an input file may be generated within the Abaqus/CAE® environment. This input file should be open in a text editor in order to manually add those features which are not built-in and are defined in user subroutines written in Fortran® language. Three user-subroutines are called in Ridracoli Dam analyses, namely two user-defined finite elements (UEL in Abaqus® terminology) and a user-defined frictional interaction property (FRIC in Abaqus® terminology):

- *ffuel3*: a UEL subroutine written by Nielsen (2014) to implement free field lateral boundaries,
- *amass1*: a UEL subroutine written by the author to implement Westergaard and Zangar formulation of added masses,
- *fric1*: a FRIC subroutine written by the author to implement a Mohr-Coulomb friction behaviour in effective stress with two parameters (tanφ' e c').

The Fortran® code in free format of amass1.for is listed in **Appendix C**, while the free format Fortran® code of fric1.for is listed in **Appendix D**.

4.4.1 Free field elements: use of ffuel3 subroutine

Some Finite Element codes specific for geotechnical applications (e.g., Plaxis®) have free-field elements available in their libraries. This is not the case for Abaqus®, which does not enlist free-field elements as native and privileges the infinite elements approach to deal with unbounded problems and non-reflecting boundaries. The general-purpose Finite Element code, however, allows for a high degree of customization by means of the powerful UEL utility. A free-field user element is therefore available, developed by Nielsen (2014) for both two-dimensional and three-dimensional analyses.

In three-dimensional problems the free-field elements implemented in *ffuel3* are only compatible with 8-noded hexahedral elements at the lateral boundaries of the truncated semi unbounded domain. Two element types, U2 and U3, are defined corresponding to the 1D corner columns and the 2D plane sections described in **Section 3.3.6**, respectively. The theoretical equations governing the free-field elements are given in **Equations 3.49** to **3.53**). For Ridracoli Dam 72 U2 elements and 3672 U3 elements are used.

With the help of the Fortran program ffmesh.f90, which is written by Nielsen (2014) and is distributed together with *ffuels3*, a new set of nodes are defined in front of boundary nodes, with an offset, w_{ff}, that may be freely chosen by the user as long as an algorithm for unsymmetric matrices is requested (UNSYMM = YES option). New nodes are aligned to existing nodes in order to have non-distorted hexahedral free-field elements. The offset w_{ff} is taken as equal to 1 m in the Ridracoli Dam model.

Besides w_{ff}, the properties to be assigned to free-field elements are the same defined for the foundation rock (i.e., mass density, ρ; elastic coefficients, E and ν; and damping coefficients, α_R and β_R). The values assigned to free-field elements are identical to those assigned to EXT-INT parts and listed in **Table 4.2**.

At the base of free-field elements both dashpot elements and equivalent seismic forces must be applied as mentioned in **Sections 4.3.6** and **4.3.7**. The same considerations as for the nodes of the main model applies; the only difference is in the definition of influence areas. Following the suggestion in Nielsen (2014) the influence area of 1D corner columns is w_{ff}^2, while that of 2D plane sections is given by:

$$A = w_{ff} \frac{\sum_{i=1}^{n} l_i^{(e)}}{2} \tag{4.1}$$

where $l_i^{(e)}$ is the side length of the i-th free-field element sharing that node and n is the number of these elements. With reference to **Figure 4.9** and considering a constant side-length of 20 m, node A has an influence area of $1m^2$, node B of 10 m^2 and node C of 20 m^2, respectively.

In two-dimensional problems, used in **Section 4.5.1** (in addition to 3D analyses) to test the reliability of *ffuel3*, the free-field elements implemented in *ffuel3* are only compatible with 4-noded bilinear plane strain elements (CPE4). The corner columns at the two lateral sides are discretized with U1 elements. The offset w_{ff} is the distance of the corner free-field column from the main model and corresponds to the influence area to be assigned to dashpots at the base.

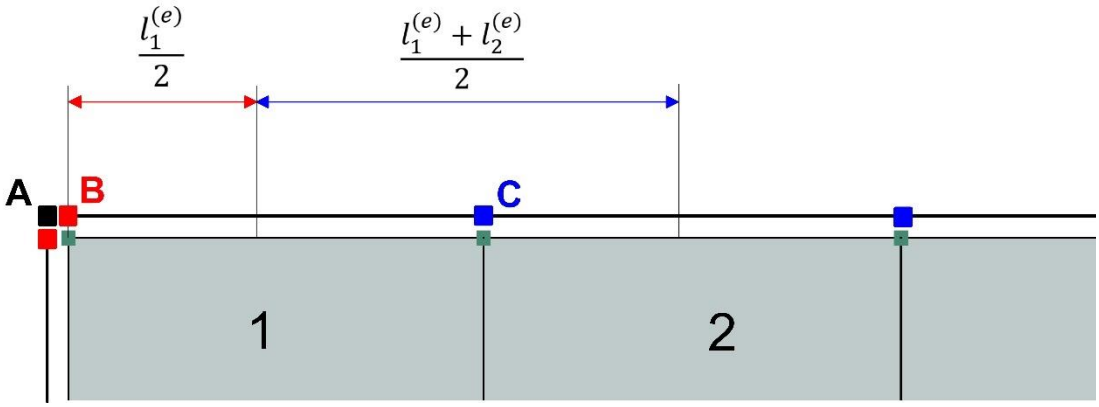

Figure 4.9. Influence area of free-field element base dashpots.

4.4.2 Added masses elements: implementation of amass1 subroutine

In order to satisfy the Abaqus® requirement of a single user subroutine of the same type (e.g, two UEL subroutine cannot be assigned to the same Abaqus® job at once), the amass1.for subroutine is written as a suboption of ffuel3.for. The added mass user element here defined is therefore called U23 to distinguish it from the free-field elements previously described (U1, U2, U3) and the infinite elements defined by Nielsen (U11, U12, U13), not used in Ridracoli Dam analyses. The 2 in U23 indicates the typology (0 = free-field, 1 = infinite, 2 = added masses) and the 3 indicates the dimension (1 = 1D FE in a 2D analysis, 2 = 1D FE in a 3D analysis, 3 = 2D FE in a 3D analysis). In the Ridracoli Dam case 5976 U23 elements are used.

It is derived from subroutine addedmass_uel.f, distributed as part of Abaqus® documentation (Abaqus, 2009) for the analysis of two-dimensional dams. Moreover, the Abaqus® subroutine suffers the original limitation of Westergaard method (i.e., a vertical upstream face of the dam).

The simple code in addedmass_uel.for is therefore adapted to three-dimensional problems and variable-orientated upstream faces. An isoparametric 4-noded linear shell element is defined in *amass1* with the following properties:

- no stiffness,
- no damping,
- a mass matrix, $\mathbf{M}_a$, given by **Equation 3.61**, and only active in dynamic steps of analysis.

Details of the formulation of Westergaard and Zangar theories and the corresponding equation written in a Finite Element notation are given in **Section 3.3.7.** For the definition of the new added-mass elements in the model the same nodes of the dam face are used. This is the main reason for the choice of using C3D8 elements for the dam body, whose faces are described with the same shape function of *amass1* elements.

The ξ-η-ζ-coordinate of the nodes of the isoparametric added mass element in the parent domain are:

$$\text{node 1:} \quad \xi = -1 \quad \eta = -1 \quad \zeta = -1 \tag{4.2a}$$

$$\text{node 2:} \quad \xi = 1 \quad \eta = -1 \quad \zeta = -1 \tag{4.2b}$$

$$\text{node 3:} \quad \xi = 1 \quad \eta = 1 \quad \zeta = -1 \tag{4.2c}$$

$$\text{node 4:} \quad \xi = -1 \quad \eta = 1 \quad \zeta = -1 \tag{4.2d}$$

A pictorial view of the isoparametric added-mass shell element attached to the face of a hexahedral C3D8 elements is given in **Figure 4.10**.

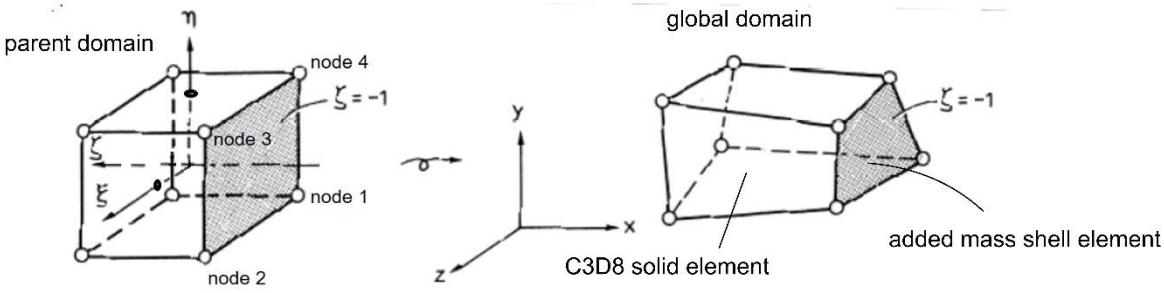

Figure 4.10. Definition of the user isoparametric added-mass element attached to the face of C3D8 dam-body elements, in the parent and the global domains.

The shape functions in the ξ-η-ζ-coordinate system are given by the following:

$$S_1^{(e)} = ((1-\xi)(1-\eta)(1-\zeta))/8 \quad (4.3a)$$

$$S_2^{(e)} = ((1+\xi)(1-\eta)(1-\zeta))/8 \quad (4.3b)$$

$$S_3^{(e)} = ((1+\xi)(1+\eta)(1-\zeta))/8 \quad (4.3c)$$

$$S_4^{(e)} = ((1-\xi)(1+\eta)(1-\zeta))/8 \quad (4.3d)$$

The element properties to be given in input are:

- reservoir maximum depth (approximately 100 m for Ridracoli Dam),
- water level in the reservoir (557.3 m a.s.l. for Ridracoli Dam, since the main model has an upward-directed Z-axis corresponding to the absolute elevation above sea level),
- water density (usually assumed equal to 1000 kg/m^3),
- Zangar c_m coefficient (c_m = 0.69, see **Equation 4.4** and **Figure 4.11**);
- element dimension (always equal to 2 for shell elements),
- number of integration points (1 or 4),
- added mass typology (1 = generalized Westergaard, 2 = Zangar).

The Zangar formulation is used in Ridracoli Dam analyses. The mass matrix in the original code was lumped with non-null terms for the DOFs corresponding to horizontal nodal displacements only. The mass matrix in amass1.for is always consistent. The single entries of the mass matrix are numerically integrated over each element with a Gauss quadrature technique. As already mentioned, it is possible to choose between two options depending on the number of Gauss points in the element (i.e., 1 or 4 Gauss points per element). The 4-points option is adopted in the analyses, owing to its capability to consider a non-uniform distribution of the added mass density over the single finite element.

The Zangar c_m coefficient for Ridracoli Dam is calculated as suggested in the Italian code for dams and barriers (NTD, 2014). The main section of the dam is schematised in **Figure 4.11**. The submersed part of the upstream face of the dam is divided into 9 segments from the bottom up with a constant elevation difference of 10 m (with the exception of the last segment that terminates at the water level, 557.3 m a.s.l.). The characteristic c_m for the definition of hydrodynamic pressures can be derived with the following weighted mean:

$$c_m = (\sum_{i=1}^{9}(90 - \alpha_i)\,\Delta L_i)/(\sum_{i=1}^{9}\,\Delta L_i) \tag{4.4}$$

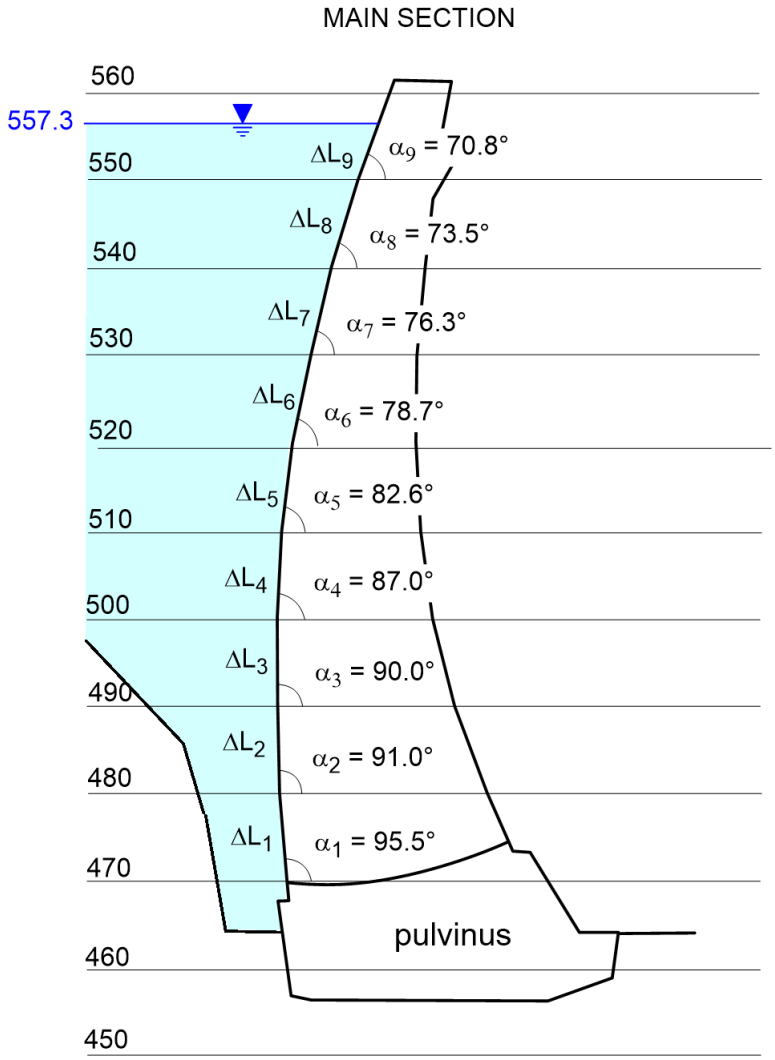

Figure 4.11. Main section of Ridracoli Dam used for calculating Zangar c_m coefficient.

4.4.3 Mohr-Coulomb interactions: Implementation of fric1 subroutine

A FRIC user subroutine in Abaqus/Standard® defines the tangential behaviour of an interaction properties between two surfaces in contact. In Ridracoli Dam analyses the subroutine *fric1* is used to model the interaction between solid bodies along the natural discontinuities of the rock mass (i.e. the laminated layers and the mid-plane of the fault described in **Sections 1.2.2** and **1.2.3**). It is supposed that all the plasticity of the rock mass is concentrated along these discontinuities of an otherwise homogeneous elastic domain.

The user subroutine fric1 is derived from subroutines technote_fric_coulomb_3.for (2D) and technote_fric_coulomb_4.for (3D) (HKS-Inc., 2001a; 2001b). These two subroutines suffer the original limitation of the native Mohr Coulomb criterion implemented in Abaqus/Standard®:

- no cohesion,
- definition in terms of total stresses.

To overcome these limitations, in *fric1* the Mohr-Coulomb criterion is modified as in **Equation 3.70**. Moreover, the frictional behaviour is suddenly shifted to a free-sliding condition whenever the normal effective stress become non-positive.

The shear strength parameters (c' and tanφ') are given in input, together with a threshold for elastic slips (γ_{cr}), and the water level (H_w) needed to calculate hydrostatic pore pressure under the hypothesis of a linear distribution with depth. The subroutine cannot consider neither the hydrodynamic oscillations of pore pressures during a seismic event, nor a possible pore pressure building-up during the shaking. The elastic slip threshold (γ_{cr}) is not given in input directly, but as a percent, $\gamma_{\%}$, of the characteristic length (l_{ch}) of element faces on the surfaces defining a contact. The following relation holds:

$$\gamma_{cr} = \gamma_{\%}\ l_{ch} \tag{4.5}$$

The subroutine is applied both for the laminated layers and the fault. In the first case dry conditions are enforced by setting a hydrostatic level lower than the minimum elevation of the surfaces in contact. This choice is motivated by a consideration on the initial closure and cementation of the laminated layers. The mid-plane of the fault, on the other hand, is considered as submerged. The plane is subdivided in four sectors with a common centre at the upstream edge of the pulvinus base (**Figure 4.12a**), aiming to roughly reproduce the filtration path around the grout curtain. Starting from the upstream sector, the hydrostatic level corresponding to the water level in the reservoir (557.3 m a.s.l.) is linearly reduced to match the water table level downstream of the dam (450.0 m a.s.l.). The mesh of the left-sided part of the fault (F-L) is given in **Figure 4.12b** for completeness.

In lack of experimental data, Mohr-Coulomb coefficients for the fault are assigned on the basis of the lithology of the core part, which has been classified as a breccia (see **Section 1.2.2**). A friction angle of 35° and a low cohesion (c' = 1.0 kPa) are chosen.

All the interaction used for Ridracoli Dam simulation are summarised in **Table 4.4**. The elastic and plastic properties of all the interactions used for Ridracoli Dam simulations are listed in **Table 4.5**.

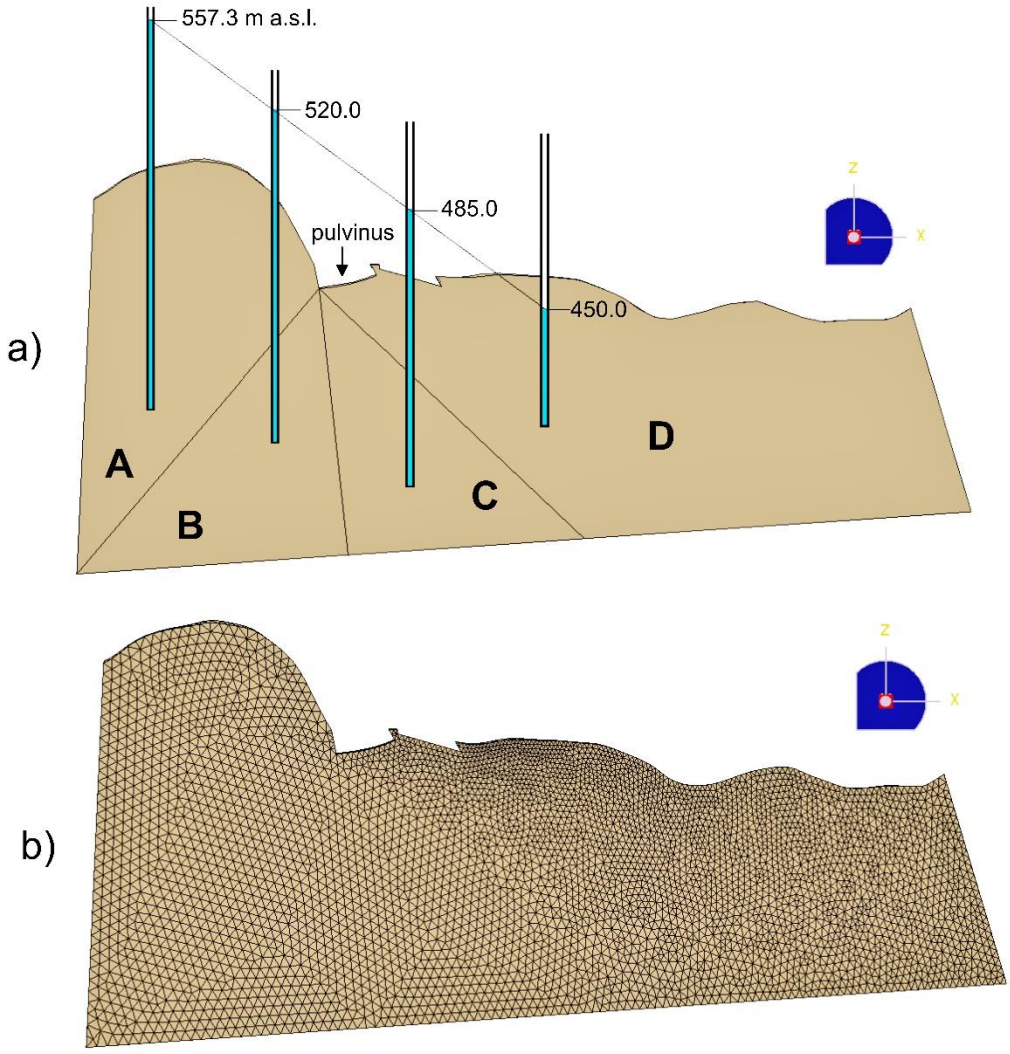

Figure 4.12. a) contact surface of the left-sided half of the fault divided in uniform sectors (A – D) with different reference water levels (linearly decreasing from left to right); b) mesh of the face.

Table 4.4. Interactions of Ridracoli Dam model.

Parts in contact	Normal behaviour		Tangential behaviour	
	"Hard"	Cohesive	Mohr-Coulomb	Cohesive
EXT-1/ EXT-2	✗	✓	✗	✓
INT-R-1/ INT-R-2 (III laminated layer)	✓	✗	✓	✗
INT-R-2/ INT-R-3 (II laminated layer)	✓	✗	✓	✗
INT-R-3/ INT-R-4 (I laminated layer)	✓	✗	✓	✗
INT-L-1/ INT-L-2 (III laminated layer)	✓	✗	✓	✗
INT-L-2/ INT-L-3 (II laminated layer)	✓	✗	✓	✗
INT-L-3/ INT-L-4 (I laminated layer)	✓	✗	✓	✗
F-R/F-L	✓	✗	✓	✗

Table 4.5. Intersections properties assigned to Ridracoli Dam interactions.

Interaction behaviour	"Hard"	Mohr Coulomb				Cohesive	
Parts in contact	K_N	$\gamma_{\%}$	tanφ'	c'	H_w	K_N	K_S
	(GN/m)	(%)	(-)	(kPa)	(m)	(GN/m)	(GN/m)
EXT/EXT	-	-	-	-	-	1000.0	1000.0
INT/ INT	1000.0	0.01	0.23	20.0	0	-	-
F/ F sector A	1000.0	0.01	0.70	1.0	557.3	-	-
F/ F sector B	1000.0	0.01	0.70	1.0	520.0	-	-
F/ F sector C	1000.0	0.01	0.70	1.0	485.0	-	-
F/ F sector D	1000.0	0.01	0.70	1.0	450.0	-	-

4.5 Numerical analyses

The capability of user-defined subroutines to reproduce simple benchmark examples is tested at first. The three different subroutines are tested separately. For *ffuel3* a comparison with other software which implement the same strategy is given, while other subroutines are tested against simple analytical results.

The numerical results of the analysis of the complete dam-water-foundation system subjected to the Coalinga (1983) earthquake are provided. The selected earthquake well approximate the Maximum Credible Earthquake (MCE), as stated in **Section 2.4.2**, and obeys to strict spectrum-compatibility requirements. The displacements at several nodes at the level of the crest are primarily examined in order to detect the natural periods of the system and examine the structural behaviour. The influence of the impounded water and the rock foundation on the overall response of the system are then pointed out. A comparison is made with literature results (Buffi, 2018) and fixed base analyses of the dam at different filling conditions of the reservoir. The plastic behaviour along natural discontinuities of the rock mass are finally analysed in terms of unrecoverable slip at the end of the analysis.

4.5.1 Testing of ffuel3

In this section several examples are documented to validate the accuracy of the direct FE method theoretically developed in **Chapter 3** and implemented in the FE program Abaqus/Standard® with the help of subroutine *ffuel3* (**Section 4.4.1**). The ability of the method to reproduce free-field motions at the surface of a flat foundation box subjected to upward-propagating shear waves (SH) is verified. In this special case, the three-dimensional seismic response exactly corresponds to that of a 1D column of soil.

One-dimensional site response analyses (SRA) can be performed with a variety of methods. A linear visco-elastic material is assumed for the soil with material properties listed in **Table 4.6**. An SRA in the frequency domain is performed with the academic Matlab®-based software MARTA (Callisto, 2020) and the results are compared with those obtained with Abaqus/Standard® and with the geotechnics-oriented FE software Plaxis2D® and Plaxis3D® (Brinkgreve et al., 2022) for a variety of geometries and strategies (**Figure 4.13**; **Table 4.7** and **4.8**).

Table 4.6. Material properties assigned in the *ffuel3* test problem.

Mass density	Linear elastic properties		Damping coefficients	
ρ (kg/m^3)	E (GPa)	ν (-)	α_R (-)	β_R (-)
2038.7	0.48	0.33	1.257	0.002829

The test problem is similar to that described in Plaxis® verification manual (Brinkgreve et al., 2022). Both 2D (plain-strain) and 3D analyses are conducted. In 2D conditions a "columnar" geometry (2x50 m) and a square geometry (50x50 m) are compared. In 3D conditions a cubic flat box (50x50x50 m) is employed (**Figure 4.13**). In order to test the effect of an extremely rigid cohesive interaction on the dynamic response (by analogy with the strategy adopted for Ridracoli Dam, see **Section 4.3.4**) a further cube is prepared, with a 30x30x30 internal cubic slot. The internal cube is in contact with the external part on 5 sides through the cohesive interaction. A single elastic layer is considered for sake of simplicity.

The natural periods of the soil column can be easily calculated with **Equation 4.5**.

$$T_N = \frac{4\,H}{n\,V_S} \tag{4.5}$$

where H is the thickness of the layer (i.e. H = 50 m), V_s is the shear wave velocity of the elastic material (i.e. V_s = 300 m/s) and n is the progressive number of natural periods. The Rayleigh coefficients, α_R and β_R, exactly correspond to a damping coefficient (ξ) of 8% for the first two natural periods of the deposit (T_1 = 0.66 s and T_2 = 0.133 s). A damping coefficient equal to 8% constant with frequencies is entered in MARTA.

The choice to use Plaxis® is due to its native free-field and compliant base elements, which are easily added to the lateral and bottom boundaries through the program user interface. The free-field elements in Plaxis® are analogous to those in *ffuel3*, while the compliant-base elements correspond to the combination of discrete dashpots and point loads implemented in Abaqus/Standard® to account for the deformability of the bedrock, and described in detail in **Section 4.3.6** and **4.3.7.**

Because of the mesh limitations in *ffuel3* (Nielsen, 2014) and in Plaxis® (i.e., the limited library of available elements), the chosen finite elements are different in the two tested FE environments. Triangle/tetrahedral elements of high order are used in Plaxis® (i.e. 15-node-TRI and 10-node-TET), while usual CPE4/C3D8 elements are selected in Abaqus/Standard®. All the meshed models are shown in **Figure 4.13**.

Apart from "free-field" boundaries, another boundary strategy typically adopted for 1D analyses is applied for comparison. It is usually referred to as tied-DOFs (TDOF) and consists in constraining the motion of each node on the right boundary to be equal to the motion of the corresponding node on the left boundary.

The seismic input is invariably applied at the base of the model. Two limit conditions are considered:

- a perfectly rigid bedrock, labelled from here after as "bedrock" (**Table 4.7**),
- a bedrock layer with the same elastic properties of the soil in the model, labelled from here after as "outcrop" (**Table 4.8**).

In the first case, the "compliant-base" strategy is unnecessary and the seismic input may be applied as an acceleration time history directly to the nodes at the base of the main model (and at the base of free field columns and plane sections). Dashpots are replaced by fixities in the non-excited directions (i.e., the vertical direction in 2D models, the vertical and one of the horizontals in 3D models). The horizontal seismic input used in the test models is taken from Plaxis® tutorials (Brinkgreve et al., 2022) and plotted in **Figure 4.14.** It corresponds to the unscaled North component of the Upland Earthquake (1990), and has a local magnitude of 5.4 and a duration of 23.44 s.

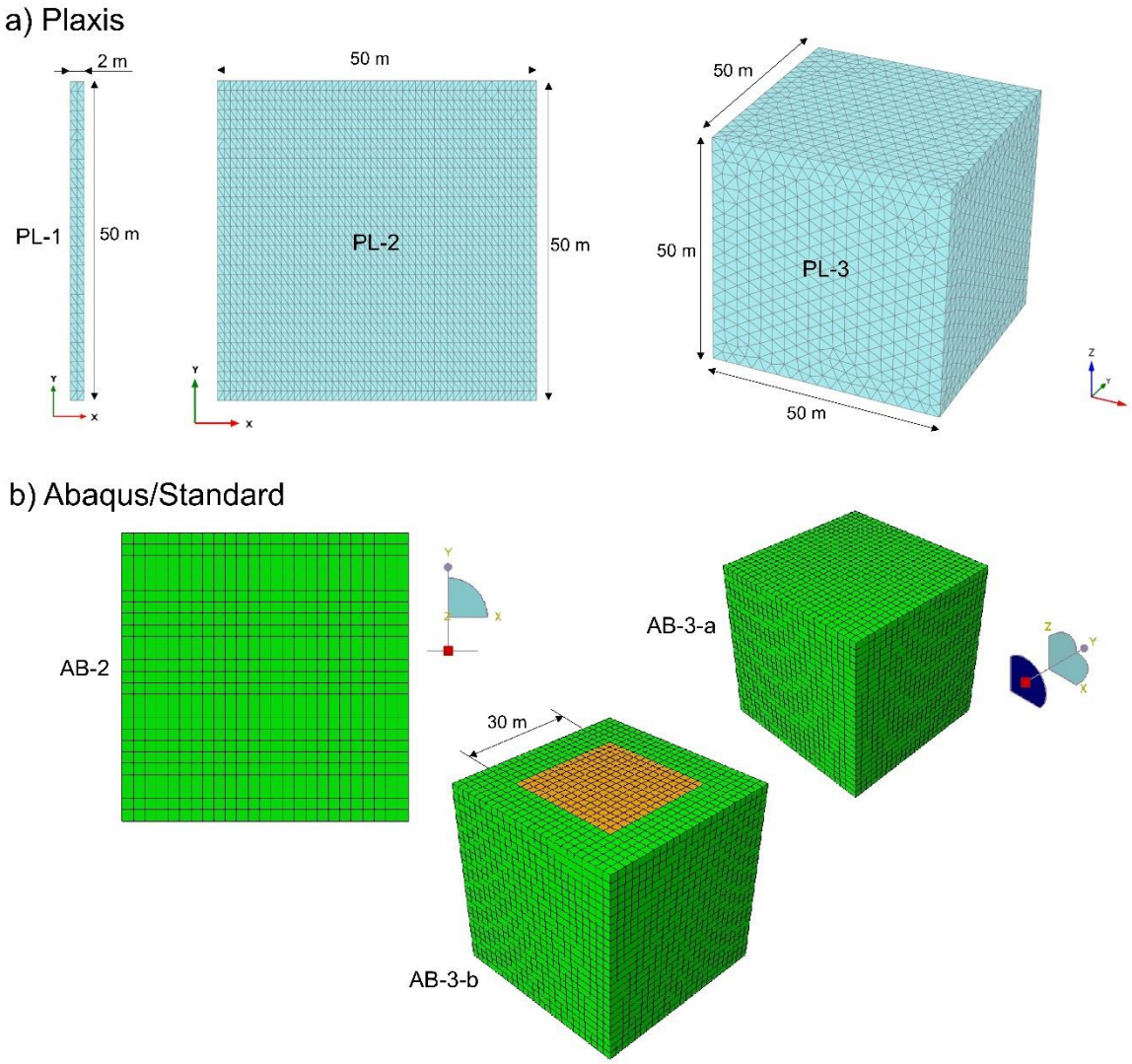

Figure 4.13. a) 2D and 3D *ffuel3* test models used in Plaxis®; b) 2D and 3D *ffuel3* test models used in Abaqus®.

Table 4.7. Meshes and geometries used with seismic input defined at bedrock.

	Software	Test analysis	Geometry	type	number
Bedrock	Marta	MARTA-B	50	-	-
	Plaxis2D®	PL-1-TDOF-B	2x50	15-node-TRI	132
		PL-2-TDOF-B	50x50	15-node-TRI	3300
		PL-1-FF-B	2x50	15-node-TRI	132
		PL-2-FF-B	50x50	15-node-TRI	3300
	Plaxis3D®	PL-3-FF-B	50x50x50	10-node-TET	20461
	Abaqus/ Standard®	AB-2-TDOF-B	50x50	CPE4	625
		AB-2-FF-B	50x50	CPE4	625
		AB-3-a-FF-B	50x50x50	C3D8	15625

Table 4.8. Meshes and geometries used with seismic input defined at outcrop (i.e., considering a deformable bedrock).

	Software	Test analysis	Geometry	Element type	Element number
Outcrop	Marta	MARTA-O	50	-	-
	Plaxis3D®	PL-3-FF-O	50x50x50	10-node-TET	20461
	Abaqus/ Standard®	AB-3-a-FF-O	50x50x50	C3D8	15625
		AB-3-b-FF-B	50x50x50 (30x30x30)	C3D8	15625 (3375)

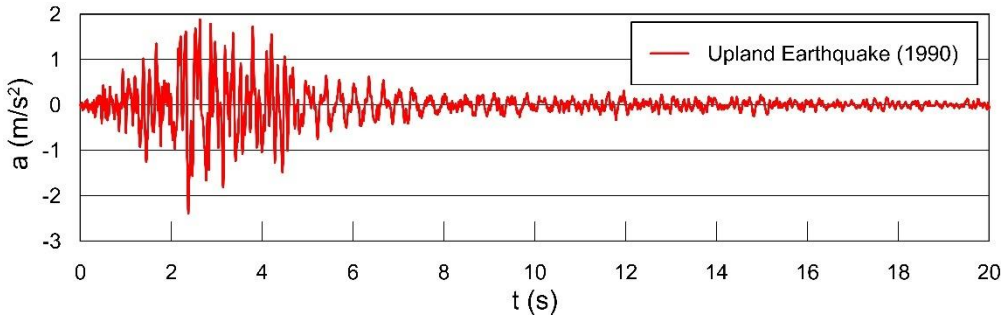

Figure 4.14. Seismic input (North component) from Upland Earthquake (1990).

The results are given in terms of ground-surface spectral accelerations (Sa) for a damping coefficient of the single degree of freedom system of 5%, in **Figure 4.15** and **Figure 4.16** for a seismic input defined at bedrock or at outcrop, respectively.

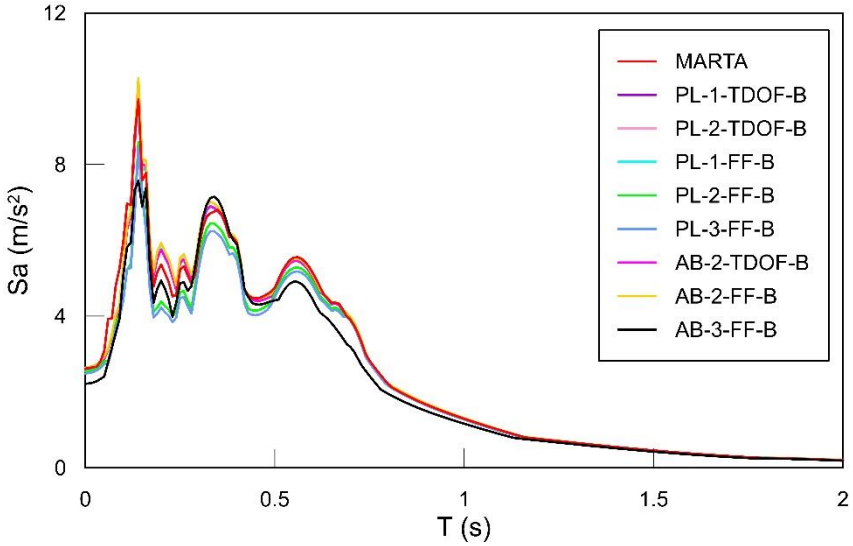

Figure 4.15. Spectral accelerations evaluated in correspondence to the mid-point of the ground surface in the different *ffuel3* test models for a seismic input applied at bedrock.

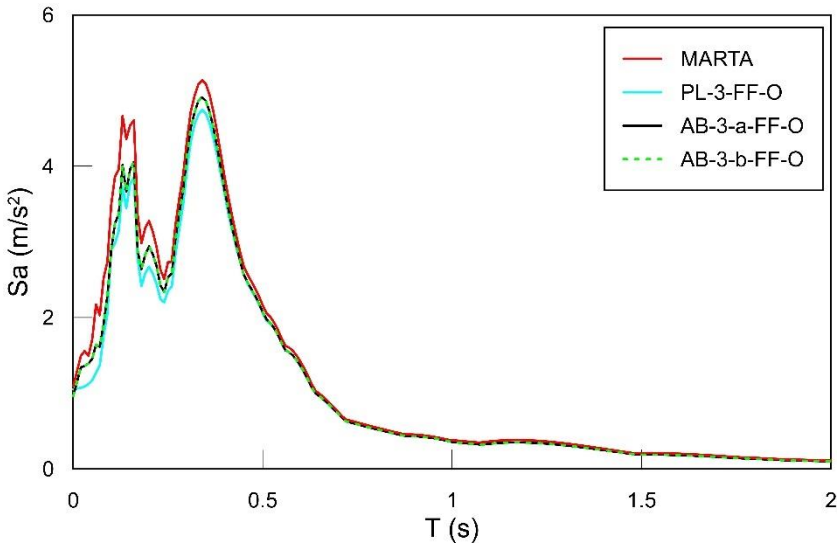

Figure 4.16. Spectral accelerations evaluated in correspondence to the mid-point of the ground surface in the different *ffuel3* test models for a seismic input applied at outcrop (i.e., considering a deformable bedrock).

All results refer to a mid-point of the ground surface. A satisfactory match with MARTA solution can be observed for all tested FE models. A near perfect match is found around the anchor frequencies of Rayleigh damping (T_1 = 0.66 s and T_2 = 0.133 s) for 2D models. Some inaccuracies arise when model width is increased without tying lateral-boundary DOFs (e.g., PL-2-FF-B). Three-dimensional models, owing to a relatively coarser mesh, are in less agreement with the reference solution obtained with MARTA. Plaxis® is more accurate than Abaqus® when the seismic input is directly applied at the base (i.e., bedrock hypothesis), while Abaqus® is slightly more accurate than Plaxis® when a deformable bedrock is assumed (i.e., outcrop hypothesis). No difference is observed between the single cube (AB-3-a) and the cube with the slot (AB-3-b), proving the effectiveness of the cohesive interaction in connecting different parts. The free-field strategy implemented in Abaqus® demonstrates to correctly reproduce free-field conditions for this simple 1D system to within FE discretization error.

4.5.2 Testing of amass1

The user-subroutine *amass1* is tested at the level of the single finite element. For this purpose a test program is written in Fortran (amasstest.f90), and attached in **Appendix E**. It has been used to calculate the hydrodynamic nodal forces, corresponding to the distributed pressure over the element face (see **Equation 3.5.4**), for a variety of nodal coordinates of the element, user-properties (i.e., water level, height of the immersed part of the dam, number of integration points, type of formulation), and acceleration distribution (i.e., constant and linear distribution). The same results can be manually calculated for a comparison and are in perfect agreement for all testing input. The combination of input parameters and output results in the attached version of the program are summarised in **Table 4.9**, while the test conditions are shown in **Figure 4.17.**

Table 4.9. Input parameters (see **Section 4.4.2**) and output results of amasstest.f90.

amass1 user parameters												
[H-h] (m)	H (m)	ρ (Kg/m^3)		c_m (-)			dim. (-)		int. pt. (-)		type (-)	
10	10	1000		0.69			2		1		1	
	Element DOFs											
Element coordinates (m)	-1	-1	2	1	-1	0	1	1	0	-1	1	2
Accelerations (m/s^2)	10	0	0	10	0	0	10	0	0	10	0	0
Hydrodynamic forces (kN)	58.7	58.7	0	58.7	58.7	0	58.7	58.7	0	58.7	58.7	0

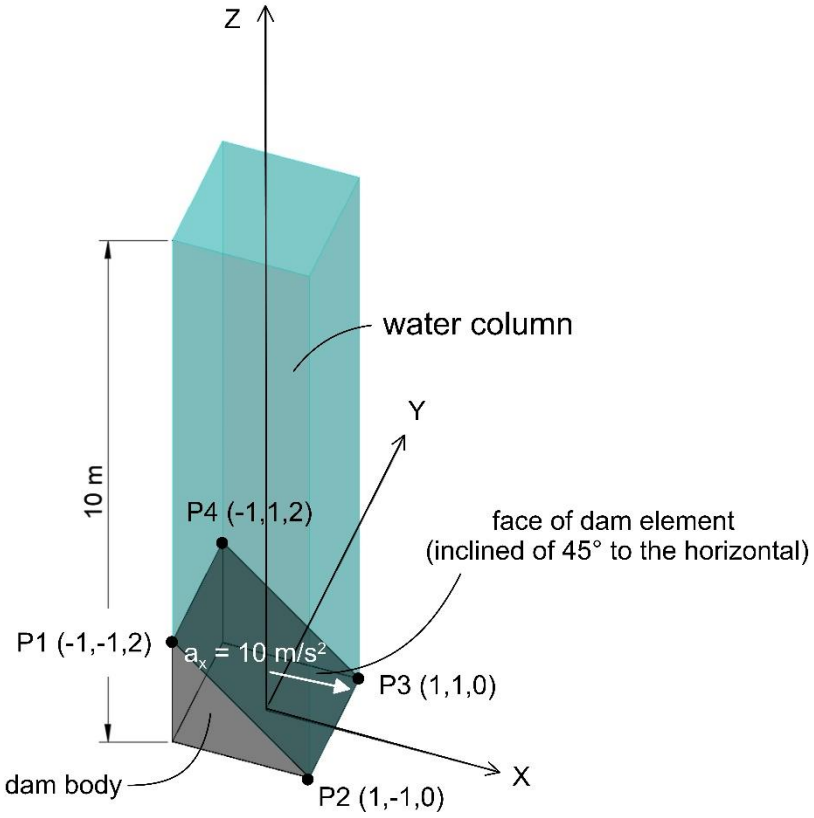

Figure 4.17. Scheme of the test problem in amasstest.f90

Further testing of *amass1* capabilities is given in **Appendix F,** where the new developed subroutine is compared with the Abaqus® freely distributed addedmass_uel.f for the 2D FE solution of Koyna Dam from Abaqus Example Problem Manual (Abaqus, 2009).

4.5.3 Testing of fric1

The user-subroutine *fric1* is tested in static conditions. A model composed of two cubes one on top of the other (50x50x50m each) is prepared in the Abaqus/CAE® environment; an interaction is inserted between the two cubes with tangential properties defined in the user-subroutine *fric1*. The reference value of the water table is placed at an elevation of 100 m above the base of the lower cube, while the a friction angle of 30° and a cohesion of 100 kPa. Elastic normal modulus of the interface is taken as equal to 1000 GN/m, while the elasticity threshold in tangential direction is given by a $\gamma_{\%}$ value of 0.01%. The lower cube is constrained with rigid links and is therefore undeformable, while the upper cube is linear elastic with a mass density of 3000 kg/m^3, a Young modulus of 1.0 GPa and a Poisson coefficient of 0.33.

The scheme of the test problem and the Abaqus® results are shown in **Figure 4.18**.

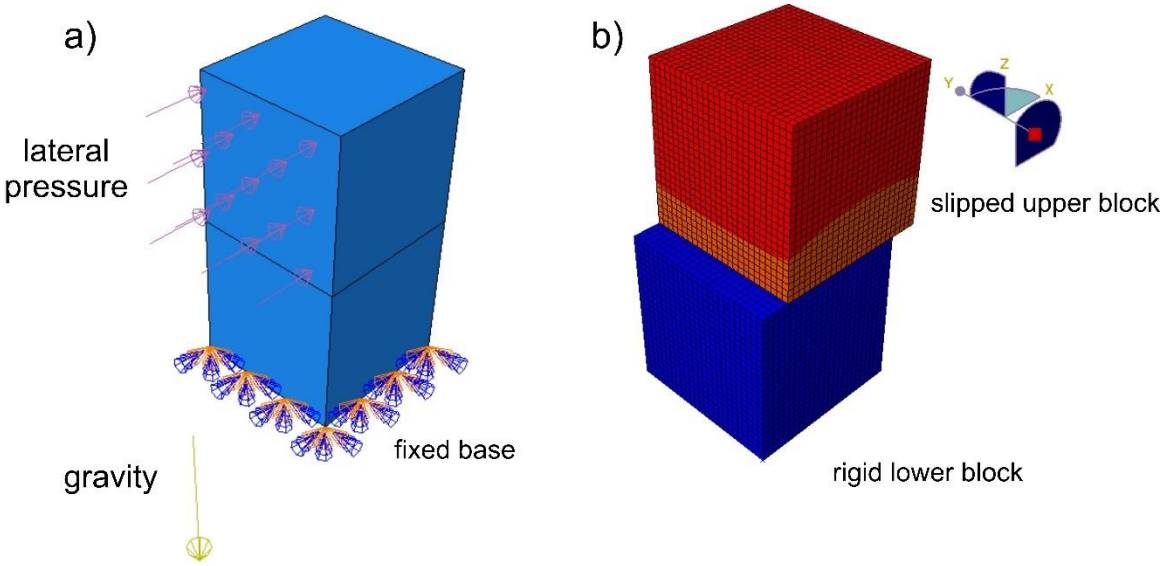

Figure 4.18. a) scheme of *fric1* test problem with applied loads and boundary conditions; b) results of Abaqus® simulation in terms of x-displacements at rupture.

The analysis is subdivided into two static steps: i) gravity loading, ii) lateral pushing. In the first step the gravity is applied to the upper cube which enters in contact with the lower rigid cube and deforms; in the second step the upper cube is pushed with a uniformly distributed normal pressure on one of its lateral sides, corresponding to a total horizontal force of 4.0 GN. The analysis interrupts after reaching a value of 1731.6 MN, while the manually calculated value under the hypothesis of unform distribution of pressures at the interface is equal to 1666.0 MN. The two values are in good agreement, the small difference being due to the deformability of the upper cube and consequent redistribution of normal pressure.

4.5.4 Choice of the seismic input

The dynamic analyses of Ridracoli Dam are conducted for the maximum credible earthquake (MCE) with a reference period of 1950 years. A concurrent hydraulic condition corresponding to the maximum water level (557.3 m s.l.m.) is considered.

The seismic input in three normal directions (North-East-Up) is selected from repositories of recordings of real earthquake events on the basis of a spectrum-compatibility in an interval of periods of interest. A detailed description of the adopted procedure is given in **Section 2.4.2**. Among the three signals selected in that context, the recording of Coalinga (1983) earthquake is the most compatible with the Uniform Hazard Response Spectrum (UHRS) estimated for Ridracoli (OGS, 2014). Moreover, the original signal is only slightly modified with a scale factor almost coincident with 1 in the horizontal direction

(composition of North and East components), and equal to 1.15 in the vertical direction. The Peak Ground Acceleration (PGA) in horizontal direction is equal to 0.63 m/s^2, perfectly matching the expected PGA at Ridracoli site. The PGA in the vertical direction slightly underestimate the expected value (with values of 0.22 m/s^2 and 0.34 m/s^2, respectively). The scaled acceleration time histories (in three directions: North-East-Up) of Coalinga (1983) earthquake are plotted in **Figure 4.19.**

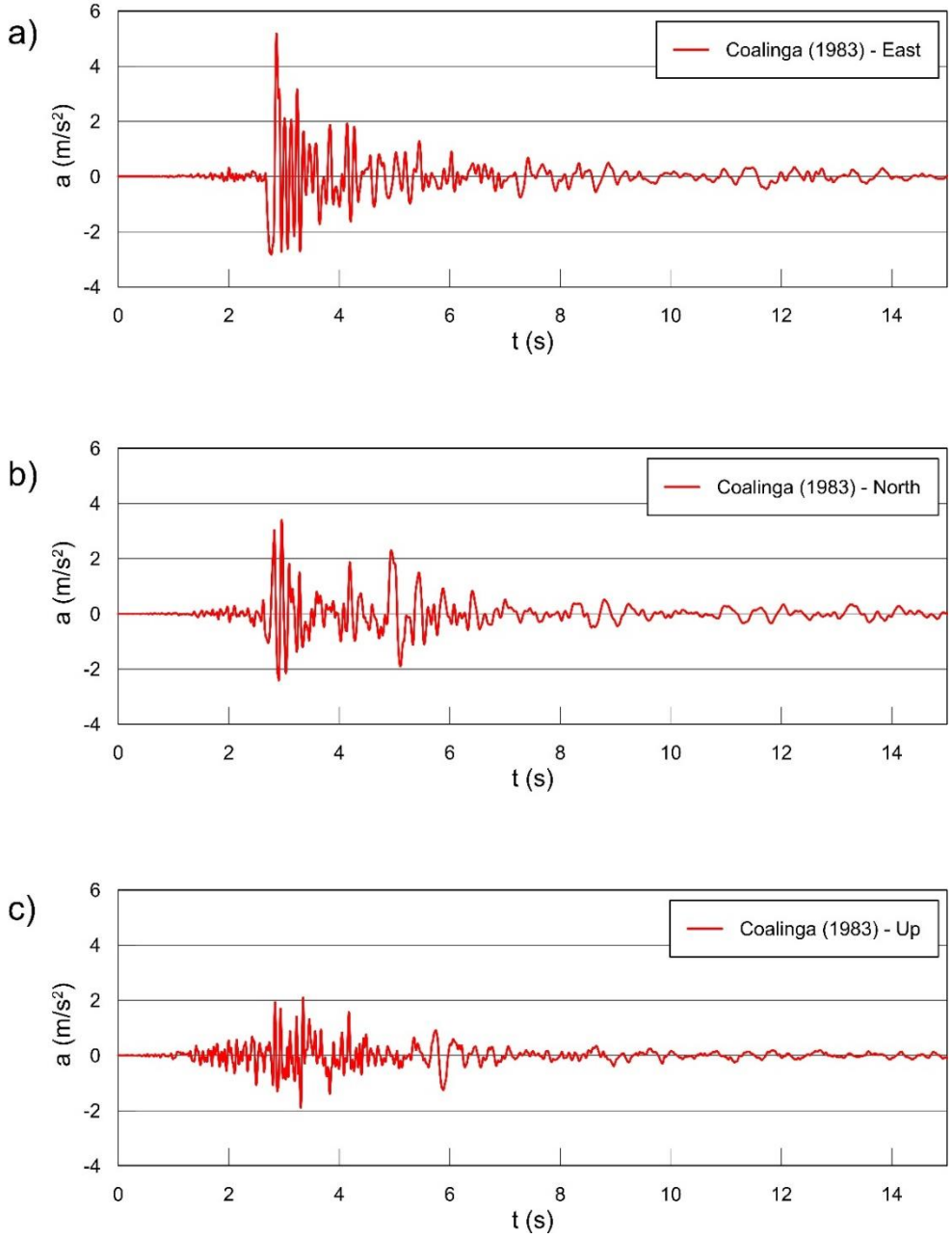

Figure 4.19. Three components of input motion from Coalinga (1983) recording: a) east component, b) north component, c) up component.

4.5.5 Preliminary static analysis

Before performing the dynamic analysis of the dam-water-foundation system of Ridracoli Dam, a preliminary initialisation of static stresses is needed. This static phase would not be necessary if the material behaviour of the whole system were assumed as linear elastic, because of the superposition principle. In Ridracoli FE model, though, a plastic behaviour of the rock mass is simulated, even if only along few known weak planes (i.e., laminated layers and fault). It is therefore necessary to include a strategy to initialise the static state of stress, at least in the portion of model affected by discontinuities.

A choice is made to disconnect the outermost external part (EXT-1, see **Section 4.3.2**), where free-field boundaries are applied, form the rest of the model. Static boundaries conditions are then imposed at the new boundaries of the reduced domain (see **Section 4.3.5**). Since the geometry is too complex for directly applying a known and equilibrated initial stress field, a static analysis phase is added with a constant gravity field applied (g = 9.81 m/s^2) to this reduced part of the domain. This portion of the model deforms under the self-weight; these displacements have no physical meaning since, in reality, the gravity was always present during the formation of the rock mass and the casting of the concrete. A strategy to reset these displacements to zero is described in the following.

Before resetting displacements, anyway, another static phase is calculated, this time adding the hydrostatic pressure exerted by the impounded water on the upstream face of the dam and on the submerged ground surface of the valley. These displacements are real, since they develop every time the water level in the reservoir varies. Under the hypothesis that the earthquake takes place when the reservoir is full, however, the zero-displacement condition is assumed to be coincident with that deformed state (and not with the empty condition). Also this portion of displacement is zeroed before proceeding to the dynamic phase.

To achieve this aim, the stress field in output of the static analysis is stored and re-applied in a static phase of a new identical model, with the same gravity and hydrostatic loads simultaneously activated. The resulting deformed mesh shows a negligible level of displacements in the reduced domain (and null outside), while stresses are correctly initialised along rock mass discontinuities.

The next step consists in reconnecting EXT-1 to the rest of the model. First of all, the static reaction forces at the lateral and bottom boundaries of the reduced domain are extracted from the output file with partial results, and applied to the still-constrained boundary nodes. They are needed to not perturb the stress balance once the static boundary conditions are deactivated in a subsequent (and last) static step of analysis. The cohesive interaction defined between EXT-2 and EXT-1 is concurrently activated in order to glue together the two disconnected portion of the model in the dynamic phase.

A schematic view of this process is given in **Table 4.10**

Table 4.10. Scheme of static phases propaedeutic to dynamic analyses.

Analysis	Step	Description
S1	G	typology: linear static analysis loads: gravity initial fields: none BCs (EXT-1): free-field elements (lateral), dashpots (base) BCs (EXT-2): fixed base, horizontally fixed lateral boundaries
	H	typology: linear static analysis loads: gravity, hydrostatic pressure initial fields: none BCs (EXT-1): free-field elements (lateral), dashpots (base) BCs (EXT-2): fixed base, horizontally fixed lateral boundaries
S2	GH	typology: linear static analysis loads: gravity, hydrostatic pressure initial fields: stresses from S1-Hydro BCs (EXT-1): free-field elements (lateral), dashpots (base) BCs (EXT-2): fixed base, horizontally fixed lateral boundaries
	RF	typology: linear static analysis loads: gravity, hydrostatic pressure, reaction forces on EXT-2 boundary from S2-Grav+Hydro initial fields: stresses from S1-Hydro BCs (EXT-1): free-field elements (lateral), dashpots (base) BCs (EXT-2): fixed base, horizontally fixed lateral boundaries
	I	typology: linear static analysis loads: gravity, hydrostatic pressure, reaction forces on EXT-2 boundary from S2-Grav+Hydro initial fields: stresses from S1-Hydro BCs (EXT-1): free-field elements (lateral), dashpots (base) BCs (EXT-2): none (cohesive interaction activated)

4.5.6 Dynamic analysis with MCE

After the static phases described in **Section 4.5.3** a dynamic phase is defined. The input motion from Coalinga (1983) recording is applied at the base of the main model and at the base of the free-field 1D and 2D systems in form of point loads, as extensively explained in **Section 4.3.7** and **4.4.1.** As outlined in **Section 3.3.5**, these concentrated forces are proportional to the velocities of the upward propagating seismic wave (**Equation 3.47b**). Considering the free-field motion at depth as not influenced by the irregular topography, these velocities can be calculated as half the outcrop motion velocities of the selected earthquake. They may be simply derived from acceleration time series by numerically integrating in the time domain with the trapezoidal rule. The trapezoidal approximation is applied in each subinterval of acquisition with a duration $\Delta t = 0.005$ s.

The East component of Coalinga earthquake, being the most intense, is applied in the stream direction of the valley (which in Ridracoli case coincide with geographic North). North component is consequently applied in the cross-stream direction (coincident with geographic West at Ridracoli site), while the vertical is applied as it was recorded: with positive values directed upward. The stream and cross-stream directions of the valley do not coincide with the local x_{DAM}-y_{DAM}-axes of the dam, because the arch-gravity structure intercepts not only Bidente river but also one of its left tributaries, which joins the main course of the river immediately upward of the dam. As a consequence, the dam does not cross the valley perpendicularly, but it is clockwise rotated of 28.65° (**Figure 4.20**).

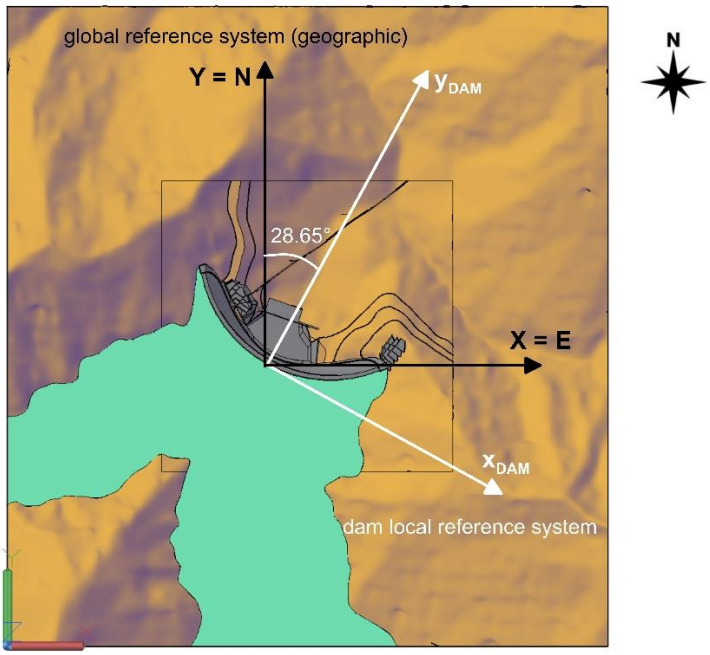

Figure 4.20. Global (in black) and dam local (in white) reference systems at Ridracoli.

4.5.7 Overall behaviour

The behaviour of the dam under the MCE is compared to its response when the seismic input is applied directly at the base of the pulvinus. Three analyses are performed:

- 2 fixed base analysis of the dam with an empty and full reservoir, respectively;
- 1 complete analysis of the dam-water-foundation interaction with a full reservoir (the analysis lasted 11 days with 6 processors in parallel on a personal i7 laptop).

As already motioned in **Section 4.3.1** a pair of Rayleigh coefficients is assigned to the dam structure corresponding to a reference damping of 2%. Løkke and Chopra (2019) suggest using a value in the interval 1-2%. The damping coefficient assumed for the rock mass, ζ = 3%, is in the interval of experimental values shown in **Figure 4.21.**

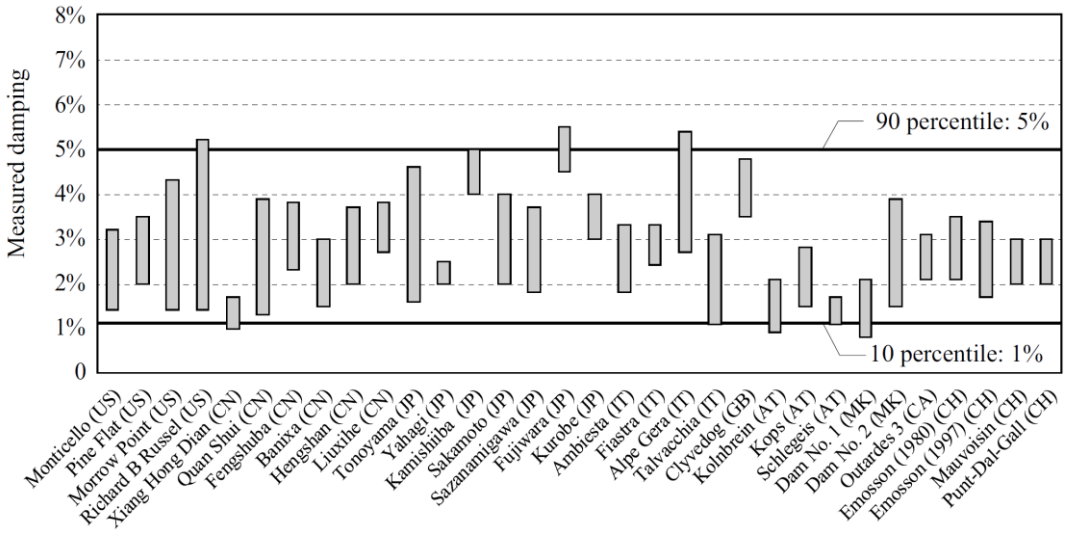

Figure 4.21. Damping at 32 concrete dams measured during vibrodyne tests or estimated from ambient vibration measurements (from Løkke and Chopra, 2019).

The acceleration time histories at the crest mid-point of the main section are extracted from the output database for all the analyses. The elastic spectrum in terms of accelerations is calculated considering a 5% damping. A shift of the peaks toward the longer periods is observed passing from empty conditions to full reservoir conditions; a further shift is observed when passing from fixed-base analyses to the complete analysis of the dam-water-foundation system. At the same time, the peak height progressively reduces. In fixed-base analyses the rock mass is considered as perfectly rigid and the seismic motion is contemporary applied along the entire extension of the dam-foundation interface, neglecting topographic effects due to the shape of the valley on the arriving signal (**Figure 4.22**). These over simplified hypotheses do not allow to properly represent the radiation

damping, nor the effects of foundation deformability, leading to an unrealistic superimposition of first arrival and reflected waves. On the contrary, the complete analysis may account for all the aforementioned phenomena. The representation of hydrodynamic effects by means of the added mass technique, the mesh density and the material properties are identical for fixed-base and complete analyses; this allows to clearly separate the effects on the natural frequencies of impounded water and foundation rock, respectively.

Two are the effects of considering the hydrodynamic forces, i.e., to slightly reduce the intensity of the seismic response and to shift peaks of spectral accelerations toward longer periods. Similarly, a further shift in peaks is observed when the rock foundation is included. Moreover, longer natural periods become predominant in the overall response. The most visible effect of including the rock foundation in the model, however, is a considerable reduction of the spectral ordinates. Two peaks can be clearly identified: the first for T = 0.21 s, corresponding to the maximum frequency content of the selected earthquake recording, and the second for T = 0.34 s, arguably coincident with the first natural period of the system. This last peak decreases of 30-40% in all directions when rock foundation deformability and radiation damping are considered. The one corresponding to the maximum frequency content of Coalinga earthquake (T = 0.21 s) is even more attenuated. The first natural period was found to correspond to T_1 = 0.3 s in empty conditions by Buffi (2018) (value confirmed by the fixed base empty analysis in the current work). The combined effect of including the interactions with water and rock foundation reduces the stiffness of the system, extending periods of vibration. Experimental values of natural periods extracted from vibrodyne tests conducted in 1987 (at the end of construction work) and from environmental vibration under past seismic events (e.g., the 2003 earthquake attached in **Appendix A**) indicate a first natural period of about 0.35 s in near-full reservoir conditions (Buffi, 2018). The same value was confirmed by Buffi (2018) model.

The reduction in the intensity of the structural response is associated to an increase in the magnitude of displacements. Total displacement time histories at some significative positions are also extracted from output databases. Starting from these values, relative displacements with respect to a node at the base of the dam are calculated in the East, North and upward vertical geographic directions, and plotted in **Figure 4.23**, limited to the mid-point of the main section at crest level. Maximum positive displacements in the North direction remain below a threshold of 4 cm (with an oscillation amplitude of about 8 cm). These values fall within the limits of the seasonal oscillations due to reservoir filling condition and temperature variations over the year (Lusini et al., 2021). The envelope of maximum displacements along the crest of the dam is provided in **Figure 4.24**. Also the envelopes along the local y-axis of the dam (y_{DAM}), corresponding to the "stream" direction, are plotted, since they exhibit the maximum/minimum values of displacements (but still around ±4 cm), and compared with the corresponding results from the fixed base analysis, which are significantly larger (about ±6 cm in the main section). The entire Ridracoli monitoring system refers to this local x_{DAM}-y_{DAM}-coordinates (i.e., cross-stream – stream directions).

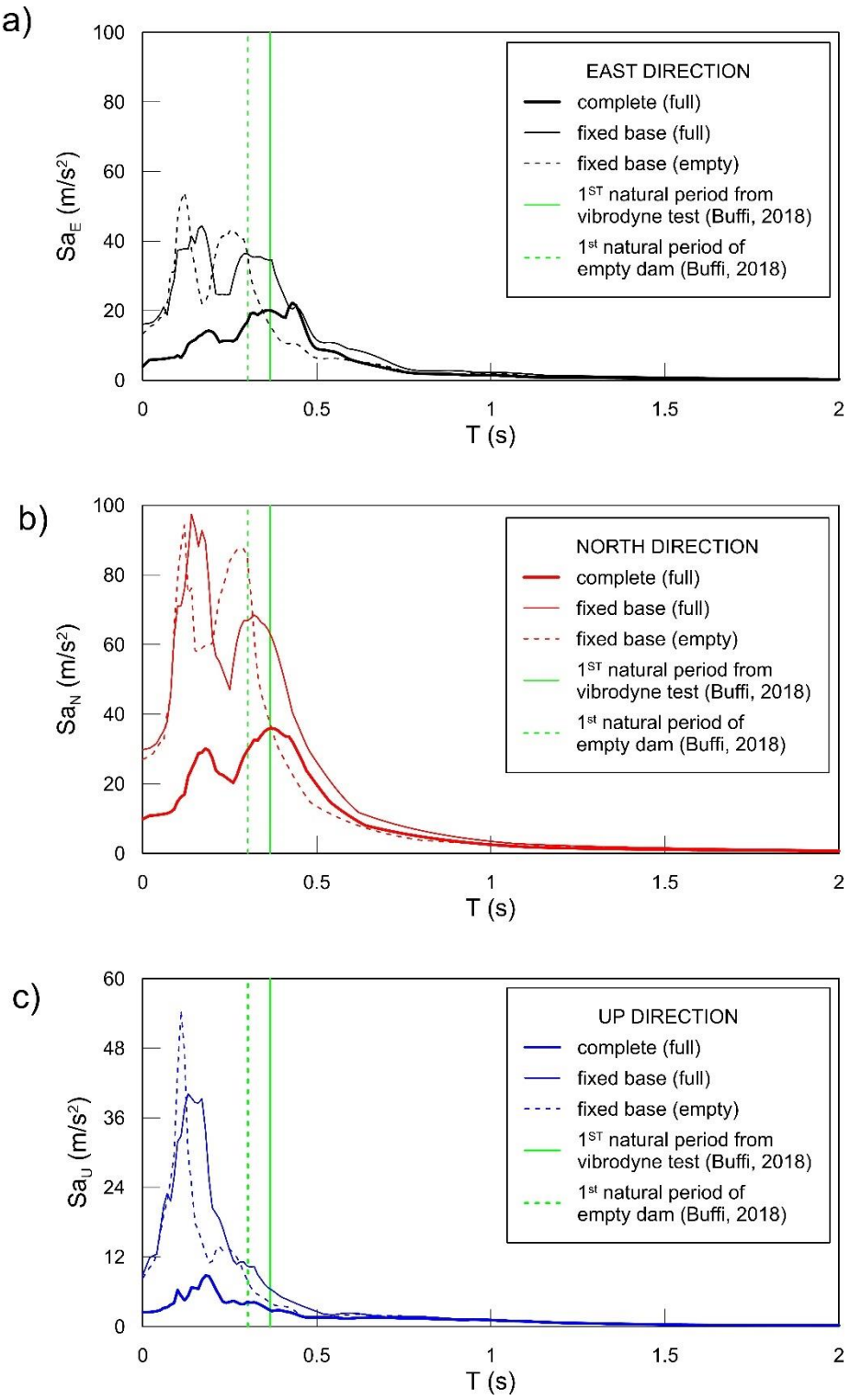

Figure 4.22. Spectral accelerations in a) East, b) North and c) Up directions for the three considered cases: fixed base analysis in empty and full reservoir conditions, and complete analysis of the dam-water-foundation model with full reservoir.

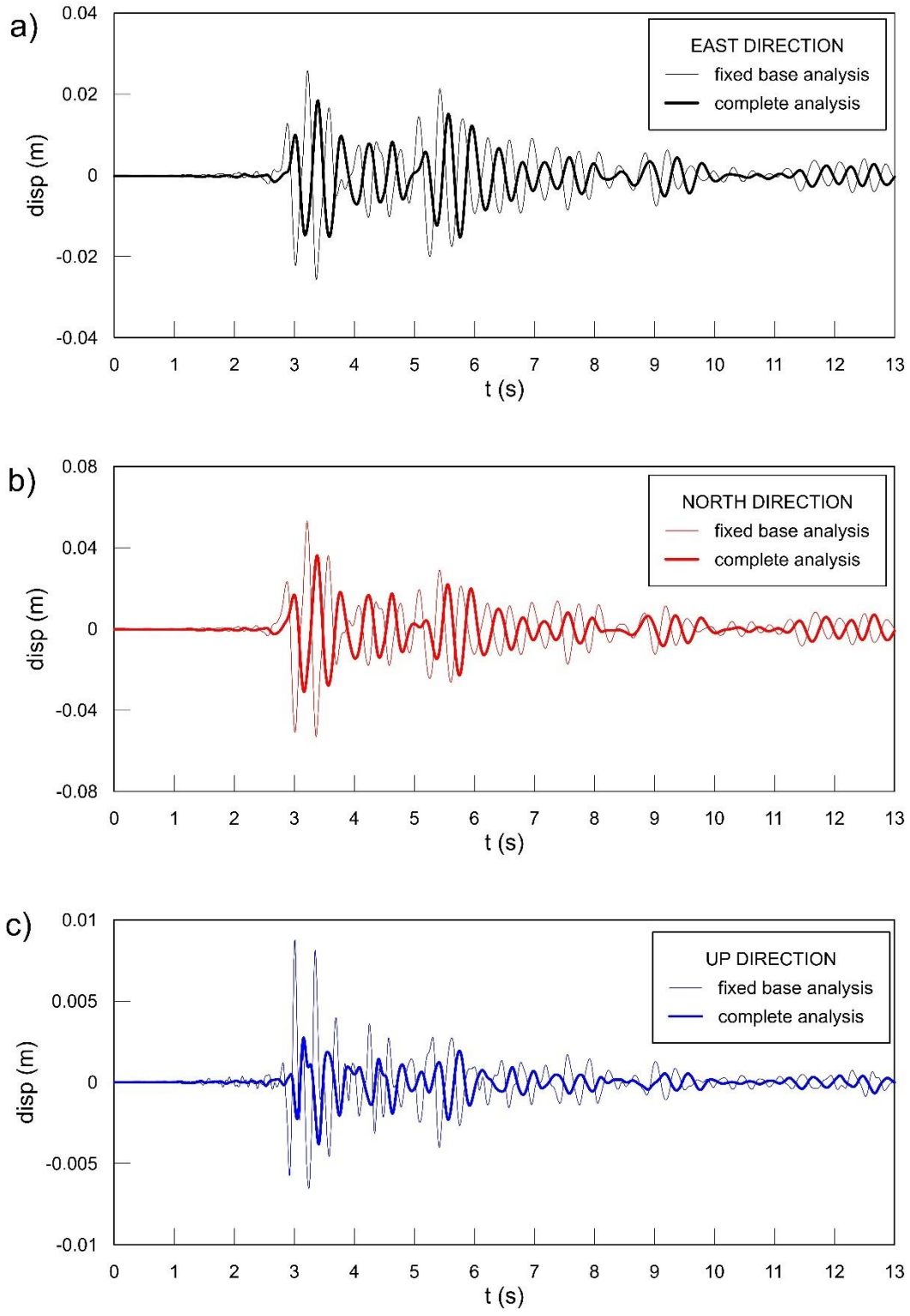

Figure 4.23. Displacement time histories at the crest mid-point of the main section in a) East, b) North and c) vertical (Up) directions for the fixed-base model and the complete system model.

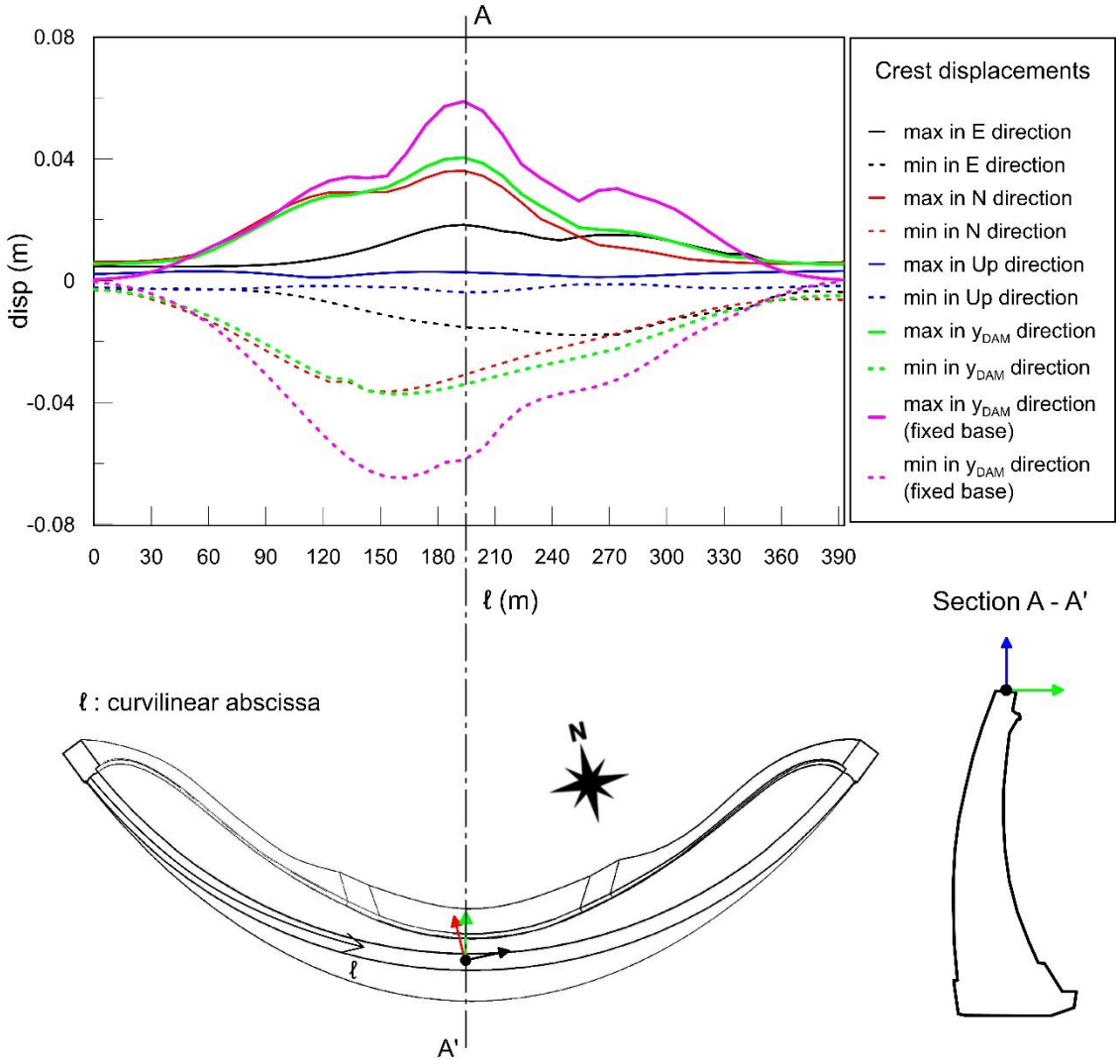

Figure 4.24. Maximum and minimum relative displacements at the crest level for the complete system model. The displacement components are given in the three geographic coordinates (East-North-Up) and in the local y_{DAM} direction (see **Figure 4.20**), in this latter case both for the complete system model and the fixed base model.

4.5.8 Plastic behaviour along discontinuities

Because of the elastic behaviour assumed for the rock mass, the main effect of the modelled discontinuities (i.e., the fault and the three laminated layers) is to limit the entity of transmitted shear stresses between the two sides of the discontinuity to a plastic threshold. The developed plastic slips (relative displacement at the two contact sides) at the end of the analysis, on the contrary, are not completely reliable, since the laminated layers and the fault do not isolate any rock wedge kinematically allowed to move. This aspect is better

explained by the scheme in **Figure 4.25**. The interactions are schematised as a series of plastic sliders connected one another and to the fixed ends by elastic springs:

a) the system is initially equilibrated.
b) a frame is captured during a dynamic analysis: some plasticity developed in correspondence of the two central sliders,
c) at the end of the dynamic excitation the temporary state of stress which caused the sliding does not exist anymore and the elastic springs force the system to return to its initial configuration.

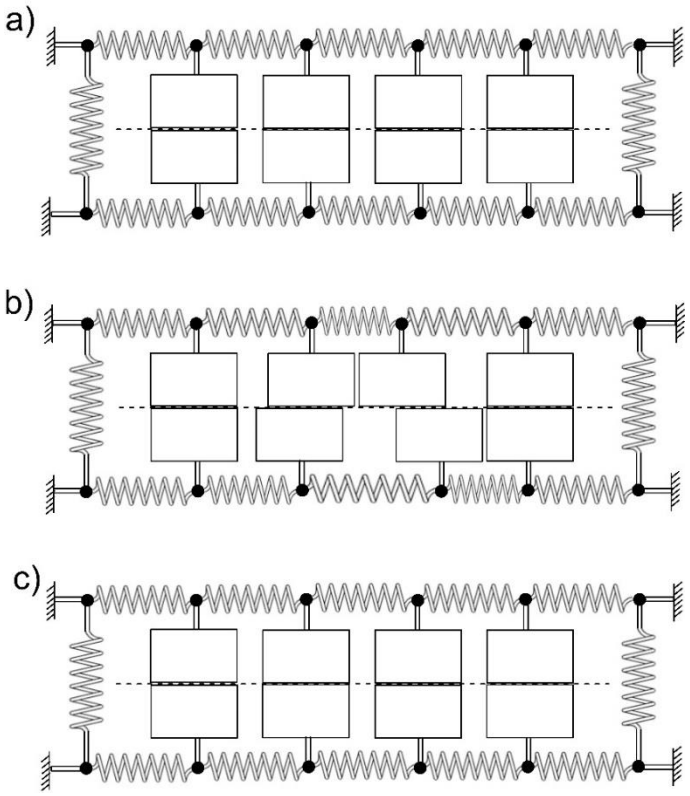

Figure 4.25. Scheme of the plastic behaviour along modelled discontinuities: a) initial conditions, b) plastic sliding under dynamic excitation, c) recover of initial conditions at the end of the earthquake.

For capturing large unrecoverable displacements, it would be necessary to add other minor discontinuities which cross the main four or to assign a diffused plastic behaviour to the rock mass elements. The larger slips (**Figure 4.26**), with a maximum of about 3 mm, develop along the fault below the bottom of the lake in a near-vertical direction (**Figure 4.26b**): the right side of the fault tends to move down relatively to the left side. They are limited to the sector (Sector A in **Figure 4.12**) where the hydrostatic water head is higher; and do not extend to touch the base of the dam.

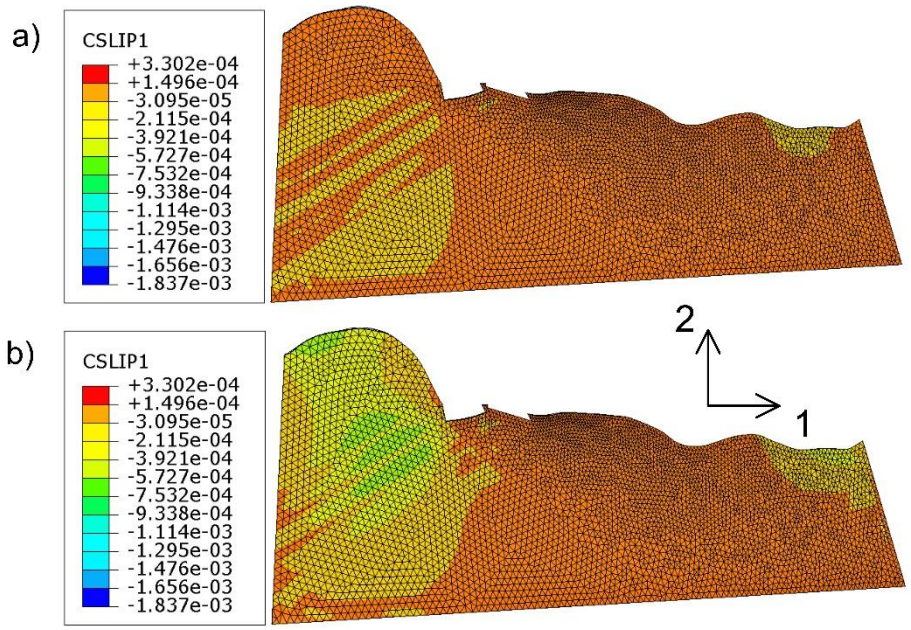

Figure 4.26. a) initial slips in horizontal direction at the beginning of the dynamic phase; b) residual horizontal slips along the fault during the complete analysis of the dam-water-foundation system (slips are plastic above a threshold of about 3 mm).

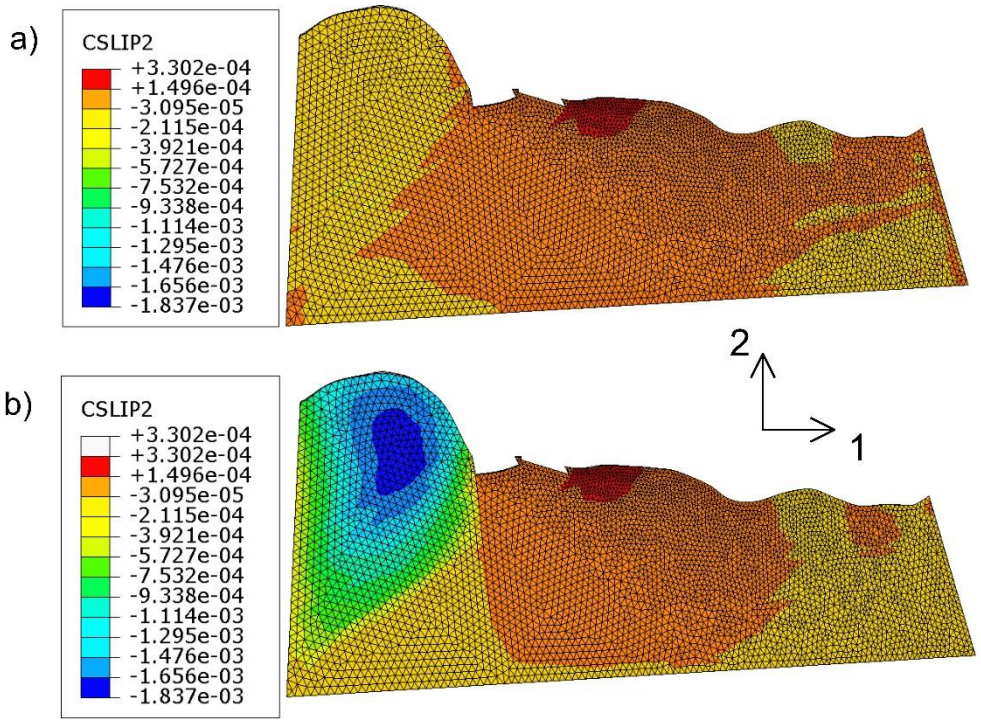

Figure 4.27. a) initial slips in vertical direction at the beginning of the dynamic phase; b) residual vertical slips along the fault during the complete analysis of the dam-water-foundation system.

The laminated layers, which are considered as dry owing to the initial cementation of the bedding planes, does not undergo any unrecoverable slip during the seismic excitation. In fact, the maximum slips are below the plastic threshold and therefore the interface behaviour remains elastic during the entire analysis. This aspect is clear when looking at the slip contours in the pre- and post-earthquake conditions for the first laminated layer (**Figures 4.28**), which are basically the same minus residual elastic oscillations. The same behaviour is observed in correspondence of the other two modelled laminated layers.

The non-zero cohesion assigned to the laminated layer (c' = 20 kPa), aims to account also for some consolidation work conducted in the rock mass surrounding the dam, in particular a system of rock anchors distributed along the two abutments (Bavestrello, 1983) and the grout curtain injections below the pulvinus (Oberti et al., 1986). To neglect it and implement a merely frictional interaction, therefore, would have been extremely on the safe side, leading to unrealistic results.

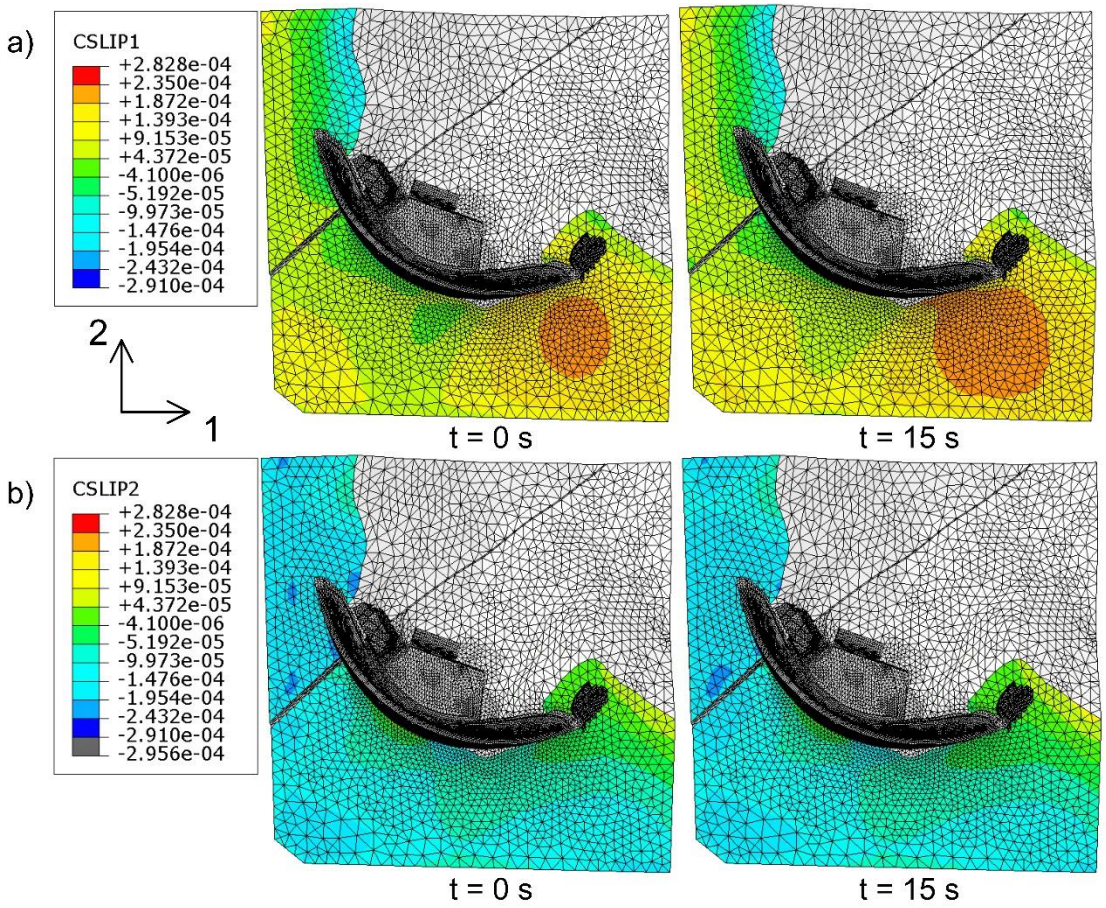

Figure 4.28. Initial (t=0s) and residual final (t=15s) slips along the first laminated layer: a) in the local 1 direction (corresponding to geographic East); b) in the local 2 direction (corresponding to geographic North).

Chapter bibliography

Abaqus, 2009. ABAQUS/Standard Example Problems Manual, Version 6.9. Dassault Systèmes Simulia Corp, Providence, Rhode Island (USA).

Alpina (Alpina S.p.A), 1974 (unpublished results). Progetto Esecutivo – Relazione Geologica – Allegato.

Brinkgreve, R.B.J., Kumarswamy, S., Swolfs, W.M., Fonseca, F., Ragi Manoj, N., Zampich, L. M., Zalamea, N., 2022. PLAXIS 3D CONNECT Edition V22 Update 1 Manual.

Bavestrello, F., 1983. Stabilizzazione temporanea degli scavi d'imposta della Diga di Ridracoli, in Proc. XV Convegno Nazionale di Geotecnica (XVCNG), Spoleto, Italy.

Buffi, G., Manciola, P., Grassi, S., Barberini, M., Gambi, A., 2017. Survey of the Ridracoli Dam: UAV–based photogrammetry and traditional topographic techniques in the inspection of vertical structures. *Geomatics, Natural Hazards and Risk.* http://dx.doi.org/10.1080/19475705.2017.1362039

Buffi, G., 2018. Assessment of seismic behaviour of large concrete dams by means of geomatics techniques and finite element modelling. PhD thesis. Firenze-Braunschweig, Italy-Germany.

Callisto, L., 2020. MARTA - a computer program for the site response analysis of a layered soil deposit. Version 1.2.0.

Falcone, G., Boldini, D., Amorosi, A., 2018. Site response analysis of an urban area: A multi-dimensional and non-linear approach. *Soil Dynamics and Earthquake Engineering*, 109, 33-45, https://doi.org/10.1016/j.soildyn.2018.02.026

HKS-Inc., 2001a. Lagrange implementation of coulomb friction using user subroutine FRIC. Tech. Rep., HKS Technical Note #1, HKS-Inc., Dallas, Texas (USA).

HKS-Inc., 2001b. Coulomb friction in user subroutine FRIC using the penalty method. Tech. Rep., HKS Technical Note #2, HKS-Inc., Dallas, Texas (USA).

Løkke, A., Chopra, A., 2019. Direct-Finite-Element Method for Nonlinear Earthquake Analysis of Concrete Dams Including Dam–Water–Foundation Rock Interaction - PEER 2019/02. Pacific Earthquake Engineering Research Center, Headquarters at University of California, Berkeley, California (USA).

Lusini, E., Boldini, D., Graziani, A., 2021. Considerations on the deformation of Ridracoli dam foundation based on the analysis of monitoring data; *IOP Conference Series Earth and Environmental Science*, 833(1). https://doi.org/10.1088/1755-1315/833/1/012147

Nielsen, A. H., 2014. Towards a complete framework for seismic analysis in Abaqus. *Proceedings of the Institution of Civil Engineers - Engineering and Computational Mechanics*, 167(1), 3-12. https://doi.org/10.1680/eacm.12.00004

Oberti, G., Bavestrello, F., Rossi, P. P., Flamigni, F., 1986. Rock mechanics investigations, design and construction of the Ridracoli dam. Rock Mechanics and Rock Engineering. 19(3), 113-142.
https://doi.org/10.1007/BF01024952

Smith, M., 2009. ABAQUS/Standard User's Manual, Version 6.9. Dassault Systèmes Simulia Corp, Providence, Rhode Island (USA).

Tarquini, S., Vinci, S., Favalli, M., Doumaz, F., Fornaciai, A., Nannipieri, L., 2012. Release of a 10-m-resolution DEM for the Italian territory: Comparison with global-coverage DEMs and anaglyph-mode exploration via the web. *Computers & Geosciences*, 38, 168-170.
https://doi.org/10.1016/j.cageo.2011.04.018

5. Conclusions

The present PhD Thesis describes the development of a Direct Finite Element approach to analyse the seismic response of an arch gravity dam with its foundation rock mass. The theoretical framework is applied to the case study of the arch-gravity dam of Ridracoli (Italy), using the Finite Element (FE) code Abaqus®. In order to obtain reliable results, the following aspects are investigated:

- the dam-foundation rock interaction via solid finite-elements and visco-elastic materials (Rayleigh formulation),
- the interaction of the dam with the impounded water of the reservoir via an added mass approach (Zangar formulation),
- the radiation damping at the fictitious boundaries of the truncated foundation rock domain via free field elements on the side boundaries and discrete viscous dampers at the bottom boundary,
- the possibility of maintaining the free-field elements and the viscous dampers as unloaded during the preliminary static phases of analysis, avoiding spurious displacements when switching from the static to the dynamic boundary conditions,
- the inclusion of a source of plasticity concentrated along natural discontinuities of the rock mass (i.e., a fault and three weak bedding planes).

In addition, the dynamic behaviour of possible rock wedges forming at the level of the abutments, which would be difficult to be correctly estimated via FE, is analysed by means of a modified three-dimensional Newmark (1965) approach. The original method developed by Verrucci et al. (2018) for generic rock wedges subjected to a seismic excitation has been adapted to the special case of arch dams for which the necessity to estimate the dynamic variability of the thrust exerted by the dam arises. Various possibilities are investigated and compared, from the simple use of the static thrust to a more accurate estimation of thrust time history by an auxiliary fixed-base FE model of the dam.

The possibility to extend the capability of a general-purpose Finite Element code like Abaqus® by means of user-subroutines to deal with complex interaction problems is shown. All developed user-subroutines are made available. A shell 4-noded isoparametric user element is developed to deal with hydrodynamic interaction in the framework of the added mass approach. It supports both general Westergaard (1933) and Zangar (1952) formulations and can be used in combination with hexahedral 8-noded elements in three-dimensional problems for immersed faces generally oriented in the space.

A second Abaqus® user-subroutine is provided which implements a Mohr-Coulomb friction law: differently from the native interaction property this version allows for the

definition of a cohesion, in addition to the pure friction, and accounts for the dependency of the shear strength on the effective normal stresses, when the interface is immersed. The water pressure is defined considering hydrostatic conditions.

The two user subroutines are used to model the Ridracoli dam-water-foundation system, together with a free-field user element written by Nielsen (2014). The capability of a combination of free-field elements on side boundaries and viscous dampers at the base is preliminary tested. A good agreement is found between Abaqus results with the free-field user element and the same problem analysed with other software (Plaxis®) and other strategies (one-dimensional analysis in the frequency domain).

Concerning the Ridracoli Dam case study the following remarks can be drawn:

i. the limited capabilities of the CAD (Computer-Aided Design) modulus which is usually included in commercial FE software are one of the more frustrating drawbacks that an engineer faces when first approaching the numerical modelling of complex geometries. A procedure is presented and applied to the case study to integrate geometric data from multiple sources, in various formats and characterised by a different level of detail: the resulting geometric model presents simple shapes that are easily treated by any CAD modulus. The topographic surface, for which a lower level of detail is required, is merged in a single NURBS (Non Uniform Rational Basis-Splines) surface which interpolates a regular 2.5D grid of points. The structural solids are greatly simplified (replacing the original faceted geometries with smooth curved faces) and used to cut the terrain model with Boolean operations, thus avoiding the risk of generating invalid geometries;

ii. a strategy is applied in Abaqus® to subdivide the terrain model in smaller parts (which are meshed separately, allowing for sudden transitions in mesh density and element type) and to stick them together with Tie Constraints and Cohesive Interaction: the first are used to connect those parts which remain jointed throughout the analysis, the second are successfully used to reconnect two parts which were originally disconnected. The last option is used to maintain unloaded the outermost part of the foundation rock (which includes free-field elements and viscous dampers) for all the phases which precede the dynamic step of analysis;

iii. the described Direct FEM procedure has been successfully applied to the case study for modelling the dynamic behaviour of Ridracoli Dam under the MCE (Maximum Credible Earthquake). The comparison with a simple fixed-base model shows the capability of the adopted adsorbing boundaries to avoid wave reflection inside the model:

   – the structural response at crest level shows a clear attenuation with respect to fixed-base results, with maximum displacements in the stream direction never exceeding 5 cm (with a double amplitude of less than 10 cm), and thus remaining within the limits of the seasonal variability;

- considering rock mass deformability and damping causes an extension of the first natural period of the dam in full reservoir conditions. Its value is found matching the experimental results;

iv. the strategy adopted to describe the plastic behaviour along the natural discontinuities allows to exclude the plasticisation of weak bedding planes (i.e., laminated layers) at a great scale, small, localised slips may possibly develop but cannot be detected with the current model;

v. a plastic behaviour is observed for the fault beneath the bottom of the reservoir; however, the entity of the developed relative displacements (less than 1 cm) is modest and the plasticised zone does not interest the rock mass in contact with the pulvinus of the dam;

vi. in order to evaluate possible local plastic slips along laminated layers at the level of the right abutment (which appears to be the most exposed to this risk) the seismic performance of two rock wedges is studied with the modified 3D Newmark approach: earthquake-related displacements never exceed 6 cm (wedge W1 under Umbria-Marche earthquake). These results are obtained under very conservative hypotheses: zero cohesion on the discontinuities, uplift forces referring to the maximum regulation level and with simplified water pressure distribution and grout curtain attenuation effects, static thrust forces calculated via a conservative analytical approach and considered as independent from wedge movements, and a 1.4 amplification coefficient considered for topographic effects (i.e. corresponding to a bidimensional crest). Based on experience on similar dams, this level of displacement could be tolerated by the manufact, without collapse. With respect to the classic limit equilibrium method (Londe, 1973), which tends to be overconservative, the developed displacement-based approach is able to offer a more accurate and reliable insight into the seismic performance of the system.

Other spectrum-compatible earthquake recordings (like those used in **Chapter 2** for the displacement analysis of rock wedges) will be applied to the dam-water-foundation system of Ridracoli for different reservoir filling conditions. The model will also be tested against past events occurred in the vicinity of the dam (and therefore recorded by the network of accelerometers of the monitoring system).

In order to better represent all plasticity sources in the rock mass a ubiquitous joint model, like Abaqus® Jointed Material Model or Plaxis® Jointed Rock Model, may be applied to the inner rock-mass parts of the model, where non-linearities are accounted for.

The developed model is perfectly compatible with a previous developed structural model of the dam (Buffi, 2018), which explicitly considers the subdivision of the dam body in blocks and contraction joints. The longer-term objective is to completely integrate the two separate models in order to provide Romagna Acque – Società delle Fonti S.p.A. with a comprehensive tool to be used for the control of dam behaviour both in static conditions and after seismic events, to possibly immediately recognise early signs of an anomalous behaviour.

Appendix A

Three-directional acceleration time-history records at stations A, B, C, D in the local reference system of the dam (see **Figure 4.20**).

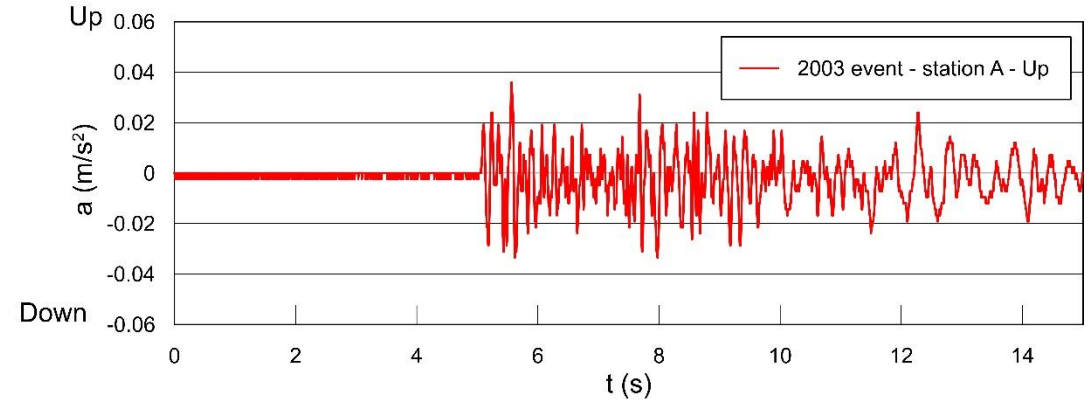

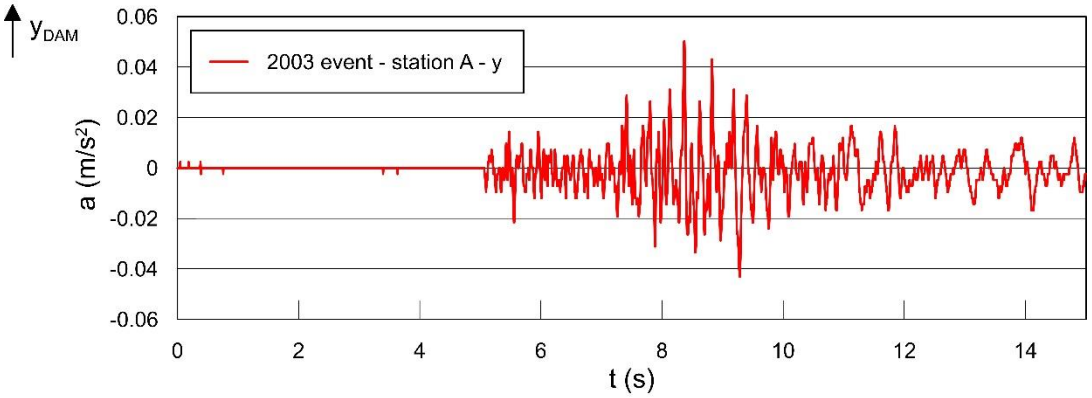

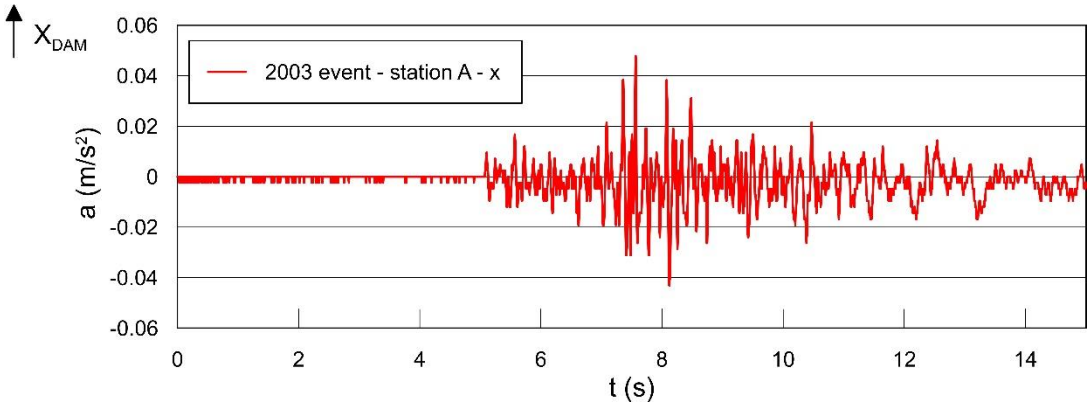

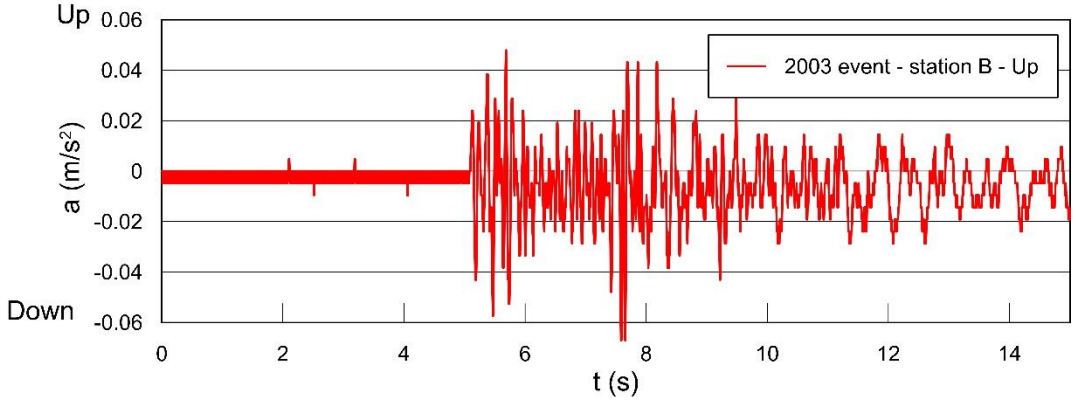
Up
Down
a (m/s²)
t (s)
2003 event - station B - Up
0.06
0.04
0.02
0
-0.02
-0.04
-0.06
0
2
4
6
8
10
12
14

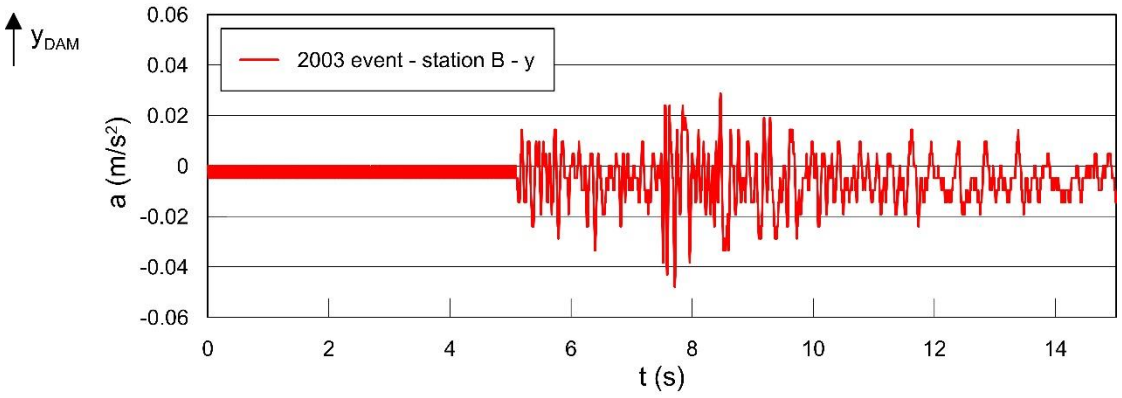
y_DAM
a (m/s²)
t (s)
2003 event - station B - y
0.06
0.04
0.02
0
-0.02
-0.04
-0.06
0
2
4
6
8
10
12
14

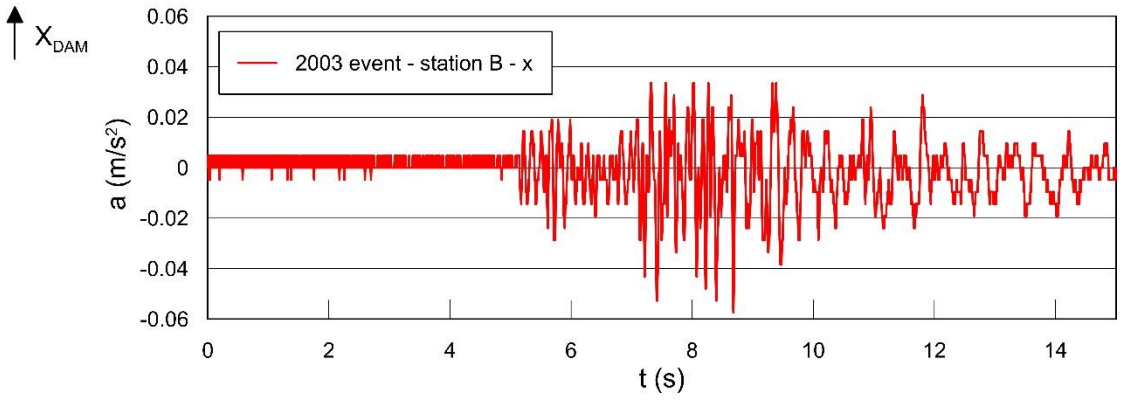
X_DAM
a (m/s²)
t (s)
2003 event - station B - x
0.06
0.04
0.02
0
-0.02
-0.04
-0.06
0
2
4
6
8
10
12
14

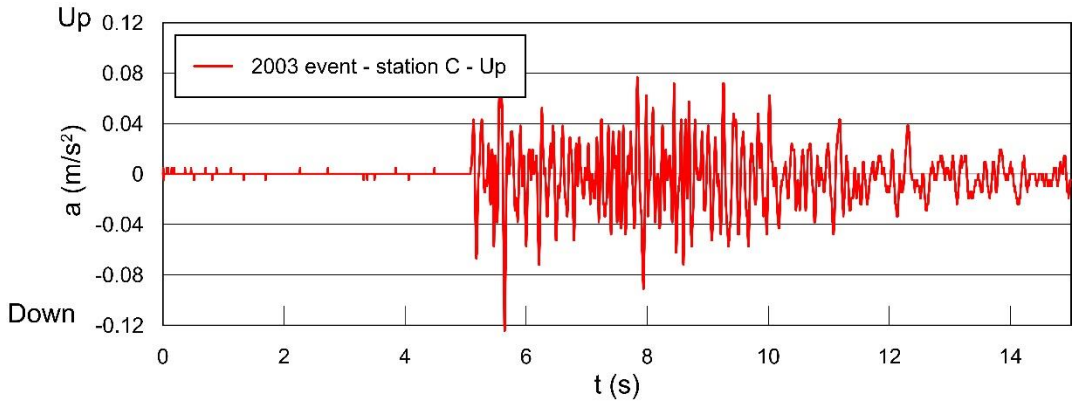
Up
Down
2003 event - station C - Up
a (m/s²)
0.12
0.08
0.04
0
-0.04
-0.08
-0.12
0
2
4
6
8
10
12
14
t (s)

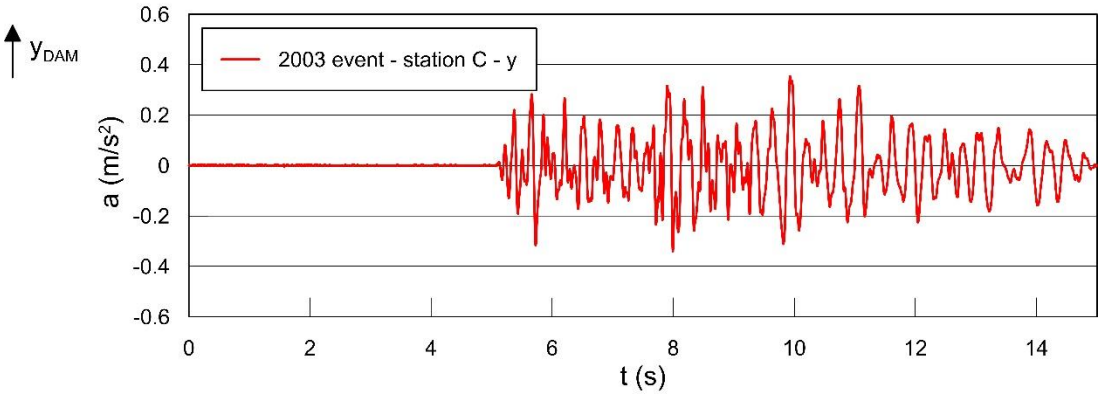
y_DAM
2003 event - station C - y
a (m/s²)
0.6
0.4
0.2
0
-0.2
-0.4
-0.6
0
2
4
6
8
10
12
14
t (s)

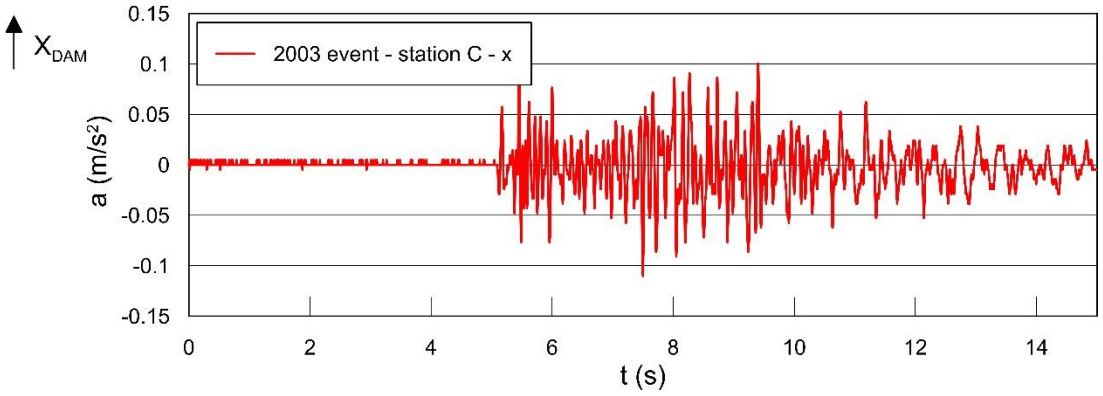
X_DAM
2003 event - station C - x
a (m/s²)
0.15
0.1
0.05
0
-0.05
-0.1
-0.15
0
2
4
6
8
10
12
14
t (s)

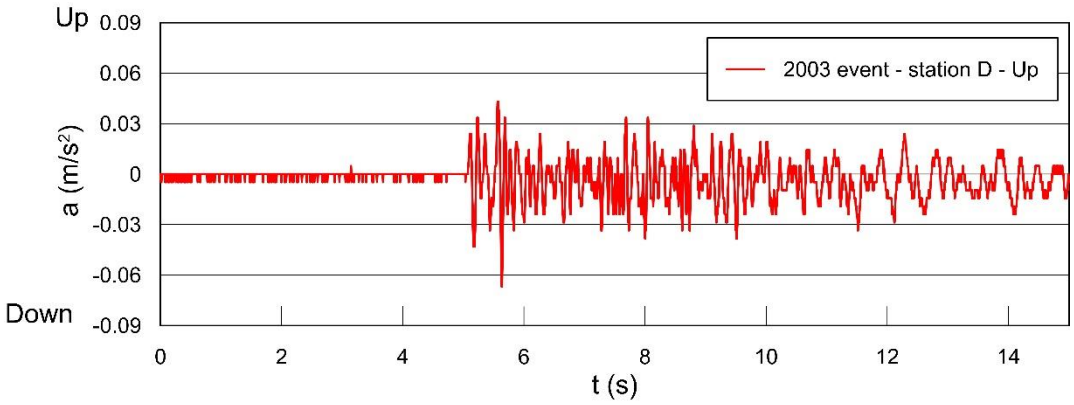
Up
Down
0.09
0.06
0.03
0
-0.03
-0.06
-0.09
a (m/s²)
2003 event - station D - Up
0
2
4
6
8
10
12
14
t (s)

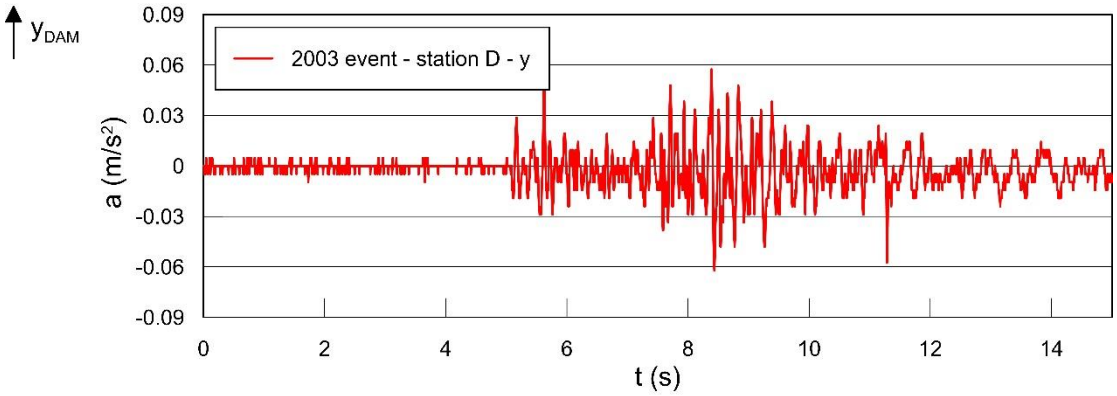
y_DAM
0.09
0.06
0.03
0
-0.03
-0.06
-0.09
a (m/s²)
2003 event - station D - y
0
2
4
6
8
10
12
14
t (s)

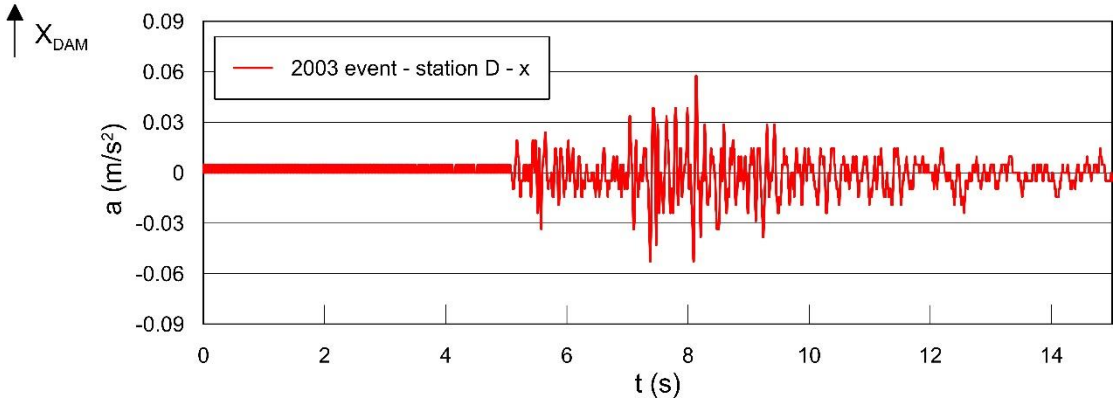
X_DAM
0.09
0.06
0.03
0
-0.03
-0.06
-0.09
a (m/s²)
2003 event - station D - x
0
2
4
6
8
10
12
14
t (s)

Appendix B

Matlab® program for transforming a contour-line based point cloud into a 2.5D grid of equally spaced points with associated an elevation value.

```
% program written by Edoardo Lusini(2022) Version 1.0
clc; clear; close all;
passo = 0.1
% import the DEM grid and the point cloud from contour lines (or point
cloud)
filename = 'countourlines.txt'; % import from .txt file
PC = importdata(filename); % import as structure data
PC = getfield( PC , 'data' ); % extract data in matrix format
filename = 'grid.txt';
grid = importdata(filename);
grid = getfield( PC , 'data' );
%% from contour lines to grid of equally spaced points
Z_updated = grid;
for j = 1:size(grid,1)
    r_value = grid(j,:);
    count = 0;
    Z = 0;
    Z_length = Z;
    D = 0;
    while ((Z*Z')/length(Z))^(1/2)==Z(1)
        count = count+1;
        R = count*passo;
        Z = 0;
        Z_length = Z;
        D = 0;
        for i = 1:size(PC,1)
            if (PC(i,1)-r_value(1,1))^2+(PC(i,2)-r_value(1,2))^2 <= R^2
                Z_length = Z_length+1;
                Z(Z_length) = PC(i,3);
                D(Z_length) = ((PC(i,1)-r_value(1,1))^2+(PC(i,2)-
r_value(1,2))^2)^(1/2);
            end
        end
    end
    for k = 1:length(D)
        if D(k) == 0
            D(k) = passo/1000;
        end
    end
    Z_updated(j,3) = (Z*(1./D)')/sum(1./D);
end
scatter3(Z_updated(:,1),Z_updated(:,2),Z_updated(:,3))
hold off
%% write the new DEM in a .txt file
filename = 'DEM10x10.txt';
PD10 = importdata(filename);
PD10 = getfield( PD10 , 'data' );
for i = 1:size(grid,1)
```

```
    for j = 1:size(PD10,1)
        if grid(i,1)==PD10(j,1) && grid(i,2)==PD10(j,2)
            PD10(j,:) = Z_updated(i,:);
        end
    end
end
%% write the new DEM in a .scr format (importable in Autocad)
output_file = 'new_points.scr';
fileID = fopen(output_file,'w');
fprintf(fileID,'%16s\n','_MULTIPLE _POINT');
for j = 1:size(PD10,1)
    fprintf(fileID,'%.0f',PD10(j,1));
    fprintf(fileID,'%1s',',');
    fprintf(fileID,'%.0f',PD10(j,2));
    fprintf(fileID,'%1s',',');
    fprintf(fileID,'%.4f\n',PD10(j,3));
end
fclose(fileID);
```

Appendix C

Abaqus® user-subroutine *amass1*

```
! ADDED MASS USER ELEMENT (amass_1) for Abaqus/Standard
! Written by Edoardo Lusini
! Version 1
! 2022

! user element to model the hydrodynamic
! pressure of reservoir on dam using
! added mass technique.

! properties:
!     props(1) = depth of reservoir
!     props(2) = y(2D) or z(3D) coordinate of water level
!     props(3) = density of water
!     props(4) = Zangar cm coefficient
!     jprops(1) = dimension of the element (1 or 2)
!     jprops(2) = integration points
!     jprops(3) =type of added mass formulation (1=Westergaard,2=Zangar)


! Element type:
! U23 : 3D Added mass shell  (nnode=4, nprops=4, njprops=3, mcrd=3,
ndofel=12, nsvars=1)

!DEC$ ATTRIBUTES ALIAS:"uel"::UEL

subroutine uel(rhs,amatrx,svars,energy,ndofel,nrhs,nsvars,&

      props,nprops,coords,mcrd,nnode,u,du,v,a,jtype,time,&

      dtime,kstep,kinc,jelem,params,ndload,jdltyp,adlmag,&

      predef,npredf,lflags,mlvarx,ddlmag,mdload,pnewdt,&
                        jprops,njprop,period)

      include 'ABA_PARAM.INC'

      integer, intent(in) :: mlvarx, ndofel, nrhs, nprops, nnode, nsvars
      integer, intent(in) :: njprop, mcrd, jtype, kstep, kinc, jelem
      integer, intent(in) :: ndload
      integer, intent(in) :: mdload, npredf
      integer, dimension(*), intent(in) :: lflags, jprops
      integer, dimension(mdload,*), intent(in) :: jdltyp
      real(8), intent(in) :: period, dtime
      real(8), dimension(2), intent(in) :: time
      real(8), dimension(nprops), intent(in) :: props
      real(8), dimension(*), intent(in) :: params
      real(8), dimension(2,npredf,nnode), intent(in) :: predef
      real(8), dimension(mdload,*), intent(in) :: ddlmag, adlmag
      real(8), dimension(ndofel), intent(in) :: u, v, a
```

```
real(8), dimension(mlvarx,*), intent(in) :: du
real(8), dimension(mcrd,nnode), intent(in) :: coords
real(8), intent(inout) :: pnewdt
real(8), dimension(8), intent(inout) :: energy
real(8), dimension(nsvars), intent(inout) :: svars
real(8), dimension(mlvarx,nrhs), intent(out) :: rhs
real(8), dimension(ndofel,ndofel), intent(out) :: amatrx


! Variables defined in amass1
integer :: i, j, ij, k, kintk, eldim, nintp, amtype
real(8) :: tmp, fi, teta, g, h, f, gval, dadu, beta
real(8) :: reservoir_depth, water_level, water_density
real(8), dimension(4) :: ds, rhob, wght
real(8), dimension(mcrd) :: bvec, cvec, nvec
real(8), dimension(nnode) :: shapef
real(8), dimension(ndofel) :: en
real(8), dimension(2,mcrd) :: amat
real(8), dimension(mcrd,nnode) :: isocoord
real(8), dimension(mcrd,mcrd) :: rot
real(8), dimension(mcrd,nnode) :: dshape
real(8), dimension(mcrd,ndofel) :: mshape
real(8), dimension(ndofel,mcrd) :: m, mm
real(8), dimension(ndofel,ndofel) :: massmat, mmm


! Parameters used in amass_1
real(8), parameter :: zero = 0.D0
real(8), parameter :: half = 0.5D0
real(8), parameter :: dmone = -1.0D0
real(8), parameter :: one = 1.0D0
real(8), parameter :: seven = 7.0D0
real(8), parameter :: eight = 8.0D0
real(8), parameter :: four = 4.0D0
real(8), parameter :: gauss = 0.577350269D0
real(8), parameter :: pi = 4.D0*datan(1.D0)
real(8), parameter :: twopi = 8.D0*datan(1.D0)

! EXECUTABLE SECTION

      reservoir_depth = props(1)
      water_level = props(2)
      water_density  = props(3)
      cm = props(4)
      eldim = jprops(1)
      nintp = jprops(2)
      amtype = jprops(3)

      if (nintp .eq. 1) then
            gval = zero
      elseif (nintp .eq. 4) then
            gval = gauss
      endif

      isocoord(1,1) = dmone
      isocoord(1,2) = one
      isocoord(1,3) = one
      isocoord(1,4) = dmone
      isocoord(2,1) = dmone
```

```
isocoord(2,2) = dmone
isocoord(2,3) = one
isocoord(2,4) = one
isocoord(3,1) = dmone
isocoord(3,2) = dmone
isocoord(3,3) = dmone
isocoord(3,4) = dmone

wght(1) = one
wght(2) = one
wght(3) = one
wght(4) = one

if (nintp .eq. 1) then
      wght(1) = four
elseif (nintp .eq. 4) then
      wght(1) = one
endif

do j = 1, ndofel
      do i = 1, ndofel
            massmat(i,j) = zero
      enddo
enddo
do kintk =1, nintp
      ! shape functions
      ! determine (g,h)
      g = isocoord(1,kintk)*gval
      h = isocoord(2,kintk)*gval
      f = isocoord(3,kintk)
      ! shape functions
      shapef(1) = (one - g)*(one - h)*(one-f)/eight;
      shapef(2) = (one + g)*(one - h)*(one-f)/eight;
      shapef(3) = (one + g)*(one + h)*(one-f)/eight;
      shapef(4) = (one - g)*(one + h)*(one-f)/eight;
      ! derivative d(Ni)/d(g)
      dshape(1,1) = -(one - h)*(one-f)/eight;
      dshape(1,2) =  (one - h)*(one-f)/eight;
      dshape(1,3) =  (one + h)*(one-f)/eight;
      dshape(1,4) = -(one + h)*(one-f)/eight;
      ! derivative d(Ni)/d(h)
      dshape(2,1) = -(one - g)*(one-f)/eight;
      dshape(2,2) = -(one + g)*(one-f)/eight;
      dshape(2,3) =  (one + g)*(one-f)/eight;
      dshape(2,4) =  (one - g)*(one-f)/eight;
      ! assemble shape matrix mshape
      do j = 1, ndofel
            do i = 1, mcrd
                  mshape(i,j) = zero
            enddo
      enddo
      do j = 1, nnode
            do i = 1, mcrd
                  ij = mcrd*(j-1)+i
                  mshape(i,ij) = shapef(j)
            enddo
      enddo

      ! print *, 'mshape(1,1) = ',mshape(1,1)   ! Debug
```

```
                  ! print *, 'mshape(2,5) = ',mshape(2,5)    ! Debug
                  ! print *, 'mshape(3,9) = ',mshape(3,9)    ! Debug


! sides of the infinite area (amat)
                  do j = 1, mcrd
                        do i = 1, eldim
                              tmp = zero
                              do k= 1, nnode
                                    tmp = tmp + dshape(i,k)*coords(j,k)
                              enddo
                              amat(i,j) = tmp
                        enddo
                  enddo

                  ! global coordinate of integration point (bvec)
                  do i= 1, mcrd
                        tmp = zero
                        do k= 1, nnode
                              tmp = tmp + shapef(k) * coords(i,k)
                        enddo
                        bvec(i) = tmp
                  enddo

                  ! vector product of side vectors (normal vector)
                  cvec(1) = amat(1,2)*amat(2,3) - amat(1,3)*amat(2,2)
                  cvec(2) = amat(1,3)*amat(2,1) - amat(1,1)*amat(2,3)
                  cvec(3) = amat(1,1)*amat(2,2) - amat(1,2)*amat(2,1)
                  ! normal unit vector and infinite area
                  tmp = zero
                  do i = 1, mcrd
                        tmp = tmp + cvec(i)*cvec(i)
                  enddo
                  tmp = sqrt(tmp)
                  do i = 1, mcrd
                        nvec(i) = cvec(i)/tmp
                  enddo
                  ds(kintk) = tmp

                  ! print *, 'ds = ', ds(kintk)             ! Debug


                  if (bvec(3).gt.water_level) then
                     rhob (kintk) = zero
               else
                  if (amtype .eq. 1) then
                        ! Westergaard original formulation
                         tmp = reservoir_depth*(water_level-bvec(3))
                         rhob(kintk)=water_density*seven/eight*sqrt(tmp)
                  else
                        ! Zangar formulation
                        tmp = (water_level-bvec(3))/reservoir_depth
                        tmp = tmp*(2-tmp)
                        rhob (kintk) = water_density*reservoir_depth* &
                                       (cm/2)*(tmp+sqrt(tmp))
                     endif
               endif

                  ! print *, 'rhob = ', rhob(kintk)         ! Debug
```

```
 ! partial 3D rotation matrix

 if (nvec(1).ge.zero .and. nvec(2).ge.zero) then
       tmp = zero
 elseif (nvec(1).ge.zero .and. nvec(2).lt.zero) then
       tmp = twopi
 else
       tmp = pi
 endif

if (nvec(1).eq.zero .and. nvec(2).eq.zero) then
    fi = zero
    teta = -(pi/2)*nvec(3)/abs(nvec(3))
elseif (nvec(1).eq.zero .and. nvec(2).ne.zero) then
    fi = zero
    teta = -atan(nvec(3)/sqrt(nvec(1)**2 + nvec(2)**2))
else
    fi = atan(nvec(2)/nvec(1))-tmp
    teta = -atan(nvec(3)/sqrt(nvec(1)**2 + nvec(2)**2))
endif

 do j = 1, mcrd
       do i = 1, mcrd
             rot(i,j) = zero
       enddo
 enddo
 rot(1,1) = cos(fi)*cos(teta)
 rot(2,1) = sin(fi)*cos(teta)
 rot(3,1) = -sin(teta)

 ! print *, 'rot(2,1) = ', rot(2,1)        ! Debug

 ! mshape'*rot
 do j = 1, mcrd
       do i = 1, ndofel
             tmp = zero
             do k = 1, mcrd
                   tmp = tmp + mshape(k,i) * rot(k,j)
             enddo
             m(i,j) = tmp
       enddo
 enddo

 ! m*rot'
 do j = 1, mcrd
       do i = 1, ndofel
             tmp = zero
             do k = 1, mcrd
                   tmp = tmp + m(i,k) * rot(j,k)
             enddo
             mm(i,j) = tmp
       enddo
 enddo

 ! mm*mshape
 do j = 1, ndofel
       do i = 1, ndofel
             tmp = zero
             do k= 1, mcrd
```

```
                                    tmp = tmp + mm(i,k) * mshape(k,j)
                              enddo
                              mmm(i,j) = tmp
                        enddo
                  enddo


! mass matrix calculation
                  do j = 1, ndofel
                        do i = 1, ndofel
                              massmat(i,j) = massmat(i,j) + &
                              mmm(i,j)*wght(kintk)*ds(kintk)*rhob(kintk)
                        enddo
                  enddo
            enddo

            ! print *, 'massmat(1,1) = ', massmat(1,1)            !Debug


            ! initialize rhs and amatrix with zeros
            do i = 1, ndofel
                  do j = 1, nrhs
                        rhs(i,j) = zero
                  enddo
                  do k = 1, ndofel
                        amatrx(k,i) = zero
                  enddo
            enddo
            ! assign zeros to svars (nvars = 1)
            do i = 1, nsvars
                  svars(i) = zero
            enddo
            ! choice of type of analysis
            if (lflags(3).eq.1) then
                  ! normal incrementation
                  if (lflags(1).eq.11.or.lflags(1).eq.12) then
                  ! *dynamic
                        beta  = params(2)
                        dadu = one/(beta*dtime**2)
                        do j = 1, ndofel
                              do i = 1, ndofel
                                    amatrx(i,j) = massmat(i,j) * dadu
                              enddo
                        enddo
                        do i = 1, ndofel
                              tmp = zero
                              do k = 1, ndofel
                                    tmp = tmp + massmat(i,k) * a(k)
                              enddo
                              rhs(i,1) = rhs(i,1) - tmp
                        enddo
                        do i = 1, ndofel
                              tmp = zero
                              do k = 1, ndofel
                                    tmp = tmp + massmat(i,k) * v(k)
                              enddo
                              en(i) = tmp
                        enddo
                        tmp = zero
```

```
                        do i = 1, ndofel
                              tmp = tmp + v(i)*en(i)
                        enddo
                        energy(1)= half*tmp
                  endif

elseif (lflags(3).eq.4) then
                  ! mass matrix
                  do j = 1, ndofel
                        do i = 1, ndofel
                              amatrx(i,j) = massmat(i,j)
                        enddo
                  enddo
            elseif (lflags(3).eq.5) then
                  ! half-step residual calculation
                  do i = 1, ndofel
                        tmp = zero
                        do k = 1, ndofel
                              tmp = tmp + massmat(i,k) * a(k)
                        enddo
                        rhs(i,1) = rhs(i,1) - tmp
                  enddo
            elseif (lflags(3).eq.6) then
                  ! initial acceleration calculation
                  do j = 1, ndofel
                        do i = 1, ndofel
                              amatrx(i,j) = massmat(i,j)
                        enddo
                  enddo
                  do i = 1, ndofel
                        tmp = zero
                        do k = 1, ndofel
                              tmp = tmp + massmat(i,k)*v(k)
                        enddo
                        en(i) = tmp
                  enddo
                  tmp = zero
                  do i = 1, ndofel
                        tmp = tmp + v(i)*en(i)
                  enddo
                  energy(1)= half*tmp
            endif

      end subroutine uel
```

Appendix D

Abaqus® user-subroutine *fric1*

```
! FRICTION PROPERTY (fric1) for Abaqus/Standard
! Written by Edoardo Lusini
! Version 1
! 2022

!DEC$ ATTRIBUTES ALIAS:"fric"::FRIC

      subroutine fric(lm,tau,ddtddg,ddtddp,dslip,sed,sfd,&
          ddtdt,pnewdt,statev,dgam,taulm,press,dpress,ddpddh,&
          slip,kstep,kinc,time,dtime,noel,ciname,slname,&
          msname,coords,rcoord,drot,temp,&
          predef,nfdir,mcrd,npred,nstatv,chrlngth,props,nprops)

      include 'ABA_PARAM.INC'

      character (len=80), intent(in) :: ciname,slname,msname
      integer, intent(inout) :: lm
      integer, intent(in) :: nprops,nstatv,npred,mcrd,nfdir,kstep,kinc
      integer, intent(in) :: noel
      real(8), intent(in) :: chrlngth,press,dpress,ddpddh,dtime
      real(8), intent(inout) :: sed,pnewdt
      real(8), intent(out) :: sfd
      real(8), dimension(2), intent(in) :: time,temp
      real(8), dimension(2,2), intent(in) :: drot
      real(8), dimension(2,*), intent(in) :: predef
      real(8), dimension(*), intent(inout) :: statev
      real(8), dimension(nprops), intent(in) :: props
      real(8), dimension(mcrd), intent(in) :: coords,rcoord
      real(8), dimension(nfdir), intent(in) :: dgam,taulm,slip
      real(8), dimension(nfdir), intent(inout) :: tau,dslip
      real(8), dimension(nfdir), intent(out) :: ddtddp
      real(8), dimension(nfdir,2), intent(out) :: ddtdt
      real(8), dimension(nfdir,nfdir), intent(out) :: ddtddg

      real(8) :: xmu,xc,gammaw,gcrit,stiff,taucrit,gcritp,dynt,hew
      real(8) :: upress,epress,taueqv,gameqv,dgsleq,tmp,tmp1
      real(8), dimension(2) :: gamma

      real(8), parameter :: zero = 0.0d0
      real(8), parameter :: one = 1.0d0
      real(8), parameter :: two = 2.0d0
      real(8), parameter :: asmall = 1.0d-27
      real(8), parameter :: precis=1.d-14
      real(8), parameter :: xks=1.d6
      real(8), parameter :: row=1.0d3
      real(8), parameter :: grav=9.81d0


    ! print *, 'nstatv = ',nstatv
    ! print *, 'nprops = ',nprops
```

```
    ! print *, 'ciname = ',ciname
    ! print *, 'props1 = ',props(1)
    ! print *, 'coords1 = ',coords(1)
    ! print *, 'coords2 = ',coords(2)
    ! print *, 'coords3 = ',coords(3)

!
!     IMPLEMENTATION OF 3-D COULOMB FRICTION IN TERMS OF EFFECTIVE
STRESSES USING PENALTY METHOD
!
!     VARIABLES USED:
!        XMU = COEFFICIENT OF FRICTION
!        XC = COHESION
!        GAMMAW = WATER SPECIFIC
!        GCRIT = CRITICAL ELASTIC SLIP
!        STIFF = ARTIFICIAL STIFFNESS
!        GAMMA(1:2) = TOTAL SLIP
!        STATEV(1:2) = ELASTIC SLIP
!        STATEV(3) = PREVIUS DPRESS
!        TAUCRIT = CRITICAL FRICTIONAL STRESS
!
      XMU = PROPS(1)
      XC = PROPS(2)
      HEW  = PROPS(3)
      DYNT = PROPS(4)
      GCRITP = PROPS(5)
!
      IF (COORDS(3).LE.HEW) THEN
         GAMMAW = ROW*GRAV
      ELSE
         GAMMAW = ZERO
      END IF
      GAMMAW = ROW*GRAV
      UPRESS  = GAMMAW*(HEW-COORDS(3))
!
      EPRESS  = PRESS-UPRESS
!
      IF (LM.EQ.2) THEN
!
!      GAP IS OPENED AT START OF THE CURRENT INCREMENT
!
         IF (XMU.LE.PRECIS) RETURN
      END IF
      LM    = 0
      GCRIT = GCRITP*CHRLNGTH
!
!                   CHECK IF PRESSURE IS NON-POSITIVE
!
      IF (EPRESS.LE.ZERO) THEN
         LM = 2
         RETURN
      ELSE
!
!                      COMPUTE FOR CRITICAL STRESS
!                      AND ARTIFICIAL STIFFNESS
!
         TAUCRIT = XMU*EPRESS+XC
         STIFF   = TAUCRIT/GCRIT
      ENDIF
```

```
!
!                    COMPUTE FOR THE TOTAL SLIP,
!                    FRICTIONAL SHEAR STRESS,
!                    AND THE EQUIVALENT SHEAR STRESS
!
      GAMMA(1) = STATEV(1) + DGAM(1)
      GAMMA(2) = STATEV(2) + DGAM(2)
      TAU(1) = STIFF*GAMMA(1)
      TAU(2) = STIFF*GAMMA(2)
      TAUEQV = SQRT(TAU(1)**2 + TAU(2)**2)
!
!                    CHECK IF THE FRICTIONAL STRESS
!                    EXCEEDS THE CRITICAL STRESS
!
      IF (TAUEQV.LT.TAUCRIT) THEN
!
!                       BEHAVIOR REMAINS ELASTIC
!
         STATEV(1)   = GAMMA(1)
         STATEV(2)   = GAMMA(2)
         DDTDDG(1,1) = STIFF
         DDTDDG(1,2) = ZERO
         DDTDDG(2,1) = ZERO
         DDTDDG(2,2) = STIFF
         DDTDDP(1)   = XMU*GAMMA(1)/GCRIT
         DDTDDP(2)   = XMU*GAMMA(1)/GCRIT
         DSLIP(1)    = ZERO
         DSLIP(2)    = ZERO
      ELSE
!
!                       BEHAVIOR IS PLASTIC
!
         GAMEQV = SQRT(GAMMA(1)**2 + GAMMA(2)**2)
         TAU(1) = GAMMA(1)*TAUCRIT/GAMEQV
         TAU(2) = GAMMA(2)*TAUCRIT/GAMEQV
         DDTDDG(1,1) = TAUCRIT/GAMEQV*(1-(GAMMA(1)/GAMEQV)**2)
         DDTDDG(1,2) = -
TAUCRIT/GAMEQV*(GAMMA(1)/GAMEQV)*(GAMMA(2)/GAMEQV)
         DDTDDG(2,1) = DDTDDG(1,2)
         DDTDDG(2,2) = TAUCRIT/GAMEQV*(1-(GAMMA(2)/GAMEQV)**2)
         DDTDDP(1)   = XMU*GAMMA(1)/GAMEQV
         DDTDDP(2)   = XMU*GAMMA(1)/GAMEQV
!
!                       COMPUTATION OF THE ELASTIC
!                       AND PLASTIC SLIP
!
         STATEV(1)   = GAMMA(1)*GCRIT/GAMEQV
         STATEV(2)   = GAMMA(2)*GCRIT/GAMEQV
         DGSLEQ      = GAMEQV - GCRIT
         DSLIP(1) = GAMMA(1)*DGSLEQ/GAMEQV
         DSLIP(2) = GAMMA(2)*DGSLEQ/GAMEQV
      ENDIF
      RETURN
      END SUBROUTINE FRIC
```

Appendix E

Fortran® program addedmasstest.f90 written for testing *amass1*

```
program addedmasstest

      implicit none

      integer :: i, k
      integer :: pmlvarx, pndofel, pnrhs, pnprops, pnnode, pnsvars
      integer :: pnjprop, pmcrd, pjtype
      integer, dimension(3) :: plflags, pjprops
      real(8) :: pdtime, ptmp
      real(8), dimension(4) :: pprops
      real(8), dimension(2) :: pparams
      real(8), dimension(12) :: pv, pa
      real(8), dimension(3,4) :: pcoords
      real(8), dimension(8) :: penergy
      real(8) :: psvars
      real(8), dimension(12,1) :: prhs, pforce
      real(8), dimension(12,12) :: pamatrx

      ! Initialise integers
      pmlvarx = 12
      pndofel = 12
      pnrhs = 1
      pnprops = 4
      pnnode = 4
      pnsvars = 1
      pnjprop = 3
      pmcrd = 3
      pjtype = 23
      plflags(1) = 11
      plflags(2) = 0
      plflags(3) = 4
      pjprops(1) = 2
      pjprops(2) = 1
      pjprops(3) = 1

      ! Initialise real
      pdtime = 0.005D0
      pprops(1) = 10D0
      pprops(2) = 10D0
      pprops(3) = 1000D0
     pprops(4) = 0.69D0
      pparams(1) = 0D0
      pparams(2) = 0.25D0
      psvars = 0D0
      do i=1,pndofel
            pv(i) = 0D0
            pa(i) = 0D0
      enddo
      pa(1) = 10D0
```

```
      pa(4) = 10D0
      pa(7) = 10D0
      pa(10) = 10D0
      pv(1) = 10D0
      pv(2) = 10D0
      do i=1,8
            penergy(i) = 0D0
      enddo
      pcoords(1,1) = -1.D0
      pcoords(1,2) = 1.D0
      pcoords(1,3) = 1.D0
      pcoords(1,4) = -1.D0
      pcoords(2,1) = -1.D0
      pcoords(2,2) = -1.D0
      pcoords(2,3) = 1.D0
      pcoords(2,4) = 1.D0
      pcoords(3,1) = 2.D0
      pcoords(3,2) = 0.D0
      pcoords(3,3) = 0.D0
      pcoords(3,4) = 2.D0

      call uel(prhs,pamatrx,psvars,penergy,pndofel,pnrhs,pnsvars,&
                  pprops,pnprops,pcoords,pmcrd,pnnode,pv,pa,pjtype,&
                  pdtime,pparams,plflags,pmlvarx,pjprops,pnjprop)

      do i = 1, pndofel
            ptmp = 0.D0
            do k = 1, pndofel
                  ptmp = ptmp + pamatrx(i,k) * pa(k)
            enddo
            pforce(i,1) = ptmp
      enddo

      ! print *, 'energy(1) = ', penergy(1)
      ! print *, 'rhs(2,1) = ', prhs(2,1)
      ! print *, 'rhs(12,1) = ', prhs(12,1)
      ! print *, 'M(12,1) = ', pamatrx(12,1)
      ! print *, 'M(3,3) = ', pamatrx(3,3)
      ! print *, 'M(12,12) = ', pamatrx(12,12)
      print *, 'force(1,1) = ', pforce(1,1)
      print *, 'force(2,1) = ', pforce(2,1)
      print *, 'force(3,1) = ', pforce(3,1)
      print *, 'force(4,1) = ', pforce(4,1)
      print *, 'force(5,1) = ', pforce(5,1)
      print *, 'force(6,1) = ', pforce(6,1)
      print *, 'force(7,1) = ', pforce(7,1)
      print *, 'force(8,1) = ', pforce(8,1)
      print *, 'force(9,1) = ', pforce(9,1)
      print *, 'force(10,1) = ', pforce(10,1)
      print *, 'force(11,1) = ', pforce(11,1)
      print *, 'force(12,1) = ', pforce(12,1)

end program addedmasstest
```

```
subroutine uel(rhs,amatrx,svars,energy,ndofel,nrhs,nsvars,&
                        props,nprops,coords,mcrd,nnode,v,a,jtype,&
                        dtime,params,lflags,mlvarx,jprops,njprop)

      integer, intent(in) :: mlvarx, ndofel, nrhs, nprops, nnode, nsvars
      integer, intent(in) :: njprop, mcrd, jtype
      integer, dimension(*), intent(in) :: lflags, jprops
      real(8), intent(in) :: dtime
      real(8), dimension(nprops), intent(in) :: props
      real(8), dimension(*), intent(in) :: params
      real(8), dimension(ndofel), intent(in) :: v, a
      real(8), dimension(mcrd,nnode), intent(in) :: coords
      real(8), dimension(8), intent(inout) :: energy
      real(8), dimension(nsvars), intent(inout) :: svars
      real(8), dimension(mlvarx,nrhs), intent(out) :: rhs
      real(8), dimension(ndofel,ndofel), intent(out) :: amatrx

      ! Variables used in amass1
      integer :: i, j, ij, k, kintk, eldim, nintp, amtype
      real(8) :: tmp, fi, teta, g, h, f, gval, dadu, beta
      real(8) :: reservoir_depth, water_level, water_density
      real(8), dimension(4) :: ds, rhob, wght
      real(8), dimension(mcrd) :: bvec, cvec, nvec
      real(8), dimension(nnode) :: shapef
      real(8), dimension(ndofel) :: en
      real(8), dimension(2,mcrd) :: amat
      real(8), dimension(mcrd,nnode) :: isocoord
      real(8), dimension(mcrd,mcrd) :: rot
      real(8), dimension(mcrd,nnode) :: dshape
      real(8), dimension(mcrd,ndofel) :: mshape
      real(8), dimension(ndofel,mcrd) :: m, mm
      real(8), dimension(ndofel,ndofel) :: massmat, mmm

      ! Parameters defined in amass1
      real(8), parameter :: zero = 0.D0
      real(8), parameter :: half = 0.5D0
      real(8), parameter :: dmone = -1.0D0
      real(8), parameter :: one = 1.0D0
      real(8), parameter :: four = 4.0D0
      real(8), parameter :: seven = 7.0D0
      real(8), parameter :: eight = 8.0D0
      real(8), parameter :: gauss = 0.577350269D0
      real(8), parameter :: pi = 4.D0*datan(1.D0)
      real(8), parameter :: twopi = 8.D0*datan(1.D0)


! EXECUTABLE SECTION
      ! condition for entering added mass partition in the complete
      ! subroutine ffuel3_amass_1
      if (jtype .eq. 23) then

      ! user element to model the hydrodynamic
      ! pressure of reservoir on dam using
      ! added mass technique.

      ! properties:
      !     props(1) = depth of reservoir
      !     props(2) = y(2D) or z(3D) coordinate of water level
      !     props(3) = density of water
```

```
!     props(4) = Zangar cm coefficient
!     jprops(1) = dimension of the element (1 or 2)
!     jprops(2) = integration points
!     jprops(3) = type of added mass formulation (1 = Westergaard,
!                 2 = Zangar)


      reservoir_depth = props(1)
      water_level = props(2)
      water_density  = props(3)
      cm = props(4)
      eldim = jprops(1)
      nintp = jprops(2)
      amtype = jprops(3)

      if (nintp .eq. 1) then
            gval = zero
      elseif (nintp .eq. 4) then
            gval = gauss
      endif

      isocoord(1,1) = dmone
      isocoord(1,2) = one
      isocoord(1,3) = one
      isocoord(1,4) = dmone
      isocoord(2,1) = dmone
      isocoord(2,2) = dmone
      isocoord(2,3) = one
      isocoord(2,4) = one
      isocoord(3,1) = dmone
      isocoord(3,2) = dmone
      isocoord(3,3) = dmone
      isocoord(3,4) = dmone

      wght(1) = one
      wght(2) = one
      wght(3) = one
      wght(4) = one

      if (nintp .eq. 1) then
            wght(1) = four
      elseif (nintp .eq. 4) then
            wght(1) = one
      endif

      do j = 1, ndofel
            do i = 1, ndofel
                  massmat(i,j) = zero
            enddo
      enddo
      do kintk =1, nintp
            ! shape functions
            ! determine (g,h)
            g = isocoord(1,kintk)*gval
            h = isocoord(2,kintk)*gval
            f = isocoord(3,kintk)
            ! shape functions
            shapef(1) = (one - g)*(one - h)*(one-f)/eight;
            shapef(2) = (one + g)*(one - h)*(one-f)/eight;
```

```
shapef(3) = (one + g)*(one + h)*(one-f)/eight;
shapef(4) = (one - g)*(one + h)*(one-f)/eight;
! derivative d(Ni)/d(g)
dshape(1,1) = -(one - h)*(one-f)/eight;
dshape(1,2) =  (one - h)*(one-f)/eight;
dshape(1,3) =  (one + h)*(one-f)/eight;
dshape(1,4) = -(one + h)*(one-f)/eight;
! derivative d(Ni)/d(h)
dshape(2,1) = -(one - g)*(one-f)/eight;
dshape(2,2) = -(one + g)*(one-f)/eight;
dshape(2,3) =  (one + g)*(one-f)/eight;
dshape(2,4) =  (one - g)*(one-f)/eight;
! assemble shape matrix mshape
do j = 1, ndofel
      do i = 1, mcrd
            mshape(i,j) = zero
      enddo
enddo
do j = 1, nnode
      do i = 1, mcrd
            ij = mcrd*(j-1)+i
            mshape(i,ij) = shapef(j)
      enddo
enddo

! print *, 'mshape(1,1) = ',mshape(1,1)   ! Debug
! print *, 'mshape(2,5) = ',mshape(2,5)   ! Debug
! print *, 'mshape(3,9) = ',mshape(3,9)   ! Debug

! sides of the infinite area (amat)
do j = 1, mcrd
      do i = 1, eldim
            tmp = zero
            do k= 1, nnode
                  tmp = tmp + dshape(i,k)*coords(j,k)
            enddo
            amat(i,j) = tmp
      enddo
enddo

! global coordinate of integration point (bvec)
do i= 1, mcrd
      tmp = zero
      do k= 1, nnode
            tmp = tmp + shapef(k) * coords(i,k)
      enddo
      bvec(i) = tmp
enddo

! vector product of side vectors (normal vector)
cvec(1) = amat(1,2)* amat(2,3) - amat(1,3) * amat(2,2)
cvec(2) = amat(1,3)* amat(2,1) - amat(1,1) * amat(2,3)
cvec(3) = amat(1,1)* amat(2,2) - amat(1,2) * amat(2,1)
! normal unit vector and infinite area
tmp = zero
do i = 1, mcrd
      tmp = tmp + cvec(i)*cvec(i)
enddo
tmp = sqrt(tmp)
```

```
                do i = 1, mcrd
                      nvec(i) = cvec(i)/tmp
                enddo
                ds(kintk) = tmp

                ! print *, 'ds = ', ds(kintk)             ! Debug


                if (bvec(3).gt.water_level) then
                   rhob (kintk) = zero
                else
                   if (amtype .eq. 1) then
                      ! Westergaard original formulation
                      tmp = reservoir_depth*(water_level-bvec(3))
                      rhob(kintk)=water_density*seven/eight*sqrt(tmp)
                else
                      ! Zangar formulation
                      tmp = (water_level-bvec(3))/reservoir_depth
                      tmp = tmp*(2-tmp)
                      rhob (kintk) = water_density*reservoir_depth* &
(cm/2)*(tmp+sqrt(tmp))
                endif
             endif

                ! print *, 'rhob = ', rhob(kintk)          ! Debug

                ! partial 3D rotation matrix

                if (nvec(1).ge.zero .and. nvec(2).ge.zero) then
                      tmp = zero
                elseif (nvec(1).ge.zero .and. nvec(2).lt.zero) then
                      tmp = twopi
                else
                      tmp = pi
                endif

               if (nvec(1).eq.zero .and. nvec(2).eq.zero) then
                   fi = zero
                   teta = -(pi/2)*nvec(3)/abs(nvec(3))
               elseif (nvec(1).eq.zero .and. nvec(2).ne.zero) then
                   fi = zero
                   teta = -atan(nvec(3)/sqrt(nvec(1)**2 + nvec(2)**2))
               else
                   fi = atan(nvec(2)/nvec(1))-tmp
                   teta = -atan(nvec(3)/sqrt(nvec(1)**2 + nvec(2)**2))
               endif

                do j = 1, mcrd
                      do i = 1, mcrd
                            rot(i,j) = zero
                      enddo
                enddo
                rot(1,1) = cos(fi)*cos(teta)
                rot(2,1) = sin(fi)*cos(teta)
                rot(3,1) = -sin(teta)

                ! print *, 'rot(2,1) = ', rot(2,1)         ! Debug

                ! mshape'*rot
```

```
                do j = 1, mcrd
                      do i = 1, ndofel
                            tmp = zero
                            do k = 1, mcrd
                                  tmp = tmp + mshape(k,i) * rot(k,j)
                            enddo
                            m(i,j) = tmp
                      enddo
                enddo

                ! m*rot'
                do j = 1, mcrd
                      do i = 1, ndofel
                            tmp = zero
                            do k = 1, mcrd
                                  tmp = tmp + m(i,k) * rot(j,k)
                            enddo
                            mm(i,j) = tmp
                      enddo
                enddo

                ! mm*mshape
                do j = 1, ndofel
                      do i = 1, ndofel
                            tmp = zero
                            do k= 1, mcrd
                                  tmp = tmp + mm(i,k) * mshape(k,j)
                            enddo
                            mmm(i,j) = tmp
                      enddo
                enddo

                ! mass matrix calculation
                do j = 1, ndofel
                      do i = 1, ndofel
                            massmat(i,j) = massmat(i,j) + &
mmm(i,j)*wght(kintk)*ds(kintk)*rhob(kintk)
                      enddo
                enddo
          enddo

          print *, 'massmat(1,1) = ', massmat(1,1)        ! Debug

          ! initialize rhs and amatrix with zeros
          do i = 1, ndofel
                do j = 1, nrhs
                      rhs(i,j) = zero
                enddo
                do k = 1, ndofel
                      amatrx(k,i) = zero
                enddo
          enddo
          ! assign zeros to svars (nvars = 1)
          do i = 1, nsvars
                svars(i) = zero
          enddo
          ! choice of type of analysis
          if (lflags(3).eq.1) then
                ! normal incrementation
```

```
      if (lflags(1).eq.11.or.lflags(1).eq.12) then
      ! *dynamic
            beta  = params(2)
            dadu = one/(beta*dtime**2)
            do j = 1, ndofel
                  do i = 1, ndofel
                        amatrx(i,j) = massmat(i,j) * dadu
                  enddo
            enddo
            do i = 1, ndofel
                  tmp = zero
                  do k = 1, ndofel
                        tmp = tmp + massmat(i,k) * a(k)
                  enddo
                  rhs(i,1) = rhs(i,1) - tmp
            enddo
            do i = 1, ndofel
                  tmp = zero
                  do k = 1, ndofel
                        tmp = tmp + massmat(i,k) * v(k)
                  enddo
                  en(i) = tmp
            enddo
            tmp = zero
            do i = 1, ndofel
                  tmp = tmp + v(i)*en(i)
            enddo
            energy(1)= half*tmp
      endif
elseif (lflags(3).eq.4) then
      ! mass matrix
      do j = 1, ndofel
            do i = 1, ndofel
                  amatrx(i,j) = massmat(i,j)
            enddo
      enddo
elseif (lflags(3).eq.5) then
      ! half-step residual calculation
      do i = 1, ndofel
            tmp = zero
            do k = 1, ndofel
                  tmp = tmp + massmat(i,k) * a(k)
            enddo
            rhs(i,1) = rhs(i,1) - tmp
      enddo
elseif (lflags(3).eq.6) then
      ! initial acceleration calculation
      do j = 1, ndofel
            do i = 1, ndofel
                  amatrx(i,j) = massmat(i,j)
            enddo
      enddo
      do i = 1, ndofel
            tmp = zero
            do k = 1, ndofel
                  tmp = tmp + massmat(i,k)*v(k)
            enddo
            en(i) = tmp
      enddo
```

```
                  tmp = zero
                  do i = 1, ndofel
                        tmp = tmp + v(i)*en(i)
                  enddo
                  energy(1)= half*tmp
            endif
      endif
end subroutine uel
```

Appendix F

The testing problem is modified from the Abaqus® online Example Problem Manual referenced in **Chapter 4**. A simple 2D user subroutine implementing an added mass finite element, addedmass_uel.f, is made available for download together with the input file of the example problem. The case study of Koyna dam is considered, which was subjected to an earthquake of magnitude 6.5 on the Richter scale on December 11, 1967. While in the original version, that can be found in the online manual, the application of the Abaqus® concrete damaged plasticity material model is included, in the testing problem here presented a simple linear elastic material with viscous damping is preferred for sake of simplicity (with Rayleigh coefficients borrowed from Ridracoli Dam values). All material parameters are given in **Table F.1**.

Table F.1. Material properties assigned to the Koyna Dam monolith.

	Mass density	Linear elastic properties		Damping coefficients	
	ρ (kg/m3)	E (GPa)	ν (-)	α_R (-)	β_R (-)
Koyna Dam	2643	31.027	0.15	0.082	0.0046

The geometry of a typical non-overflow monolith of the Koyna dam is illustrated in **Figure F.1**. The monolith is 103 m high and 70 m wide at its base. With the usual notation, the depth of the reservoir at the time of the earthquake is H-h = 91.75 m. In the Example Problems Manual, a two-dimensional analysis of the non-overflow monolith assuming plane stress conditions is presented. The finite element mesh used for the analysis is shown in **Figure F.2a**, consisting of 760 first order, reduced-integration, plane stress elements (CPS4R). The same plane stress conditions are simulated in a three-dimensional model in order to verify the capability of the new developed amass.f subroutine to reproduce this simple test problem. A solid dam monolith of unit thickness, unconstrained at the lateral faces, is considered. Its finite element mesh is shown in **Figure F.2b**, consisting of 825 first order, reduced-integration, 8-node brick elements (C3D8R).

The upstream wall of the monolith is assumed to be straight and vertical. In this special configuration the added mass contribution to the inertia of the wall calculated inside *addedmass_uel* exactly matches the formulation implemented in *amass1* when a Westergaard distribution of hydrodynamic pressures is assumed.

The transverse and vertical components of the ground accelerations recorded during the Koyna earthquake are shown in **Figure F.3** and applied to the base of the monolith considered as fixed. Differently from the Example Problem, no static steps are considered before the dynamic analysis.

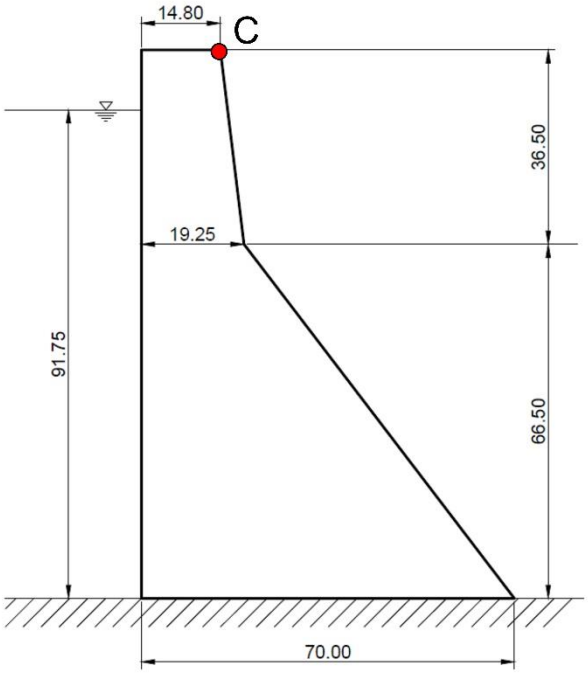

Figure F.1. Geometry of the testing problem (Koyna Dam).

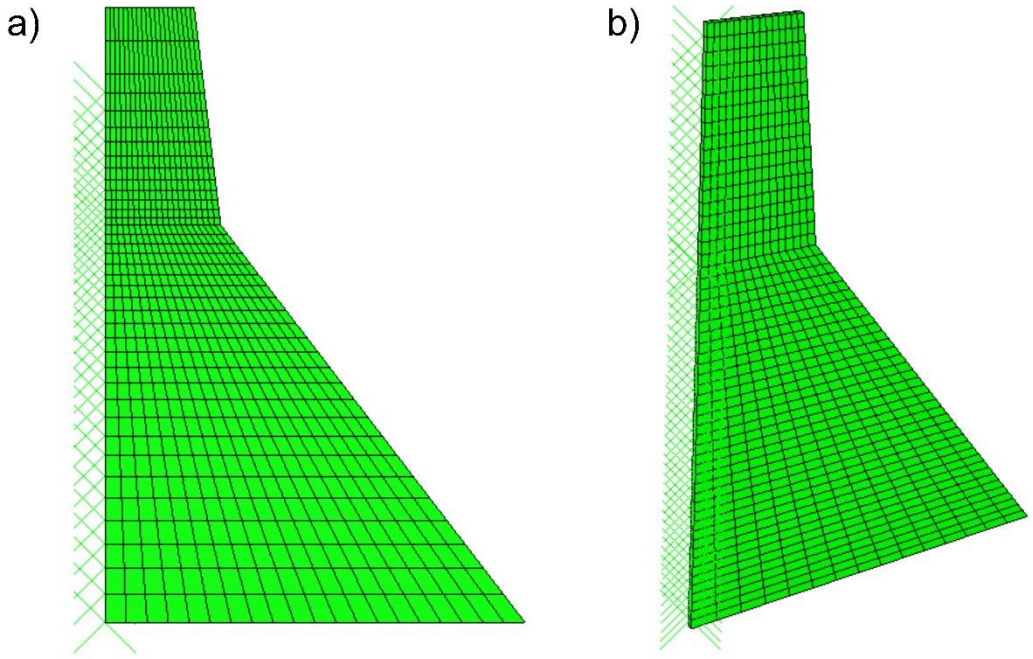

Figure F.2. a) Mesh of the original 2D Example Problem Geometry; b) Mesh of the 3D problem which implements *amass1* subroutine.

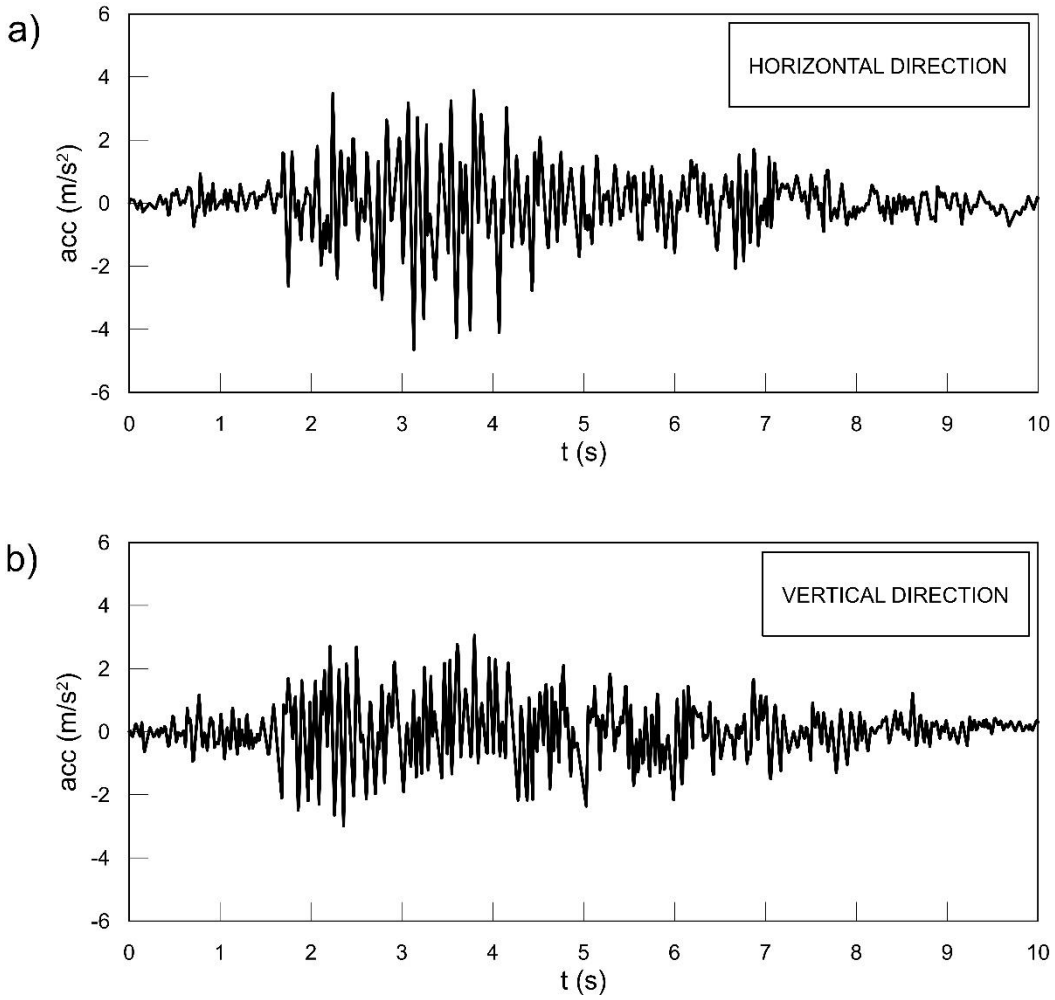

Figure F.3. Koyna earthquake: (a) transverse and (b) vertical ground accelerations.

As visible in **Figure F.2**, the green crosses representing added-mass nodes stop at the considered water level (i.e., H-h = 91.75 m) in the 2D model, while they reach the crest level of the dam in the 3D model. This apparent contradiction does not affect the results of the analyses since, differently from the original *addedmass_uel*, the hydrodynamic pressures are automatically set to zero within amass1.f for each node that is located above the reference water level of the reservoir. The *amass1* properties are selected as summarised in **Table F.2**.

Table F.2. Input parameters for *amass1*.

amass1 user parameters						
[H-h] (m)	H (m)	ρ (Kg/m^3)	c_m (-)	dim. (-)	int. pt. (-)	type (-)
91.75	91.75	1000	1.0	2	1	1

In order to compare the results of the 2D and 3D analyses, the same results, in terms of acceleration time series, are extracted for the control point C, located on the upper downstream corner/edge of the dam (see **Figure F.1**). Both accelerograms in horizontal and vertical directions for 2D and 3D analyses are plotted together in **Figure F.4**.

A perfect match is observed between the curves, which confirms the reliability of the new implemented subroutine, at least in this simple configuration.

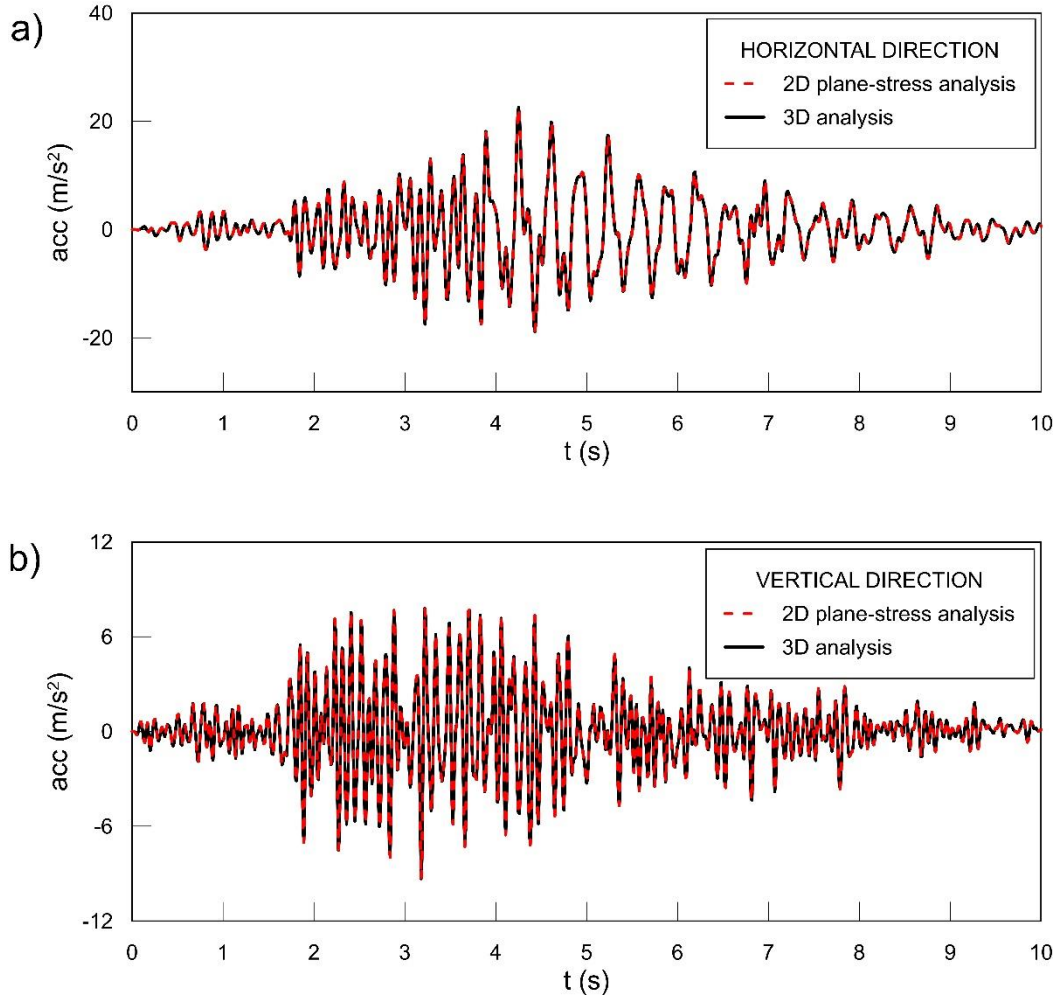

Figure F.4. Results of the test problem in terms of a) horizontal and b) vertical acceleration on the control point C.

List of figures

List of tables